



# Coordination and Ionic compounds of benzamide and related molecules and metal halides

by

Stefan Coetzee

*Presented in partial fulfillment of the requirements for the degree of*

*Masters in Science*

*at*

*The University of Pretoria*

Department of Chemistry

Faculty of Natural and Agricultural Sciences

Supervisor: Dr. M. Rademeyer

July 2012

# Declaration

---

## DECLARATION OF ORIGINALITY UNIVERSITY OF PRETORIA

The Department of Chemistry places great emphasis upon integrity and ethical conduct in the preparation of all written work submitted for academic evaluation.

While academic staff teach you about referencing techniques and how to avoid plagiarism, you too have a responsibility in this regard. If you are at any stage uncertain as to what is required, you should speak to your lecturer before any written work is submitted.

You are guilty of plagiarism if you copy something from another author's work (eg a book, an article or a website) without acknowledging the source and pass it off as your own. In effect you are stealing something that belongs to someone else. This is not only the case when you copy work word-for-word (verbatim), but also when you submit someone else's work in a slightly altered form (paraphrase) or use a line of argument without acknowledging it. You are not allowed to use work previously produced by another student. You are also not allowed to let anybody copy your work with the intention of passing it off as his/her work.

Students who commit plagiarism will not be given any credit for plagiarised work. The matter may also be referred to the Disciplinary Committee (Students) for a ruling. Plagiarism is regarded as a serious contravention of the University's rules and can lead to expulsion from the University.

The declaration which follows must accompany all written work submitted while you are a student of the Department of Chemistry. No written work will be accepted unless the declaration has been completed and attached.

Full names of student: **Stefan Coetzee**

Student number: **24374882**

Topic of work: **Coordination and Ionic Compounds of Benzamide and Related Molecules and Metal Halides**

## Declaration

1. I understand what plagiarism is and am aware of the University's policy in this regard.
2. I declare that this **dissertation** is my own original work. Where other people's work has been used (either from a printed source, Internet or any other source), this has been properly acknowledged and referenced in accordance with departmental requirements.
3. I have not used work previously produced by another student or any other person to hand in as my own.
4. I have not allowed, and will not allow, anyone to copy my work with the intention of passing it off as his or her own work.

## SIGNATURE

.....

# Acknowledgements

---

I dedicate this work to my loving and patient wife Chandré. Without her love and inexorable support this would not have been possible. I also dedicate this work to all scientists embracing their inner child asking, everyday, relentlessly, of all things... “Why?”

I would like to thank the following people/ entities for their support during the duration of this project:

- My parents Gert and Lorraine for their monetary and emotional support.
- The University of Pretoria for the opportunity to complete this degree, and for their financial support during 2011.
- My project advisor, Dr. Melanie Rademeyer for the opportunity to conduct a research project under her supervision, her superb leadership, support and amazing eye for detail.
- Dr. Bruce Anderson for introducing me to many incredibly knowledgeable experts in the scientific community and his support during the duration of this work.
- The computational experts from SASOL. Their guidance and knowledge contributed extensively in this work.
- The staff of the chemistry department at the University of Pretoria for their support and encouragement.
- Mr. Dave Liles for his contribution toward the crystallographic analysis of the presented work.
- The CHPC for hosting the Materials Studio license and the computational resources they provided.





# Conferences

---

South African Chemical Institute's Convention 2011, WITS University, Johannesburg, 16 – 21 January 2011, Poster Presentation, "Amide-containing Ionic and Coordination Organic-Inorganic Hybrids", S. Coetzee\*, M. Rademeyer, D.C. Liles

# Abstract

---

Organic-inorganic hybrid materials of divalent transition metal halides and simple organic molecules are known to exhibit interesting properties, with both the organic and the inorganic metal halide components contributing to the overall properties of the material (Aakeroy, Champness and Janaik, 2010) (Alexandre et al., 2007) (Aruta et al., 2004) (Criado et al., 1999) (Chondroudou and Mitzi, 1999) (Mitzi, Chondroudou and Kagan, 2001) (Robin and Fromm, 2006).

The benzamide molecule was chosen as the primary organic component in this study, due to its potential to form aromatic interactions, and the fact that it possesses two potential sites for hydrogen bonding or protonation or coordination, *via* the amide group. In addition, the 4-aminobenzamide molecule was investigated due to its similarity to the benzamide molecule, except for an additional functional group on the opposite side of the amide group. A range of inorganic, divalent transition metal chlorides and bromides were selected as inorganic components, including  $\text{CuX}_2$ ,  $\text{CdX}_2$ ,  $\text{CoX}_2$ ,  $\text{MnX}_2$ ,  $\text{HgX}_2$  and  $\text{ZnX}_2$ , where X = Cl or Br.

Both ionic and neutral coordination type materials can be formed through the combination of the organic components and inorganic components described above, and the outcome of the reaction is controlled by the presence or absence of acid in the reaction medium. In acidic medium protonation of the organic component results in the formation of an ionic material, and in the absence of an acid a neutral coordination material results from the coordination of the organic component to the metal atom of the metal halide component. The stoichiometry and concentration of the acid will also have an influence on the structure as some of the organic ligand may remain unprotonated.

In this study seven novel neutral coordination type structures and one ionic material were characterised by single crystal X-ray diffraction. Four isostructural, neutral, one-dimensional coordination polymer structures were observed for the combination of benzamide with  $\text{CuCl}_2$ ,  $\text{CuBr}_2$ ,  $\text{CdCl}_2$  and  $\text{CdBr}_2$  respectively. In this isostructural series the metal ions adopt an octahedral geometry in the case of the Cd analogues, and a tetragonal geometry, due to Jahn-Teller distortion, for the Cu members of the series. The combination of  $\text{ZnCl}_2$  with benzamide yielded an isolated, zero-dimensional, neutral coordination compound in which the zinc(II) ion displays a tetrahedral geometry. An octahedral, paddle wheel-type, isolated, zero-dimensional coordination molecule formed from the combination of  $\text{MnBr}_2$  and benzamide. In all the coordination compounds of benzamide, coordination was found to occur through the oxygen atom of the amide group, while the  $\text{NH}_2$  group participates in intra- and intermolecular hydrogen bonding interactions. Due to the poor basicity of benzamide, only one ionic compound of this organic component was characterised structurally. In this compound, formed in combination with  $\text{HgBr}_2$ , half of the benzamide molecules are protonated, and a unique, novel, one-dimensional perhalometallate anion was observed in this structure.

The combination of 4-aminobenzamide with  $\text{CoBr}_2$  yielded an isolated, zero-dimensional, neutral coordination structure, in which the cobalt(II) ion adopts an octahedral geometry. The neutral, coordination compound formed between 4-aminobenzamide and  $\text{CuBr}_2$  has a trigonal bipyramidal

geometry, and in addition to the organic and halogeno ligands, aqua ligands are also coordinated to the metal ion in both of the 4-aminobenzamide-containing molecules.

Hydrogen bonding and aromatic interactions occur in all of the structures, and these interaction geometries were analysed in detail. It was found that these interactions play an important role in the cohesion of the units in the structure, with exception of the ionic compound of benzamide, which displays strong hydrogen bonding interactions but long aromatic centroid-to-centroid distances.

Diffuse reflectance spectroscopy (DRS) was employed to measure the band gaps of the series of isostructural, one-dimensional coordination polymers. These measurements indicated that the Cd analogues in this series have band gaps that place them in the category of electronic insulators. The Cu members of this series were found to be two-band gap materials, with the lower of the two band gaps falling within the conductor range, while the higher band gap falls in the semi-conductor range for the structure containing  $\text{CuBr}_2$  and benzamide and the structure containing  $\text{CuCl}_2$  and benzamide.

The suitability of Density Functional Theory (DFT) calculations to theoretically calculate the electronic structures and band gap values of the isostructural series of one-dimensional coordination polymers was tested in this study. The plane-wave cut off energy and k-point grid were optimised for the structures, and a range of functionals were tested. The best performing functional was used to calculate the band gap energies, the band structures and the density of states for the four isostructural materials. DFT calculations are known to underestimate band gap energies, and even though the calculated band gaps differ from the experimentally measured band gaps, this difference is smaller than expected. In addition, the DFT calculations were successful in predicting and providing insight into the electronic characteristics of the materials.

# Table of contents

---

## Chapter One - Introduction

Crystal engineering .....	1
Interactions .....	2
Covalent and coordination interactions .....	2
Non-covalent interactions .....	2
Hydrogen bonding .....	3
$\pi$ - $\pi$ interactions.....	3
Molecular recognition.....	4
Supramolecular chemistry .....	5
Hybrid materials.....	5
Neutral and Ionic Hybrid Materials.....	5
Ionic hybrid materials .....	6
Neutral (coordination) hybrid materials.....	6
The inorganic component.....	7
Structural Dimensionality .....	8
Zero-dimensional coordination complexes .....	8
One-dimensional coordination polymers .....	9
Two-dimensional coordination polymers.....	10
Three-dimensional coordination polymers .....	11
Applications of hybrid materials .....	11
Ionic Hybrid Materials.....	12
Neutral Coordination Hybrids.....	12
Computational Chemistry .....	15
Band Structure and Band Gap.....	15
K-points and Brillouin zone .....	16
Density Functional Theory .....	19
Exchange Correlation Functionals.....	20
Local Density Approximation .....	20
Generalized Gradient Approximations (GGA).....	20
Success of DFT.....	22
Band gap calculations .....	23

Aspects of this Study .....	23
The Organic component .....	24
Organic constituent: Benzamide.....	24
Organic constituent: 4-aminobenzamide .....	26
Inorganic component.....	27
Problem definition and approach.....	27
Research aims .....	29
Bibliography .....	29
<b>Chapter Two – Experimental techniques</b>	
A. Experimental Investigation .....	35
Materials .....	35
Synthesis .....	35
catena-(Benzamide-κO)-μ <sub>3</sub> -chlorido-μ-chloridocopper(II), CuCl-BA .....	36
catena-(Benzamide-κO)-μ <sub>3</sub> -bromido-μ-bromidocopper(II), CuBr-BA .....	36
catena-(Benzamide-κO)-μ <sub>3</sub> -chlorido-μ-chloridocadmium(II), CdCl-BA .....	36
catena-(Benzamide-κO)-μ <sub>3</sub> -bromido-μ-bromidocadmium(II), CdBr-BA.....	36
<i>Trans</i> -(Tetrabenzamide(κO)-dibromidomanganese(ii)), MnBr-BA.....	36
Di(benzamide-κO)dichloridozinc(II), ZnCl-BA.....	36
Dibenzamide (Dibenzamide hydrogen) [catena-μ <sub>3</sub> -bromido-μ-bromido-dibromidomercuate(II)], HgBr-BA.....	36
<i>Trans</i> -di(4-amino-κN-benzamide)diaquadibromidocobalt(II), CoBr-4ABA.....	37
<i>Trans</i> -di(4amino-κN-benzamide)aquadibromidocopper(II), CuBr-4ABA.....	37
Single crystal X-ray Diffraction.....	37
Theory .....	37
Experimental Data collection:.....	38
Structure solution: .....	39
Other .....	39
Diffuse reflectance spectra .....	39
Theory .....	39
Determination of the band gap from DRS .....	40
Experimental Data Collection .....	41
B. Computational Investigation .....	41
Bibliography .....	42



### Chapter Three – Experimental results

Structural Analysis .....	44
<i>Trans</i> -(Tetrabenzamide( $\kappa$ -O)-dibromidomanganese(II)), MnBr-BA.....	49
catena-(Benzamide- $\kappa$ O)- $\mu_3$ -chlorido- $\mu$ -chloridocopper(II), CuCl-BA .....	53
catena-(Benzamide- $\kappa$ O)- $\mu_3$ -bromido- $\mu$ -bromidocopper(II), CuBr-BA .....	57
Di(benzamide- $\kappa$ O)dichloridozinc(II), ZnCl-BA.....	60
catena-(Benzamide- $\kappa$ O)- $\mu_3$ -chlorido- $\mu$ -chloridocadmium(II), CdCl-BA .....	65
catena-(Benzamide- $\kappa$ O)- $\mu_3$ -bromido- $\mu$ -bromidocadmium(II), CdBr-BA.....	68
Dibenzamide (Dibenzamide hydrogen) [catena- $\mu_3$ -bromido- $\mu$ -bromido-dibromidomercuate(II)], HgBr-BA .....	72
<i>Trans</i> -di(4-amino- $\kappa$ N-benzamide)diaquadibromidocobalt(II), CoBr-4ABA.....	78
<i>Trans</i> -di(4amino- $\kappa$ N-benzamide)aquadibromidocopper(II), CuBr-4ABA.....	81
Experimental determination of band gap energies .....	85
Bibliography .....	89

### Chapter Four - Computational results

Plane-wave convergence .....	90
K-point convergence .....	92
Choice of functional .....	94
Calculated band gaps .....	95
Calculated band structures .....	100
Density of States .....	101
Cadmium containing compounds .....	101
Copper containing compounds .....	104
Bibliography .....	109

### Chapter Five – Discussion

Structural Comparison .....	110
Comparison of all Crystal Structures: .....	110
Stoichiometry.....	110
Structural Dimensionality .....	110
Geometry of organic component.....	111
Coordination geometry.....	113
Ligand Coordination Site .....	114
Hydrogen bonding interactions .....	114

Aromatic Interactions .....	114
Comparison of Isostructural compounds with each other and with literature structures.....	115
Unit cell parameters.....	115
Intralayer/ Interlayer spacing .....	117
Benzamide ligand tilt angle relative to inorganic plane.....	119
Metal-to-metal distances in the coordination polymer .....	119
Ring-to-Ring distances .....	120
Comparison of isostructural compounds with literature structures.....	124
Comparison of ZnCl-BA with literature structure .....	126
Comparison of the CuBr-4ABA structure with literature structures .....	129
Comparison of Experimental Band Gaps of Isostructural Compounds .....	129
Comparison of Computational Results for Isostructural Compounds .....	133
Comparison of Cadmium Containing Compounds.....	133
Comparison of Copper Containing Compounds .....	134
Comparison of calculated and measured band gap results for isostructural compounds.....	136
Composition effect on properties.....	138
Bibliography .....	138
<b>Chapter 6 - Conclusions and future work</b>	
Conclusions .....	140
Future work.....	141
<b>Contents of CD</b>	
Crystallographic information and related files of:	
MnBr-BA	
CuCl-BA	
CuBr-BA	
ZnCl-BA	
CdCl-BA	
CdBr-BA	
HgCl-BA	
CoBr-4ABA	
CuBr-4ABA	

# List of figures

## Chapter One - Introduction

Figure 1: A schematic illustrating the preferred orientation of metal-halide hydrogen bonding (Yap et al., 1995) .....	3
Figure 2: $\pi$ - $\pi$ stacking. Different $\pi$ - $\pi$ stacking modes (left), Forces governing $\pi$ - $\pi$ stacking (right) (Janiak, 2000) .....	4
Figure 3: Example of an anionic coordination polymer. Blue metal atoms are bridged by purple halogeno ligands. Repetition of this bridging would result in the formation of a one-dimensional coordination polymer, or two- or three-dimensional network solid.....	7
Figure 4: A general scheme illustrating an ionic structure consisting of isolated cations and a polymeric, one-dimensional anion. Consider the inorganic component to be repeated an infinite number of times. ....	7
Figure 5: A general scheme illustrating a coordination polymer. Consider this unit to be repeated an infinite number of times. ....	8
Figure 6: Example of an isolated, zero-dimensional coordination compound (CSD Refcode: VUCVAR) (Savinkina et al., 2009).....	9
Figure 7: Example of an edge shared one-dimensional neutral coordination polymer (Hu, Kalf and Englert, 2007).....	10
Figure 8: Two-dimensional ionic inorganic polymer. (CSD Refcode: BAKHIF) (Mitzi, Dimitrakopoulos and Kosbar, 2001) .....	10
Figure 9: Example of an edge shared two-dimensional tetrahedral neutral coordination polymer (Graham and Pike, 2000). ....	11
Figure 10: Three dimensional neutral coordination polymer with orange spheres representing Mn ions. Blue spheres represent the azide bridging anions, and red spheres represent the organic 4-aminobenzoic acid ligands (Chen et al., 2009). ....	11
Figure 11: Schematic representation of a copper(I) nanowire (Mateo-Marti et al., 2008).....	13
Figure 12: Intricate one-dimensional polymer with semi-conductive properties (Liu et al., 2009). ....	13
Figure 13: Copper(I) hetero-bridged polymer. (Li et al., 2011).....	14
Figure 14: Thermochromic behavior of a copper(I) hetero-bridged polymer (Li et al., 2011) .....	14
Figure 15: Example of a Brillouin zone, and the use of special characters to indicate specific positions on the Brillouin zone ( <a href="http://en.wikipedia.org/wiki/Brillouin_zone">http://en.wikipedia.org/wiki/Brillouin_zone</a> ).....	17
Figure 16: Example of a band structure diagram. Accessed online at ( <a href="http://www.fhi-berlin.mpg.de/th/fhi98md/doc/main/node19.html">http://www.fhi-berlin.mpg.de/th/fhi98md/doc/main/node19.html</a> ) .....	17
Figure 17: An example of the DOS (left) of Silicon with accompanying band structure (left). Accessed online at <a href="http://www.theochem.unito.it/crystal_tuto/mssc2008_cd/tutorials/properties/properties_tut.html">http://www.theochem.unito.it/crystal_tuto/mssc2008_cd/tutorials/properties/properties_tut.html</a> .....	18
Figure 18: Illustration of Direct (left) and Indirect (right) band gaps. ....	18
Figure 19: Line structure and resonance structures of benzamide .....	24
Figure 20: Protonation of an amide a.) Nitrogen protonated b.) Oxygen protonated and c.) Additional resonance structure. ....	26
Figure 21: Line structure of 4-aminobenzamide.....	27



## Chapter Two – Experimental techniques

Figure 22: Praying Mantis Diffuse Reflection Accessory. Accessed online at <a href="http://www.harricksci.com/ftir/accessories/group/Praying-Mantis%E2%84%A2-Diffuse-Reflection-Accessory">http://www.harricksci.com/ftir/accessories/group/Praying-Mantis%E2%84%A2-Diffuse-Reflection-Accessory</a> .....	40
Figure 23: Example of diffuse reflectance spectra. (Morales, Mora and Pal, 2007)	40
Figure 24: Example of the band gap determination through the Kubelka-Munk remission function using a Tauc plot (Morales, Mora and Pal, 2007) (Tauc and Menth, 1972). .....	41

## Chapter Three – Experimental results

Figure 25: Asymmetric unit of MnBr-BA showing the atomic numbering scheme. Displacement ellipsoids are drawn at the 50% probability level and hydrogen atoms are drawn as spheres of arbitrary radii. ....	49
Figure 26: Coordination geometry of MnBr-BA, showing the paddle wheel structure of the molecule. ....	49
Figure 27: Aromatic ring orientation in MnBr-BA. Some of the neighbouring ligands and hydrogen atoms were omitted for clarity. ....	51
Figure 28: Packing diagram of MnBr-BA along the a). <i>a</i> -axis b). <i>b</i> -axis and c). <i>c</i> -axis. Hydrogen atoms omitted for clarity. ....	51
Figure 29: a). Hydrogen bonding of MnBr-BA with a). Intramolecular hydrogen bonding shown b). hydrogen bonding network viewed along the <i>a</i> -axis and c). hydrogen bonding network viewed along the <i>b</i> -axis. Note that the aromatic rings were not shown in b and c for clarity. ....	52
Figure 30 : Asymmetric unit of CuCl-BA showing the atomic numbering scheme. Displacement ellipsoids are drawn at the 50% probability level and hydrogen atoms are drawn as spheres of arbitrary radii. ....	53
Figure 31: Octahedral coordination geometry of CuCl-BA illustrating the Jahn-Teller elongation of the axial bonds, and compression of the equatorial bonds. ....	54
Figure 32: Polymeric one-dimensional motif of CuCl-BA. ....	54
Figure 33: Polyhedral representation of the one-dimensional inorganic polymer. Organic ligand not shown for clarity. ....	55
Figure 34: Packing of polymeric units in CuCl-BA. a). Arbitrary view b). Viewed down the <i>a</i> -axis c). Viewed down the <i>b</i> -axis d). Viewed down the <i>c</i> -axis. ....	55
Figure 35: Hydrogen bonding interactions of CuCl-BA viewed along the <i>a</i> -axis. ....	56
Figure 36 : Asymmetric unit of CuBr-BA showing the atomic numbering scheme. Displacement ellipsoids are drawn at the 50% probability level and hydrogen atoms are drawn as spheres of arbitrary radii. ....	57
Figure 37: Coordination geometry of CuBr-BA showing elongation of the axial bonds to the bromido ligands. ....	57
Figure 38: Polymeric one dimensional motif of CuBr-BA. ....	58
Figure 39: Polyhedral representation of the one dimensional inorganic polymer. Organic ligand not shown for brevity. ....	58

Figure 40: Packing of polymeric units in CuBr-BA. a). Arbitrary view b). View down a-axis c). View down b-axis and d). View down c-axis .....	59
Figure 41: Hydrogen bonding interactions of CuBr-BA viewed along the $a$ -axis.....	59
Figure 42: Asymmetric unit of ZnCl-BA showing the atomic numbering scheme. Displacement ellipsoids are drawn at the 50% probability level and hydrogen atoms are drawn as spheres of arbitrary radii. ....	60
Figure 43: Comparison of the two molecules contained in the asymmetric unit. ....	61
Figure 44: Comparison of molecule 1 (Left) and molecule 2 (right) of ZnCl-BA .....	61
Figure 45: Packing diagram of ZnCl-BA along the a). $a$ -axis b). $b$ -axis and c). $c$ -axis. ....	62
Figure 46: Intra-sheet and intramolecular hydrogen bonding ZnCl-BA.....	63
Figure 47: Hydrogen bonding network in ZnCl-BA. Carbon and hydrogen atoms are omitted for clarity. ....	63
Figure 48: Different intermolecular hydrogen bonding formation of molecule 1 (Left) and molecule 2 (right). ....	64
Figure 49 : Asymmetric unit of CdCl-BA showing the atomic numbering scheme. Displacement ellipsoids are drawn at the 50% probability level and hydrogen atoms are drawn as spheres of arbitrary radii. ....	65
Figure 50: Coordination geometry of CdCl-BA.....	65
Figure 51: Polymeric one-dimensional motif of CdCl-BA.....	66
Figure 52: Polyhedral representation of the one-dimensional inorganic polymer. Organic ligand not shown for brevity. ....	66
Figure 53: Hydrogen bonding interactions of CdCl-BA viewed along the $a$ -axis. ....	67
Figure 54: Packing of polymeric units in CdCl-BA. a). Arbitrary view b). View down $a$ -axis c). View down $b$ -axis and d). View down $c$ -axis .....	67
Figure 55: Asymmetric unit of CdBr-BA showing the atomic numbering scheme. Displacement ellipsoids are drawn at the 50% probability level and hydrogen atoms are drawn as spheres of arbitrary radii. ....	68
Figure 56: Coordination geometry of CdBr-BA. ....	69
Figure 57: Polymeric one dimensional motif of CdBr-BA .....	69
Figure 58: Polyhedral representation of the one-dimensional inorganic polymer. Organic ligand not shown for brevity. ....	70
Figure 59: Packing of polymeric units in CdBr-BA. a). Arbitrary view b). View down $a$ -axis c). View down $b$ -axis and d). View down $c$ -axis .....	71
Figure 60: Hydrogen bonding interactions of CdBr-BA viewed along the $a$ -axis.....	71
Figure 61: Initial asymmetric unit of HgBr-BA showing the atomic numbering scheme. Displacement ellipsoids are drawn at the 50% probability level. Hydrogen atoms including protonation sites have been omitted for brevity.....	72
Figure 62: a). Location of proton as determined by neutron diffraction in the structure of acetamide hemihydrochloride, CSD refcode: ACAMCL01. Figures showing proximity of oxygen atoms in protonated amide structures b). ACAMBR02 c). BZAMTI01 d). SUCABT (Dahan and Lefebvre-Soubeyran, 1976) e). current structure, HgBr-BA.....	73
Figure 63: Asymmetric unit of HgBr-BA showing the atomic numbering scheme. Displacement ellipsoids are drawn at the 50% probability level, and hydrogen atoms are shown as spheres of arbitrary radius. ....	74

Figure 64: Coordination geometries of the two mercury ions in HgBr-BA. Note the compression of the axial Br4-Hg2 bonds and elongation of the Br3-Hg1 and Br2-Hg1 bonds. .... 74

Figure 65: Polyhedral representation of the one dimensional inorganic polymer. Organic ligand not shown for clarity. .... 75

Figure 66: Packing of polymeric units in HgBr-BA viewed along the a). View down *a*-axis b). View down *b*-axis and c). View down *c*-axis ..... 76

Figure 67: a). Hydrogen bonding interactions b). resulting hydrogen bonded sheet. .... 77

Figure 68: Asymmetric unit of CoBr-4ABA showing the atomic numbering scheme. Displacement ellipsoids are drawn at the 50% probability level and hydrogen atoms are drawn as spheres of arbitrary radii. .... 78

Figure 69: Coordination geometry of CoBr-4ABA..... 79

Figure 70: Packing diagram of CoBr-4ABA viewed along the a). *a* –axis b). *b*-axis and c). *c*-axis. .... 79

Figure 71: View along the *b*-direction of the parallel and angles arrangement of aromatic rings in CdBr-4ABA..... 80

Figure 72: Three-dimensional hydrogen bonding network viewed along the a). *a*-axis and b). *b*-axis. .... 80

Figure 73: Asymmetric unit of CuBr-4ABA showing the atomic numbering scheme. Displacement ellipsoids are drawn at the 50% probability level and hydrogen atoms are drawn as spheres of arbitrary radii. .... 81

Figure 74: Packing diagram of CuBr-4ABA viewed along the a). *a* –axis b). *b*-axis and c). *c*-axis. .... 82

Figure 75: Orientation of aromatic groups in CuBr-4ABA..... 82

Figure 76: Novel one dimensional "triple helix" formed by CuBr-4ABA molecules. .... 83

Figure 77: One dimensional hydrogen bonded network of CuBr-4ABA..... 83

Figure 78: Three-dimensional hydrogen bonded network of CuBr-4ABA ..... 84

Figure 79: DRS spectrum of CdCl-BA (top). Tauc plot of CdCl-BA (bottom). The intersection of the linear absorption edge and the maximum reflectance line is the estimated band gap energy..... 85

Figure 80: DRS spectrum of CdBr-BA (top). Tauc plot of CdBR-BA (bottom). The intersection of the linear absorption edge and the maximum reflectance line is the estimated band gap energy..... 86

Figure 81: DRS spectrum of CuCl-BA..... 86

Figure 82: Tauc plot of CuCl-BA. The intersection of the linear absorption edge and the maximum reflectance line is the estimated band gap energy..... 87

Figure 83: DRS spectrum of CuBr-BA. .... 88

Figure 84: Tauc plot of CuBr-BA. The intersection of the linear absorption edge and the maximum reflectance line is the estimated band gap energy..... 88

#### Chapter Four - Computational results

Figure 85: Plane wave cut-off energy convergence of CdCl-BA. The blue graph shows the free energy, with reference to the left axis, and the red graph illustrates the relative free energy, associated with the right axis. .... 91

Figure 86: Plane wave cut-off energy convergence of CdCl-BA, CdBr-BA, CuCl-BA and CuBr-BA. The CuBr-BA and CuCl-BA convergence values for 650 eV and 750 eV are in the order of  $5 \times 10^{-4}$  and  $2 \times 10^{-4}$  respectively and are not shown..... 92

Figure 87: K-point convergence scheme of CdCl-BA. The change in free energy of 1x1x1, 2x1x1 and 2x2x2 were omitted as they were orders of magnitude larger. The blue graph shows the free energy (left axis), and the red graph the relative free energy (right axis). ..... 93

Figure 88: Determination of the true magnetic state of a material ..... 96

Figure 89: Calculated band structures of CuCl-BA (top left) CuBr-BA (top right) CdCl-BA (bottom left) and CdBr-BA (bottom right). Arrows indicate the transitions from valence band to conduction band. The red band indicates a  $\beta$ -orbital whilst a blue band indicated an  $\alpha$ -orbital..... 100

Figure 90: Total and Partial DOS of CdCl-BA. Note all of the DOS are shown to the same scale. .... 101

Figure 91: Total and partial DOS of CdBr-BA. Note all of the DOS are shown to the same scale..... 102

Figure 92: Aromatic- $\pi$  HOMO (left) and Aromatic- $\pi^*$  LUMO orbitals (right) of CdCl-BA (top) and CdBr-BA (bottom). All orbitals are drawn at an iso-value of 0.01. .... 103

Figure 93: Total and partial DOS of CuCl-BA. Note that the DOS are not all to the same scale for clarity. .... 104

Figure 94: The HOMO; alpha spin (top left), LUMO; beta spin (top right) and combined HOMO/LUMO orbitals of CuBr-BA. The HOMO and LUMO orbitals shown differ by the band gap quoted in Table 36. All orbitals were drawn at an iso-value of 0.01 ..... 105

Figure 95: Total and partial DOS of CuBr-BA. Note that the DOS are not all to the same scale for clarity. .... 106

Figure 96: The HOMO; alpha spin (top left), LUMO; beta spin (top right) and combined HOMO/LUMO orbitals of CuBr-BA. The HOMO and LUMO orbitals shown differ by the band gap quoted in Table 36. All orbitals were drawn at an iso-value of 0.01 ..... 107

## Chapter Five – Discussion

Figure 99: Comparison of isostructural compounds' unit cell parameters. .... 116

Figure 100: Unit cell volume comparison for the isostructural compounds. .... 117

Figure 101: Comparison of the intralayer spacing for the isostructural compounds..... 118

Figure 102: The angle formed between the aromatic ring plane and the inorganic layer plane..... 119

Figure 103: Definition of the Metal-toMetal distances used in this section. .... 120

Figure 104: Schematic representing how the plane to plane distance can remain constant with rotational compensation from the aromatic rings. a: metal to metal distance, b: centroid to centroid distance, c: plane to plane distance and d: slippage ..... 122

Figure 105: Definition of the angle between adjacent metals and the plane of the aromatic ring. ... 122

Figure 106: Simplified scheme depicting how to determine the angle that rings rotate to accommodate larger metal to metal distances. .... 123

Figure 107: Examples of CdCl<sub>2</sub> containing analogous structures. Structures MURCDC (left) and ZZZECM01 (right) shown (Nardelli, Coghi and Azzoni, 1958) (Furmanova et al., 1996)..... 125

Figure 108: Overlay comparison of the ZnCl-BA (blue) (molecule 1 left and molecule 2 right) and ZnI-BA (red) structures..... 126

Figure 109: Comparison of ZnCl-BA (top) with similar ZnI-BA structure (bottom)..... 128

Figure 110: Comparison of packing diagrams of ZnCl-BA (left) with ZnI-BA structure (right). Top: View down *b* for ZnCl-BA and view down *a* for ZnI-BA. Middle: View down *a* for ZnCl-BA and view down *b* for ZnI-BA. Bottom: View down *a* for ZnCl-BA and view down *b* for ZnI-BA ..... 128

Figure 111: Indirect/direct interband transition..... 131

Figure 112: Possible explanation of the diffuse reflectance spectra..... 132

Figure 113: Calculated band structures of CuCl-BA (left) CuBr-BA (right). The black arrows indicate the electronic transitions from valence band to conduction band 1 ( $E_{g1}$ ) and red arrows indicate the electronic transitions from the valence band to the second conduction band ( $E_{g2}$ ). The red band indicates a  $\beta$ -orbital whilst a blue band indicated an  $\alpha$ -orbital. .... 134

Figure 114: Upper conduction band orbitals of CuBr-BA. The  $\alpha$ -orbitals are shown in blue and the  $\beta$ -orbitals are shown in red. .... 135

Figure 115: Upper conduction band orbitals of CuCl-BA. The  $\alpha$ -orbitals are shown in blue and the  $\beta$ -orbitals are shown in red. .... 135

# List of tables

---

## Chapter One - Introduction

Table 1: Examples of the sharing of bonds in one-dimensional coordination polymers.....	9
Table 2: Divalent metal halides used in this study.....	27

## Chapter Three – Experimental results

Table 3: Crystallographic parameters for all structures .....	45
Table 4: Selected bond lengths of MnBr-BA.....	50
Table 5: Selected bond lengths of MnBr-BA.....	50
Table 6: Hydrogen bonding parameters.....	52
Table 7: Selected bond lengths of CuCl-BA.....	54
Table 8: Selected bond angles .....	54
Table 9: Hydrogen bonding parameters.....	56
Table 10: Selected tetragonal bond lengths of CuBr-BA .....	58
Table 11: Selected angles.....	58
Table 12: Hydrogen bonding parameters.....	60
Table 13: Selected.....	61
Table 14: Selected coordination angles.....	61
Table 15: Selected Centroid parameters for ZnCl-BA.....	62
Table 16: Hydrogen bond parameters for ZnCl-BA.....	64
Table 17: Selected bond lengths of CdCl-BA.....	66
Table 18: Selected angles of CdCl-BA.....	66
Table 19: Hydrogen bonding parameters.....	68
Table 20: Selected Octahedral bond lengths of CdBr-BA .....	69
Table 21: Selected angles.....	69
Table 22: Hydrogen bonding parameters.....	72
Table 23: Comparison of O...O distances for selected amides found in the CSD.....	73
Table 24: Selected coordination bond lengths of HgBr-BA.....	75
Table 25: Selected coordination angles of HgBr-BA.....	75
Table 26: Hydrogen bonding parameters for HgBr-BA.....	77
Table 27: Hydrogen bonding parameters for CdBr-4ABA.....	81
Table 28: Selected bond distances.....	81
Table 29: Selected angles of CoBr-4ABA.....	81
Table 30: Hydrogen bonding parameters of CuBr-4ABA.....	84
Table 31: Summary of band gap energies as measured by DRS.....	89

## Chapter Four - Computational results

Table 32: Convergence of the k-point grid in the <i>a</i> -direction.....	94
Table 33: Convergence of the k-point grid in the <i>b</i> - and <i>c</i> -direction.....	94









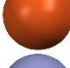

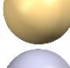

Table 34: Functional validation for CdBr-BA.....	95
Table 35: Functional validation for CdCl-BA .....	95
Table 36: Calculated band gap energies (GGA-PBESol, 850 eV, 6x2x2).....	96
Table 37: Effect of the addition of the Hubbard potential (U) on calculated band gap energies of CuBr-BA.....	97
Table 38: Comparison of different functionals for CdBr-BA .....	98
Table 39: Summary of calculated band gap energies (GGA-PBESol, 850 eV, 6x2x2).....	108

## Chapter Five – Discussion

Table 40: Comparison of synthetic molar ratios and experimental molar ratios.....	110
Table 41: Comparison of amide group rotation relative to aromatic ring for benzamide containing structures .....	111
Table 42: Comparison of M-N-C angles of the coordinated amine group in the 4-aminobenzamide containing structures .....	112
Table 43: Comparison of amide group rotation relative to aromatic ring for the 4-aminobenzamide containing structures .....	112
Table 44: Comparison of the C-O bond lengths for the amide group of the benzamide containing structures.....	113
Table 45: Comparison of coordination geometries .....	113
Table 46: Comparison of $\pi$ - $\pi$ interaction parameters.....	115
Table 47: Unit cell parameters for the isostructural compounds.....	116
Table 48: Intralayer distances of the isostructural compounds .....	117
Table 49 : Interlayer spacing of the isostructural compounds .....	118
Table 50: Comparison of the angles formed between the aromatic ring plane and the inorganic layer plane. ....	119
Table 51: Comparison of the metal-to-metal distances for the isostructural compounds .....	120
Table 52: Comparison of the ring-to-ring distances of the isostructural compounds.....	121
Table 53: Calculated angles of the rings with respect to the metal-metal-oxygen plane .....	123
Table 54: Calculation of change in angle of aromatic rings with respect to an increase of metal to metal distances. ....	124
Table 55: Analogous structures to isostructural compounds found in the CSD.....	125
Table 56: Analogous CdCl <sub>2</sub> and amide containing compounds' bond distance comparison with CdCl-BA. ....	126
Table 57: Comparison of bond distances (Å) and bond angles (°) of ZnI-BA and ZnCl-BA (This study). Values for both moieties in the asymmetric unit of ZnCl-BA are given. (Standard deviation given in brackets) .....	127
Table 58: Comparison of band gap energies as measured by DRS for the isostructural compounds. ....	129
Table 59: Comparison of calculated band gap energies for the isostructural compounds.....	133
Table 60: Summary of calculated band gap energies for the isostructural compounds.....	136
Table 61: Comparison of experimental and calculated band gaps.....	137

# Definition of atomic colors

---

	Hydrogen
	Carbon
	Nitrogen
	Oxygen
	Chlorido
	Bromido
	Manganese
	Cobalt
	Copper
	Zinc
	Cadmium
	Mercury

*“No amount of experimentation can ever prove me right; a single experiment can prove me wrong”*

*Albert Einstein*



# Chapter One - Introduction

---

In the field of material science there is always a constant drive toward improving electronically interesting, optically interesting and generally interesting properties in materials, with the ultimate aim of identifying materials suitable for specific applications. To firstly create these materials, a good understanding of their chemical composition, their chemical structures, as well as the role of composition on crystalline structure, is required. In addition, a fundamental understanding of how a material's structure controls its physical and chemical properties is needed.

The first of these aspects, the relationship between chemical composition and structure, can be better understood through crystal engineering. However, crystal engineering also aims to reach further, by providing a way of understanding the properties of a material through its structure. To understand the relationship between the structure of a material and its properties, the experimental measurement of properties, and the correlation of the measured properties with the structure of the material, are required, as well as the interpretation of the results using crystal engineering concepts.

In addition to experimental studies, the use of computational techniques to obtain information on the structures and properties of materials has become increasingly popular in recent years. The ultimate goal of these theoretical techniques would be the calculation of structural characteristics and properties of a new material, without preparing the material in the laboratory. However, in general, this level of accuracy in theoretical calculations has not been attained yet. This does not, however, prevent the exploration of the applicability of the currently available techniques and methods to the materials of interest in this project.

Thus, the current investigation aims to employ the principles of the field of crystal engineering and computational chemistry to better understand the electronic structure of organic-inorganic hybrid materials formed through the combination of transition metal halides and benzamide or benzamide derivatives.

This first chapter introduces concepts that are key to the investigation, including an introduction to crystal engineering and supramolecular chemistry, as well as an explanation of why the organic-inorganic hybrids were selected for the study.

## Crystal engineering

Crystal engineering can be defined as the purposeful design of molecular "building blocks" or synthons to yield the unique properties desired (Brammer, 2004). Traditionally the first attempt to purposely design crystals was attributed to Schmidt in 1971 with his work in photodimerisation in the solid state of cinnamic acid acids. However, the proceedings of the American Physical Society Meeting held in Mexico City in August 1955 (*Phys. Rev.*, 1955, 100, 952) report an even earlier abstract titled "Crystal Engineering: a new concept in crystallography", by R. Pepinsky of the Pennsylvania State University. The abstract reads as follows:

*“Crystallization of organic ions with metal-containing complex ions of suitable sizes, charges and solubilities results in structures with cells and symmetries determined chiefly by packing of complex ions. These cells and symmetries are to a good extent controllable: hence crystals with advantageous properties can be ‘engineered’”* (Braga, 2003).

Development of this concept by Desiraju lead to the modern day definition of crystal engineering: “It is the understanding of intermolecular interactions in the context of crystal packing and in the utilization of such understanding in the design of new solids with desired physical and chemical properties” (Desiraju, 1997). Crystal engineering is then basically defined as the deliberate design of crystals from basic building blocks or “synthons” based on intermolecular interactions, and covalent bonds to achieve desired physical properties. Synthons are defined by Corey (1967) as: “...*structural units within molecules which can be formed and/or assembled by known or conceivable synthetic operation*”.

Before proper design of these synthons can even begin, a fundamental understanding of all the factors that affect the positioning, assembly and stabilization of the synthons should be acquired. It should be attempted to understand the role of each synthon in the structure to understand why a certain structure is obtained.

## Interactions

The building blocks can interact via several types of interactions ranging from the strong (covalent) to the weak (intermolecular interactions). These forces act in certain ways, dictated by the type of interaction; some forces’ result will be more pronounced, whereas some forces may hardly play a role in the end product, the crystal structure. These forces are in a state of equilibrium at a point where the crystal exists in a state of minimal energy. Therefore, in order to understand the “equilibrium state” a crystal inherently adopts, a thorough understanding of the abovementioned interactions is needed.

### Covalent and coordination interactions

Covalent and coordination interactions are considered in chemistry as very strong interactions. Rigid covalent interactions in crystal engineering do not however affect the packing of a crystal to a great extent, based on the assumption that most of the covalent interactions are fixed before the crystal lattice starts to pack. Before the material in question is synthesized, most of the covalent bonds have formed in solution. Flexibility in these bonds may, however, play a role in the structure adopted, and the polymorph formed. Covalent interactions, due to their strong nature, do however play a role in the configuration of molecules in a crystal lattice. The formation of covalent bonds will override any weaker interactions that may want to be kept apart.

### Non-covalent interactions

The non-covalent interactions are to structural chemistry what gravity is to Newtonian physics and is therefore perhaps the most prevalent and important variable to consider in crystal engineering. These interactions exist between molecules or molecular ions and result in the overall attraction of molecules to one another at a certain distance where the attractive forces are balanced by the repulsive forces.

These non-bonding interactions dictate how, and to what degree, two molecules “stick together”. These forces are essential to the formation of the crystal structures observed in supramolecular structures. Some of these forces include: van der Waals interactions, hydrogen bonding, electrostatic interactions,  $\pi$ - $\pi$  interactions and hydrophobic interactions. Some of these interactions affect the packing of a crystal structure more than others and only those observed and most relevant to this study will be discussed.

### Hydrogen bonding

Hydrogen bonding is the interaction that is observed when a hydrogen atom that is covalently bonded to an electronegative atom, the donor atom, also interacts with an electronegative species like oxygen, nitrogen or even a halogen atom, the acceptor atom. The interaction energy of a hydrogen bond can vary over more than two orders of magnitude (-0.2 – 40 kcal/mol) (Steiner, 2002). It is typically weaker than an ionic bond or covalent bond but still stronger than van der Waals interactions. Strong hydrogen bonds may even have energies comparable to covalent bonds, but these examples are few. Hydrogen bonds play a critical role in the way in which many structures are held together. In a classical hydrogen bond, the hydrogen atom is shared between a single hydrogen bond donor, and a single hydrogen bond acceptor. Bifurcated hydrogen bonds occur when a single hydrogen atom is shared between two hydrogen bond acceptors. Similarly, in a trifurcated hydrogen bond a hydrogen atom is shared between three hydrogen bond acceptors (Steiner, 2002). The definition of a hydrogen bond however is still a controversial matter in the literature (Arunan, 2007).

Recent developments in the literature have suggested interesting alternatives to the classical hydrogen bond. Hydrogen bonding has been demonstrated with benzene ring  $\pi$ -electron density as hydrogen bond acceptors by Worth and Wade with respect to the importance it holds in protein structures (Worth and Wade, 1995). Hydrogen bonding also occurs with halides as hydrogen bond acceptors and restricted angles in hydrogen bonding is observed for halogen hydrogen bond acceptors bonded to transition metals. The perpendicular nature of these hydrogen bonds is due to the basicity of the unhybridized p-orbitals perpendicular to M-Halogen bonds as shown below (Yap et al., 1995).

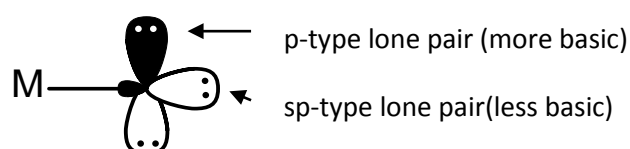


Figure 1: A schematic illustrating the preferred orientation of metal-halide hydrogen bonding (Yap et al., 1995)

In this study the following definition of a hydrogen bonding interaction will be used:  $H...A < r(A) + 2.000$  Angstroms and  $\langle DHA \rangle > 110^\circ$ , where  $r(A)$  represents the van der Waals radius of the acceptor atom, and  $\langle DHA \rangle$  represents the angle formed between the donor atom, the hydrogen atom and the acceptor atom.

### $\pi$ - $\pi$ interactions

Another interaction commonly employed in crystal engineering is  $\pi$ - $\pi$  stacking, which refers to the stacking of aromatic rings close to one another in crystal structures. Several modes of  $\pi$  interactions exist namely, eclipsed, staggered and T-shaped interactions. This stacking is as a result of the

competition between the electrostatic attraction of the partially negative  $\pi$ -orbital of the ring with the partially positive  $\sigma$ -orbital and the electrostatic repulsion of the negative  $\pi$ -orbitals and positive  $\sigma$ -orbitals with themselves as shown in Figure 2.

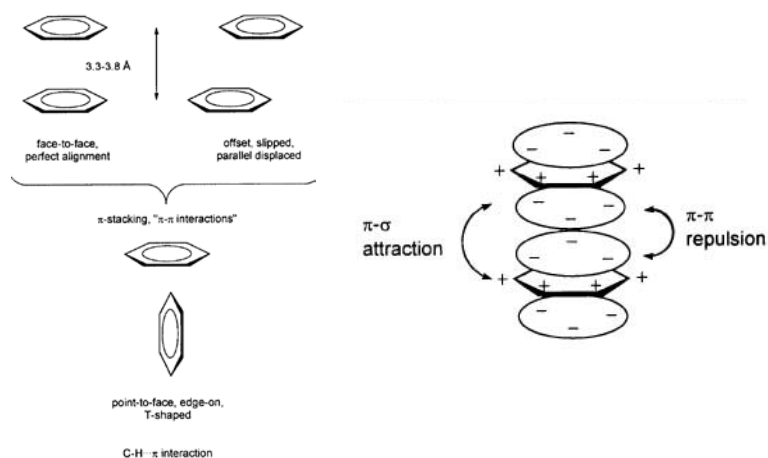


Figure 2:  $\pi$ - $\pi$  stacking. Different  $\pi$ - $\pi$  interaction modes (left), Forces governing  $\pi$ - $\pi$  stacking (right) (Janiak, 2000)

Typical distances between the centroids of stacked rings are 3.6 Å - 4.6 Å and typical angles between staggered stacked rings are 20° (Janiak, 2000).

The concept of aromatic systems, rather than simply rings, engaging in  $\pi$ - $\pi$  interactions, is not unfamiliar as Hunter & Sanders demonstrated for large porphyrin systems (Hunter and Sanders, 1990).

All of these interactions, and others not discussed here, result in the self-assembly of molecules in a crystal lattice as the molecules “recognize” each other through non-covalent interactions.

## Molecular recognition

Molecular recognition is the interaction that arises between two molecules, which is as a result of the non-bonding forces between molecules. In general this phenomenon is well recognised in biochemical systems as enzymes become activated or in the folding of proteins (Gellman, 1997), but is also applicable to the ordered assembly of molecules into a crystal structure. This interaction is fueled by hydrogen bonding, van der Waals forces, hydrophobic interactions and  $\pi$ - $\pi$  electrostatic interactions. Molecules essentially recognize one another through functional groups present on the molecules (Li et al., 2007), and this leads to organization of the molecules to obtain a minimal energy state. This may not necessarily be the global minimum conformer one may observe in the gas phase or liquid phase, but rather a minimum conformer keeping all longer range interactions in mind. This mechanism of recognition is analogous to a lock and key: certain features of both the lock and key leads to a certain orientation to which interaction or docking can occur. Essentially this means that, for example, if a functional group has two potential hydrogen bond acceptors or two possible modes in which hydrogen bonding can occur, it will preferentially form a hydrogen bond or bond in a certain mode to one of the acceptors, thereby “recognising” its counterpart.

## Supramolecular chemistry

The term “supramolecular” has been concisely defined as “that which is beyond the molecule” (Desiraju, 1997). Supramolecular chemistry refers to the interactions beyond the molecule itself, the macro assembly of the crystal structure. Desiraju suggests that very small long range interactions dictate the supramolecular structure of the molecule as the small effect over a few unit cells accumulates in effect, and eventually defines the macro assembly of the crystal (Desiraju, 1997).

## Hybrid materials

Even though the term “hybrid material” is used very broadly in material science, this study will consider an organic-inorganic hybrid material to consist of an organic and an inorganic building block. These materials self-assemble at the nano-scale, and the integration of the two components into a single material may result in interesting magnetic, optical and electrical properties. The inorganic constituent can potentially add interesting structural, magnetic and electronic conductive properties or rigidity and mechanical hardness to a material whilst the organic constituent may also contribute to the structural diversity, non-linear optical properties or photoluminescent behavior (Ayyappan et al., 2004) (Habib et al., 2009) (Habib et al., 2009). As a result, a hybrid material is often a multi-functional material, thus a material that combines more than one desired property within a single material.

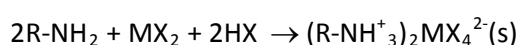
Divalent metal halide-based hybrid compounds, in which metal halide building blocks are combined with organic components, have been of considerable interest in recent years, not only from a structural point of view, but also due to their interesting properties, which will be discussed later in this Chapter (Englert, 2010). These materials also form the focus of current investigation, and relevant background information on this type of materials will be given in the following section.

## Neutral and Ionic Hybrid Materials

The term “organic-inorganic hybrid” is often used to refer to a material that consists of separate anionic and cationic moieties, hence an ionic hybrid material. However, for the purpose of this study the term will also be used to refer to materials formed by the coordination of the organic building blocks to the metal atoms in the metal halide building block, to form a neutral coordination hybrid material. Thus, the metal halide based hybrid materials considered here can be classified into two groups, ionic hybrid materials and neutral hybrid materials.

### Ionic hybrid materials

An ionic hybrid material forms when the hybrid material is prepared in the presence of a strong acid, and hence protonation of the organic component can occur. The resulting material consists of organic cations and inorganic anions. An example of a reaction involving an organic amine is given below, to illustrate a possible reaction.



The organic cations are typically isolated, while the inorganic component can take the form of an isolated anion, or a polymeric anion, which will be discussed in more detail later. Please note that

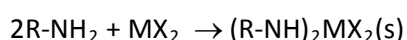
even in an ionic material, the halogeno ligands are coordinated to the metal atom, hence the anion is a coordination unit, and this is not to be confused with the neutral coordination hybrid material defined in the next section.

Strong, charge assisted hydrogen bonding interactions are prevalent in these materials, with the organic component acting as hydrogen bonding donor, while the perhalometallate anion is the hydrogen bonding acceptor.

The organic components in ionic materials normally serve as a templating agent, and protonation site in the ionic materials (Mitzi, 2001). There is no covalent interaction between the inorganic component and the organic component. Ionic hybrids often exhibit structures consisting of two-dimensional inorganic layers separated by an organic layer, but they are by no means limited to two-dimensional sheets, and many different types of structures have been observed. Ionic hybrids have been a subject of study for quite some time, and many examples of these materials exist in literature.

### Neutral (coordination) hybrid materials

Neutral (coordination) hybrid materials are formed when the synthesis of the material occurs without the presence of an acid, and the organic molecule coordinates to the metal center, while retaining the halide ligands, as illustrated by the following reaction:



In this type of material, the resulting coordination molecules may be isolated, or bridging may occur through either the organic or inorganic ligands, to form a coordination polymer, which will be discussed in a following section.

When the organic ligand is terminally coordinated to the metal center i.e. not linked to another metal center, intermolecular interactions are often present between the organic species of neighboring polymers.

### The inorganic component

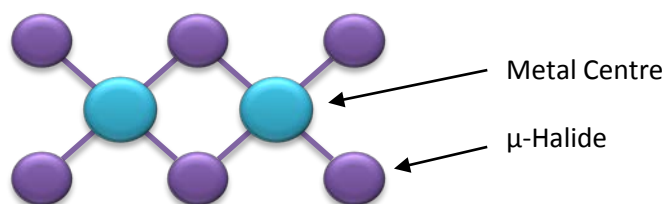
The inorganic part of the hybrid material consists of halogeno ligands coordinated to divalent transition metal ions. In this part of the structure, halogeno ligands may bridge neighbouring metal ions, and this is one of the factors that may determine the type of structure, as well as the dimensionality of the structure obtained, in both ionic and neutral (coordination) hybrid materials. It is stressed here that the components that constitute hybrid materials do not separately determine the structure or dimensionality of the material. It is the interaction between these components that yields the many different structures observed.

If isolated blocks of bridged metal atoms are present in the structure, the structural dimensionality remains zero. When infinite bridging of metal ions by halogeno ligands occurs such that a one-

dimensional structure is formed, the material is a coordination polymer, or when a two-dimensional or three-dimensional structure is formed, the material is a coordination network solid, according to the nomenclature recently suggested by Batten (Batten et al., 2012).

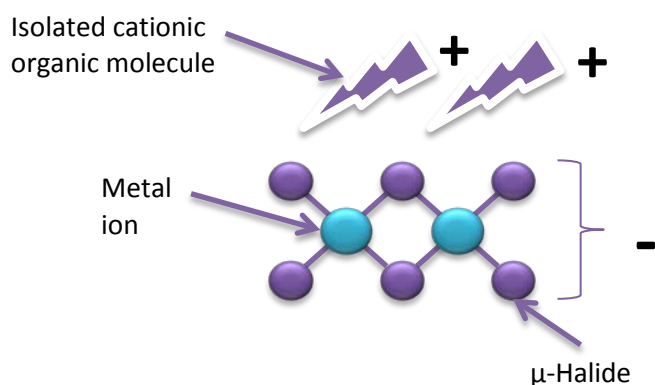
The polymeric motifs obtained when metals are bridged by inorganic ligands are subject to the coordination geometry of the metal center and the type of bridging.

An example of bridging occurring between two metal atoms, to form an anionic inorganic polymeric chain is illustrated in Figure 3.



**Figure 3: Example of an anionic coordination polymer. Blue metal atoms are bridged by purple halogeno ligands. Repetition of this bridging would result in the formation of a one-dimensional coordination polymer, or two- or three-dimensional network solid.**

Due to their relevance to the current project, the one-dimensional structures that can be obtained for the two types of hybrid materials will be pointed out. In one-dimensional ionic hybrid materials, the organic cations are isolated from the polymeric inorganic perhalometallate anions, as illustrated in Figure 4. However, in neutral hybrid materials, the organic ligands are coordinated to the metal atoms in the inorganic coordination polymer, forming an overall one-dimensional, neutral, coordination polymer, as illustrated in Figure 5.



**Figure 4: A general scheme illustrating an ionic structure consisting of isolated cations and a polymeric, one-dimensional anion. Consider the inorganic and organic components to be repeated an infinite number of times.**

Due to the important influence of structural dimensionality on the properties of these materials, as well as the wide range of interesting types of structures that can be obtained through the bridging of metal ions through halogeno ligands, these aspects, together with some illustrative examples, are discussed in more detail in the next section.

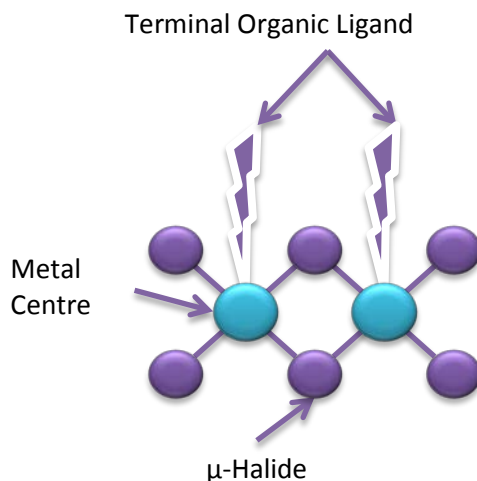


Figure 5: A general scheme illustrating a coordination polymer. Consider this unit to be repeated an infinite number of times.

## Structural Dimensionality

The dimensionality of the structure is determined by the presence of covalent or coordination bonds. The different types of coordination geometries that can be adopted by metal atoms, and the different ways in which the bridging of metal ions by both organic and inorganic ligands can occur, leads to a multitude of possible structures which can be categorized based on how they propagate along the crystal lattice.

The concept of structural dimensionality applies both to the ionic and neutral types of hybrid materials, and it is often, but not exclusively, found that inorganic ligand sharing in the inorganic portion of the structure determines the dimensionality of the structure. This bridging of metal atoms by inorganic halogeno ligands has already been discussed, but it should be noted that bridging through the organic ligands may also affect the dimensionality of a structure and is dependent on the number of available coordination sites in the organic ligand chosen, as well as the relative stoichiometry of organic and inorganic components, and kinetic and thermodynamic factors.

The concept of structural dimensionality will be illustrated by employing examples of neutral coordination hybrid materials, but the same concepts apply in the case of ionic hybrid materials.

## Zero-dimensional coordination complexes

These coordination compounds do not show bridging of metal ions via organic or inorganic ligands, and hence crystallize as isolated coordination compounds. zinc(II) is an example of a divalent metal that usually forms isolated, tetrahedral complexes, with an example shown in Figure 6.

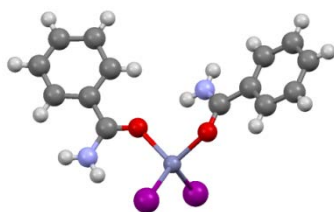


Figure 6: Example of an isolated, zero-dimensional coordination compound (CSD Refcode: VUCVAR) (Savinkina et al., 2009)

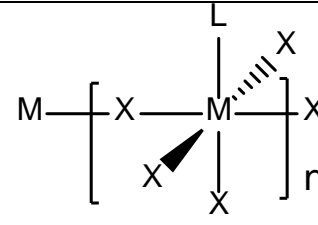
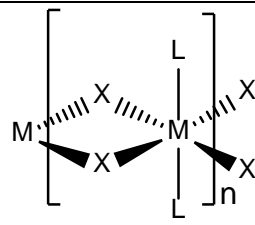
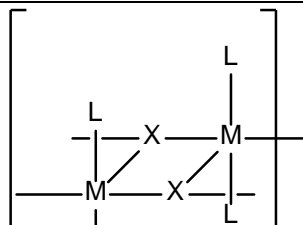
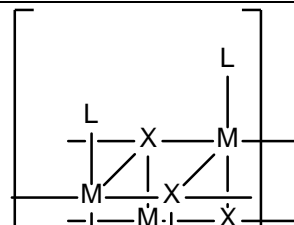


## One-dimensional coordination polymers

These polymers can be described simply as being ribbons or strings, i.e. propagation of the polymer along one axis. Propagation often occurs through the sharing of inorganic ligands between metal ions in the inorganic portion of the structure in neutral and ionic hybrid materials, however, in neutral hybrid materials, organic ligands may also act as bridges between metal ions to form this type of one-dimensional structure.

In the case of inorganic ligand bridging, the one-dimensional polymer can exhibit a wide range of different forms depending on the metal ion geometry, and the type of bridging that links metal centers. The inorganic part commonly contains metallic cations to which anionic halides or other anionic ligands are coordinated. In contrast to ionic hybrid materials, the charge of the inorganic component is typically neutral as the cationic and anionic parts combine such that the cationic and anionic charges are balanced. In the ionic polymers, the charge is typically negative due to the addition of anions as a byproduct of the protonation of the organic component. Examples of some basic sharing motifs are shown Table 1 for the octahedral geometry.

Table 1: Examples of the sharing of bonds in one-dimensional coordination polymers

Corner sharing	Edge sharing	Staggered edge sharing	Bi-layer edge sharing
			

An example of an edge shared one-dimensional structure found by Hu et. al. (2007) is illustrated in Figure 7 (Hu, Kalf and Englert, 2007). The inorganic component consists of a mercury (II) chloride backbone, to which a series of disubstituted pyridine ligands are coordinated.

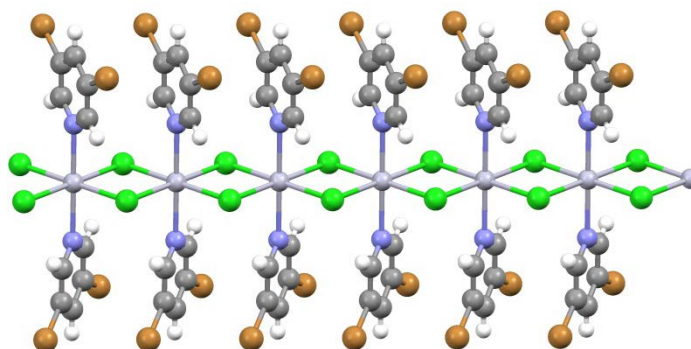


Figure 7: Example of an edge shared one-dimensional neutral coordination polymer (Hu, Kalf and Englert, 2007).

The ways in which the inorganic constituents combine to form the polymers is by no means limited to those listed in Table 1 and many other more complex systems have been demonstrated in the literature. Tetrahedral coordination geometries, square planar and tetragonal bipyramidal sharing can also occur. An incorporation of several types of coordination geometries into one inorganic polymer is possible and will be showcased later. For a more comprehensive review on the different types of coordination motifs, refer to (Alexeev et al., 2010).

### Two-dimensional coordination polymers

Two-dimensional polymers are generally sheets along specific directions in a crystal and may contain the organic part in between the sheets like an inorganic-organic-inorganic sandwich as illustrated in Figure 8. This ionic hybrid material structure has a perovskite type inorganic layer comprised of tin(II) cations and iodide anions where the octahedra engage in corner sharing. The protonated cationic (2-(4-fluorophenyl)ethylammonium) molecules occupy the space between the two-dimensional inorganic layers (Mitzi, Dimitrakopoulos and Kosbar, 2001).

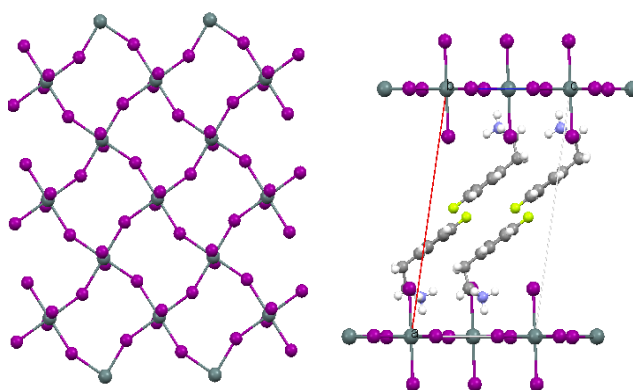


Figure 8: Two-dimensional ionic inorganic polymer. (CSD Refcode: BAKHIF) (Mitzi, Dimitrakopoulos and Kosbar, 2001)

Two-dimensional neutral coordination polymers have been demonstrated in the literature. An example of edge shared tetrahedra is shown in Figure 9. The copper(I) ions are coordinated by bridging iodo ligands to form a one dimensional inorganic polymer along one axis whereas the bidentate ligand provides the polymerization of the coordination polymer along a second direction (Graham and Pike, 2000).

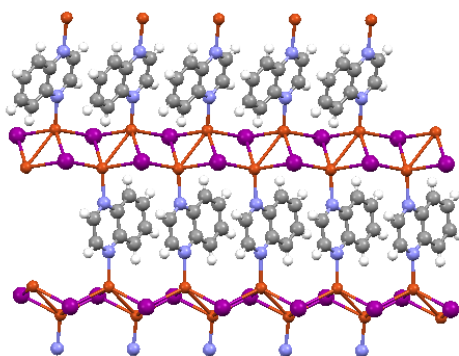


Figure 9: Example of an edge shared two-dimensional tetrahedral neutral coordination polymer (Graham and Pike, 2000).

## Three-dimensional coordination polymers

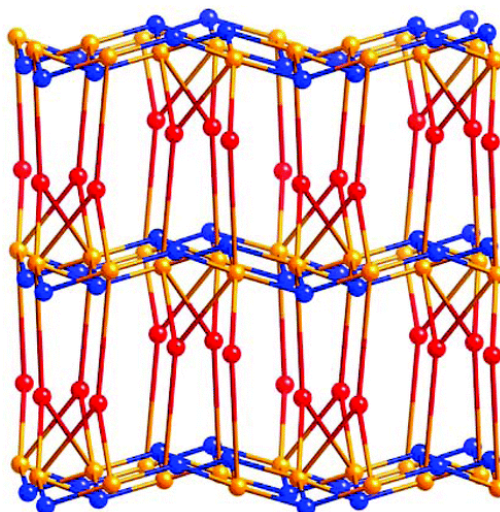


Figure 10: Three dimensional neutral coordination polymer with orange spheres representing Mn ions. Blue spheres represent the azide bridging anions, and red spheres represent the organic 4-aminobenzoic acid ligands (Chen et al., 2009).

A three-dimensional neutral coordination polymer was demonstrated by Chen et. al. (2009) The inorganic component consists of Mn(II) cations and  $N_3^-$  anionic ligands in a two dimensional sheet as illustrated in Figure 10 (Chen et al., 2009). The two-dimensional inorganic sheets are linked by 4-aminobenzoic acid molecules to form a three-dimensional coordination polymer.

## Applications of hybrid materials

Now that the important features and characteristics of metal halide based organic-inorganic hybrid materials have been highlighted, we can move on to another pertinent question: why has there been so much interest in the structures and properties of these materials in recent years?

The answer to this question is two-fold. Firstly, from a crystal engineering perspective, these materials exhibit a range of interesting structural types and dimensionalities, and understanding and controlling these structures using the concepts of crystal engineering has been a challenge. Robust synthons and structural motifs have been identified for certain systems, and allow for a degree of predictability, however, there are often exceptions, and many structures have been reported that do not follow the expected trends (Brammer et al., 2002) (Rademeyer et al., 2011). However, the fundamental understanding of these materials still remains a challenge.

Another important reason for the interest in these materials is certainly the wide range of very interesting properties that have been observed and reported for these compounds. These properties include: Thermal, Optical, Semi-conducting, Magnetic, Photoluminescent, Photomagnetic and Photo-chromic properties (Aakeröy, Champness and Janaik, 2010) (Robin and Fromm, 2006). It is these properties, and the fact that more than one property is often exhibited by the same material, which fuels the development and exploration of metal halide based hybrid materials with the aim to create truly novel and unique materials that may have the potential to advance technology.

Examples of interesting properties of ionic and neutral metal halide based hybrid materials are discussed below. This discussion is by no means exhaustive, but aims to serve as an introduction.

### Ionic Hybrid Materials

The research group of Mitzi investigated the electronic properties of number of ionic organic inorganic hybrids, and also reviewed their chromophoric and luminescent properties (Mitzi, Chondroudis and Kagan, 2001). It was illustrated that in the perovskite-type ionic hybrids the two-dimensional inorganic layers are semi-conducting, affording semi-conductor properties and high electronic mobility to the materials. Different organic components, as well as a change in the relative ratio of organic and inorganic component can be used to alter the electronic properties of the materials. In addition, the design and construction of an organic-inorganic light emitting diode (OLED) from a lead iodide and oligothiophene ionic hybrid material was demonstrated.

In addition, interesting magnetic, thermal, (Criado et al., 1999), electroluminescent (Chondroudis and Mitzi, 1999), optical and transport properties (Aruta et al., 2004) have been reported for ionic hybrid materials.

### Neutral Coordination Hybrids

The field of molecular electronics aims to miniaturize electronic devices, and in these devices, “wires” are required for electronic transport. The tendency of neutral metal halide based hybrids to form one-dimensional coordination polymers has led to the investigation of the electronic properties of these coordination polymers, specifically with the view of using them as “molecular wires” or “nano-wires” (Alexandre et al., 2007). These molecular wires may make the miniaturization of electronic devices such as processors possible.

Mateo-Marti et al. demonstrated evidence of the formation of nanowires based on a one-dimensional ladder coordination polymer formed between isonicotinic acid and copper(I) bromide (Mateo-Marti et al., 2008). The polymer was found to be a one-dimensional ladder. The copper atoms are tetrahedrally coordinated and engage in edge sharing of the tetrahedra, as illustrated in Figure 11. The compound was successfully deposited onto a gold surface; and fibres of the coordination polymer were imaged using atomic force microscopy. A single crystal of this material was reported to have semi-conductive properties.

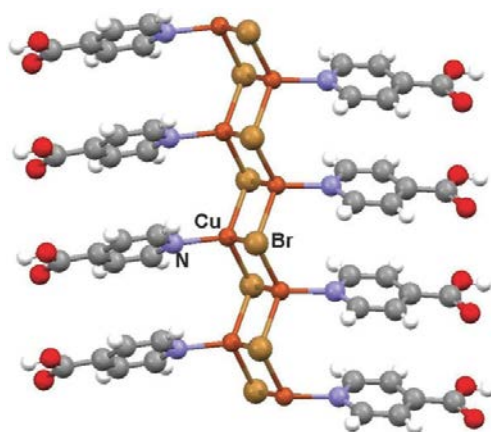


Figure 11: Schematic representation of a copper(I) nanowire (Mateo-Marti et al., 2008).

Liu et al. demonstrated the semi-conductive properties of a copper(I)iodide and 1,10-phenanthroline neutral coordination hybrid (Liu et al., 2009). The polymer exhibited an intricate one-dimensional polymer in which copper ions are tetrahedrally coordinated to form a hexagonal grid chain. The result is an infinite one-dimensional polymer of four metal centers wide as shown in Figure 12.

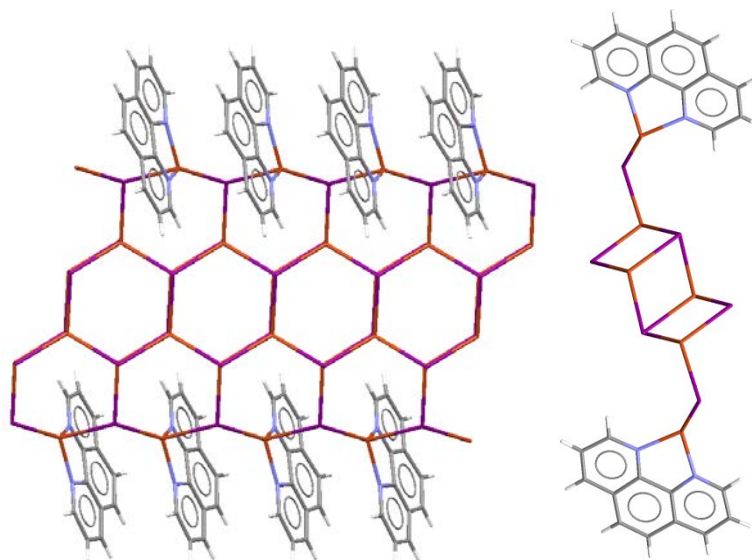


Figure 12: Intricate one-dimensional polymer with semi-conductive properties (Liu et al., 2009).

They report a band gap of 2.09 eV for this compound, as measured by diffuse reflectance spectroscopy which is consistent with semi-conductive behavior. They also suggest that the organic phenanthroline  $\pi^*$  band effectively lowers the band gap and may be used as a property control species.

A “reduced” band gap material was reported by Li et. al. with a theoretically calculated band gap of 1.36 eV. The material consisted of a one-dimensional lead iodide inorganic polymer with 4,5-diazafluoren-9-one (dafone) as organic component. They suggest that the organic ligand acts as a control mechanism altering the conductivity of the material based on small differences in the organic ligand. They suggest that hydrogen bonds can also play a major role in the “tuning” of the band gap (Li et al., 2010).

A highly conductive one dimensional platinum-iodo nano-ribbon coordinated by a 1,1-ethanedithiol ligand was demonstrated by Welte (Welte et al., 2010). They suggested that coordination polymers could offer a viable alternative to carbon-based materials in the development of molecular electronics.

In addition to electronic properties, other properties of neutral coordination polymers have been reported in the literature. These include magnetic properties (Lande et al., 2003) (Herringer et al., 2010) imparted by unpaired electrons in transition metal ions.

Li et al. demonstrated that an interesting hetero-bridged copper(I) neutral coordination hybrid exhibits luminescent and thermochromic properties (Li et al., 2011). The inorganic component

consists of a copper atom coordinated by two sulfur and two iodido ligands to form a one-dimensional, infinite chain, as illustrated in Figure 13.

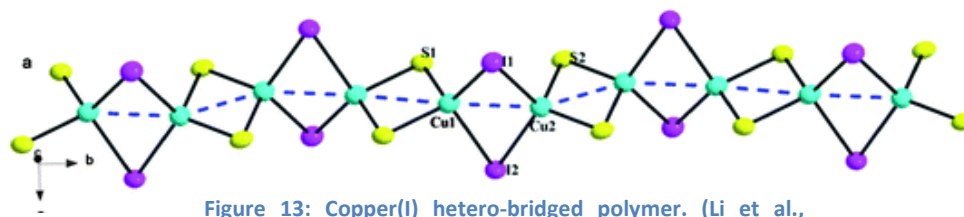


Figure 13: Copper(I) hetero-bridged polymer. (Li et al., 2011)

This compound exhibited chromophoric behavior as it changed from an orange to a yellow color upon heating to 120°C as shown in Figure 19.

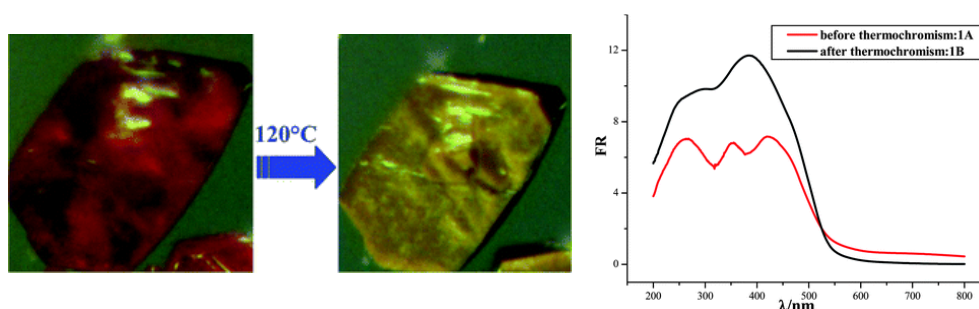


Figure 14: Thermochromic behavior of a copper(I) hetero-bridged polymer (Li et al., 2011)

It is evident from the literature that many interesting properties are inherent to these materials. Further investigation into the fundamental nature of these materials, with the aim of better understanding their structures and properties, have the potential to possibly lead to improved materials, with significant advances in materials science set as a long term goal.

## Computational Chemistry

In recent years, good progress has been made in the development of Density Functional Theory (DFT) approaches to determine the structures and physical properties of materials. The ultimate aim is to understand, on a quantum level, how to control the properties of materials. Concepts and background information pertaining to the use of DFT in computational chemistry are discussed in this section. Of specific interest in the current project is the calculation of band gaps, employing DFT.

### Band Structure and Band Gap

An atom has a specific number of valence electrons. The molecular orbital approach defines that in order for a bond to form between two species, one electron each should be donated by each species. The atomic orbitals combine into a molecular bonding interaction, non-bonding and anti-bonding orbitals. Increasing the number of atoms bound increases the number of molecular bonding interactions, non-bonding and anti-bonding orbitals.

The atomic orbitals no longer have discrete energy values, and the energy difference between them is very small. As a result of this continuous energy bands are formed, which give the allowed



energies of electrons with respect to a specific direction in the crystal lattice, the k-vector, which will be defined in more detail shortly. These energy bands form the band structure of the material.

From the slope of the band structure the density of states (DOS) can be obtained, which gives the number of electronic states that have a specific energy. Theoretically, the number of states are infinite, but due to the fact that the number of available electrons are limited, only certain states will be filled, starting with the lowest energy state. The highest filled state is known as the Fermi level.

Electronic conduction involves the excitation of electrons from a state below the Fermi level into any state higher than the Fermi level. The valence band is the first electronic band located below the Fermi level, the conduction band is the first band above the Fermi level, and the energy gap between the two is known as the band gap. In some materials, the gaps between the valence and the conduction bands may be so small that at room temperature, the electrons have enough energy from thermal sources that they allow the electrons to elevate from the valence band to the conduction band, and this type of material is referred to as a conductor. In a semi-conductor the band gap is wider, and at 0 K all the electrons will be in the valence band. However, at higher temperatures, if electrons possess enough energy, they may overcome this band gap, and move into the conduction band, resulting in conduction. It is also possible that the band gap is too large to be bridged, leading to a material that is an insulator (Tilley, 2004). Materials may be characterised electronically according to their band gap values, and a rough guideline is: Conductors have very small band gaps, and in fact the smaller the band gap is, the better it conducts electricity. Semi-conductors have slightly larger band gaps. Silicon, a common material used in electronic devices has a band gap energy of 1.1 eV at 302 K. An insulator typically has a very wide band gap. The values for band gaps are deliberately not defined here. The band gap range for semi-conductors cannot really be clearly defined, since the border between a semi-conductors' and an insulators' band gap value is not clearly defined. Strehlow & Cook stated that semiconductors typically have band gaps in the region of 0-4 eV and insulators have band gaps of 4-12 eV (Strehlow & Cook 1973). However, the band gaps become systematically larger in going from a semi-conductor to an insulator therefore there are no clear boundaries between semiconductors and insulators (Streetman and Banerjee, 2000).

The band gap energy will determine the likely electronic applications of a material. If a material such as silicon, with a band gap of approximately 1 eV is used, it is seen as a semiconductor and applied to transistors and diodes. But a 1 eV band gap would not be useful in creating LED's.

The wavelength of light emitted from a light emitting diode (LED) is dependent on the band gap energy. The higher the band gap energy, the higher the emitted wave or color observed. Koizumi et. al. reported the use of diamond, with a band gap of 5.27 eV, as a UV-emitting LED and compared it to a gallium nitride compound, with a band gap energy of 3.47 eV, emitting light in the visible region (Koizumi et. al. 2001). Although diamond is classified as an insulator according to Strehlow & Cook, it is applicable as a UV LED.

It is important to note that the band gap energy measured is dependent on temperature. Silicon has a temperature dependent band gap of  $E_g = 1.12 - 3.6 \times 10^{-4} \times T$ . The temperature dependence of band gaps therefore requires the careful design of electronics to only work between a certain temperature range. This band gap temperature dependence can be tuned by selecting materials with wider or smaller band gaps. It allows the design of electronics to work under different

conditions. Wide band gap materials are commonly used to selectively absorb certain frequencies of light in photovoltaic cells.

Semi-conductors with band gaps falling between 1 eV and up to 6 eV have been demonstrated, each with different applications, based on their band gap width.

For non-magnetic materials, DFT assumes the occupation of orbitals with electron pairs rather than one spin up and one spin down electron. This assumption enables much faster calculation of the electronic properties. In contrast, magnetic materials have unpaired electrons. DFT considers both the spin up and spin down electrons individually rather than pairs of electrons. The orientation of the spins is arbitrary, i.e. if an alpha electron is spin up, then by mere definition, a beta electron will have spin down orientation and vice versa. In magnetic materials there will be an associated energy band, and associated orbitals for each of the alpha and beta spins.

## K-points and Brillouin zone

Because a crystal is a periodic arrangement of unit cells, a complete picture of the band gap should also take this periodicity into account. This can be done by making use of the symmetry operations in the space group of the material.

In crystallography, reciprocal space is given by the Fourier transform of the original lattice. In the field of physics, the reciprocal space is also called the k-space. The Brillouin zone is a primitive cell, defined in reciprocal space, in a unique way. The edges of the Brillouin zone is defined by planes oriented relative to specific points in the reciprocal lattice - it is obtained by drawing vectors from a reciprocal lattice point to all the nearest reciprocal lattice points. These vectors are then bisected, and a perpendicular line is drawn at the point of bisection, to give the Brillouin zone.

The concept of a Brillouin zone very important in the Bloch wave description of waves in a periodic system, which will be discussed later. These Bloch waves are solutions to the Schrödinger equation for the crystal, and their behaviour in a single Brillouin zone can be used to obtain a complete characterization of these waves.

Due to the relationship that exists between the condition of reflection and the Brillouin zone, the Brillouin zone shows all the wave vectors that can be diffracted by a crystal according to Bragg's Law. Higher order Brillouin zones may also be defined.

Special points on the Brillouin zone are of interest due to their specific position on the Brillouin zone, for example in the centre, on an edge, or on a corner of the Brillouin zone. These points are known as critical points, and are typically denoted by Greek symbols or uppercase letters, as shown in Figure 15.



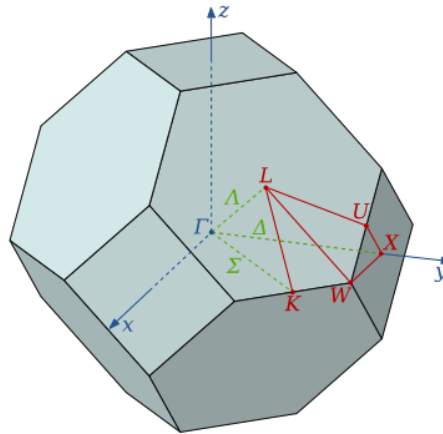


Figure 15: Example of a Brillouin zone, and the use of special characters to indicate specific positions on the Brillouin zone ([http://en.wikipedia.org/wiki/Brillouin\\_zone](http://en.wikipedia.org/wiki/Brillouin_zone))

As mentioned before,  $k$ , the wave vector, is related to the direction in which the electron moves in the crystal, and the possible values of this  $k$ -vector are given by the points mentioned above. The energy of the electron is also a function of  $k$ , and in a typical band structure diagram, the bands are given as a function of  $k$ . An example of a band structure diagram is given in Figure 16.

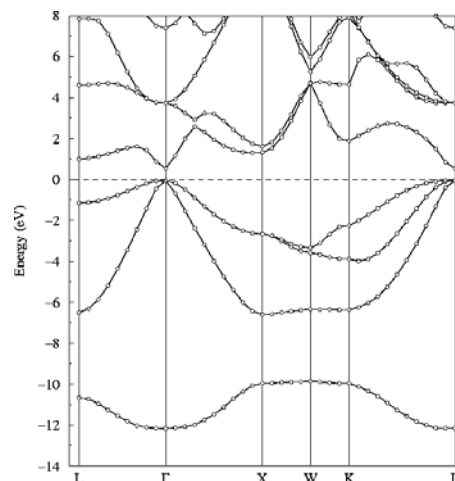


Figure 16: Example of a band structure diagram. Accessed online at (<http://www.fhi-berlin.mpg.de/th/fhi98md/doc/main/node19.html>)

Each of the bands seen in Figure 16 indicates that there is an electronic band and simply just that. The band however is not quantized in terms of its size, or its composition. Revealing the electronic state of a crystalline system, the Density of States, abbreviated DOS quantifies the number of electronic states per energy unit that are available for the occupation of electrons. This DOS is calculated as follows:

The density of states (DOS) for a given band  $n$ ,  $N_n(E)$ , is defined as:

$$N_n(E) = \int \frac{d\mathbf{k}}{4\pi^3} \delta(E - E_n(\mathbf{k}))$$

where  $E_n(\mathbf{k})$  describes the dispersion of the given band and the integral is determined over the Brillouin zone. The total density of states,  $N(E)$ , is obtained by summation over all bands. The integral of  $N(E)$  from minus infinity to the Fermi level gives the total number of electrons in the unit cell. An example of a typical DOS is shown in Figure 17.

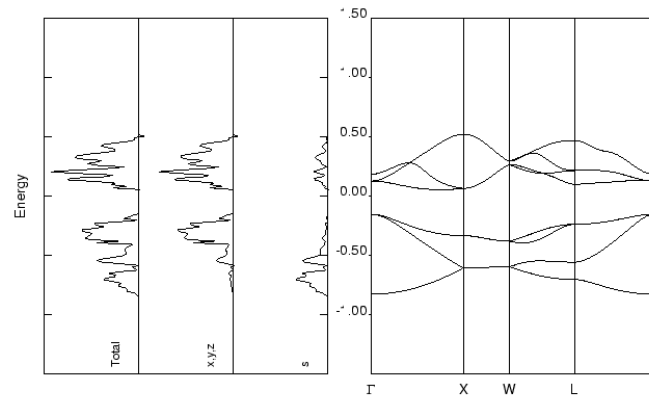


Figure 17: An example of the DOS (left) of Silicon with accompanying band structure (left). Accessed online at [http://www.theochem.unito.it/crystal\\_tuto/mssc2008\\_cd/tutorials/properties/properties\\_tut.html](http://www.theochem.unito.it/crystal_tuto/mssc2008_cd/tutorials/properties/properties_tut.html)

Two types of band gaps exist, direct and indirect band gaps. Direct band gaps are those for which the momentum ( $k$ -vector) of the excited electron in the valence band is the same as the hole it will occupy in the conduction band, therefore a direct excitation of an electron can occur between the valence and conduction bands. In simpler terms if the electronic transition occurs within the same  $k$ -point, it is a direct band gap and is illustrated in Figure 18(left). Direct band gap materials have the ability that they can emit photons if current is applied to them, and are broadly used as LED's. The emission of photons is possible due to the direct transition of electrons from the valence to the conduction band.

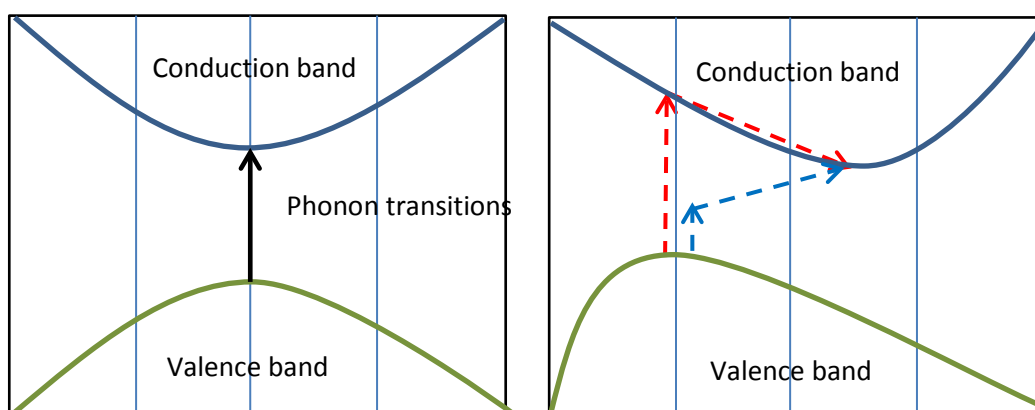


Figure 18: Illustration of Direct (left) and Indirect (right) band gaps.

The second type of band gap, also a termed phonon-assisted indirect band gap, involves the transition of an electron from the valence band to the conduction band, but in the indirect case the momentum ( $k$ -vector) of the electron in the valence band is not equal to the momentum of the hole it will occupy in the conduction band. A phonon in solid state physics is a quantum of vibrational energy that is generated from oscillating atoms in a crystal lattice. This phonon-assisted transition

requires the electron to be excited to a finite energy and the assistance of a phonon vibration to the minimum of the conduction band. There are two types of phonon assistance methods possible.

The first type occurs when the photonic energy absorbed by the electron is less than the band gap energy. The excited electron has to absorb a phonon vibration and this process is illustrated by the blue arrows in Figure 18 (right). This phonon absorption is an endothermic process.

The second type occurs when the photonic energy absorbed by the electron is more than the band gap energy. The electron is directly excited from the valence band to the conduction band along the same k-vector, but the excited electron then returns to the minimum of the conduction band, and emits a phonon vibration in the form of heat, and this pathway is illustrated by the red arrows in Figure 18 (right). The emission and absorption of phonons are in the order of 0.01 eV and are small compared to the band gap energies. The phonon vibration assisted process is a very slow kinetic process, and results in the indirect band gap materials not being able to emit light if current is applied. Due to the phonon dependence of indirect band gap materials, the absorption of light is greatly dependent on temperature. At low temperature less phonon vibrations are available, and this reduces the likelihood of an indirect phonon absorption assisted transition occurring (van Zeghbroeck, 2011).

## Density Functional Theory

The developments that occurred in the field of quantum mechanics in the 1920's opened new doors to the fundamental understanding of materials and their properties. In quantum mechanics, the electrons can be considered separately from the nucleus due to the difference in their masses and time-scales, according to the Born-Oppenheimer approximation.

To obtain the quantum mechanical description of a chemical system, the many-body Hamiltonian must be solved. This Hamiltonian contains three terms, a term related to the kinetic energy of the electrons, a potential energy term due to the interaction between the nuclei and the electrons, and a term that takes into account the Coulombic repulsion between electrons. This latter term complicates the situation, and an exact solution cannot be obtained for a system that represents a real solid, in which the number of units is in the order of Avogadro's number.

A solution to this problem is to consider the full Hamiltonian, but to search for an approximate solution, instead of an exact solution. This is the approach followed in Density Functional Theory (DFT). The many-body problem is solved by using "functionals" that represent the electron density in space. The functional is a "function of another function", and represents the time-averaged potential determined by the nuclei and other electrons. This approximation is made according to the two Hohenberg-Kohn theorems (Hohenberg and Kohn, 1964) the first of which states that the electron density uniquely defines the properties of the ground state of a many-electron system. The use of the electron density, which depends on only 3 spatial coordinates, allows for a drastic reduction in the number of electrons that need to be considered to solve the many-body problem. By using a functional in a system of N electrons, with 3N spatial coordinates, the number of spatial coordinates is reduced from 3N to 3. According to the second Hohenberg-Kohn theorem, an energy functional can be defined, which is minimized by the correct ground state electron density.

Kohn and Sham (Kohn and Sham, 1965) introduced a method, based on the Hohenberg–Kohn theorem, which solves the many-body problem by considering the interacting electrons that move in a static field, as non-interacting electrons moving in an effective potential (Sousa, Fernandes and Ramos, 2007). This effective potential takes into account both the static potential, and the exchange interactions between the electrons. Exchange interactions between electrons refer to a quantum mechanical effect, and does not have a classical analogue. Modeling of the exchange and correlation interactions may be problematic in this method, which is known as the Kohn-Sham DFT (KS-DFT) method, and this is discussed in the next section.

A clear definition of the term DFT is made here. The term “DFT” will be used to refer only to the periodic application of DFT in this work. There are significant differences in the methodology used for periodic systems vs. the more commonly used unimolecular application. The amount and nature of approximations of the two applications are vastly different and warrants a distinction. The DFT functionals discussed below are only pertinent to the periodic application of DFT.

## Exchange Correlation Functionals

Several functionals or rather DFT approaches have been employed with varied success in the last thirty years. The main problem facing DFT calculations is the nature of the exchange-correlation functional which includes all the unknown quantum effects not covered by the Kohn-Sham equations.

### Local Density Approximation

The Local Density Approximation (LDA) functional uses the Thomas-Fermi model, which considers the electrons as an electron gas in a constant external potential, thus the charge density remains constant. The exchange correlation energy is obtained from the electronic density in space. The orbitals of this homogeneous electron gas are, by symmetry, plane waves. The Local Density Spin Approximation (LDSA) functional is similar to the LDA functional, but it takes spin polarization into account (Slater, 1951). In the LDA+U approach, the electrons are separated into two categories, firstly localised d (or f) electrons, for which Coloumb interactions are taken into account by introducing a term for this interaction, and delocalised s- and p-electrons, which are described by a traditional LDA method. The LDA+D method refers to the general method of adding dispersion corrections to a functional. The dispersion correction includes a better description of the non-covalent forces present in the structure. The dispersion corrections are typically semi-empirical of nature and may not be equally applicable to all systems.

### Generalized Gradient Approximations (GGA)

In the LDA approach, the energy of the true density is approximated by using the energy of a local constant density, but this method does not work well when the density changes rapidly, for example in molecules. In the GGA method, the gradient of the electron density is considered, and this can lead to an improvement. The Perdew-Burke-Enzerhof (PBE) functional gives a direct generalized-gradient parameterization of the free electron gas, but does not have any free parameters.

The RPBE implementation of GGA improves upon the adsorption energies of molecules onto metal surfaces. The PBEsol is one of the most recent applications of the GGA approach and was specifically optimized for closely packed molecules. The optimization of the PBEsol exchange correlation functional yields better equilibrium properties is able to describe the electronic structure more accurately.

In general, the GGA methods result in a significant improvement compared to the local LDA methods.

In a hybrid functional the exchange correlation of a conventional GGA method is combined with a Hartree-Fock exchange. An example is the B3LYP function.

Central to DFT based methods in solid state is Bloch's theorem which states that solutions to the Schrödinger equation have the following form:

Equation 1

$$\phi_{\mathbf{k}}(r) = \exp(i\mathbf{k} \cdot \mathbf{r})u_{\mathbf{k}}(r)$$

The theorem makes it possible to solve the Schrödinger equation for each value of  $\mathbf{k}$  independently.

The first part of the function  $\exp(i\mathbf{k} \cdot \mathbf{r})$  is called a plane wave which has a real space and a reciprocal space vector. It is mathematically easier to solve the equation above with respect to  $\mathbf{k}$  (k-space) than for  $\mathbf{r}$  (real space). It is possible to define a primitive lattice in reciprocal space namely the *Brillouin zone* (abbreviated BZ), as explained earlier. Solving the equation above requires the numerical evaluation of integrals in reciprocal space for all possible values of  $\mathbf{k}$  within the Brillouin zone, and this is done computationally as the weighted sum over a number of k-points. The number of k-points defined in the BZ is dependent on the contents of the unit cell. K-points can be seen as probes of the electron density at certain special points defined by the BZ. For small values of  $\mathbf{k}$  the energy of the computed wave function differs greatly as the BZ is not properly "probed". Therefore the number of k-points or rather the k-point grid has to be converged with respect to the total energy calculated in order to model the system to a certain convergence criteria set by the user's need for accuracy vs. time. Monkhorst and Pack (Monkhorst and Pack, 1979) proposed a method by which an equally spaced mesh can be obtained in the Brillouin zone, and these points can then be used in the calculation of the weighted sum.

A special consideration of k-points should be made when studying metal containing species. The integrals mentioned earlier assume a continuous function, but for reasons beyond this discussion the function is discontinuous at the HOMO orbital (the Fermi level) in the case of metals. The integral is "smeared" to a continuous function at the Fermi level in order to conserve the "continuity" of the integral.

The second part of the function  $u_{\mathbf{k}}(r)$  defines the plane wave "basis set" and can be expanded to into a set of plane waves as follows:

Equation 2

$$u_{\mathbf{k}}(r) = \sum_{\mathbf{G}} c_{\mathbf{G}} \exp[i\mathbf{G} \cdot \mathbf{r}]$$

and combining Equation 1 and 2 and yields:

Equation 3

$$\phi_{\mathbf{k}}(r) = \sum_{\mathbf{G}} c_{\mathbf{k}+\mathbf{G}} \exp[i(\mathbf{k} + \mathbf{G})\mathbf{r}]$$

requiring an infinite sum over all values of  $\mathbf{G}$  for every possible value of  $\mathbf{k}$ . Solutions with lower energies are more important than those with higher energies, therefore it is possible to truncate the infinite sum of  $\mathbf{G}$  to a finite amount below a certain kinetic energy,  $E_{cut}$ :

$$E_{cut} = \frac{\hbar^2}{2m} G_{cut}^2$$

$E_{cut}$  therefore is defined as the plane wave cut off energy and is once again dependent on the contents of the unit cell. The plane wave cut off energy or plane wave “basis set” has to be converged with respect to the total energy to a defined criteria. It is important to note that the k-point and plane wave cut off energies of any system need to be the same. Defining a smaller k-point grid for different systems introduces a systematic error in the energy values obtained and should therefore be avoided (Sholl and Steckel, 2009).

Perhaps the greatest limitation to solid state DFT is the use of *pseudopotentials*. This method is also referred to as *frozen core* treatment. The inner core electrons of atoms are frozen and treated as a continuous static charge around the atom, based on empirical data, and only the valence electrons are considered as quantum mechanically defined electrons. This approximation comes at a great cost in accuracy, but does make DFT calculations possible in the solid state. Considering that the asymmetric units of the materials studied here have approximately 150 electrons each, and only 70 valence electrons, a full treatment of all the electrons in a periodic system would take  $(N_{All\ electrons} - N_{Valence})^2$  i.e. 6400 times longer than the pseudopotential method. The RAM requirements for a full electron calculation of our system would also be astronomical. The pseudopotential method, as simplified and flawed as it is, is still the only way to treat large systems effectively.

Two approximations are used to define the pseudopotentials of a system; namely norm-conserving and ultrasoft pseudopotentials. The main difference is that the norm-conserving pseudopotentials are described by more Fourier components than the ultrasoft pseudopotentials. Norm-conserving pseudopotentials however come at a greater computational cost, but increase the accuracy of the calculation to a large degree, especially since norm-conserving pseudopotentials describes transition metals excellently (Bachelet, Hamann and Schluter, 1982).

The free energies reported in this study are the Kohn-Sham energies  $E_{ks}$ , which ignores the entropy contribution to the energy. This value is corrected to include an artificial enthalpy term, corrected to 0K. A temperature correction can be applied to this energy level by including the Fermi-Dirac smearing method where 11604.5 K/eV can be applied. It is usually the 0K energy that is used in the comparison and the smearing energy is applied to the system only to improve the convergence of systems that contain metals. The Mermin energy refers to the electronic energy calculated from the specific plane wave method used in the CASTEP software package and has no physical meaning as it is a mathematical indication of the electronic energy of a system (Accelrys Software Inc, 2010).

## Success of DFT

In many material systems the local spin density approximation (LSDA) approach to density functional theory (DFT) has been very successful, however problems were reported for other systems, specifically, when DFT-LSDA is applied to materials containing transition metal ions with partially filled d orbitals. For example, it has been reported that DFT-LSDA typically underestimates equilibrium lattice constants and overestimates binding energies (Dudarev et al., 1998). Hybrid

density functional theory is required to overcome these problems, since these functionals take electron correlation into account better, but these functionals come at a far greater computational cost. It seems then that the functionals are very dependent on the system they are applied to. Testing of the functionals performance in different tasks against experimental values is imperative.

## Band gap calculations

Relevant to the current project, the computational investigation of the electronic structure of metal halide based hybrid materials is still in its infancy.

The starting point of these investigations is typically the experimentally determined crystal structure, or, if this is not available, a calculated crystal structure may even be used, but this is a more risky procedure. Different modeling approaches need to be benchmarked against one another for a specific material system to determine the most applicable approach to the system. Once this has been achieved to a satisfactory level, properties of materials may be calculated, but should always be compared with experimentally measured properties to ensure the applicability of the theoretical calculations.

A logical starting point in the modeling of these materials would be to consider the literature focusing on the DFT modeling of transition metal halides, since this part of the structure plays a central role in determining the electronic characteristics of the material. A number of studies have reported the calculation electronic properties of transition metal oxides, and the problems associated with these calculations (Chen et al., 2009), however, to our knowledge very few studies have focused on DFT calculations performed on transition metal halides (Banks et al., 2009). A 2005 study by Ramírez showed that in order to describe the electronic parameters of a simple  $\text{CuCl}_2$  structure fully - by incorporating the differential correlation effects - requires a very large basis set and an advanced functional (Ramírez-Solís et al., 2005). Literature reports on DFT studies of metal halide based, neutral coordination polymers are also very scarce (Alexandre et al., 2007). Li et al (2010 and 2011) reported band gap calculations for  $\text{PbI}_2$  coordination polymers of 4,5-diazafluoren-9-one and 1,10-phenanthroline derivatives, and (Tang, Zhou and Chen, 2012) carried out DFT calculations on a two-dimensional network sheet formed by isonicotinic acid and  $\text{Cu(I)Br}$ . However, these studies did not compare the calculated values with experimentally obtained band gap values.

## Aspects of this Study

A large number of crystal structures of both ionic and coordination hybrid materials consisting of divalent transition metal halides and aryl- and alkylamines have been reported in the literature (Clement, Rapko and Hay, 1998) (Robin and Fromm, 2006). However, limited structural data is available on hybrid materials containing organic components with other functional groups. One of the aims of the current study was to investigate the materials containing organic components with functional groups other than the amine group, specifically amide functional groups, either exclusively, or in combination with other functional groups. The type of structure obtained for hybrids of amide containing organic components is of interest, in order to better understand the role of this functional group on the structural characteristics of the hybrid materials, since very little information is available on these types of hybrids.



Only nine neutral coordination hybrid structures containing simple amides combined with metal halides could be located in the Cambridge Structural Database. The simple amide ligands considered here consist of a single amide functional group combined with carbon and hydrogen atoms, and are all monodentate, and coordinated through the amide group where applicable. Only structures for which coordinates have been reported were taken into account. Five structures of metal halides combined with formamide have been reported; the coordination combination of formamide with  $ZnI_2$  (CSD refcode: DIYGUO; Savinkina et al., 2008) results in an isolated zero-dimensional structure, while the coordination compounds formed between formamide and  $CdCl_2$  (CSD refcodes: CDCFAM10; Mitschler, Fischer and Weiss, 1967),  $FeCl_2$  (CSD refcode: CFORFE; Constant, Daran and Jeannin, 1971),  $CuCl_2$  (CSD refcode: AXUTAP; Shtukenberg, P'yankova and Punin, 2010) and  $MnCl_2$  (CSD refcode: AXUTET; Shtukenberg, P'yankova and Punin, 2010) all give one-dimensional coordination polymers.

Two zero-dimensional coordination compounds have been reported for the coordination compounds formed between acrylamide and  $CuCl_2$  and  $CoCl_2$  respectively (CSD refcodes: NEDPUI; Girma et al., 2006 and QAPJUN; Girma et al., 2005). Acetamide and  $ZnI_2$  combine through coordination to give a zero-dimensional compound (CSD refcode: VIDBOA; Savinkina et al., 2007), while the coordination of benzamide to  $ZnI_2$  also give a zero-dimensional coordination compound (CSD refcode: VUCVAR; Savinkina et al., 2009).

No structure of an ionic amide-containing metal halide hybrid, which fulfills the definition stated above, could be located in the literature.

No structures of 4-aminobenzamide bonded to any transition metals were found.

## The Organic component

For the current investigation, the benzamide and 4-aminobenzamide molecules were chosen as organic components, and the specific reasons for this selection, as well as information on these two inorganic compounds are given in the following section.

### Organic constituent: Benzamide

The benzamide molecule consists of a benzene ring with an amide functional group bonded to it, as can be seen the line structure below. Benzamide is a white crystalline solid of which two polymorphs are known, however only one polymorph is reported to be stable (Blagden et al., 2005). Benzamide might seem like a simple molecule, but the amide group adds a lot of interesting features as opposed to a benzoic acid molecule.

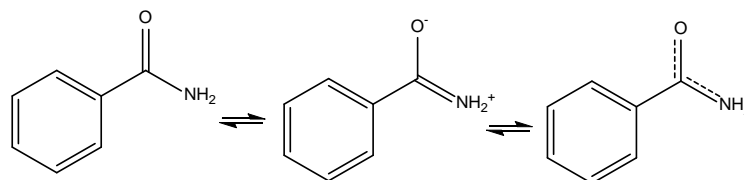


Figure 19: Line structure and resonance structures of benzamide.

Benzamide can readily form a resonance structure between the carbonyl carbon atom, oxygen atom and the nitrogen atom, as illustrated in Figure 19. Due to the resonance shown in Figure 19, rotation of the bond between the benzene ring and the carbonyl atom bond is somewhat restricted. A planar



molecule is not expected, however, due to steric interactions between the aromatic hydrogen atom and the nitrogen bonded hydrogen atom. In addition, an orthogonal configuration with respect to the aromatic ring is also not expected as a hydrogen  $\pi$  interaction may also occur, and which would not be possible in an orthogonal configuration. Crystallographic data (Penfold and White, 1959) (Blake and Small, 1972) (Blagden et al., 2005) and neutron diffraction data (Gao et al., 1991), in conjunction with gas phase electron diffraction and supportive molecular modeling (Takeuchi et al., 1999) suggests that the amide group is rotated by between 16-24° relative to the aromatic ring plane. This was proposed to be due to steric effects between the nitrogen bonded hydrogen and the nearby hydrogen atom bonded to the aromatic ring (Penfold & White, 1959).

An important consideration in using benzamide as a ligand is the site of coordination. It can potentially coordinate to a metal atom through the oxygen atom or nitrogen atom. However, there is no evidence in the literature of nitrogen-metal coordination occurring for benzamide, and only one nitrogen coordinated amide complex in the CSD (CSD Refcode: ACACDC, Cavalca, Nardelli and Coghi, 1957) which did not contain any coordinates and is therefore omitted from in this discussion. In the acetamide and  $ZnI_2$  structure, coordination of acetamide occurs through the oxygen (CSD refcode: VIDBOA; Savinkina et al., 2007), whilst the coordination of benzamide to  $ZnI_2$  also coordinated through the oxygen atom (CSD refcode: VUCVAR; Savinkina et al., 2009).

Another prevalent feature of benzamide is its poor basicity; it has a  $pK_a$  value of -1.54 (Cox, 2008), and a proton affinity of  $872 \text{ kJ mol}^{-1}$  (Grützmacher and Caltapanides, 1998). Protonation of either the oxygen atom or the nitrogen atom is difficult and is ascribed to the resonant nature of the amide functional group. In this molecule, delocalization of the nitrogen lone pair of electrons occurs due to the electron withdrawing nature of the carbonyl group, resulting in a poor base. Due to the resonance effect, amides are generally seen as oxygen bases (Clayden et al., 2001) (Cox, 2008), as explained below.

Protonation of the nitrogen atom of the amide group would result in a formal positive charge on the nitrogen atom, along with a partially positive charge on the carbonyl carbon. This would lead to an energetically unfavoured configuration as there is a breakdown in the resonance stabilization, and the creation of a strong dipole in the carbon oxygen bond.

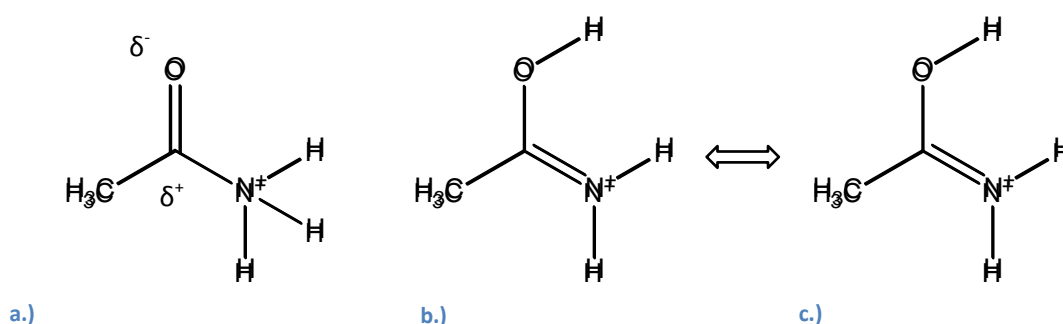


Figure 20: Protonation of an amide a.) Nitrogen protonated b.) Oxygen protonated and c.) Additional resonance structure.

Protonation of the oxygen atom, however, results in the additional positive charge being delocalized throughout the nitrogen, carbon and oxygen atoms, therefore benefitting from resonance in order to lower the electronic energy (Clayden et al., 2001). Only one crystal structure containing a

protonated benzamide molecule was found in the CSD, namely that of BENZAMTI01 (Herbstein et al., 1981). It was reported to be protonated on the nitrogen atom, which contradicts the resonance theory of protonation discussed above. The structure did however not include any hydrogen atoms and is therefore not included in the discussions to follow. The question of the site of protonation in benzamide will be investigated further in this investigation.

As bonding through coordination is similar to protonation in terms of electrostatics, the same type of logic may apply; If L-type (lone pair) donation of nitrogen's lone pair occurs to a positively charged metal centre, a net positive charge would result on the nitrogen group. Similar to the above mentioned arguments, there is no resonance structure able to stabilize the net positive charge that is again adjacent to the carbonyl carbon. In contrast if L-type coordination occurs through the oxygen atom, the lone pair on the nitrogen atom can delocalize to the resonance form, and thus stabilize the oxygen metal bond. The low basicity of benzamide is however a cause for concern as it will most likely also be a bad electron donor to a metal atom and therefore be difficult to coordinate.

With respect to supramolecular chemistry, the benzamide molecule possesses three distinct characteristics which make it a good organic constituent for forming hybrid supramolecular crystals. Firstly, the benzene ring of benzamide molecule may result in the formation of  $\pi$ - $\pi$  stacking interactions in the solid state. Secondly, the hydrogen atoms on the nitrogen atom can form intra- and intermolecular hydrogen bonds with electronegative hydrogen bond acceptors and the amide group oxygen may also act as a hydrogen bond acceptor (Vishweshwar, Nangia and Lynch, 2003). Lastly, the benzene ring is hydrophobic which may give rise to hydrophobic interactions. As mentioned previously, all of these non-bonding interactions will have an effect on the structure of the crystal formed, thus the more interactions a ligand has to offer, the more likely it is to form coordination polymers or supramolecular crystals. It also allows for the study of potential "recognition" between functional groups.

#### Organic constituent: 4-aminobenzamide

The second organic component considered in this study is a benzamide derivative, 4-aminobenzamide as shown in Figure 21. It was introduced in this study as it has many similar features to that of benzamide. 4-Aminobenzamide (4ABA) has an amine group in the para position of the aromatic ring and this group introduces another potential coordination site, potential protonation site and possible hydrogen bonding site. In the case of 4-aminobenzamide, only neutral coordination compounds were considered, since no compounds of this type could be located in the CSD, and because a number of ionic compounds of this organic component have already been reported (Overbeek, 2011).

The proton affinity of 4-aminobenzamide was reported to be  $930 \pm 4 \text{ kJ mol}^{-1}$ , making it a slightly stronger base than the weak base benzamide, which has a proton affinity of  $872 \text{ kJ mol}^{-1}$ .

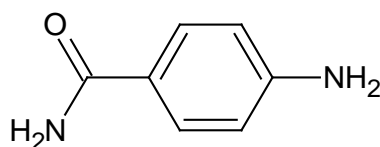


Figure 21: Line structure of 4-aminobenzamide

In the previously reported ionic 4-aminobenzamide structures (Overbeek, 2011), protonation was found to occur on the amine group of the molecule, while the amide group remained unprotonated. This implies that the basicity of the amine group exceeds that of the amide group.

As expected, protonation will occur on the amine functional group due to its higher basicity, and the amide functional group will remain unprotonated. Once the amine is protonated, the positive charge on the ammonium group is stabilized by the aromatic electron density. The amine group will also show a much higher reactivity towards metals compared to the amide group. Coordination will most likely occur through the amine group rather than the amide group. Because of the  $sp^3$  hybridization on the nitrogen, the coordination angle to the metal will most likely be at an angle consistent with  $sp^3$  hybridization. If coordination occurs through the amine rather than the amide, the formation of amide dimers may incur some interesting features.

## Inorganic component

This study focuses on the use of divalent transition metal halides in combination with the organic ligands discussed above. The following metal halides were used in this study:

**Table 2: Divalent metal halides used in this study.**

CuCl <sub>2</sub>	CuBr <sub>2</sub>
MnCl <sub>2</sub>	MnBr <sub>2</sub>
CoCl <sub>2</sub>	CoBr <sub>2</sub>
CdCl <sub>2</sub>	CdBr <sub>2</sub>
HgCl <sub>2</sub>	HgBr <sub>2</sub>
ZnCl <sub>2</sub>	ZnBr <sub>2</sub>

The iodides generally have solubility issues and in some cases redox reactions with ligands can complicate synthesis, for these reasons, the iodides were not considered. Fluorides readily decompose into several toxic/harmful compounds and are also excluded from this study.

## Problem definition and approach

From the interesting properties reported for metal halide based organic-inorganic hybrid materials in the literature it is evident that these types of materials may have the potential to be used in applications in the field of material science. However, to fully exploit what these materials have to offer, a fundamental understanding of their structures, as well as how their structures influence their properties, is required. In addition, the types of metal halide-based materials should be expanded to include functional groups other than the amine functional group, which has traditionally been used, in order to note the effect of this on the structure and properties of the material.

A better understanding of the structures of the materials can be achieved through the structural analysis of a family of materials, by systematic variation of the building blocks of the material. In the current study four parameters are varied, namely metal ion, halogeno ligand, organic constituent and stoichiometry. A matrix of materials is prepared, and where possible, the materials are characterized structurally by means of single crystal X-ray diffraction. This allows for the

identification of structural trends, as well as changes induced in the structure through a change in the composition of the material.

In addition to the experimental approach described above, the computational modeling of the materials will add to the knowledge on the materials, and will assist in understanding the materials and their structures and properties from a quantum mechanical point of view. Once it has been shown that the properties of the compounds can be successfully computed, the properties of novel materials may be calculated in advance, in order to determine whether they display desired properties.

However, before this can be achieved, an applicable computational model must be identified. This model must be tested through comparison of calculated properties with experimentally measured properties, to ensure the validity of the parameters of the model.

It is clear from the literature survey that very few studies employing DFT calculations to calculate the physical properties of these materials have been reported. In addition, a number of problems have been associated with the modeling of transition metals with partially filled d-orbitals.

At a more fundamental level, it is not always obvious from the literature how exactly the specific properties arise in these materials, and what the contributions of the different building blocks are. The question can be asked if it is simply the composition of the material that dictates what properties a material will have or if the structure of the material holds the key to its properties, or both? The logical answer to this question is that both the structure and the composition have an influence, but proving the role of both variables simultaneously is akin to solving a multi variable equation, and only having one equation to do it with. There are simply too many variables to consider in order in getting a sensible answer. Therefore two separate experiments need to be constructed to determine the answer to each question, and upon combining the answers we may learn the true relationship between the structure, composition and properties of these hybrid materials.

The first would be to attempt to create materials with similar structures and different compositions, thus a family of isostructural materials. So, in order to determine the role of composition on the properties observed in these materials we need to have materials which have very similar, almost identical structures. This removes the variable that different structures introduce to a degree. As will be reported in a later chapter, four isostructural natural coordination compounds of benzamide were successfully prepared, and studied via single crystal X-ray diffraction, Diffuse Reflectance Spectroscopy, and Density Functional Theory calculations.

To test the role that structure plays we need to synthesize materials with the same composition but different structures, hence different polymorphic forms, thereby removing the role that composition has on the material. Achieving this is, however, much more challenging. Materials usually pack in such a way that the energy of the material is at a minimum. Each structure will have a certain energy price tag, and creating a material with different structures may mean complex synthetic methods to isolate these different structures, and even then it may not be possible to obtain a different polymorph. Additionally, using similar ligands may induce different structures and not alter the composition of a material much. Unfortunately no polymorphs of any hybrid material could be prepared in this investigation.

## Research aims

1. To synthesize, structurally characterize and identify the structural trends observed for the materials generated when selected divalent transition metal halides are combined with benzamide and when selected divalent transition metal halides are combined with 4-aminobenzamide.
2. To experimentally measure the band gaps of isostructural materials to determine the electronic nature of the materials, and elucidate the role of composition on the electronic properties of the isostructural neutral coordination polymers.
3. To perform DFT calculations on isostructural materials to identify suitable computational parameters, and obtain band gap energies, density of states and other output parameters.
4. To explore the applicability of DFT calculations to the study of these materials in general.

## Bibliography

Aakeroy, C.B., Champness, N.R. and Janaik, C. (2010) 'Recent advances in crystal engineering', *Cryst. Eng.*, vol. 12, pp. 22-43.

Accelrys Software Inc (2010) *Materials Studio Release Notes, Release 5.5*, San Diego: Accelrys Software Inc.

Alexandre, S.S., Soler, J.M., Sanz Miguel, P.J., Nunes, R.W. and Yndurain, F. (2007) 'Design of molecular based wires based on one dimensional coordination polymers.', *Appl. Phys. Lett.*, p. 90.

Alexeev, Y.E., Kharisov, B.I., Hernandez Garcia, T.C. and Garnovskii, A.D. (2010) 'Coordination motifs in modern supramolecular chemistry', *Coord. Chem. Rev.*, vol. 254, pp. 794-831.

Arunan, E. (2007) 'Hydrogen bonding and other molecular interactions', *Curr. Sci.*, pp. 17-18.

Aruta, C., Licci, F., Zapettini, A., Bolzoni, F., Rastelli, F., Ferro, P. and Besagni, T. (2004) 'Growth and optical, magnetic and transport properties of  $(C_4H_9NH_3)_2(MCl_4)$  organic-inorganic hybrid films', *Appl. Phys. A*.

Ayyappan, , Sirokman, , Evans, O.R., Warren, T.H. and Lina, (2004) 'Non-linear optically active zinc and cadmium p-pyridinecarboxylate coordination networks', *Inorg. Chim. Acta*, p. 3999-4004.

Bachelet, G.B., Hamann, D.R. and Schluter, M. (1982) 'Pseudopotentials that work: From H to Pu', *Phys. Rev. B*, vol. 26, pp. 4199-4228.

Banks, M.G., Kremer, R.K., Hoch, C., Simon, A., Ouladdiaf, Broto, J.-M., Rakoto, H., Lee, C. and Whangbo, M.-H. (2009) 'Magnetic ordering in the frustrated Heisenberg chain system cupric chloride  $CuCl_2$ ', *Phys. Rev. B*, vol. 80, no. 024404.

Batten, S.R., Champness, N.R., Chen, X.-M., Garcia-Martinez, J., Kitagawa, S., Öhrström, L., O'Keeffe, M., Suh, M.P. and Reedijk, J. (2012) 'Coordination polymers, metal-organic frameworks and the need for terminology guidelines', *Cryst. Eng.*, p. Advance article.

- Blagden, N., Davey, R., Dent, G., Song, M., David, W., Paulham, C. and Shankland, K. (2005) 'Woehler and Liebig Revisited: A small molecule reveals its secrets- the crystal structure of the unstable polymorph of benzamide solved after 173 years', *Cryst. Growth Des.*, vol. 5, no. 6, pp. 2218-2224.
- Blake, C.C.F. and Small, R.W.H. (1972) 'The crystal structure of benzamide', *Acta Crystallogr., Sect. B: Struct. Sci.*, vol. 28, pp. 2201-2206.
- Braga, D. (2003) 'Crystal engineering, Where from? Where to?', *Chem. Commun.*, pp. 2751-2754.
- Brammer, L. (2004) 'Developments in inorganic crystal engineering', *Chem. Soc. Rev.*, vol. 33, pp. 476-489.
- Brammer, L., Swearingen, J.K., Bruton, E.A. and Sherwood, P. (2002) 'Hydrogen bonding and perhalometallate ions: A supramolecular synthetic strategy for new inorganic materials', *PNAS*, vol. 99, no. 8, pp. 4956-4961.
- Cavalca, L., Nardelli, M. and Coghi, L. (1957) 'La struttura del cloruro di (di)acetamide-cadmio', *Nuovo Cimento Soc. Ital. Fis.*, vol. 6, p. 278.
- Chen, X.-Q., Fu, C.L., Franchini, C. and Podloucky, R. (2009) 'Hybrid density-functional calculation of the electronic and magnetic structures of tetragonal CuO', *Phys. Rev. B*, vol. 80, no. 094527.
- Chen, Z.-L., Jiang, C.-F., Yan, W.-H., Liang, F.-P. and Batten, a.S.R. (2009) 'Three-dimensional metal azide coordination polymers with amino carboxylate coligands: synthesis, structure, and magnetic properties', *Inorg. Chem.*, vol. 48, no. 11, p. 4674-4684.
- Chondroudis, K. and Mitzi, D.B. (1999) 'Electroluminescence from an organic-inorganic perovskite incorporating a quaterthiophene dye within lead halide preovskite layers', *Chem. Mater.*, pp. 11, 3028-3030.
- Clayden, J., Greeves, N., Warren, S. and Wothers, P. (2001) 'Organic Chemistry', 1<sup>st</sup> edition, New York: Oxford University Press.
- Clement, O., Rapko, B.M. and Hay, B.P. (1998) 'Structural aspects of metal-amide complexes', *Coord. Chem. Rev.*, vol. 170, pp. 203-243.
- Constant, G., Daran, J.C. and Jeannin, Y. (1971) 'Compose de coordination forme entre le chlorure ferreux et la formamide: Catena- $\mu$ -dichlorobis [formamido-o] fer (II)', *J. Inorg. Nucl. Chem.*, vol. 33, p. 4209.
- Cox, R.A. (2008) 'Benzamide hydrolysis in strong acids - The last word', *Can. J. Chem.*, vol. 86, pp. 290-297.
- Criado, J.J., Jimenez-Sanchez, A., Cano, F.H., Saez-Puche, R. and Rodriguez-Fernandez, E. (1999) 'Preparation and characterization of tetrachlorocobaltates(ii) of alkylenediammonium. Magnetic and thermal properties.', *Acta Crystallogr., Sect. B: Struct. Sci.*, vol. 55, pp. 947-952.
- Desiraju, G.R. (1997) 'Designer crystals: intermolecular interactions, network', *Chem. Commun.*, pp. 1475-1482.

- Dudarev, S.L., Savrasov, S.Y., Humphreys, C.J. and Sutton, A.P. (1998) 'Electron-energy-loss spectra and the structural stability of nickel oxide: An LSDA1U study', *Phys. Rev. B*, vol. 57, no. 3, pp. 1505-1509.
- Englert, U. (2010) 'Halide-bridged polymers of divalent metals with donor ligands – structures and properties', *Coord. Chem. Rev.*, vol. 254, no. 5-6, pp. 537-554.
- Gao, Q., Jeffrey, G.A., Ruble, J.R. and McMullan, R.K. (1991) 'A single-crystal neutron diffraction refinement of benzamide at 15 and 123 K', *Acta Crystallogr., Sect. B: Struct. Sci.*, vol. 47, pp. 742-745.
- Gellman, S.H. (1997) 'Introduction: Molecular recognition', *Chem. Rev.*, vol. 97, no. 5.
- Girma, K.B., Lorenz, V., Blaurock, S. and Edelman, F.T. (2005) 'Coordination chemistry of acrylamide: 1. cobalt (ii) chloride complexes with acrylamide—synthesis and crystal structures', *Z. Anorg. Allg. Chem.*, vol. 631, p. 1419.
- Girma, K.B., Lorenz, V., Blaurock, S. and Edelman, F.T. (2006) 'Coordination chemistry of acrylamide. 5. crystal structures of complexes of metal(II) perchlorates and tetrafluoroborates with acrylamide' *Inorg. Chim. Acta*, vol. 359, p. 364.
- Graham, P.M. and Pike, R.D. (2000) 'Coordination polymers of copper(I) halides', *Inorg. Chem.*, vol. 39, no. 22, pp. 5121-5123.
- Grützmacher, H.-F. and Caltapanides, A. (1998) 'Proton affinity of some substituted 2,6-dimethylbenzamides and their N,N-dimethyl derivatives', *Eur. Mass Spectrom.*, vol. 4, pp. 349-357.
- Habib, H.A., Hoffmann, A., Höpfe, H.A. and Janiak, C. (2009) 'Crystal structures and solid-state CPDAS 13C NMR correlations in luminescent zinc(II) and cadmium(II) mixed-ligand coordination polymers constructed from 1,2-bis(1,2,4-triazol-4-yl)ethane and benzenedicarboxylate', *J. Chem. Soc., Dalton Trans.*, pp. 1742-1751.
- Habib, H.A., Hoffmann, A., Höpfe, H.A., Steinfeld, and Janiak, (2009) 'Crystal structure solid-state cross polarization magic angle spinning 13C NMR correlation in luminescent d10 metal-organic frameworks constructed with the 1,2-Bis(1,2,4-triazol-4-yl)ethane Ligand', *Inorg. Chem.*, pp. 2166-2180.
- Herbstein, F.H., Kaftory, M., Kapon, M. and Saenger, W. (1981) 'Structures of three crystals containing approximately—linear chains of triiodide ions' *Z. Kristallogr. Kristallgeom. Kristallphys. Kristallchem.*, vol. 11, p. 154.
- Herringer, S.N., Longendyke, A.J., Turnbull, M.M., Landee, C.P., Wikaira, J.L., Jameson, G.B. and Telfer, S.G. (2010) 'Synthesis, structure, and magnetic properties of bis(monosubstituted-pyrazine)dihalocopper(II)', *J. Chem. Soc., Dalton Trans.*, pp. 39: 2785-2797.
- Hohenberg, P. and Kohn, W. (1964) 'Inhomogeneous electron gas', *Phys. Rev. B*, vol. 136, pp. 864-871.
- Hu, C., Kalf, I. and Englert, U. (2007) 'Pyridine complexes of mercury(II)halides: Implications of a soft metal center for crystal engineering.', *Cryst. Eng.*, vol. 9, no. 7, pp. 603-610.



- Hunter, C.A. and Sanders, J.K.M. (1990) 'The nature of  $\pi$ - $\pi$  interactions', *J. Am. Chem. soc.*, vol. 112, pp. 5525-5534.
- Janiak, C. (2000) 'Critical account in pi-pi stacking in metal complexes with aromatic nitrogen containing ligands', *J. Chem. Soc., Dalton Trans.*, pp. 3885-3896.
- Koizumi, S., Watanabe, K., Hasegawa, M., Kanda, H., (2001) 'Ultraviolet emission from a diamond pn junction' *Science*, vol. 292, pp. 1899.
- Kohn, W. and Sham, L.J. (1965) 'Self-consistent equations including exchange and correlation effects.', *Phys. Rev. A*, vol. 140, p. 1133.
- Landee, C.P., Delcheva, A., Galeriu, C., Pena, G., Turnbull, M.M. and Willett, R.D. (2003) 'Molecular-based quantum magnets: the isotropic spin ladder  $\text{Cu}(\text{quinoxaline})\text{Br}_2$ ', *Polyhedron*, pp. 22: 2325-2329.
- Li, H.-H., Chen, S.-Y., Dong, H.-J., Wu, Y.-L. and Chen, Z.-R. (2011) 'An iodoargentate hybrid coordination polymer constructed by methyl viologen: structure, properties and theoretical study', *J. Chem. Crystallogr.*, pp. 41: 858-863.
- Liu, J.-B., Li, H.-H., Chen, Z.-R., Li, J.-B., Chen, X.-B. and Huang, C.-C. (2009) 'A new semi-conductive copper(I) halide coordination polymer: synthesis, structure and theoretical study', *J. Cluster Sci.*, vol. 20, pp. 515-523.
- Li, X., Zhen, L., Fan, X. and Zeng, Q. (2007) 'Crystal engineering based on polymeric hydrogen-bonded supramolecules by self-assembling of 4,4'-(9-fluorenylidene)diphenol and 4,4'-cyclohexylidenebisphenol with bipyridines', *Int. J. Mol. Sci.*, vol. 8, pp. 241-258.
- Li, H.-H., Zheng, Q.-S., Chen, Z., Dong, H.-J., Wu, Y.-L. and Wang, M. (2010) 'Reduced band gap in  $[\text{Pb}_2\text{I}_4(\text{datone})_2]$ : Synthesis, properties and calculations', *J. Mol. Struct.*, pp. 28-32.
- Mateo-Marti, E., Welte, L., Amo-Ochoa, P., Sanz Miguel, J., Gomez-Herrero, J., Martin-Gago, J.A. and Zamora, F. (2008) 'Direct evidence of nanowires formation from a Cu(I) coordination polymer', *Chem Commun.*, pp. 945-947.
- Mitschler, A., Fischer, J. and Weiss, R. (1967) 'Structure cristalline du dichlorure de cadmium diformamide,  $\text{CdCl}_2 \cdot 2\text{HCONH}_2$ ', *Acta Crystallogr.*, vol. 22, p. 236.
- Mitzi, D.B. (2001) 'Templating and structural engineering in organic-inorganic perovskites', *J. Chem. Soc., Dalton Trans.*, pp. 1-12.
- Mitzi, D.B., Chondroudis, K. and Kagan, C.R. (2001) 'Organic – inorganic electronics', *IBM J. Res. Dev.*, p. 45:1.
- Mitzi, D.B., Dimitrakopoulos, C.D. and Kosbar, L.L. (2001) 'Structurally tailored organic-inorganic perovskites: optical properties and solution-processed channel materials for thin-film transistors', *Chem. Mater.*, vol. 13, no. 10, p. 3728–3740.



Monkhorst, H.J. and Pack, J.D. (1979) 'Special points for Brillouin-zone integrations', *Phys. Rev. B*, vol. 13, p. 5188-5192.

Overbeek, G.E. (2011) 'Crystallographic and thermal investigation of coordination and ionic compounds of metal halides and 4-aminobenzoic acid and related molecules', *MSc thesis submitted to the University of Pretoria*.

Penfold, B.R. and White, J. (1959) 'The crystal and molecular structure of benzamide', *Acta Crystallogr.*, vol. 12, pp. 130-135.

Perdew, J., Ruzsinszky, A., Csonka, G.I., Vydrov, O.A., Scuseria, G.E., Constantin, L.A., Zhou, X. and Burke, K. (2008) 'Restoring the density-gradient expansion for exchange in solids and surfaces', *Phys. Rev. Lett.*, p. 100: 136406.

Rademeyer, M., Tsouris, C., Billing, D.G., Lemmerer, A. and Charmante, J. (2011) 'Robust motifs in 2-phenylethylammonium and related tetrahalometallates', *Cryst. Eng.*, no. 13, pp. 3845-3497.

Ramírez-Solís, A., Poteau, R., Vela, A. and Daudey, J.P. (2005) 'Comparative studies of the spectroscopy of CuCl<sub>2</sub>: DFT versus standard', *J. Chem. Phys.*, vol. 122, no. 164306.

Robin, A.Y. and Fromm, K.M. (2006) 'Coordination polymer networks with O- and N-donors: What they are, why and how they are made', *Coord. Chem. Rev.*, pp. 2127-2157.

Savinkina, E.V., Buravlev, E.A., Zamilatskov, I.A. and Albov, D.V. (2007) 'Bis(acetamide-O)diodidozinc(II)', *Acta Crystallogr., Sect. E: Struct. Rep. Online*, vol. 63, p. 1094.

Savinkina, E.V., Buravlev, E.A., Zamilatskov, I.A., Albov, D.V., Kravchenko, V.V., Zaitseva, M.G. and Mavrin, B.N. (2009) 'Zinc iodide complexes of propaneamide, benzamide, dimethylurea, and thioacetamide: syntheses and structures' *Z. Anorg. Allg. Chem.*, vol. 635, p. 1548.

Savinkina, E.V., Zamilatskov, I.A., Buravlev, E.A., Albov, D.V. and Tsivadze, A.Y. (2008) 'Reactions of manganese and zinc iodides with formamide in aqueous solution', *Mendeleev Commun.*, vol. 18, p. 92.

Scholl, D.S. and Steckel, J.A. (2009) 'Density functional theory: A practical introduction', 1<sup>st</sup> edition, New Jersey: John Wiley & Sons.

Shtukenberg, A.G., P'yankova, L.A. and Punin, Y.O. (2010) 'Crystal structure and infrared spectroscopy of MCl<sub>2</sub>·2CONH<sub>3</sub> (M = Cu, Mn)' *Zh. Strukt. Khim.*, vol. 51, p. 945.

Slater, J.C. (1951) 'A simplification of the Hartree-Fock method', *Phys. Rev.*, vol. 81, p. 385.

Sousa, S.F., Fernandes, P.A. and Ramos, M.J. (2007) 'General performance of density functionals', *J. Phys. Chem. A*, vol. 111, pp. 10439-10452.

Steiner, T. (2002) 'Hydrogen bond in the solid state', *Angew. Chem. Int. Ed.*, vol. 41, pp. 48-76.

Strehlow, W. H. (1973) 'Compilation of energy band gaps in elemental and binary compound semiconductors and insulators.', *J. Phys. Chem. Ref. Data*, vol. 2, no. 1.

Streetman, B.G. and Banerjee, S. (2000) 'Solid State Electronic Devices', 5<sup>th</sup> edition, New Jersey: Prentice Hall.

Takeuchi, H., Sato, M., Tsuji, T., Takashima, H., Egawa, T. and Konaka, S. (1999) 'Molecular structure of benzamide as studied by gas-phase electron diffraction', *J. Mol. Struct.*, vol. 485-486, pp. 175-181.

Tang, Q., Zhou, Z. and Chen, Z. (2012) 'Single-layer  $[\text{Cu}_2\text{Br}(\text{IN})_2]_n$  coordination polymer: electronic and magnetic properties, and implication for molecular sensors', *J. Phys. Chem. C*, vol. 116, no. 6, p. 4119-4125.

Tilley, R. (2004) 'Understanding solids', 1<sup>st</sup> edition, West Sussex: John Wiley & Sons.

van Zeghbroeck, B. (2011) 'Principles of electronic devices' Accessed online from: [http://ecee.colorado.edu/~bart/book/book/chapter4/ch4\\_6.htm](http://ecee.colorado.edu/~bart/book/book/chapter4/ch4_6.htm) on 27 March 2012.

Vishweshwar, P., Nangia, A. and Lynch, V.M. (2003) 'Supramolecular synthons in phenol-isonicotinamide adducts', *Cryst. Eng.*, vol. 5, pp. 164-168.

Welte, L., Calzolari, A., Di Felice, R., Zamora, F. and Gomez-Herrero, J. (2010) 'Highly conductive self-assembled nanoribbons of coordination polymers', *Nat. Nanotechnol.*, vol. 5, pp. 110-115.

Worth, G.A. and Wade, R.C. (1995) 'The aromatic-(i+20) amine interaction in peptides', *J. Phys. Chem.*, vol. 99, pp. 17473-17482.

Yap, G.A.P., Rheingold, A.L., Das, P. and Crabtree, R.H. (1995) 'A three-center hydrogen bond in 2,6-diphenylpyridinium tetrachloroaurate', *Inorg. Chem.*, vol. 34, pp. 3474-3476.

# Chapter 2- Experimental Techniques

---

## A. Experimental Investigation

### Materials

All materials used were reagent quality and used as purchased without any further purification.

### Synthesis

#### Synthetic strategy

Two phases of synthesis were conducted and a general method will be discussed for each phase. The products which yielded crystal structures will be discussed separately and in more detail.

Phase 1: Solutions with mol ratio 1:1, 1:3, 1:5, 5:1 and 3:1 (benzamide to  $\text{MX}_2$ ) (where  $\text{MX}_2 = \text{MnBr}_2, \text{MnCl}_2, \text{CoCl}_2, \text{CoBr}_2, \text{CuCl}_2, \text{CuBr}_2, \text{ZnCl}_2, \text{ZnBr}_2, \text{CdCl}_2, \text{CdBr}_2, \text{HgBr}_2$  and  $\text{HgCl}_2$ ) mol ratio were prepared for each metal halide. 0.5 g Benzamide was weighed off and placed into 75 polytops. The corresponding mass of metal halide was added to the polytops to obtain the mol ratio stated above for each metal. The samples were dissolved in a minimal amount of ethanol. The metal salts of cadmium and mercury did not dissolve in water or ethanol. These metals were dissolved in an acidified ethanol solution and then added to the benzamide-ethanol solution. For the specific volumes and type of acid added see the synthesis procedures below. The powders that were obtained from these reactions were re-dissolved in a range of different solvents, with the aim of obtaining good quality single crystals of the products.

Phase 2: A second phase of synthesis involved the combination of either benzamide or 4-aminobenzamide with  $\text{MnBr}_2, \text{MnCl}_2, \text{CoCl}_2, \text{CoBr}_2, \text{CuCl}_2, \text{CuBr}_2$  and  $\text{FeCl}_3$  (trivalent). A 1:1 molar ratio was used here, and 0.5 g of benzamide or 4-aminobenzamide was combined with the equimolar amount of metal halide salt. For these combinations of organic and inorganic, several different methods (heating, reflux and the order that reagents were added together) were employed, as well as a range of different solvents including methanol, 1-propanol, Tetrahydrofuran, Dimethyl sulfoxide, acetonitrile, water and some combination of these to promote crystal growth. The obtained powders were re-dissolved in a range of solvents in an effort to obtain good quality single crystals of the materials.

Powder diffraction was employed to investigate the products of which single crystals could not be obtained, however, problems were experienced due to the fact that unreacted metal halide reacted with the aluminium sample holder used for powder diffraction, hence this method of characterization could not be used.

Single crystals of good quality were obtained from the specific procedures described below, and these products were analysed further by single crystal X-ray diffraction.

Please note that structures will be referred to by an abbreviation that indicates both the inorganic and the organic components used to construct the material. For the inorganic part, the abbreviation MX indicates the metal and the halogen, while the abbreviation BA will be employed for the organic

molecule benzamide, and 4ABA for the organic molecule 4-aminobenzoic acid. As an example, the abbreviation CuCl-BA refers to the structure of the compound prepared from the combination of CuCl<sub>2</sub> and benzamide. Note that divalent metal halides, barring FeCl<sub>3</sub>, were employed in this study, and also note that the abbreviations do not give any information regarding the stoichiometry between the organic and the inorganic component in the structure.

### Synthetic procedures

#### *catena-(Benzamide-κO)-μ<sub>3</sub>-chlorido-μ-chloridocopper(II), CuCl-BA*

0.50 g (4.1 mmol) of benzamide and 0.56 g (4.2 mmol) of anhydrous CuCl<sub>2</sub> were added to a glass beaker and dissolved in a minimum amount of 1-propanol. The mixture was heated to boiling point for approximately 10 minutes, allowed to cool to room temperature and allowed to evaporate. Olive green needle like crystals were harvested and washed with chloroform.

#### *catena-(Benzamide-κO)-μ<sub>3</sub>-bromido-μ-bromidocopper(II), CuBr-BA*

0.50 g (4.1 mmol) of benzamide and 0.93 g (4.2 mmol) of CuBr<sub>2</sub> were added to a glass beaker and dissolved in a minimum amount of water and ~2 ml 0.5 M HBr was added to this. The mixture allowed to evaporate at room temperature over a period of four weeks. Dark brown compacted, needle like crystals were harvested and washed with chloroform.

#### *catena-(Benzamide-κO)-μ<sub>3</sub>-chlorido-μ-chloridocadmium(II), CdCl-BA*

0.50 g (4.1 mmol) of benzamide and 0.76 g (4.2 mmol) of CdCl<sub>2</sub> were added to a glass beaker and dissolved in a minimum amount of ethanol. The mixture was allowed to evaporate at room temperature. White/opaque prismatic crystals were harvested after four weeks and washed with chloroform.

#### *catena-(Benzamide-κO)-μ<sub>3</sub>-bromido-μ-bromidocadmium(II), CdBr-BA*

0.50 g (4.1 mmol) of benzamide was added to a glass beaker and dissolved in a minimum amount of ethanol. 1.13 g (4.2 mmol) of CdBr<sub>2</sub> was dissolved in water. The metal salt solution was then added to the benzamide solution. The mixture was allowed to evaporate at room temperature. White/opaque needle crystals were harvested after four weeks and washed with chloroform.

#### *Trans-(Tetrabenzamide(κO)-dibromidomanganese(ii)), MnBr-BA*

0.50 g (4.1 mmol) of benzamide and 0.90 g (4.2 mmol) of MnBr<sub>2</sub> were added to a glass beaker and dissolved in a minimum amount of ethanol. The mixture was heated for approximately 10 min, allowed to cool to room temperature and allowed to evaporate at room temperature. Light orange cubic crystals were harvested after four weeks and washed with chloroform.

#### *Di(benzamide-κO)dichloridozinc(II), ZnCl-BA*

0.50 g (4.1 mmol) of benzamide and 0.57 g (4.2 mmol) of ZnCl<sub>2</sub> were added to a glass beaker and dissolved in a minimum amount of ethanol. The mixture was allowed to evaporate at room temperature. White/opaque prismatic crystals were harvested after four weeks and washed with chloroform.

#### *Dibenzamide (Dibenzamide hydrogen) [catena-μ<sub>3</sub>-bromido-μ-bromido-dibromidomercuate(II)], HgBr-BA.*

1.50 g (4.2 mmol) of HgBr<sub>2</sub> was dissolved in ethanol and approximately 1 ml of 0.5 M HBr was needed to aid in the dissolution of the HgBr<sub>2</sub> salt in the ethanol. This solution was added to a

solution of 0.50 g (4.1 mmol) of benzamide dissolved in a minimum amount of ethanol. The mixture was allowed to evaporate at room temperature. White/opaque needle crystals were harvested after four weeks and washed with chloroform.

#### ***Trans-di(4-amino-κN-benzamide)diaquadibromidocobalt(II), CoBr-4ABA***

0.50 g (4.1 mmol) of 4-aminobenzamide and 0.80 g (4.2 mmol) of  $\text{CoBr}_2$  were added to a glass beaker and dissolved in a minimum amount of ethanol. The mixture was heated for approximately 10 min, allowed to cool to room temperature and allowed to evaporate at room temperature. Wine red cubic crystals were harvested after four weeks and washed with chloroform.

#### ***Trans-di(4amino-κN-benzamide)aquadibromidocopper(II), CuBr-4ABA***

0.25 g (1.859 mmol) 4-aminobenzamide was dissolved in 80 ml distilled water in a glass beaker, and heated to approximately 40 °C on a hot plate. In a separate beaker 0.21 g  $\text{CuBr}_2$  (0.928 mmol) was dissolved in 20 ml distilled water. The  $\text{CuBr}_2$  solution was added to the 4-aminobenzamide solution and left open to the air at room temperature. Dark brown, needle-like crystals formed on evaporation of the solvent, over a period of four weeks.

## **Single crystal X-ray Diffraction**

### **Theory**

X-Ray Crystallography is historically the synergy of two separate fields. The scientific investigation of crystals started in the 17<sup>th</sup> century when Johannes Kepler hypothesized that the strange beautiful shapes of snowflakes were due to the regular packing of water molecules. (Kepler, 1611). Several mathematical descriptors including the Miller indices, still prevalently used in modern crystallography, were researched, but it was not until the discovery of X-ray radiation in 1895 that Crystallography really found its roots as a diverse and very widely applied field of study. A large number of publications using this technique was published annually and this technique has become a very useful tool in many industries.

Similar to other forms of electromagnetic radiation, X-rays exhibit properties of both particles and waves. The wave like property of X-rays produce an interference pattern, much like the ripples observed when a few rocks are thrown into a pond. Fully explaining the interpretation of this pattern is slightly beyond the scope of this discussion, but the basic principles will be highlighted. Bragg discovered that when X-rays are scattered from crystals, an interference pattern could be observed, based on this interference he deduced the following equation:

$$2d\sin\theta = n\lambda$$

Where  $d$  is the spacing between layers of atoms in the crystals,  $\theta$  is the incident angle of the X-ray beam,  $n$  is an integer and  $\lambda$  is the wavelength of the X-rays used. This primitive equation gave birth to the field of modern crystallography. The equation basically predicts at what angles (the integer  $n$  produces a series of angles) the maximum interference can be found, but more importantly if the maximum peak in the interference pattern is observed, the spacing between layers of atoms could be determined. For this equation to hold, the wavelength of the X-rays and the spacing between the layers  $d$  has to be in the same order of magnitude. Bragg interpreted this interference pattern as the

X-rays colliding with the atoms, but did not understand at that time that the interference pattern from the diffracted X-rays “painted” a picture of the electron density in a crystalline substance.

The incident X-rays in fact disturb the electron cloud around atoms and cause the emission of a photon of the same energy and therefore wavelength as the incident wave, therefore the “picture” referred to above is actually the topology of the electron density around the atoms in their solid state. This electron density topology is then used to estimate the positions of the atomic nuclei. The term electron density is used explicitly as the amount of X-rays diffracted is dependent on the density of the electronic cloud. The denser it is, the higher the number of X-rays diffracted from that position. In chemical terms, the higher the number of electrons around an atom, the more intense the diffraction of X-rays at the corresponding position. In this manner different atoms can be placed based upon the position and intensity of the electron density that atom would generate in a crystal lattice.

The typical procedure of obtaining the atomic positions in a crystal lattice requires at least three steps. Firstly, and often the most difficult, is obtaining a suitable crystal for X-ray diffraction. A few decades ago a very good quality crystal with very few imperfections had to be used, but with the technological advancement of diffractometers the harsh criteria in terms of quality and size of a crystal has made it possible to determine structures even if the crystal is of poor quality. The second step in this process involves the X-ray bombardment of the single crystal. The crystal is typically rotated in the beam of X-rays. The interference peaks are logged for thousands of orientations, and from the interference pattern, a set of data is generated. The third step involves the interpretation of this data set into the atomic positions. Arriving at the positions of the atoms is not however trivial. It requires a vast number of computations, as well as a skilled placement of the “guessed” positions of atoms. The process starts with guessing the best position to place an atom based on the intensity electron density map. The positions of the “guessed” atomic positions are then refined by a computational tool to provide a better guess structure. This process is repeated several times and the positions of atoms are refined as to best imitate the electron density observed from the X-ray diffraction. This explanation of the procedure is kept as simple as possible. There are many approaches in obtaining the crystal structure through X-ray diffraction and each has advantages and disadvantages depending on the crystal under investigation. Therefore this section only serves as introduction into the topic and the reader is advised to refer to more advanced texts for additional information.

### **Experimental Data collection:**

Single crystal X-ray diffraction data were collected on three different instruments, with the specific structures, and the instruments on which their data were collected, given below.

#### ***CuCl-BA, MnBr-BA and CoBr-BA***

Good quality crystals were selected and mounted on a glass fiber using epoxy resin glue. X-Ray diffraction data were recorded at 100(2) K using a Panalytical X-PertPro X-Ray Diffractometer equipped with a Bruker APEX DUO 4K-CCD, employing graphite-monochromated Mo-K $\alpha$  radiation, using  $\phi$  and  $\omega$  scans. The frames were integrated with the Bruker SAINT (Bruker AXS Inc., Madison, Wisconsin, USA., 2007) software package using a narrow-frame algorithm. Data were corrected for absorption effects using the multi-scan method (SADABS).

### *CuBr-BA, CdCl-BA, CdBr-BA, HgBr-BA and ZnCl-BA*

Good quality single crystals were selected and mounted on a glass fiber using epoxy resin glue. X-ray diffraction data were collected at 293(2) K on a Siemens P4 diffractometer fitted with a Bruker 1K CCD detector employing graphite-monochromated Mo-K $\alpha$  radiation, using  $\phi$  and  $\omega$  scans. The data were reduced using the SAINT+ (Bruker AXS Inc., Madison, Wisconsin, USA., 2007) software, and absorption corrections were performed using SADABS (Bruker AXS Inc., Madison, Wisconsin, USA., 2001).

### *CuBr-4ABA*

Good quality single crystals were selected and X-ray diffraction data were collected at 180(2) K on a Bruker Nonius diffractometer fitted with a Nonius Kappa CCD detector employing graphite-monochromated Mo-K $\alpha$  radiation, using  $\phi$  and  $\omega$  scans. The data were reduced using the SAINT+ (Bruker AXS Inc., Madison, Wisconsin, USA., 2007) software, and absorption corrections were performed using SADABS (Bruker AXS Inc., Madison, Wisconsin, USA., 2001).

### **Structure solution:**

All of the structures were solved using SHELXS (Sheldrick, 2008), and refined employing SHELXL-97 (Sheldrick, 2008) as part of the WinGX 1.7 (Farrugia, 1999) suite of programs. All H atoms were refined using a riding model, with C-H distances of 0.97 Å (CH<sub>2</sub>) or 0.98 Å (CH) and N-H distances of 0.90 Å, with Uiso(H) = 1.2Ueq(C) or 1.2Ueq(N). Structural analysis was performed employing the software PLATON (Spek, 2003), and graphics were generated using Mercury 3.0 (Macrae et al., 2006)

### **Other**

#### *Cambridge Structural Database*

The Cambridge Structural Database (CSD) is a central collective database where the crystal structures of compounds are published and stored. This database allows users to search for compounds based on an abundant amount of search criteria including but by no means limited to, journal references, chemical composition, and most importantly search for structures that are similar based on a user drawn structure. The database contains 603,297 after the February 2012 update.

The CSD v5.33 (up to February 2012) was used in all the CSD searches.

### **Diffuse reflectance spectra (DRS)**

#### **Theory**

The determination of the forbidden band gap of a material from optical methods is likely the easiest and most accurate method. The optical transitions at specific wavelengths are a measure of the gap between the occupied valence band into the unoccupied conduction band.

Any UV/VIS technique can theoretically be used to determine the band gap. However the crystalline materials are typically opaque and do not allow the transmission of light through them, therefore typical absorption data cannot be collected, as the samples refract the light away from the detector, yielding false high absorption data. A solution to this would be to use reflectance of light off a sample. The sample can be ground to a fine powder, and irradiated with light. The light scatters in every direction. Collection of this scattered light with an integration sphere, shown in Figure 22, collimates the light into a single beam that can be spectrally analysed.



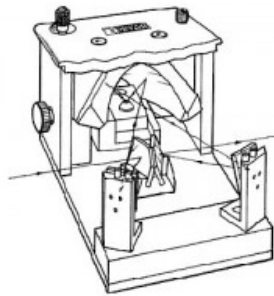


Figure 22: Praying Mantis Diffuse Reflection Accessory. Accessed online at <http://www.harricksci.com/ftir/accessories/group/Praying-Mantis%E2%84%A2-Diffuse-Reflection-Accessory>

The result is a set of data with % reflectance for each wavelength that can be plotted as shown in Figure 23. Typically a region of high reflectance is observed in the long wavelength (low energy) region. This is due to the photonic energy not being sufficient to excite electrons to higher electronic states and results in the reflection of the light.

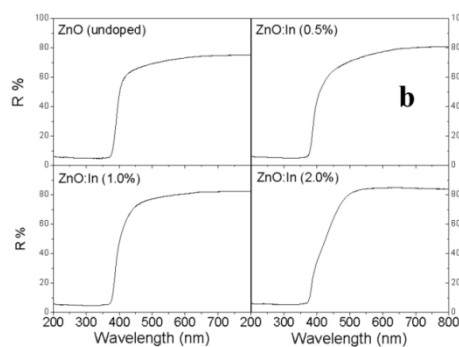


Figure 23: Example of diffuse reflectance spectra. (Morales, Mora and Pal, 2007)

As the photonic energy increases, with shorter wavelengths, the photons have enough energy to excite electrons from the valence band to the conduction band, and therefore span the band gap. In the process the photon energy is absorbed. This region is referred to as the absorption edge. The absorption increases to a maximum plateau as the photonic energy is increased. Photons here have enough energy to excite electrons from occupied bands into unoccupied bands above the band gap.

### Determination of the band gap from DRS

The determination of the band gap, however, has been a contentious issue in the literature and consequently as many as eleven methods have been developed and the different methods result in a maximum error of 0.5 eV. The DRS method still remains the best estimate of the optical band gap of solids (Nowak, Kauch and Szperlich, 2009).

All of these methods are based on the Kubelka-Munk theory (Kubelka and Munk, 1931). The theory was originally used to describe the scattering of light from paint surfaces, but it lead to the development of a useful equation. In the limiting case of an infinitely thick sample, the Kubelka-Munk equation at any wavelength becomes:



**Equation 4**

$$\frac{K}{S} = \alpha = \left( \frac{(1 - R_{\infty})^2}{2R_{\infty}} \right) \equiv F(R_{\infty})$$

Where  $F(R_{\infty})$  is called the Kubelka-Munk remission function where  $S$  is the scattering factor and is approximately equal to one for very fine particles,  $\alpha$  is the absorption coefficient of radiation and,

$$R_{\infty} = \frac{R_{sample}}{R_{standard}} = \%R$$

For a parabolic band structure, the band gap  $E_g$ , and the absorption coefficient of a band gap are related by:

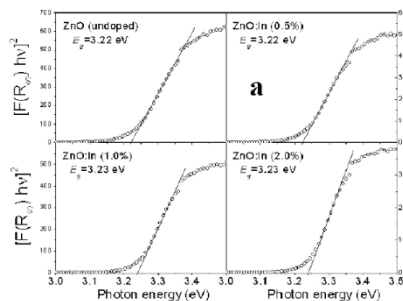
**Equation 5**

$$ahv = C_1(hv - E_g)^{1/2}$$

Where  $h$  is Planck's constant and  $v$  is frequency. Combining Equation 4 and 5 yields:

$$(F(R_{\infty})hv)^{1/2} = C_2(hv - E_g)$$

By plotting  $(F(R_{\infty})hv)^{1/2}$  v.s  $hv$  the  $E_g$  value can be extrapolated as shown in Figure 24 (Nowak, Kauch and Szperlich, 2009). This plot is also referred to as a Tauc plot (Tauc and Menth, 1972). We assume in this study that an indirect band gap exists for all the measured samples as the goal of this study is not to determine if the materials have direct or indirect band gaps. The assumption is based on the energy difference between a direct and indirect transition being very small compared to the energy of the photons used to irritate the sample with (van Zeghbroeck, 2011). Irrespective of the method used, the band gap can most likely only be estimated to within 0.5 eV, and evaluation of all the different methods of band gap determination is beyond the scope of this work.



**Figure 24: Example of the band gap determination through the Kubelka-Munk remission function using a Tauc plot (Morales, Mora and Pal, 2007) (Tauc and Menth, 1972).**

**Experimental Data Collection**

The DRS spectra were recorded at room temperature using a Cary 500 UV-Vis-NIR spectrophotometer equipped with a Praying Mantis Diffuse Reflectance Accessory. The diffuse reflectance spectra of CdCl-BA and CdBr-BA were recorded between 120 nm and 800 nm. The diffuse reflectance spectra of CuCl-BA and CuBr-BA were recorded in the same 120 nm to 800nm region, but the high absorbance plateau normally observed in DRS was not present. It was therefore rerecorded from 200nm - 1600 nm. Above 1600 nm, and below 200 nm, absorbance of atmospheric gases interfere with the spectra and do not provide any additional information. The single crystals of CuCl-BA, CuBr-BA, CdCl-BA and CdBr-BA were ground finely, and packed into a standard sampling cup. The samples were overfilled each time, and scraped flat with a small spatula. Band gaps were determined by the utilization of the Kubelka-Munk remission function and Tauc plots.

## B. Computational Investigation

The CASTEP (Segall et al., 2005) software package as implemented in the Materials Studio v5.5 (Accelrys Software Inc, 2010) software suite was used to perform all calculations.

Firstly, several functionals' performance were tested for CdBr-BA and CdCl-BA using default settings within CASTEP. The atomic positions and unit cell parameters were fully relaxed and a full geometry optimization was performed. Normally this procedure is manually repeated for each of the unit cell parameters. Since the structures studied here have a triclinic crystal lattice, six independent variables ( $a$ ,  $b$ ,  $c$ ,  $\alpha$ ,  $\beta$  and  $\gamma$ ) would have to be evaluated. This would be an enormous task and is not viable for triclinic systems. Therefore the assumption is made that the geometry optimisations were able to locate the global energy minima of all six variables. The functionals were tested with respect to their estimation of the cell parameters and is discussed further in Chapter 4. The PBESol (Perdew et al., 2008) functional performed the best among the different functionals.

The PBESol functional was then used to test the convergence of the k-point grid. The default "Fine" plane wave cut off energy for each structure was used as an initial plane wave cut-off energy. The k-point grid was then converged to within criteria that will be discussed in Chapter 4.

The converged k-point grid of 6x2x2 was then used to converge the plane wave cut-off energy. The plane wave cut-off energy was converged to within the criteria as discussed in Chapter 4.

This converged plane wave cut-off energy of 850 eV was then finally used to re-converge the k-point grid to within the criteria discussed in Chapter 4 to a value of 6x2x2.

The functionals' performances were again tested and the results of those calculations are the results presented in Chapter 4.

All of the band gap calculations, unless stated otherwise, were performed with fixed atomic positions and unit cell parameters. The PBESol functional was used with a plane wave cut-off energy of 850 eV and a k-grid of 6x2x2. For CdCl-BA and CdBr-BA a non-spin polarized calculation was performed and for CuCl-BA and CuBr-BA a spin-polarized calculation was performed but only the ferromagnetic structures were considered due to reasons discussed in Chapter 4.

## Bibliography

Accelrys Software Inc (2010) *Materials Studio Release Notes, Release 5.5*, San Diego: Accelrys Software Inc.

Bruker AXS Inc., Madison, Wisconsin, USA. (2001) 'SADABS'.

Bruker AXS Inc., Madison, Wisconsin, USA. (2007) 'SAINT+'.

Farrugia, L.J. (1999) 'WINGX', *J. Appl. Cryst.*, vol. 32, pp. 837-838.

Kepler, J. (1611) 'Strena seu de Nive Sexangula'.

Kubelka, P. and Munk, F. (1931) 'A contribution to the optics of pigments', *Z. Tech. Phys.*, p. 593 - 599.

Macrae, C.F., Edgington, P.R., McCabe, P., Pidcock, E., Shields, G.P., Taylor, R., Towler, M. and Streek, J.v.d. (2006) 'Mercury: visualization and analysis of crystal structures', *J. Appl. Crystallogr.*, vol. 39, pp. 453-457.

Morales, A.E., Mora, E.S. and Pal, U. (2007) 'Use of diffuse reflectance spectroscopy for optical characterization of', *Rev. Mex. Fis.*, vol. 53, no. 5, p. 18–22.

Nowak, M., Kauch, B. and Szperlich, P. (2009) 'Determination of energy band gap of nanocrystalline SbSI using diffuse reflectance spectroscopy', *Rev. Sci. Instrum.*, vol. 80, no. 4, p. 046107.

Perdew, J., Ruzsinszky, A., Csonka, G.I., Vydrov, O.A., Scuseria, G.E., Constantin, L.A., Zhou, X. and Burke, K. (2008) 'Restoring the density-gradient expansion for exchange in solids and surfaces', *Phys. Rev. Lett.*, p. 100: 136406.

Segall, M., Probert, M., Pickard, C., Hasnip, P., Clark, S., Refson, K. and Payne, M. (2005) 'First principles methods using CASTEP', *Z. Kristallogr.*, vol. 220, no. 5-6, pp. 567-570.

Sheldrick, G.M. (2008) 'SHELX', *Acta Crystallogr., Sect. A: Found. Crystallogr.*, vol. 64, pp. 112-122.

Spek, A.L. (2003) 'PLATON', *J. Appl. Crystallogr.*, vol. 36, pp. 7-13.

Tandon, S.P. and Gupta, J.P. (1970) 'Measurement of forbidden energy gap of semiconductors by diffuse reflectance technique', *Phys. Status Solidi B*, vol. 38, no. 1, p. 363–367.

Tauc, J. and Menth, A. (1972) 'States in the gap', *J. Non-Cryst. Solids*, vol. 8-10, p. 569–585.

# Chapter Three – Experimental Results

---

## Structural Analysis

In this chapter the nine novel single crystal structures obtained in this study will be discussed. Of these structures eight are coordination compounds, while one ionic structure was obtained. Structural phenomena such as the geometry of the molecules, packing arrangement and hydrogen bonding will be highlighted for each structure.

Crystallographic parameters for all the structures are listed in Table 3. Data for isostructural compounds are printed in blue.

Table 3: Crystallographic parameters for all structures

Identification code	MnBr-BA	ZnCl-BA	CuCl-BA	CuBr-BA	CdCl-BA
<b>Empirical Formula</b>	<i>trans</i> - [(C <sub>7</sub> H <sub>7</sub> NO) <sub>4</sub> MnBr <sub>2</sub> ]	[(C <sub>7</sub> H <sub>7</sub> NO) <sub>2</sub> ZnCl <sub>2</sub> ]	[C <sub>7</sub> H <sub>7</sub> NOCuCl <sub>2</sub> ] <sub>n</sub>	[C <sub>7</sub> H <sub>7</sub> NOCuBr <sub>2</sub> ] <sub>n</sub>	[C <sub>7</sub> H <sub>7</sub> NOCdBr <sub>2</sub> ] <sub>n</sub>
<b>Formula Weight (g.mol<sup>-1</sup>)</b>	699.28	378.56	255.59	344.49	304.45
<b>Lattice</b>	Tetragonal	Monoclinic	Triclinic	Triclinic	Triclinic
<b>Space group</b>	<i>I</i> 4 <sub>1</sub> / <i>a</i>	<i>P</i> 2 <sub>1</sub> / <i>c</i>	<i>P</i> $\bar{1}$	<i>P</i> $\bar{1}$	<i>P</i> $\bar{1}$
<b>Unit cell dimensions</b>					
<b><i>a</i> (Å)</b>	12.863(2)	20.683(2)	3.8311(8)	4.0472(8)	3.8512(4)
<b><i>b</i> (Å)</b>	12.863(2)	7.5193(8)	10.702(2)	10.908(2)	11.3340(12)
<b><i>c</i> (Å)</b>	17.856(3)	29.121(2)	11.122(2)	11.288(2)	11.6292(12)
<b><math>\alpha</math> (°)</b>	90	90	110.501(4)	110.915(3)	112.6170(10)
<b><math>\beta</math> (°)</b>	90	134.554(5)	95.756(4)	94.395(3)	95.091(2)
<b><math>\gamma</math> (°)</b>	90	90	95.147(4)	94.617(4)	98.308(2)
<b>Volume (Å<sup>3</sup>)</b>	2954.4(10)	3227.3(6)	421.14(14)	460.99(17)	457.83(8)
<b>Z</b>	4	8	2	2	2
<b>Calculated Density (g.cm<sup>-3</sup>)</b>	1.572	1.558	2.016	2.482	2.208
<b>Temperature (K)</b>	100(2)	293(2)	100(2)	293(2)	293(2)
<b>Crystal size (mm)</b>	0.20 x 0.28 x 0.29	0.18 x 0.36 x 0.38	0.04 x 0.04 x 0.23	0.36 x 0.36 x 0.39	0.12 x 0.15 x 0.42
<b>F(000)</b>	1404	1536	254	186	292
<b>Absorption coefficient (mm<sup>-1</sup>)</b>	3.191	1.857	3.169	10.984	2.915
<b>Radiation</b>	Mo K $\alpha$	Mo K $\alpha$	Mo K $\alpha$	Mo K $\alpha$	Mo K $\alpha$
<b>Wavelength (Å)</b>	0.71073	0.71073	0.71073	0.71073	0.71073
<b>Reflections for cell parameters</b>	2826	5673	4057	2196	2383
<b>Crystal description</b>	Block	Irregular fragment	Needle	Plate	Prism
<b>Crystal colour</b>	Colourless	Colourless	Yellow	Dark brown	Colourless
<b>Diffractometer type</b>	Bruker APEX DUO 4K- CCD	Bruker Siemens CCD	Bruker APEX DUO 4K- CCD	Bruker Siemens CCD	Bruker Siemens CCD
<b>Scan type</b>	$\phi$ and $\omega$ scans	$\phi$ and $\omega$ scans	$\phi$ and $\omega$ scans	$\phi$ and $\omega$ scans	$\phi$ and $\omega$ scans

Table 3 Continued: Crystallographic parameters for all structures

Identification code	MnBr-BA	ZnCl-BA	CuCl-BA	CuBr-BA	CdCl-BA
<b>Absorption correction method</b>	Multiscan	Multiscan	Multiscan	Multiscan	Multiscan
<b>Transmission factors (<math>T_{\min}</math>; <math>T_{\max}</math>)</b>	(0.8838; 0.5295)	(0.584; 0.716)	(0.8838; 0.5295)	(0.019; 0.517)	(0.561; 0.705)
<b>Measured reflections</b>	5873	6108	9783	1602	1657
<b>Independent reflections observed reflections with <math>I &gt; 2\sigma(I)</math></b>	2826	5633	2095	1474	1602
<b>Internal Fit</b>	0.0185	0.027	0.0385	0.0298	0.0201
<b>Index ranges</b>					
<b><math>h</math> (min; max)</b>	(-10; 17)	(-25; 17)	(-4; 5)	(-5; 2)	(-4; 1)
<b><math>k</math> (min; max)</b>	(-17 ; 14)	(-9; 9)	(-14; 14)	(-13; 11)	(-13; 13)
<b><math>l</math> (min; max)</b>	(-23; 13)	(-11; 36)	(-14; 14)	(-13; 13)	(-12; 14)
<b>Final R indices [<math>F^2 &gt; 2\sigma(F^2)</math>]</b>	$R_1 = 0.0193$ $wR(F^2) = 0.0453$	$R_1 = 0.0956$ $wR(F^2) = 0.2246$	$R_1 = 0.0365$ $wR(F^2) = 0.1037$	$R_1 = 0.0607$ $wR(F^2) = 0.1630$	$R_1 = 0.0353$ $wR(F^2) = 0.0861$
<b>Goodness of fit on <math>F^2</math></b>	1.024	1.200	1.070	1.087	0.965
<b>Parameters</b>	117	379	129	117	109
<b>Maximum shift (<math>\Delta/\sigma</math>)<sub>max</sub></b>	0.000	0.000	0.006	0.000	0.016
<b>Largest diff. peak (e.Å<sup>-3</sup>)</b>	0.40	0.75	1.29	1.96	0.55
<b>Largest hole (e.Å<sup>-3</sup>)</b>	-0.21	-0.97	1.07	-1.87	-1.33

Table 3 Continued: Crystallographic parameters for all structures

Identification code	CdBr-BA	HgBr-BA	CuBr-4ABA	CoBr-4ABA
<b>Empirical Formula</b>	$[C_7H_7NOCdBr_2]_n$	$(C_7H_8NO^+)_2(C_7H_7NO)_2$ $[Hg_3Br_8^{2-}]_n$	$[(C_7H_7N_2O)_2(H_2O)CuBr_2]$	$[(C_7H_7N_2O)_2(H_2O)_2CoBr_2]$
<b>Formula Weight (g.mol<sup>-1</sup>)</b>	393.36	1727.53	513.67	527.07
<b>Lattice</b>	Triclinic	Triclinic	Monoclinic	Monoclinic
<b>Space group</b>	$P\bar{1}$	$P\bar{1}$	$C 2/c$	$P 2_1/c$
<b>Unit cell dimensions</b>				
<b><i>a</i> (Å)</b>	3.9564(3)	8.5260(18)	24.838(2)	11.5320(11)
<b><i>b</i> (Å)</b>	11.5384(9)	11.098(2)	10.3973(8)	5.7406(5)
<b><i>c</i> (Å)</b>	11.6946(9)	12.472(3)	15.996(2)	13.8088(13)
<b><math>\alpha</math> (°)</b>	112.5550(10)	107.336(3)	90	90
<b><math>\beta</math> (°)</b>	93.8340(10)	93.053(3)	122.558(3)	93.163(2)
<b><math>\gamma</math> (°)</b>	98.4520(10)	110.148(3)	90	90
<b>Volume (Å<sup>3</sup>)</b>	483.22(6)	1041.5(4)	3481.8(6)	912.76(15)
<b>Z</b>	2	1	8	2
<b>Calculated Density (g.cm<sup>-3</sup>)</b>	2.703	2.754	1.96	1.918
<b>Temperature (K)</b>	293(2)	293(2)	180(2)	100(2)
<b>Crystal size (mm)</b>	0.02 x 0.24 x 0.42	0.90 x 0.24 x 0.42	0.23x 0.35x 0.45	0.12 x 0.21 x 0.39
<b>F(000)</b>	364	778	2024	522
<b>Absorption coefficient (mm<sup>-1</sup>)</b>	10.478	18.737	5.866	5.345
<b>Radiation</b>	Mo K $\alpha$	Mo K $\alpha$	Mo K $\alpha$	Mo K $\alpha$
<b>Wavelength (Å)</b>	0.71073	0.71073	0.71073	0.71073
<b>Reflections for cell parameters</b>	2893	3877	70836	2306
<b>Crystal description</b>	Needle	Thick-plate	Block	Block
<b>Crystal colour</b>	Colourless	Colourless	Dark red	Light-pink

Table 3 Continued: Crystallographic parameters for all

Identification code	CdBr-BA	HgBr-BA	CuBr-4ABA	CoBr-4ABA
<b>Diffractometer type</b>	Bruker Siemens CCD	Bruker Siemens CCD	Nonius Kappa CCD	Bruker APEX DUO 4K-CCD
<b>Scan type</b>	$\phi$ and $\omega$ scans	$\phi$ and $\omega$ scans	$\phi$ and $\omega$ scans	$\phi$ and $\omega$ scans
<b>Absorption correction method</b>	Multiscan	Multiscan	Multiscan	Multiscan
<b>Transmission factors (<math>T_{\min}</math>; <math>T_{\max}</math>)</b>	(0.561; 0.705)	(0.016; 0.185)	(0.869; 0.943)	-
<b>Measured reflections</b>	1754	3786	3000	2287
<b>Independent reflections observed reflections with <math>I &gt; 2\sigma(I)</math></b>	1601	3265	2233	1995
<b>Internal Fit</b>	0.0188	0.0484	0.0871	0.0229
<b>Index ranges</b>				
<b><math>h</math> (min; max)</b>	(-1; 4)	(-10; 10)	(-29; 27)	(-15; 15)
<b><math>k</math> (min; max)</b>	(-14; 13)	(-13; 11)	(-12; 12)	(-7; 7)
<b><math>l</math> (min; max)</b>	(-14; 13)	(-4; 15)	(-12; 18)	(-18; 18)
<b>Final R indices [<math>F^2 &gt; 2\sigma(F^2)</math>]</b>	$R_1 = 0.0416$ $wR(F^2) = 0.1328$	$R_1 = 0.0581$ $wR(F^2) = 0.1573$	$R_1 = 0.0450$ $wR(F^2) = 0.0868$	$R_1 = 0.0228$ $wR(F^2) = 0.0527$
<b>Goodness of fit on <math>F^2</math></b>	1.102	1.011	1.042	1.024
<b>Parameters</b>	109	215	223	131
<b>Maximum shift (<math>\Delta/\sigma</math>)<sub>max</sub></b>	0.005	0.000	0.001	0.002
<b>Largest diff. peak (<math>e.\text{\AA}^{-3}</math>)</b>	1.10	3.37	0.53	0.70
<b>Largest hole (<math>e.\text{\AA}^{-3}</math>)</b>	-1.40	-1.77	-0.62	-0.40



## *Trans*-(Tetrabenzamide( $\kappa$ -O)-dibromidomanganese(II)), MnBr-BA

Chemical Formula: *trans*-[(C<sub>7</sub>H<sub>7</sub>NO)<sub>4</sub>MnBr<sub>2</sub>]

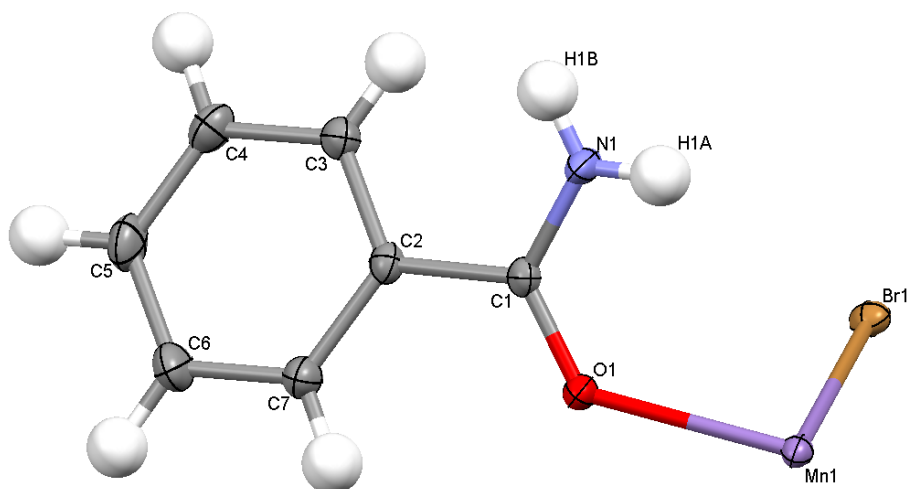


Figure 25: Asymmetric unit of MnBr-BA showing the atomic numbering scheme. Displacement ellipsoids are drawn at the 50% probability level and hydrogen atoms are drawn as spheres of arbitrary radii.

The asymmetric unit of MnBr-BA is shown in Figure 25 and consists of a manganese ion coordinated by one bromido ligand at a Mn1-Br1 distance of 2.6380(5) Å and one benzamide ligand coordinated through the oxygen atom with a Mn1-O1 bond distance of 2.2313(9) Å, as shown in Figure 25. The manganese atom occupies a special position, and is located on a four-fold rotoinversion axis, and the complete molecule is generated from the asymmetric unit by this symmetry operator. One molecule is comprised of four asymmetric units, and the unit cell contains four molecules, with each molecule displaying four-fold symmetry.

In this molecule, the manganese ion has an almost perfect octahedral coordination geometry, with the Br1-Mn1-Br1 angle equal to 180°, and O1-Mn1-Br1 angle of 90.49(3)°, as shown in Figure 26. The benzamide ligands are coordinated *cis* to one another and the bromido ligands are coordinated *trans* to one another. Selected bond distances and angles are listed in Table 4 and Table 5.

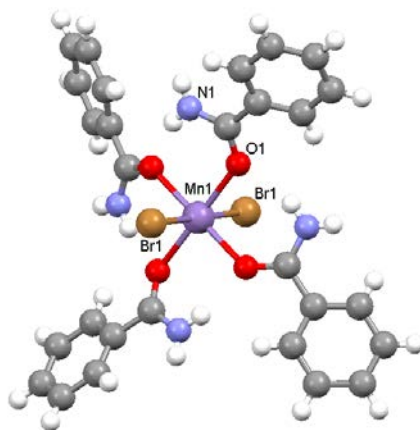


Figure 26: Coordination geometry of MnBr-BA, showing the paddle wheel structure of the molecule.

Table 4: Selected bond lengths of MnBr-BA

Bond	Length (Å)	Axial/Equatorial
Mn1-Br1	2.6380(5)	Axial
Mn1-O1	2.2313(9)	Equatorial

Table 5: Selected bond lengths of MnBr-BA

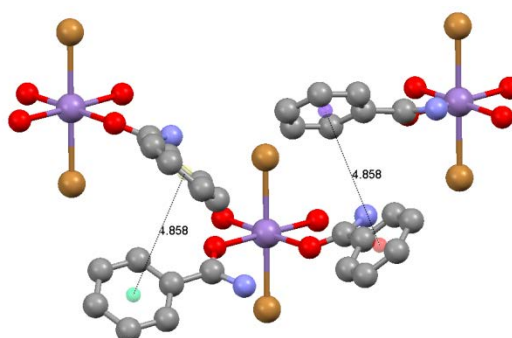
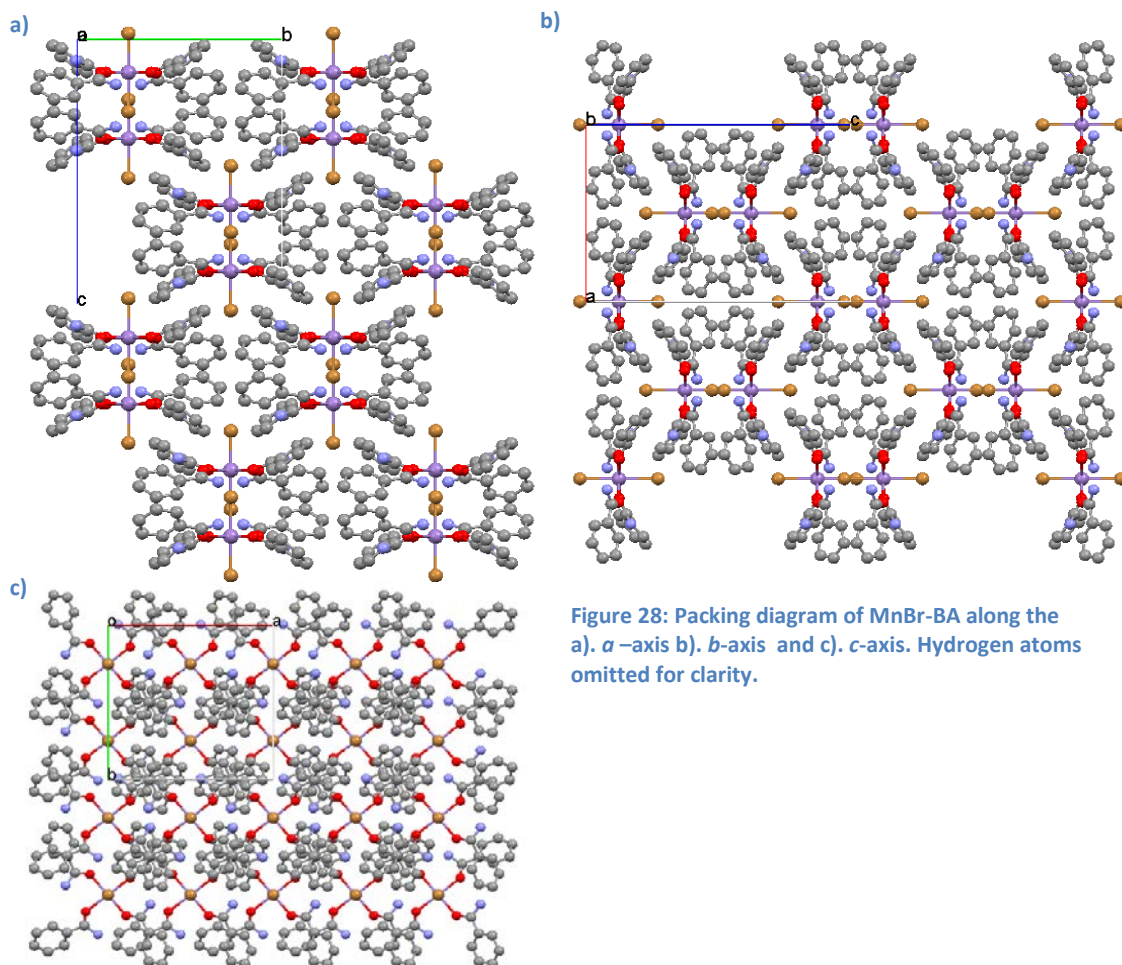
Angles (°)	
Axial to axial (Br1-Mn1-Br1 <sup>i</sup> )	180.00(1)
Equatorial (O1-Mn1-O1)	90.00(4)
Axial to equatorial (Br1 <sup>i</sup> -Mn1-O1 <sup>ii</sup> )	89.51 (3)

<sup>i</sup>  $y-1/4, -x+1/4, -z+1/4$ <sup>ii</sup>  $-y+1/4, x+1/4, -z+1/4$ 

In this molecule the benzamide ligands are coordinated to the manganese atom with an C1-O1-Mn1-Br1 torsion angle of  $-59.6(1)^\circ$ . The amide group of the benzamide ligand is rotated by a torsion angle of  $20.8(2)^\circ$  (C7-C2-C1-O1) with respect to the aromatic ring. The result is that the aromatic rings of benzamide units form an angle of  $42.39^\circ$  relative to the plane through the four oxygen atoms.

The MnBr-BA structure does not form any polymeric motifs through the sharing of halogeno ligands between metal atoms, thus consists of isolated coordination molecules. The coordination motif observed for the benzamide ligands can be described as a “paddle wheel” as the Br1-Mn1-Br1 bonds can be seen as the axis of the paddle wheel, and the benzamide ligands as the paddles. All of the Br-Mn-Br bonds or “axes” pack parallel to the *c*-axis. Packing diagrams are shown in Figure 28.

It is of interest to note that the packing diagrams of the molecules viewed down the *a*-axis and the *b*-axis look exactly the same, as illustrated in Figure 28 a) and Figure 28 b). Here it can be seen that hydrophilic pockets containing aromatic rings are formed, but the bromine atoms penetrate these pockets.



The aromatic rings of neighbouring molecules form close contacts, but are slanted with respect to one another with a centroid-to-centroid distance of 4.858 Å as illustrated in Figure 27. There is no evidence of  $\pi$ - $\pi$  interactions as the centroid-to-centroid distance is quite large for such interactions, and the rings are not orientated in a manner suggesting  $\pi$ - $\pi$  interactions.

Each  $\text{NH}_2$  group forms two hydrogen bonds including an intramolecular N1-H1A...O1 hydrogen bond through to the oxygen atom of the neighbouring benzamide ligand and another intermolecular N1-

H1B...Br1 bond to form a hydrogen bonded dimer with an adjacent molecule as shown in Figure 29. Each molecule forms four dimer pairs with its neighbours resulting in a three-dimensional hydrogen bonded network that links molecules together. Hydrogen bonding parameters are listed in Table 6.

Table 6: Hydrogen bonding parameters.

Bond	H...A (Å)	D...A (Å)	<DHA (°)
N1-H1A...O1	2.02(2)	2.833(2)	162(2)
N1-H1B...Br1	2.62(2)	3.390(1)	158(2)

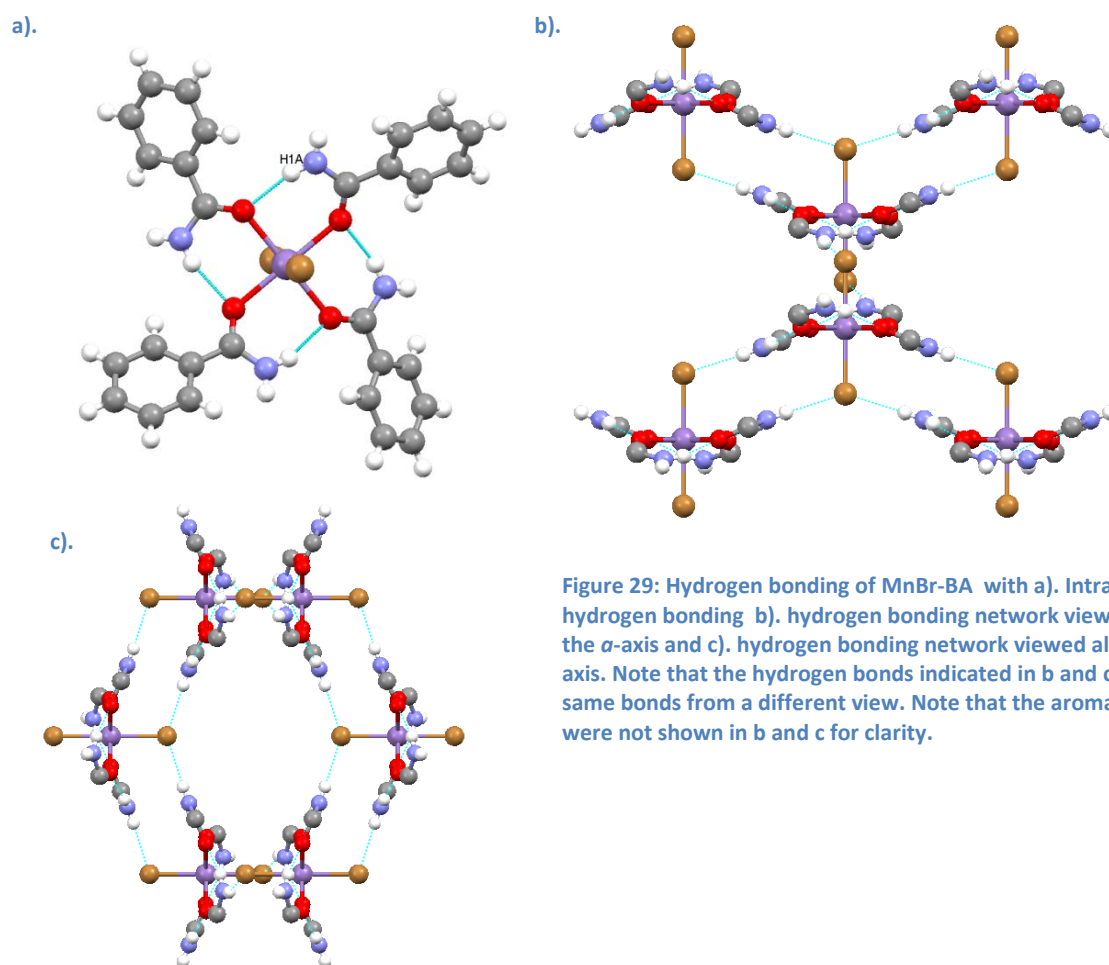
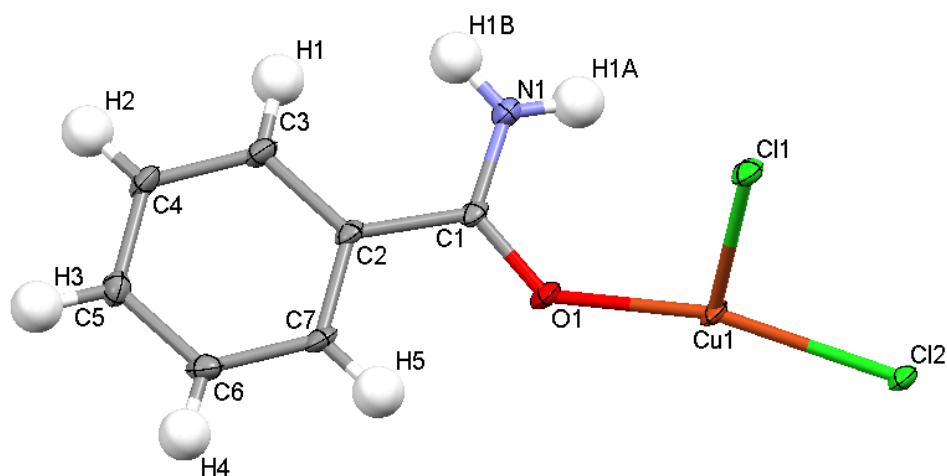


Figure 29: Hydrogen bonding of MnBr-BA with a). Intramolecular hydrogen bonding b). hydrogen bonding network viewed along the *a*-axis and c). hydrogen bonding network viewed along the *b*-axis. Note that the hydrogen bonds indicated in b and c are the same bonds from a different view. Note that the aromatic rings were not shown in b and c for clarity.

## catena-(Benzamide- $\kappa$ O)- $\mu_3$ -chlorido- $\mu$ -chloridocopper(II), CuCl-BA

Chemical Formula:  $[C_7H_7NOCuCl_2]_n$



**Figure 30 :** Asymmetric unit of CuCl-BA showing the atomic numbering scheme. Displacement ellipsoids are drawn at the 50% probability level and hydrogen atoms are drawn as spheres of arbitrary radii.

The asymmetric unit of CuCl-BA is comprised of one copper metal centre, to which two chlorido ligands and one benzamide ligand are coordinated as shown in Figure 30. The benzamide ligand is coordinated through the oxygen atom with a Cu-O bond length of 1.935(2) Å. There are two asymmetric units per unit cell and the copper metal atom has an octahedral coordination geometry with Jahn Teller effects prevalent in its geometry as illustrated in Figure 31. Elongation of the axial bonds is clearly visible with axial Cu-Cl bonds of approximately 3 Å as listed in Table 7. The elongation of the Cu-Cl bond is compared to the equatorial bonds. The asymmetric unit can be expanded to form a one-dimensional coordination polymer, as illustrated in Figure 32. In this polymer five chlorido ligands and one benzamide ligand are coordinated to the copper metal centre. The benzamide ligand is coordinated to one of the equatorial positions, while the chlorido ligands occupy equatorial and axial positions. The octahedral angles are slightly distorted with the most distortion occurring in the equatorial Cu-O bond (Refer to Figure 31). This may be to accommodate hydrogen bonding to the top chlorido ligand. The benzamide ligand is coordinated with a C1-O1-Cu1-Cl1 torsion angle of 58.9(2)°. The plane of the amide group is rotated by 3.0(3)° (C7-C2-C1-O1) with respect to the aromatic ring plane. In the uncoordinated gas phase benzamide molecule, this torsion angle is normally 21° as measured by gas phase electron diffraction of benzamide (Takeuchi et al., 1999). In this case, the ligand is considered to be more planar than normal, and this may be attributed to the effects of either  $\pi$ - $\pi$  stacking of the aromatic rings adjacent to one another overriding the steric effects that normally occur in the planar form or simply the effect of coordination on the ligand.

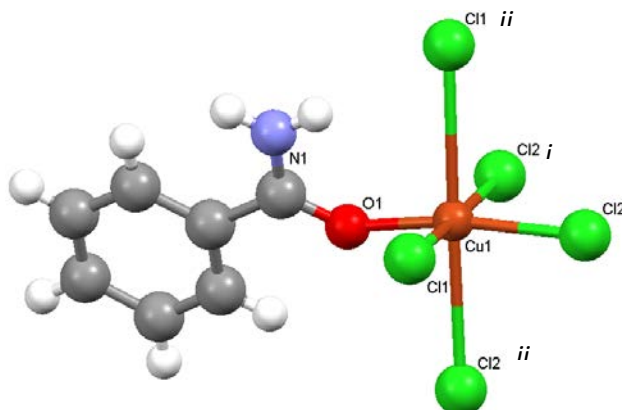


Figure 31: Octahedral coordination geometry of CuCl-BA illustrating the Jahn-Teller elongation of the axial bonds, and compression of the equatorial bonds.

Table 7: Selected bond lengths of CuCl-BA.

Bond	Length (Å)	Axial/Equatorial
Cu1-Cl1	2.2776(7)	Equatorial
Cu1-Cl2	2.2831(9)	Equatorial
Cu1-O1	1.935(2)	Equatorial
Cu1-Cl2 <sup>i</sup>	2.3178(7)	Equatorial
Cu1-Cl2 <sup>ii</sup>	2.9410(8)	Axial
Cu1-Cl1 <sup>ii</sup>	3.0433(8)	Axial

<sup>i</sup> 1-x,1-y,1-z

<sup>ii</sup> 1+x,y,z

Table 8: Selected bond angles

Angles (°)	
Axial to axial (Cl1 <sup>ii</sup> -Cu1-Cl2 <sup>ii</sup> )	178.87(2)
Equatorial (Cl1-Cu1-Cl2 <sup>i</sup> )	177.23(3)
Equatorial (Cl2-Cu1-O1)	166.37(6)

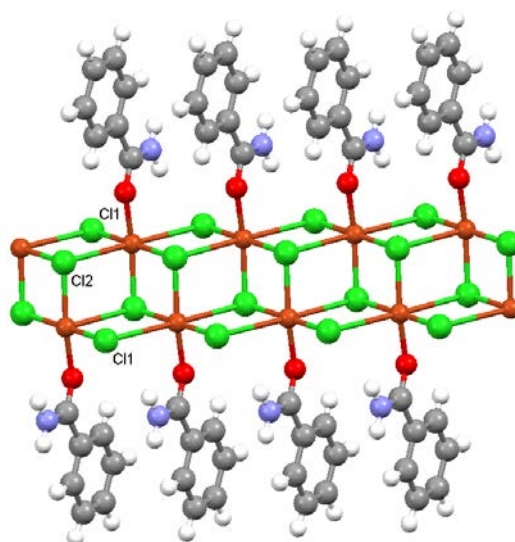


Figure 32: Polymeric one-dimensional motif (pattern) of CuCl-BA.

In the polymer, the copper metal centres are bridged by two types of  $\mu_x$ -chlorido atoms where  $x = 2$  or 3. In the first type two copper metal centres are bridged by a single “flanking”  $\mu$ -chlorido ligand, Cl1, and in the second type three metal centres are bridged by one “central”  $\mu_3$ -chlorido ligand, Cl2, as shown in Figure 32. The octahedra engage in an alternating edge sharing motif resulting in a zig-



zag or stepped one-dimensional ribbon flanked by bridging chlorido ligands. A polyhedral representation of the inorganic layer is shown in Figure 33.

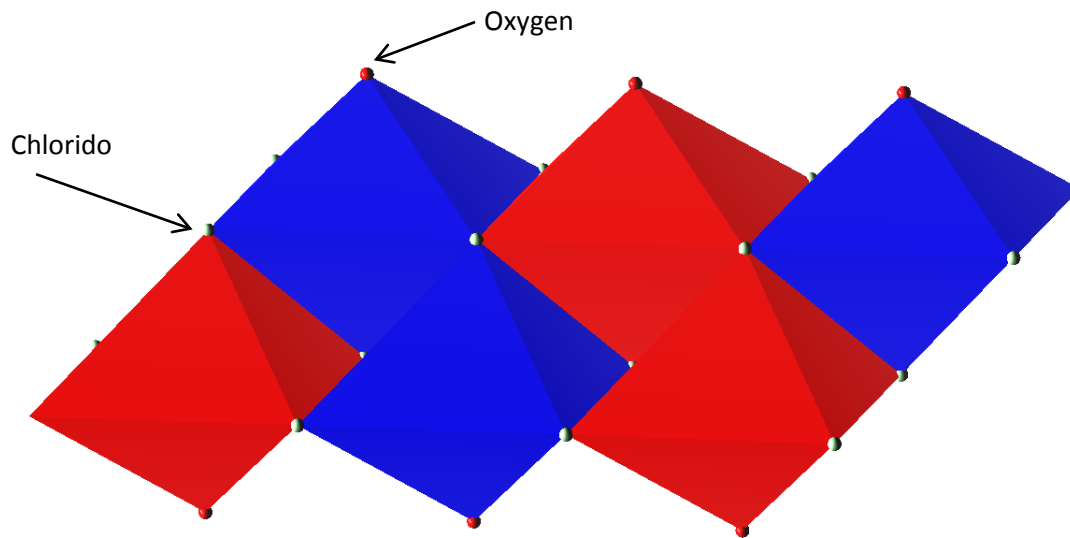


Figure 33: Polyhedral representation of the one-dimensional inorganic polymer. Organic ligand not shown for clarity.

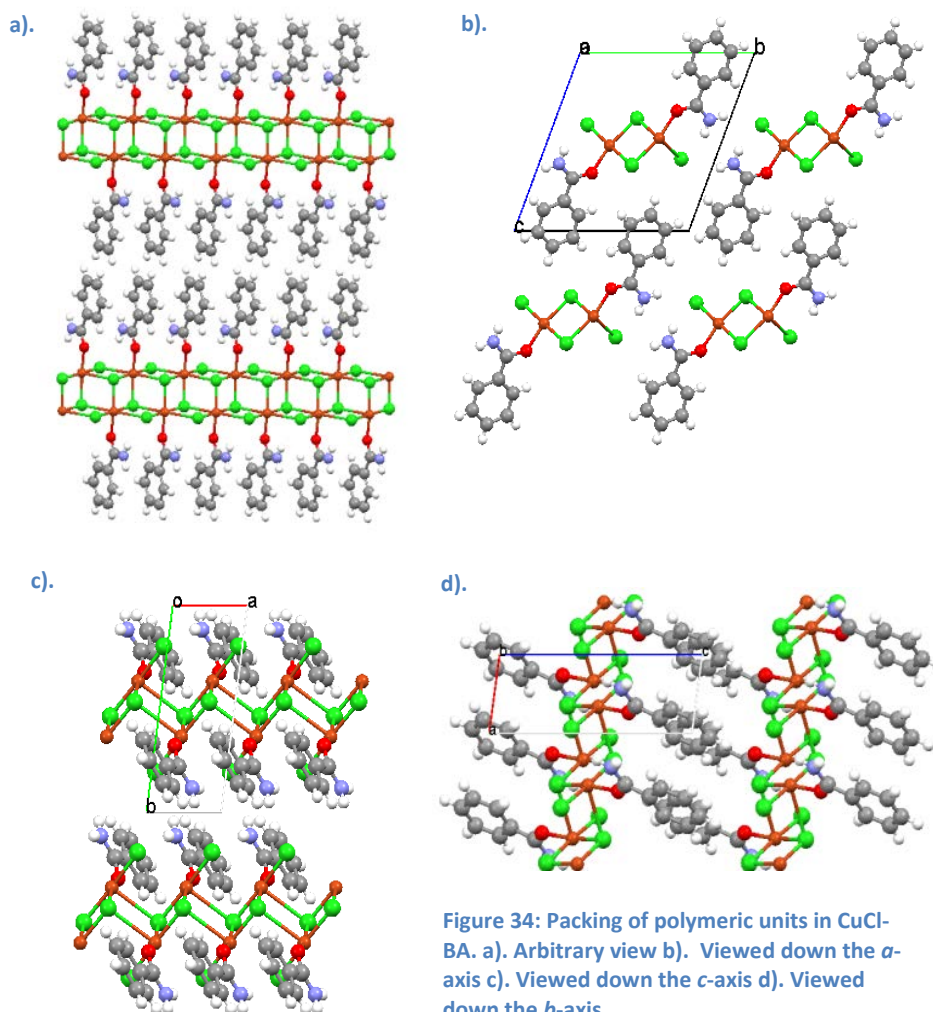


Figure 34: Packing of polymeric units in CuCl-BA. a). Arbitrary view b). Viewed down the  $a$ -axis c). Viewed down the  $c$ -axis d). Viewed down the  $b$ -axis.

The one-dimensional polymeric unit of CuCl-BA packs to form a layered structure. The inorganic layer is comprised of the inorganic polymers, while the organic layer is comprised of two benzamide ligands, coordinated to different neighbouring inorganic polymers, orientated such that their hydrophobic regions are directed at each other in the organic layer, hence forming an organic bilayer as illustrated in Figure 34. In the organic layer the aromatic ring planes pack in a parallel fashion with a centroid-to-centroid distance of 3.831 Å with a plane-to-plane distance of 3.381 Å and a slippage distance of 1.925 Å, which indicate the presence of  $\pi$ - $\pi$  interactions between the aromatic groups.

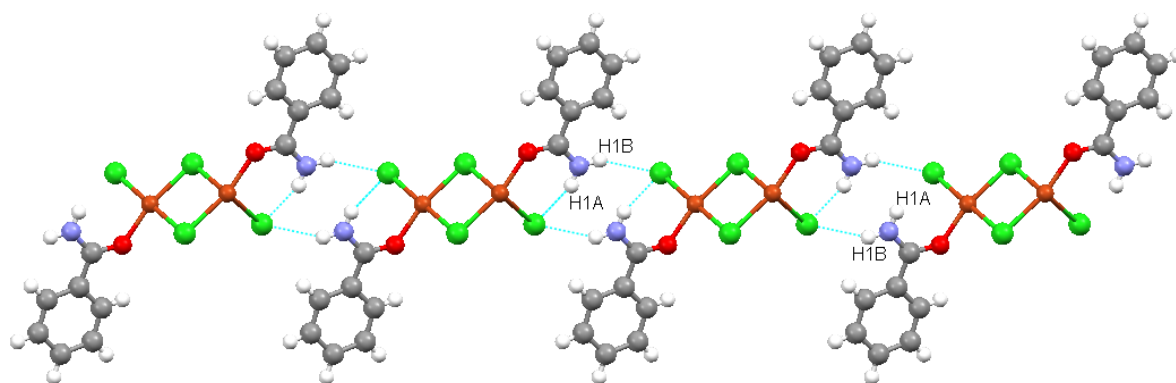


Figure 35: Hydrogen bonding interactions of CuCl-BA viewed along the  $a$ -axis.

An intramolecular hydrogen bond exists between the  $\text{NH}_2$  group of the benzamide ligand and a chlorido ligand in the same polymer. In addition, one atom in a neighboring polymer is linked through an intermolecular  $\text{N-H}\dots\text{Cl}$  hydrogen bond involving the second hydrogen on the  $\text{NH}_2$  group to form a two-dimensional hydrogen bonded sheet parallel to the  $ab$ -plane as shown in Figure 35. Hydrogen bonding parameters are listed in Table 9.

Table 9: Hydrogen bonding parameters.

Hydrogen bond	H...Cl (Å)	N...Cl (Å)	$\angle\text{NHCl}$ (°)	Symmetry operator
N1-H1A...Cl1 <sup>i</sup>	2.5198(8)	3.317(2)	154.5(1)	i: $1+x,y,z$
N1-H1B...Cl1 <sup>ii</sup>	2.6250(8)	3.405(2)	151.4(1)	ii: $1-x,2-y,1-z$



## catena-(Benzamide- $\kappa$ O)- $\mu_3$ -bromido- $\mu$ -bromidocopper(II), CuBr-BA

Chemical Formula:  $[\text{C}_7\text{H}_7\text{NOCuBr}_2]_n$

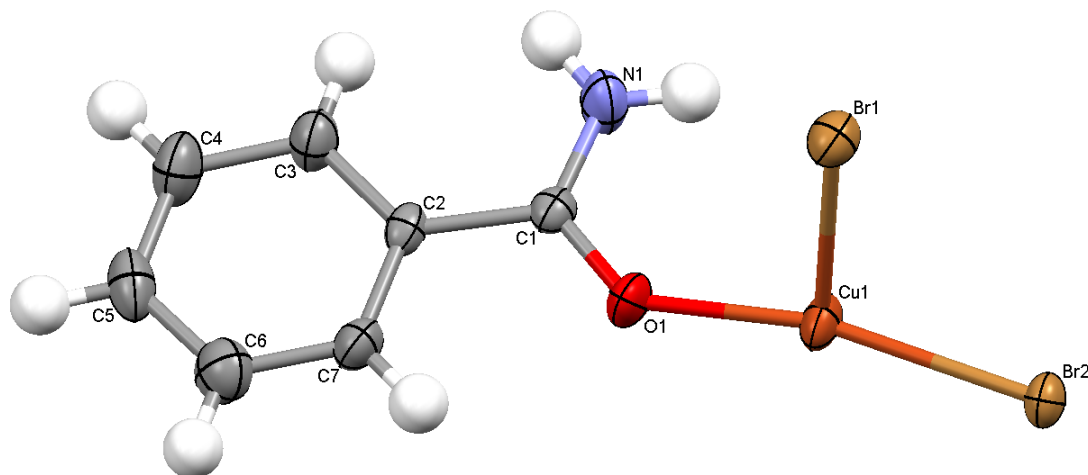


Figure 36 : Asymmetric unit of CuBr-BA showing the atomic numbering scheme. Displacement ellipsoids are drawn at the 50% probability level and hydrogen atoms are drawn as spheres of arbitrary radii.

The structure of CuBr-BA was found to be isostructural to that of CuCl-BA. The structural discussion of CuBr-BA will be less detailed, considering the detailed discussion already given for the CuCl-BA structure, in order to avoid duplication. The asymmetric unit of CuBr-BA consists of one benzamide ligand and two bromido ligands coordinated to the copper metal ion as shown in Figure 36. The benzamide ligand is coordinated to the copper ion with a Cu-O bond distance of 1.939(6) Å.

The unit cell is comprised of two asymmetric units related by P-1 symmetry. Expansion of the structure shows that the copper ion exhibits a Jahn-Teller distorted tetragonal (2 + 4) coordination geometry, with the benzamide ligand coordinated to one of the equatorial positions and the other positions are occupied by bromido ligands, as shown in Figure 37. The equatorial bond distances are approximately 2.4 Å and the axial bonds are elongated to approximately 3.1 Å and as listed in Table 10. The tetragonal angles are distorted from their ideal values, with the most prevalent distortion occurring in the O1-Cu1-Br2 bond angle, with a value of 167.0(2)°.

Selected angles are listed in Table 11. The ligand is coordinated with a torsion angle of 62.8° (C1-O1-Cu1-Br1) and the amide group has a torsion angle of 2(1)° with respect to the aromatic ring plane (C7-C2-C1-O1).

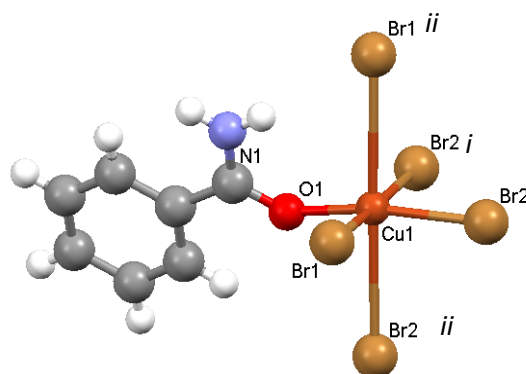


Figure 37: Coordination geometry of CuBr-BA showing elongation of the axial bonds to the bromido ligands.

**Table 10: Selected tetragonal bond lengths of CuBr-BA**

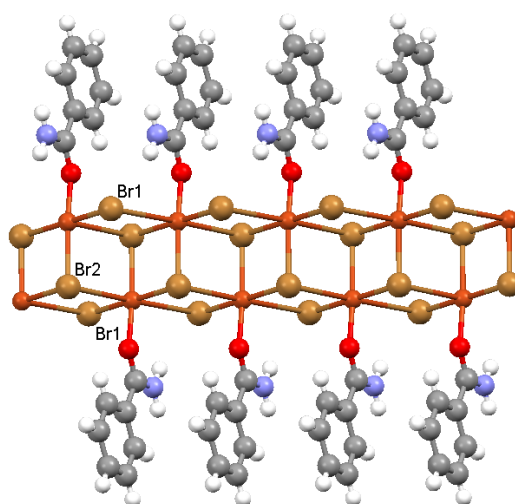
Bond	Length (Å)	Axial/Equatorial
Cu1-Br1	2.412(1)	Equatorial
Cu1-Br2	2.411(1)	Equatorial
Cu1-O1	1.939(6)	Equatorial
Cu1-Br2 <sup>i</sup>	2.453(1)	Equatorial
Cu1-Br2 <sup>ii</sup>	3.129(1)	Axial
Cu1-Br1 <sup>ii</sup>	3.247(1)	Axial

<sup>i</sup> 1-x,1-y,1-z

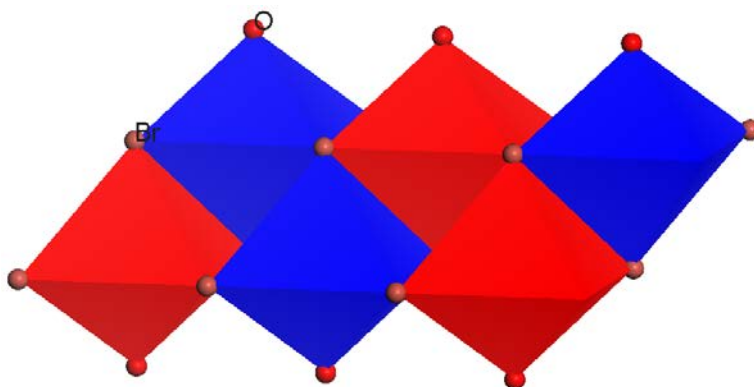
<sup>ii</sup> 1+x,y,z

**Table 11: Selected angles**

Selected angles (°)	
Axial to axial (Br <sub>1</sub> <sup>ii</sup> -Cu-Br <sub>2</sub> <sup>ii</sup> )	178.87(4)
Equatorial (Br <sub>1</sub> -Cu-Br <sub>2</sub> <sup>i</sup> )	177.01(5)
Equatorial (Br <sub>2</sub> -Cu-O)	167.0(2)


**Figure 38: Polymeric one dimensional motif of CuBr-BA.**

The asymmetric unit can be expanded along the *a*-axis to form a one-dimensional polymer as shown in Figure 38. The resulting central coordination polymer portion contains two rows of metal atoms, and two types of bridging ligands form the flanked infinite ribbon polymer. Firstly two of the copper atoms are flanked by a  $\mu$ -bromido ligand, Br1. Secondly two copper atoms are bridged in the centre of the inorganic polymer by a  $\mu_3$ -bromido ligand, Br2. The octahedra are shared in an alternating edge sharing motif to form the flanked ribbon structure. A polyhedral representation of the inorganic portion layer is shown in Figure 39.


**Figure 39: Polyhedral representation of the one dimensional inorganic polymer. Organic ligand not shown for brevity**

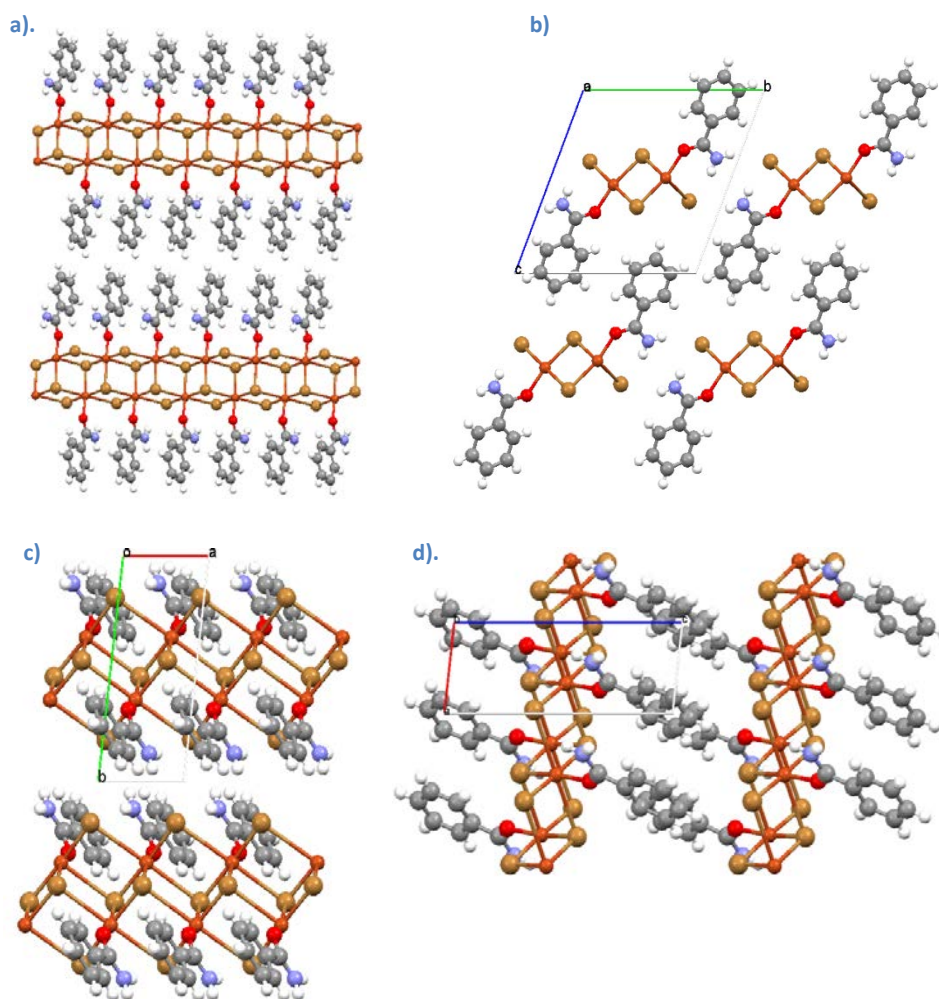


Figure 40: Packing of polymeric units in CuBr-BA. a). Arbitrary view b). Viewed down the  $a$ -axis c). Viewed down the  $c$ -axis d). Viewed down the  $b$ -axis

The CuBr-BA coordination polymer chains pack to form a layered structure in which the organic layer is formed by the alternating orientation of the benzamide ligands such that their hydrophobic regions are directed toward one another, resulting in an organic bilayer as shown in Figure 40. The aromatic rings in the organic layer pack in parallel with a centroid-to-centroid separation of 4.074 Å, a plane-to-plane distance of 3.399 Å and a slippage distance of 2.246 Å, which is evidence of the presence of  $\pi$ - $\pi$  interactions between the aromatic groups.

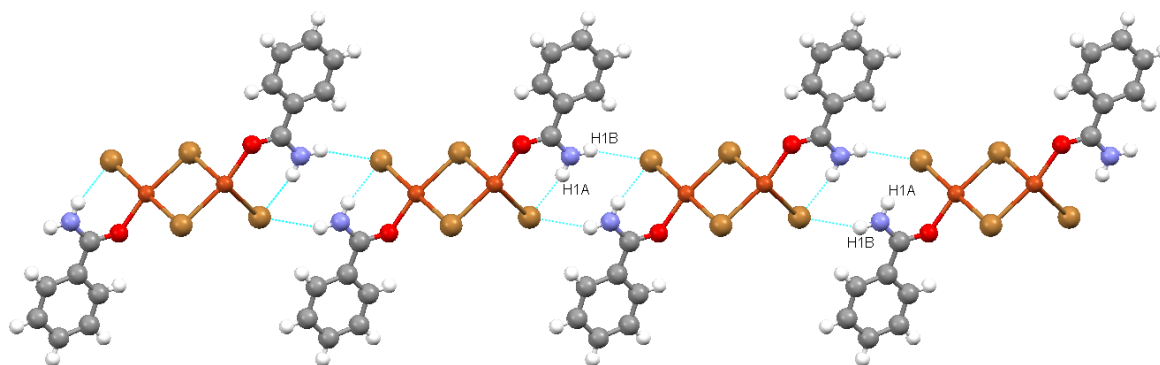


Figure 41: Hydrogen bonding interactions of CuBr-BA viewed along the  $a$ -axis.

The NH<sub>2</sub> group's hydrogen atoms form both intramolecular hydrogen bonds with bromido ligands in the same polymer, and intermolecular hydrogen bonds to a neighbouring polymer, as shown in Figure 41. In both cases hydrogen bonds are formed to the  $\mu$ -bromido ligand Br1. This results in the formation of a two-dimensional hydrogen bonded sheet. Additional hydrogen bonding parameters are listed in Table 12.

Table 12: Hydrogen bonding parameters.

Hydrogen bond	H...Br (Å)	N...Br (Å)	<NHBr (°)	Symmetry operator
N-H1A...Br1	2.646(1)	3.462(6)	158.7(5)	1+x,y,z
N-H1B...Br1	2.746(1)	3.531(7)	152.4(5)	1-x,2-y,1-z

### Di(benzamide- $\kappa$ O)dichloridozinc(II), ZnCl-BA

Chemical Formula: [(C<sub>7</sub>H<sub>7</sub>NO)<sub>2</sub>ZnCl<sub>2</sub>]

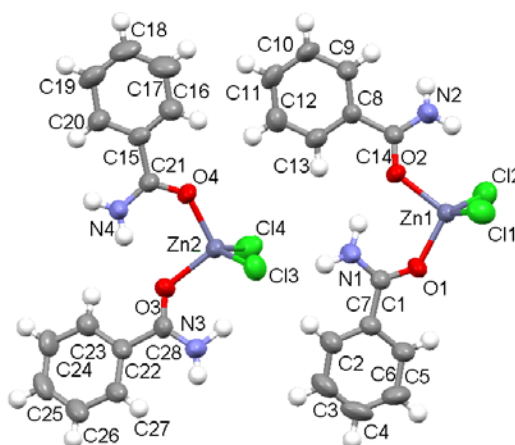


Figure 42: Asymmetric unit of ZnCl-BA showing the atomic numbering scheme. Displacement ellipsoids are drawn at the 50% probability level and hydrogen atoms are drawn as spheres of arbitrary radii.

The asymmetric unit of ZnCl-BA consists of two isolated coordination molecules as illustrated in Figure 42. There are small differences between these molecules in terms of their geometry and they are therefore considered to be crystallographically unique entities. A Platon (Spek, 2003) check for additional symmetry confirmed that no additional symmetry is present in the structure. The differences in the geometry of the two molecules were confirmed to be valid therefore both moieties are included in the asymmetric unit of this crystal structure. The molecules containing atoms Zn1 and Zn2 will be referred to as molecules 1 and 2 respectively, in order to distinguish between them.

In both the coordination molecules, the zinc ion is tetrahedrally coordinated by two chlorido ligands with Zn-Cl bonds ranging from 2.184 Å to 2.235 Å and two benzamide ligands, via the oxygen atom on the amide group, with Cu-O bonds ranging from 1.961 Å to 2.016 Å. Table 13 lists selected coordination bond distances. The tetrahedral angles are slightly distorted from their ideal value of 109.5°, and are listed in Table 14.

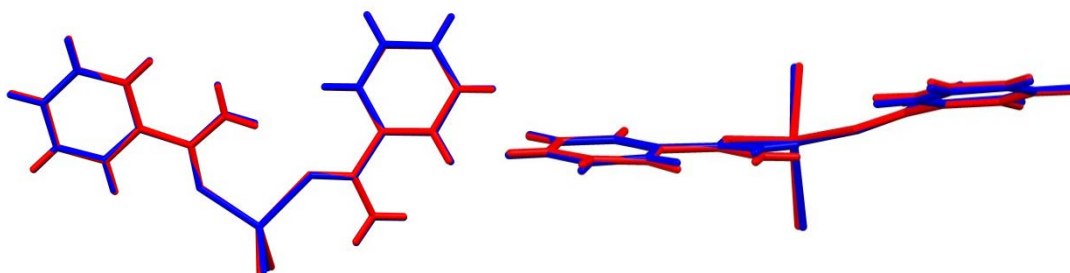
**Table 13: Selected coordination bond distances**

Bond	Length (Å)
Zn1-Cl1	2.201(3)
Zn1-Cl2	2.211(3)
Zn1-O1	1.961(6)
Zn1-O2	2.011(6)
Zn2-Cl3	2.235(3)
Zn2-Cl4	2.184(4)
Zn2-O3	2.016(6)
Zn2-O4	1.969(6)

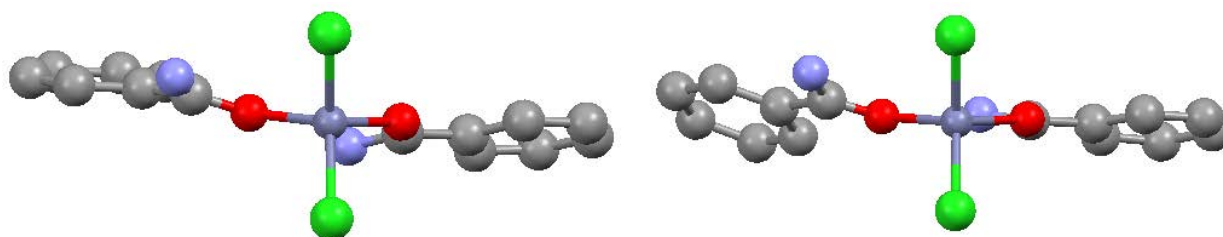
**Table 14: Selected coordination angles.**

Angles (°)	
Cl1-Zn1-Cl2	114.3(1)
O1-Zn1-O2	100.3(3)
Cl3-Zn2-Cl4	114.8(1)
O3-Zn2-O4	101.6(3)

The ZnCl-BA structure is a zero-dimensional structure and no polymerization of the inorganic component through the sharing of chloride ligands is observed. The formation of zero-dimensional, isolated coordination molecules is expected for zinc halides, in fact, there are very few cases in the literature in which halogeno ligands bridge Zn ions, and these tend to form isolated blocks of inorganic units, not infinite polymers.


**Figure 43: Comparison of the two molecules contained in the asymmetric unit. Molecule 1 (blue) and Molecule 2 (red).**

The unit cell consists of eight molecules or four asymmetric units related by  $P2_1/c$  symmetry. Figure 43 compares the geometries of the two molecules in the asymmetric unit, by overlaying Zn1 onto Zn2, Cl1 onto Cl4, and Cl2 onto Cl3.


**Figure 44: Comparison of molecule 1 (Left) and molecule 2 (right) of ZnCl-BA**

In molecule 1, the angles between the plane through the atoms Cl1, Zn1 and Cl2, which bisects the molecule, and the aromatic ring planes C1-C6 and C8-C13, are  $85.8(5)^\circ$  and  $86.5(4)^\circ$  respectively, and in molecule 2, these angles are  $88.5(4)^\circ$  and  $73.6(4)^\circ$  for the ring planes C15-C20 and C22-C27. This difference in molecular geometry is also evident from the figures indicating the superposition in Figure 43. Thus, the relative position of one of the benzamide ligands (the ligand containing atom N1 in molecule 1 and the ligand containing atom N4 in molecule 2) in the molecules is similar, and this ligand approximately lies in the O-Zn-O plane of both molecules, but they differ in the orientation of



the second benzamide ligand, as illustrated in Figure 44. This difference is a direct consequence of the hydrogen bonding network formed in the structure, and will be discussed later.

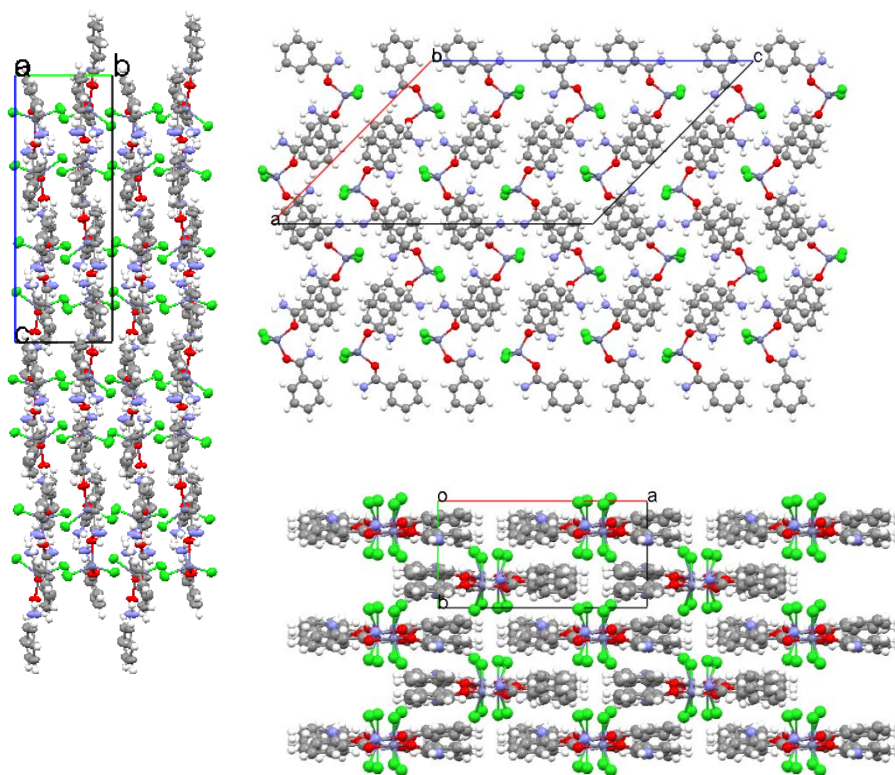


Figure 45: Packing diagram of ZnCl-BA along the a). *a*-axis b). *b*-axis and c). *c*-axis.

A layered structure is formed, as can be seen in Figure 45, with layers containing the aromatic rings alternating with layers consisting of the metal ions and halogeno ligands. Hydrogen bonding interactions link the isolated molecules to form a hydrogen bonding network. Hydrogen bonding parameters are listed in Table 16.

Each molecule is linked to two others in a staggered brick formation by  $\pi$ - $\pi$  interactions. The aromatic rings engage in a staggered face stacking motif. Molecule 1 is linked to two other molecule 2 moieties via the two benzamide aromatic rings. The centroid-to-centroid distances are listed in Table 15. The centroid parameters are within expected values for  $\pi$ - $\pi$  interactions.

Table 15: Selected Centroid parameters for ZnCl-BA.

Centroids in Molecule 1 (Zn1)	Centroids in Molecule 2 (Zn2)	Centroid-to-centroid (Å)	Centroid-to-plane (Å)	Slippage (Å)
C2 C3 C4	C9 C10 C11	3.901	3.497	1.729
C5 C7 C6	C12C13 C14			
C2' C3' C4'	C9' C10' C11'	3.945	3.633	1.538
C5' C7' C6'	C12' C13' C14'			

Each of the molecules in the asymmetric unit exhibits two intramolecular hydrogen bonds, with each of the NH<sub>2</sub> groups of the benzamide ligands involved in one intramolecular hydrogen bond. In one of the intramolecular hydrogen bonds, the oxygen atom of the second benzamide ligand on the molecule acts as hydrogen bond acceptor, and in the other one of the chlorido ligands on the same molecule is the hydrogen bond acceptor. In molecule 1 there is one N1-H1A...O2 intramolecular hydrogen bond at a D-A distance of 2.930(11) Å, as well as a N2-H2A...Cl2 intramolecular hydrogen bond at a distance of 3.370(11) Å. For molecule 2 a N3-H3A...Cl3 intermolecular hydrogen bond occurs at a distance of 3.384(10) Å, and one N4-H4A...O3 intramolecular hydrogen bond at a distance of 2.908(11) Å, as shown in Figure 46.

In addition to the intramolecular hydrogen bonds, intermolecular hydrogen bonds link neighbouring molecules to form a three-dimensional hydrogen bonded network, as illustrated in Figure 46. The intermolecular interactions are listed in Table 16. Figure 47 shows the propagation of the hydrogen bonding interactions to form a network throughout the structure. In this figure all carbon and hydrogen atoms have been omitted for clarity.

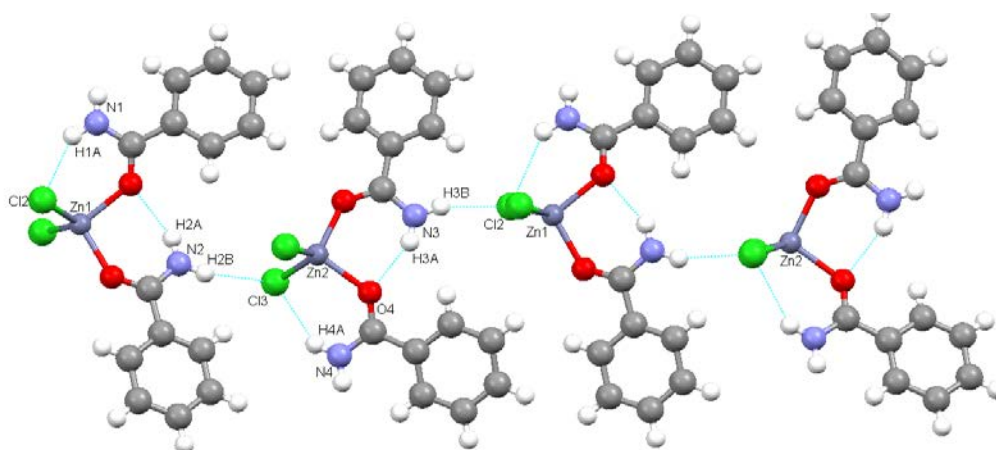


Figure 46: Intra-sheet and intramolecular hydrogen bonding ZnCl-BA.

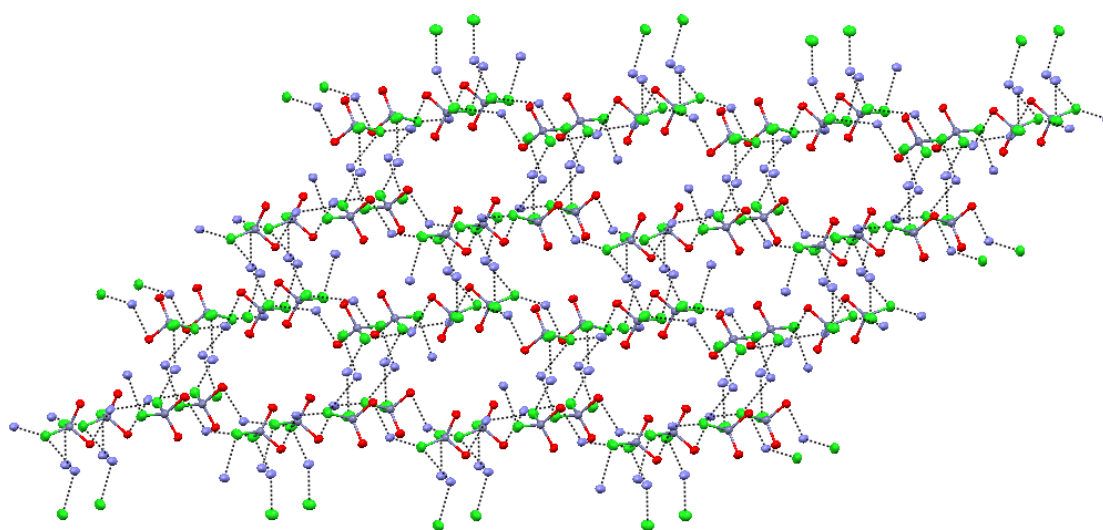


Figure 47: Hydrogen bonding network in ZnCl-BA. Carbon and hydrogen atoms are omitted for clarity.

Table 16: Hydrogen bond parameters for ZnCl-BA

Hydrogen Bond	H...A (Å)	D...A (Å)	D - H...A (°)	Symmetry operator	Type
N1-H1A...O2	2.17	2.930(11)	147.8	-	Intramolecular
N1-H1B...Cl3	2.66	3.446(10)	151.8	-	Intermolecular
N2-H2A...Cl2	2.69	3.370(11)	137.3	-	Intramolecular
N2-H2B... Cl1 <sup>i</sup>	2.55	3.366(10)	157.6	i: $-x, y+1/2, -z-1/2$	Intermolecular
N3-H3A...Cl3	2.63	3.384(10)	146.6	-	Intramolecular
N3-H3B...Cl4 <sup>ii</sup>	2.6	3.389(10)	153.2	ii: $-x+1, y-1/2, -z-1/2$	Intermolecular
N4-H4A...O3	2.12	2.908(11)	151.9	-	Intramolecular
N4-H4B...Cl2 <sup>iii</sup>	2.76	3.487(10)	143.7	iii: $x, -y-1/2, z-1/2$	Intermolecular

As mentioned previously, the difference in the molecular geometry of molecules 1 and 2 may be explained by considering the intra- and intermolecular hydrogen bonding interactions in these molecules. The difference in geometry may be attributed to the position of chlorido ligands that act as hydrogen bonding acceptors, in neighbouring molecules. As can be seen in Figure 48, the NH<sub>2</sub> group in one of the ligands in molecule 2 adopts a different orientation relative to the corresponding ligand in molecule 1 to allow for the formation of a hydrogen bond to a neighbouring molecule. In both the molecules, the benzamide ligand which lies in the O-Zn-O plane is involved in an intramolecular hydrogen bond, which locks it in the same position in both molecules.

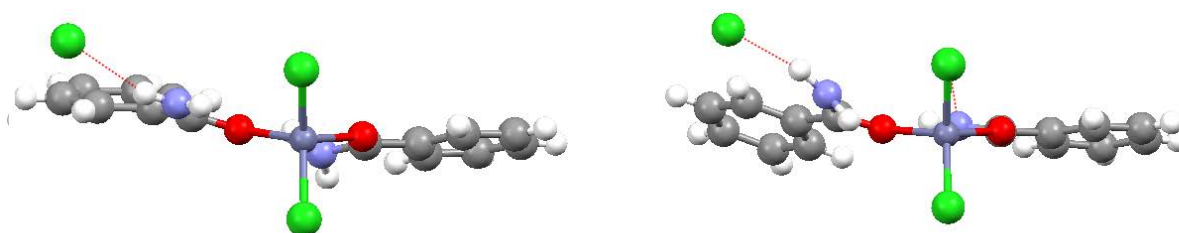


Figure 48: Different intermolecular hydrogen bonding formation of molecule 1 (Left) and molecule 2 (right).



### catena-(Benzamide- $\kappa$ O)- $\mu_3$ -chlorido- $\mu$ -chloridocadmium(II), CdCl-BA

Chemical Formula:  $[C_7H_7NOCdCl_2]_n$

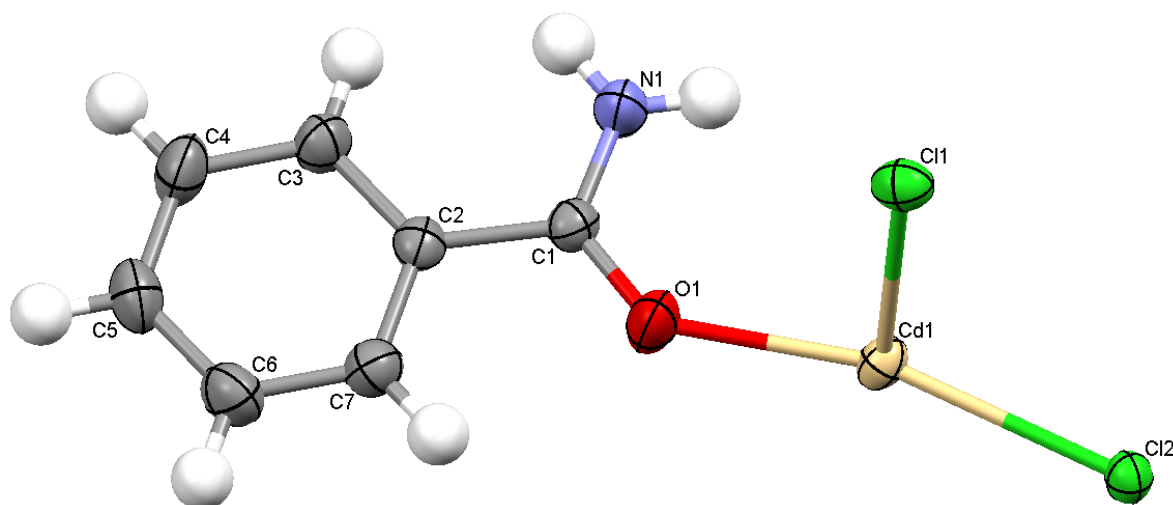


Figure 49 : Asymmetric unit of CdCl-BA showing the atomic numbering scheme. Displacement ellipsoids are drawn at the 50% probability level and hydrogen atoms are drawn as spheres of arbitrary radii.

The structure obtained for the combination of  $CdCl_2$  and benzamide was found to be isostructural to that of the  $CuCl$ -BA and  $CuBr$ -BA structures discussed previously, however, a major difference is that no Jahn-Teller distortion is observed in this structure, as expected, since a  $d^{10}$  metal does not undergo Jahn-Teller distortion. Important structural features of this compound will be pointed out, but a detailed discussion of the structure will not be included, for brevity.

The asymmetric unit of CdCl-BA is comprised of one cadmium ion to which two chlorido ligands and one benzamide ligand are coordinated, as shown in Figure 49. The unit cell is comprised of two asymmetric units related by an inversion centre. The cadmium ion has an octahedral geometry as illustrated in Figure 50 with Cd-Cl bonds ranging from 2.6276(9) Å to 2.6816(7) Å as listed in Table 17, and a Cd-O bond length of 2.243(3) Å. The asymmetric unit can be expanded to form a one-dimensional polymer along the  $a$ -axis, as shown in Figure 51.

In this polymer, five chlorido ligands and one benzamide ligand are coordinated to the cadmium ion. The octahedral angles are distorted from their ideal value, with the most prevalent distortion occurring in the O-Cd-Cl angles, as listed in Table 18. The benzamide ligand is coordinated with a torsion angle of  $68.0(4)^\circ$  (C1-O1-Cd1-Cl1), and the amide group is rotated by  $-0.1(5)^\circ$  (C7-C2-C1-O1) relative to the aromatic ring which is planar.

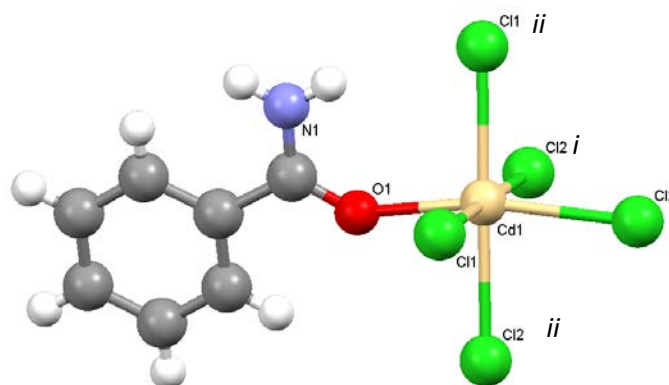


Figure 50: Coordination geometry of CdCl-BA.

**Table 17: Selected bond lengths of CdCl-BA**

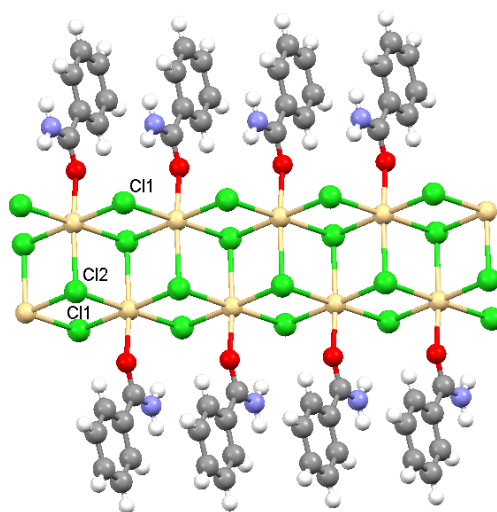
Bond	Length (Å)	Axial/Equatorial
Cd1-Cl1	2.6276(9)	Equatorial
Cd1-Cl2	2.632(1)	Equatorial
Cd1-O1	2.243(3)	Equatorial
Cd1-Cl2 <sup>i</sup>	2.6729(9)	Equatorial
Cd1-Cl2 <sup>ii</sup>	2.6816(7)	Axial
Cd1-Cl1 <sup>ii</sup>	2.6304(7)	Axial

<sup>i</sup> 1-x,1-y,1-z

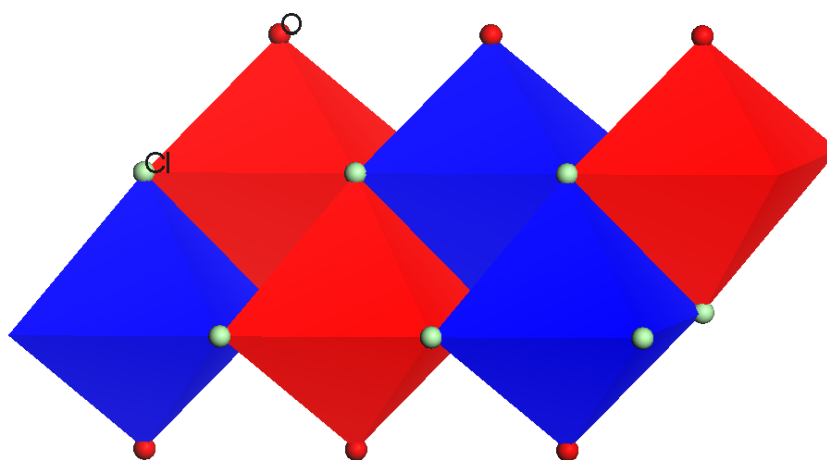
<sup>ii</sup> 1+x,y,z

**Table 18: Selected angles of CdCl-BA**

Selected angles (°)	
Axial to axial (Cl1 <sup>ii</sup> -Cd1-Cl2 <sup>ii</sup> )	178.96(3)
Equatorial (Cl1-Cd1-Cl2 <sup>i</sup> )	178.83(3)
Equatorial (Cl2-Cd1-O1)	165.16(7)


**Figure 51: Polymeric one-dimensional motif of CdCl-BA.**

In the polymer, the cadmium metal centres are bridged by two types of  $\mu_x$ -chlorido bonds where  $x = 2$  or  $3$ . In the first type two cadmium atoms are bridged by a “flanking”  $\mu$ -chlorido ligand, Cl1, and the second, three cadmium atom are bridged by a “central”  $\mu_3$ -chlorido ligand, Cl2 as shown in Figure 51. This results in a “flanked” zig-zag or stepped one-dimensional polymer along the  $a$ -axis. A polyhedral representation of the inorganic layer is shown in Figure 52.


**Figure 52: Polyhedral representation of the one-dimensional inorganic polymer. Organic ligand not shown for brevity.**

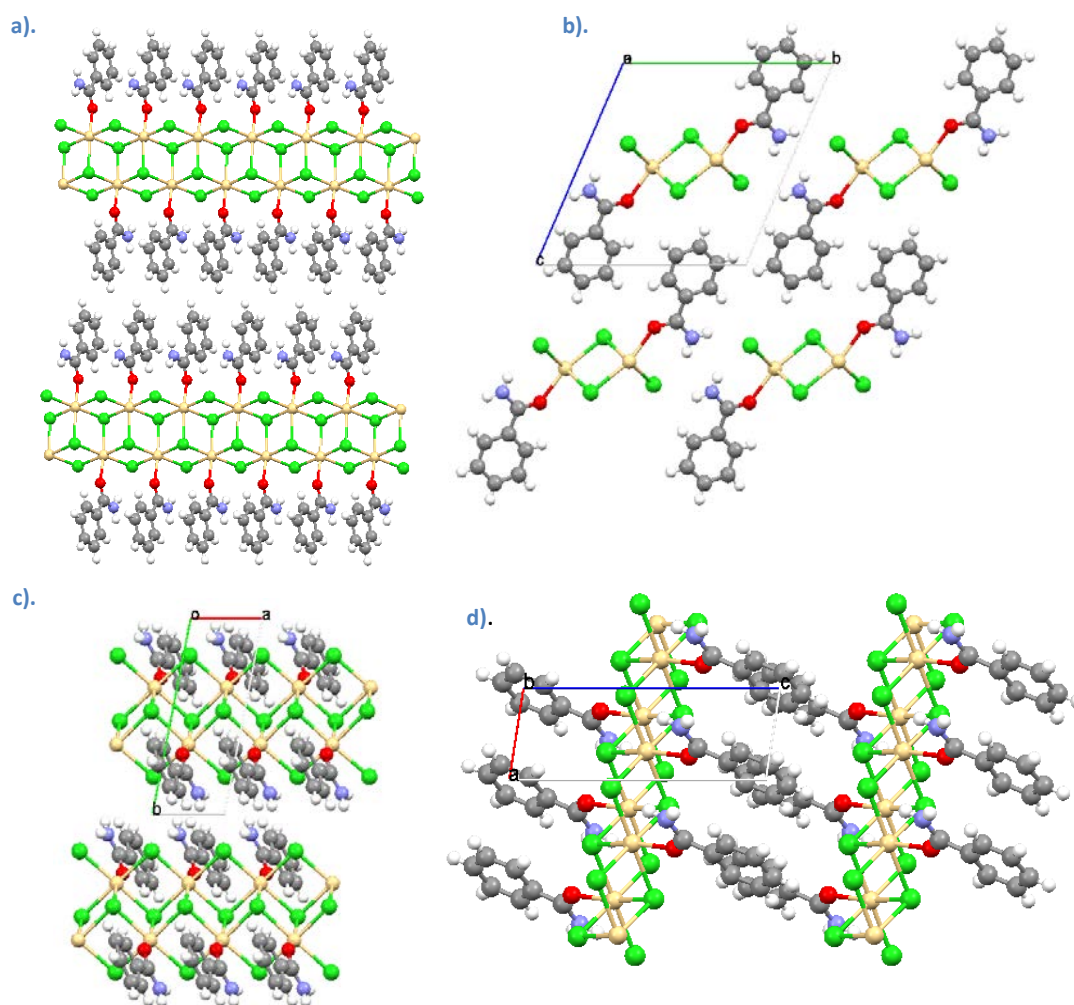


Figure 54: Packing of polymeric units in CdCl-BA. a). Arbitrary view b). Viewed down the *a*-axis c). Viewed down the *c*-axis d). Viewed down the *b*-axis

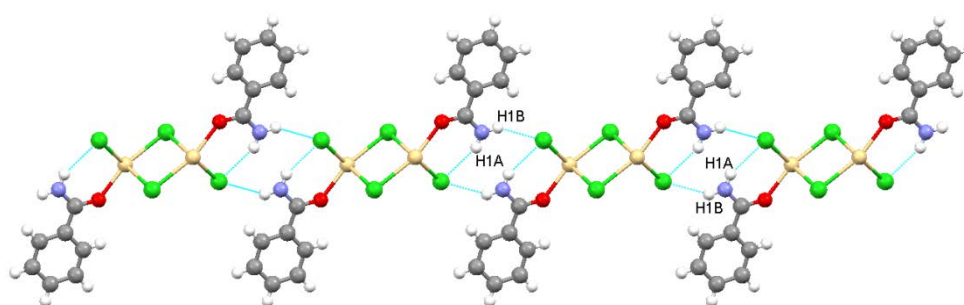


Figure 53: Hydrogen bonding interactions of CdCl-BA viewed along the *a*-axis.

Packing diagrams of the structure of CdCl-BA are shown in Figure 54. In structure Figure 54a it can be seen that a layered structure is formed, which is comprised of alternating organic and inorganic layers. The inorganic layer is comprised of the inorganic polymer whilst the organic layer is formed by the aromatic rings of the benzamide ligands directed such that their hydrophobic regions are pointing toward each other as shown in Figure 54. In the organic layer, the aromatic rings pack in a parallel manner with a centroid-to-centroid distance of 3.851 Å, a plane-to-plane distance of 3.452 Å

and a slippage distance of 1.707 Å, which is consistent with the formation of  $\pi$ - $\pi$  interactions in the structure.

One intramolecular hydrogen bond is evident between the H1A atom on N1 of the benzamide ligand and a chlorido ligand in the same polymer. In addition, one intermolecular hydrogen bond is formed between the H1B atom on N1 of the benzamide ligand and a chlorido ligand bonded to an adjacent coordination polymer, as illustrated in Figure 53. Hydrogen bonding parameters are listed in Table 19.

Table 19: Hydrogen bonding parameters.

Hydrogen bond	H...Cl (Å)	N...Cl (Å)	$\angle$ NHCl (°)	Symmetry operator
N-H1A...Cl1	2.642(1)	3.441(3)	155.0(2)	1+x,y,z
N-H1B...Cl1	2.7318(8)	3.472(3)	145.1(2)	1-x,2-y,1-z

### catena-(Benzamide- $\kappa$ O)- $\mu_3$ -bromido- $\mu$ -bromidocadmium(II), CdBr-BA

Chemical Formula:  $[C_7H_7NOCdBr_2]_n$

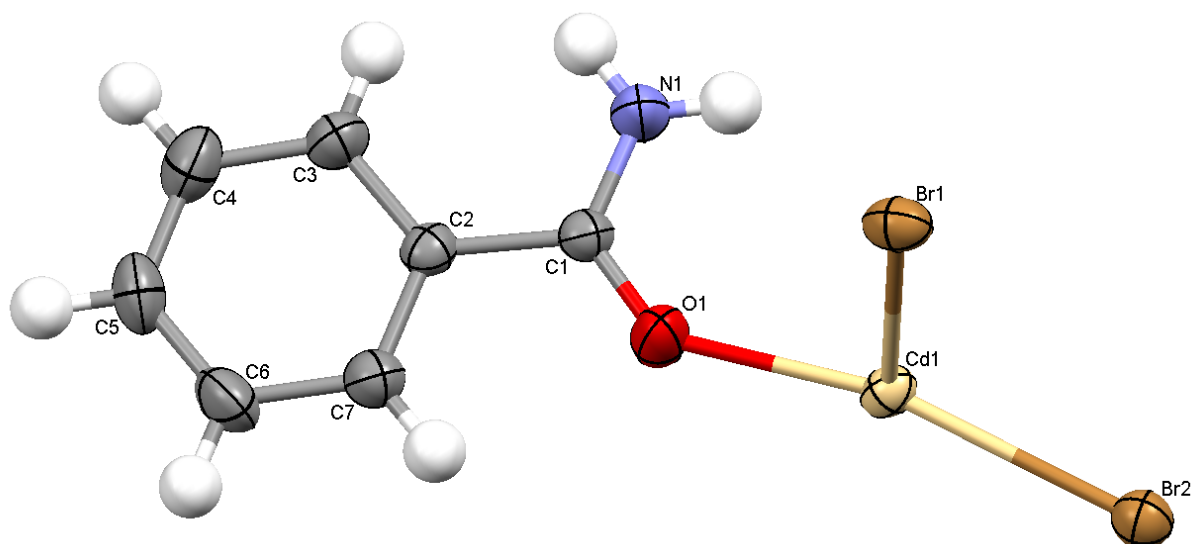


Figure 55: Asymmetric unit of CdBr-BA showing the atomic numbering scheme. Displacement ellipsoids are drawn at the 50% probability level and hydrogen atoms are drawn as spheres of arbitrary radii.

The structure obtained for the combination of  $CdBr_2$  and benzamide was found to be isostructural to that of the  $CdCl$ -BA structure discussed previously. Important structural features of this compound will be pointed out, but a detailed discussion of the structure will not be included, for brevity.

The asymmetric unit of CdBr-BA is comprised of one cadmium ion to which two bromido ligands and one benzamide ligand are coordinated, as shown in Figure 55. The unit cell is comprised of two asymmetric units related by an inversion centre. The cadmium ion has an octahedral geometry as illustrated in Figure 56 with Cd-Br bonds ranging from 2.7432(9) Å to 2.7932(8) Å and a Cd-O bond length of 2.257(7) Å as listed in Table 20. The asymmetric unit can be expanded to form a one-dimensional polymer along the a-axis, as shown in Figure 57. In this polymer, five chlorido ligands and one benzamide ligand are coordinated to the cadmium ion. The octahedral angles are distorted

from their ideal value, with the most prevalent distortion occurring in the Cd1-O1-Br2 angle, as listed in Table 21. The benzamide ligand is coordinated with a torsion angle of 65.7(8) ° (C1-O1-Cd1-Br1), and the amide group is rotated by 1(1) ° (C7-C2-C1-O1) relative to the aromatic ring which is planar.

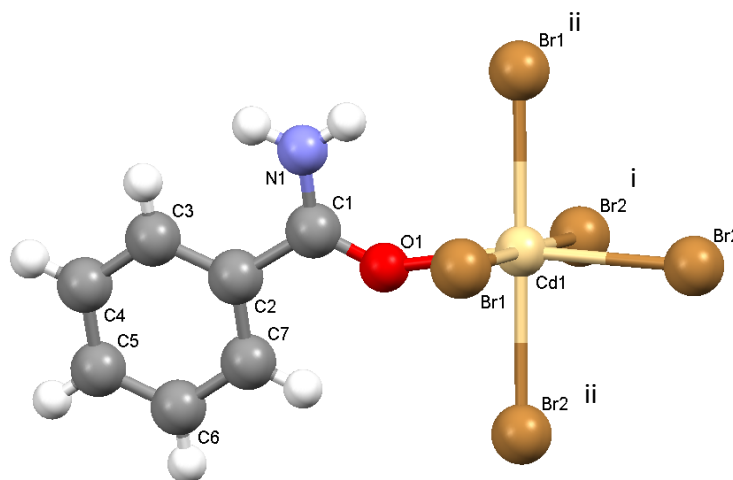


Figure 56: Coordination geometry of CdBr-BA.

Table 20: Selected Octahedral bond lengths of CdBr-BA

Bond	Length (Å)	Axial/Equatorial
Cd1-Br1	2.7432(9)	Equatorial
Cd1-Br2	2.742(1)	Equatorial
Cd1-O1	2.257(7)	Equatorial
Cd1-Br2 <sup>i</sup>	2.7705(9)	Equatorial
Cd1-Br2 <sup>ii</sup>	2.7932(8)	Axial
Cd1-Br1 <sup>ii</sup>	2.7516(8)	Axial

<sup>i</sup> 1-x,1-y,1-z

<sup>ii</sup> 1+x,y,z

Table 21: Selected angles

Selected angles (°)	
Axial to axial (Br1 <sup>ii</sup> -Cd1-Br2 <sup>ii</sup> )	179.23(3)
Equatorial (Br1-Cd1-Br2 <sup>i</sup> )	178.99(3)
Equatorial (Br2-Cd1-O1)	167.0(2)

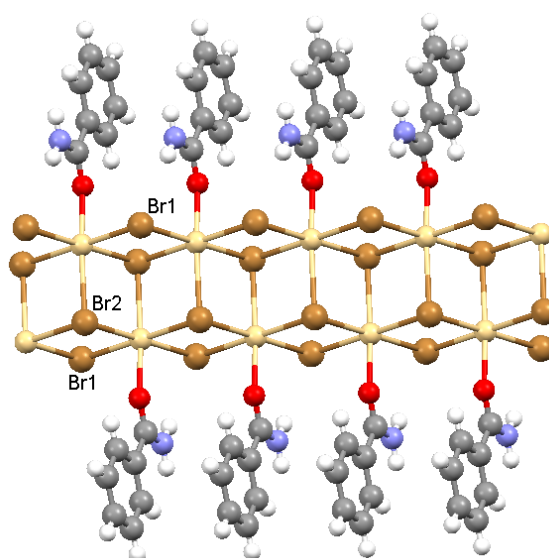


Figure 57: Polymeric one dimensional motif of CdBr-BA

In the polymer, the cadmium metal centres are bridged by two types of  $\mu_x$ -bromido bonds where  $x = 2$  or  $3$ . In the first type two cadmium atoms are bridged by a “flanking”  $\mu$ - bromido ligand, Br1, and the second, three cadmium atoms are bridged by a “central”  $\mu_3$ -bromido ligand, Br2 as shown in Figure 57.

This results in a “flanked” zig-zag or stepped one-dimensional polymer along the  $a$ -axis. A polyhedral representation of the inorganic layer is shown in Figure 58.

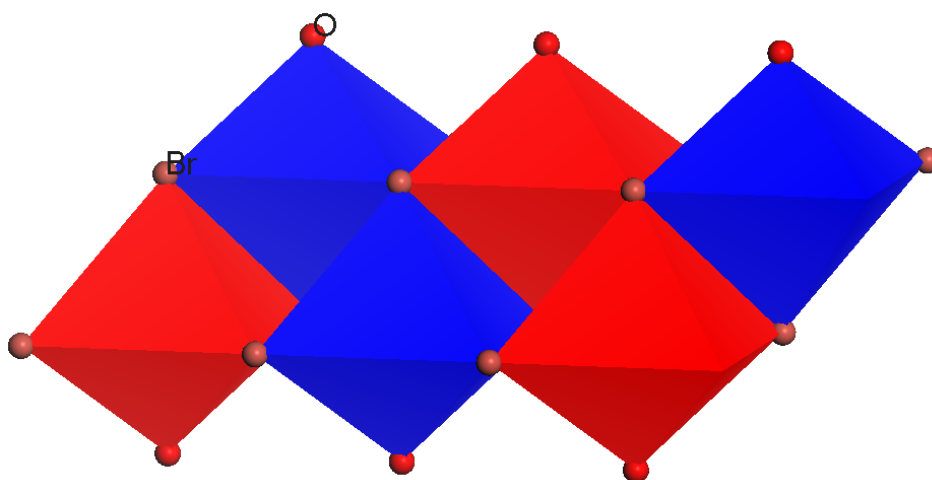


Figure 58: Polyhedral representation of the one-dimensional inorganic polymer. Organic ligand not shown for brevity.

Packing diagrams of the structure of CdBr-BA are shown in Figure 59. In structure Figure 59a it can be seen that a layered structure is formed, which is comprised of alternating organic and inorganic layers. The inorganic layer is comprised of the inorganic polymer whilst the organic layer is formed by the aromatic rings of the benzamide ligands directed such that their hydrophobic regions are pointing toward each other as shown in Figure 59. In the organic layer, the aromatic rings pack in a parallel with a centroid-to-centroid distance of  $3.956 \text{ \AA}$ , a plane-to-plane distance of  $3.498 \text{ \AA}$  and a slippage distance of  $1.848 \text{ \AA}$ , which is consistent with the formation of  $\pi$ - $\pi$  interactions in the structure.



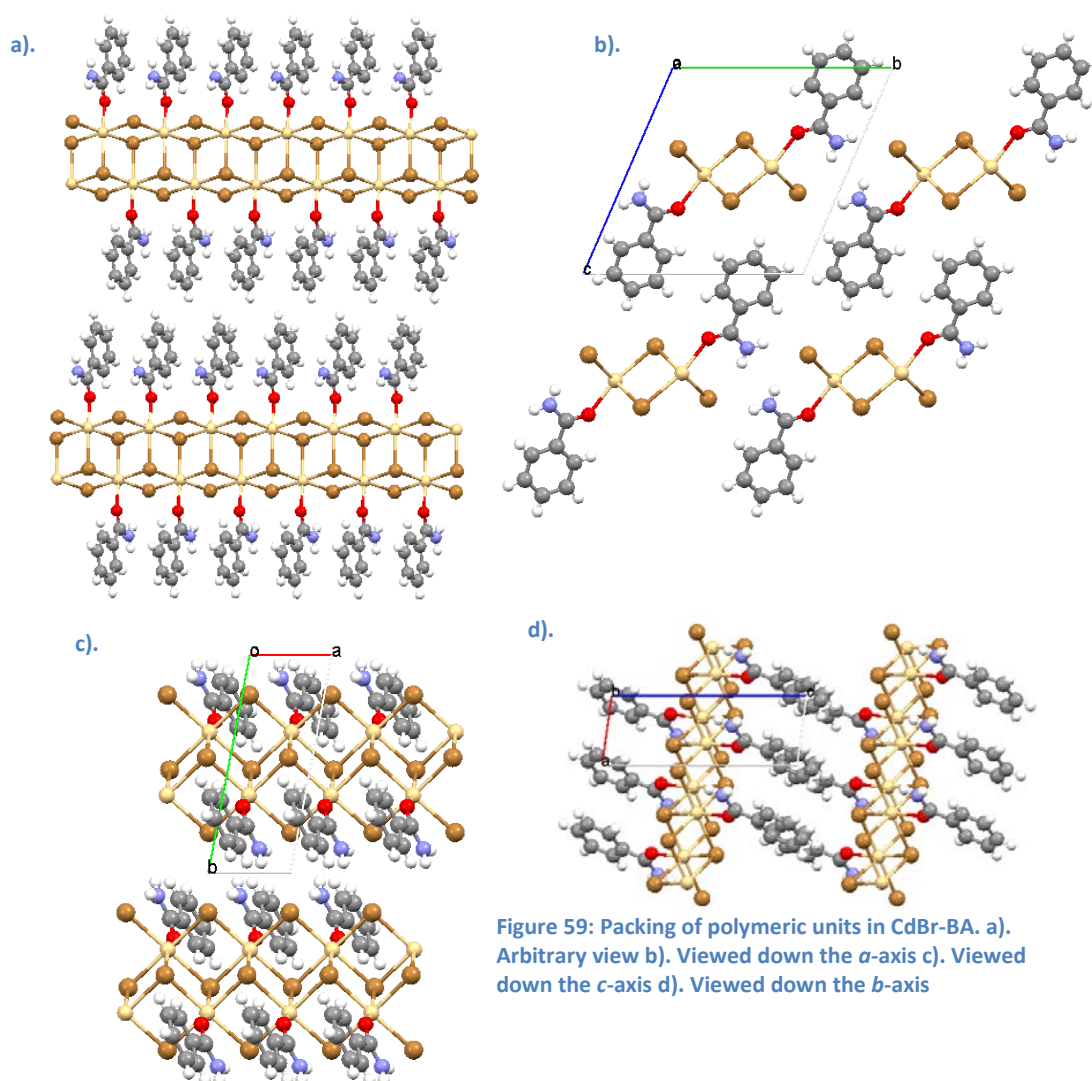


Figure 59: Packing of polymeric units in CdBr-BA. a). Arbitrary view b). Viewed down the *a*-axis c). Viewed down the *c*-axis d). Viewed down the *b*-axis

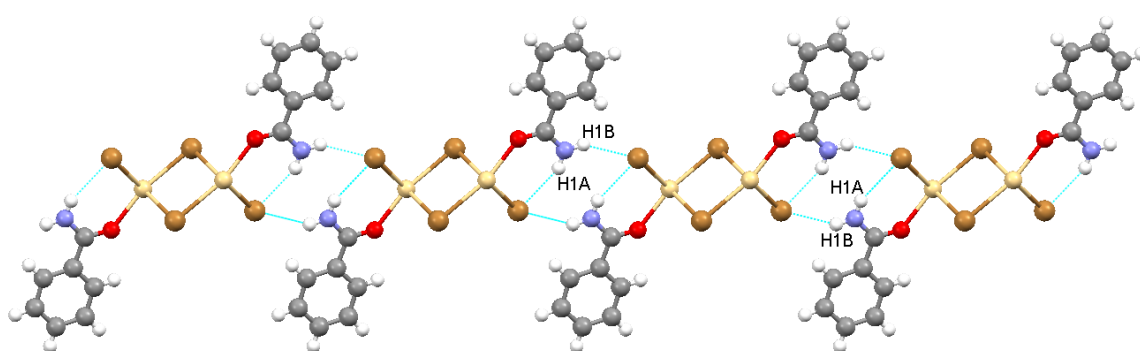


Figure 60: Hydrogen bonding interactions of CdBr-BA viewed along the *a*-axis.

One intramolecular hydrogen bond is evident between the H1A atom on N1 of the benzamide ligand and a bromido ligand in the same polymer. In addition, one intermolecular hydrogen bond is formed between the H1B atom on N1 of the benzamide ligand and a bromido ligand bonded to an adjacent coordination polymer, as illustrated in Figure 60. Hydrogen bonding parameters are listed in Table 22.

Table 22: Hydrogen bonding parameters.

Hydrogen bond	H...Br (Å)	N...Br (Å)	<NHBr (°)	Symmetry operator
N-H1A...Br1	2.752(1)	3.553(7)	156.5(5)	1+x,y,z
N-H1B...Br1	2.8212(8)	3.557(9)	144.0(5)	1-x,2-y,1-z

## Dibenzamide (Dibenzamide hydrogen) [catena- $\mu_3$ -bromido- $\mu$ -bromido-dibromidomercuate(II)], HgBr-BA.

Chemical Formula:  $(C_7H_8NO^+)_2(C_7H_7NO)_2 [Hg_3Br_8^{2-}]_n$

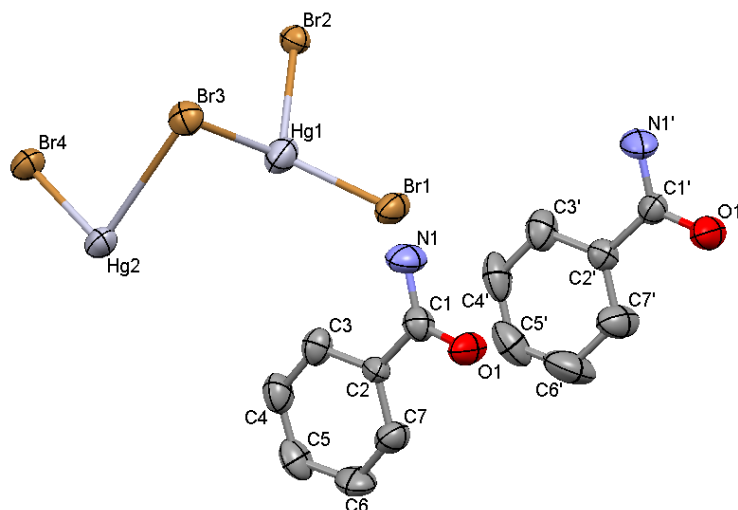


Figure 61: Initial asymmetric unit of HgBr-BA showing the atomic numbering scheme. Displacement ellipsoids are drawn at the 50% probability level. Hydrogen atoms including protonation sites have been omitted for brevity.

In the asymmetric unit of HgBr-BA, one of the mercury ions constituting the inorganic component, Hg1, is located on a special position, and has a site occupancy of 0.5. This means that the formula of the inorganic component in the asymmetric unit is  $[Hg_{1.5}Br_4]^{1-}$ . The asymmetric unit contains two organic components, and in order to ensure that the charges balance, one of the organic components needs to be protonated, as expected from the observation that in this structure the organic component is not coordinated to the inorganic component, and also the fact that the material was prepared in acidic solution. Note that no additional symmetry was found in the structure.

Due to the fact that a relatively large number of heavy atoms, both mercury and bromine, are present in the structure, the location of the proton in the structure could not be observed in the difference Fourier map, hence it could not be directly determined which of the two organic components is protonated.

The matter of protonation of the organic benzamide constituent is further complicated by the fact that, in theory, protonation can occur on either the oxygen or the  $NH_2$  groups of either of the two organic molecules.

It has been mentioned previously, that coordination occurs through the oxygen atom of the amide group, and that resonance also predicts coordination and protonation to occur on the oxygen atom. One protonated benzamide structure has been reported in the literature, that of benzamide



hydrogen tri-iodide (CSD refcode: BZAMTI01; (Herbstein et al., 1981)) but in this case no hydrogen atoms were included in the structure, hence the position of protonation was not determined.

To obtain additional information on the protonation of amide groups in general, a CSD search was performed. Only structures that showed the position of all the hydrogen atoms, including the proton of interest, were considered. This search yielded only one structure, that of acetamide hemihydrochloride, with two entries of the structure under the CSD refcodes ACAMCL and ACAMCL01 (Muir and Speakman, 1979) (Speakman et al., 1981). Notably, the structure given in the entry ACAMCL01 was determined by neutron diffraction, a technique that is superior to X-ray diffraction in the location of hydrogen atom positions. In this structure it was found that the proton is located symmetrically between the two oxygen atoms of different amide groups, as shown in Figure 62a, which is also the protonation site on the amide group predicted by resonance. This type of symmetrical hydrogen bond is expected to be much stronger than normal hydrogen bonds, and may be as strong as a covalent bond (Steiner, 2002).

Interestingly, when considering the structures found through the search of protonated amines, but where the proton position was not included in the structure, all of these structures also show oxygen atoms at a distance similar to that observed in the structure ACAMCL01, as listed in Table 23, and with some examples shown in Figure 62.

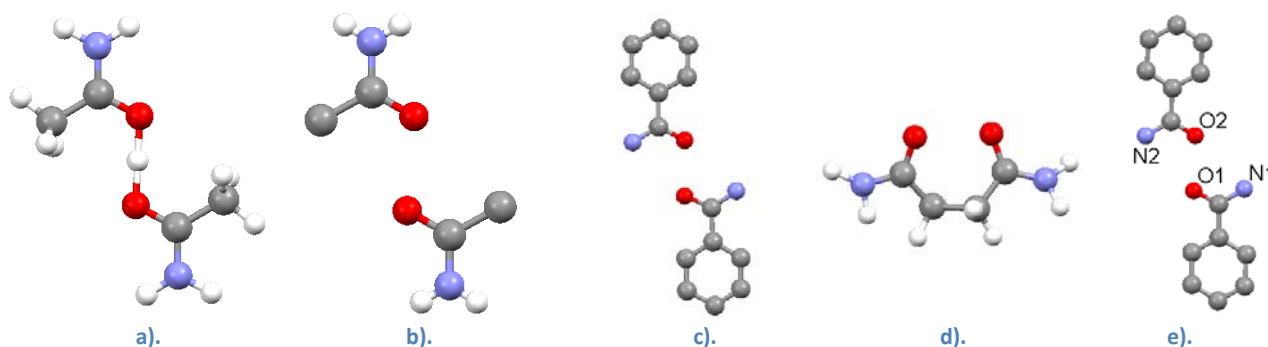


Figure 62: a). Location of proton as determined by neutron diffraction in the structure of acetamide hemihydrochloride, CSD refcode: ACAMCL01. Figures showing proximity of oxygen atoms in protonated amide structures b). ACAMBR02 c). BZAMTI01 d). SUCABT (Dahan and Lefebvre-Soubeyran, 1976) e). current structure, HgBr-BA

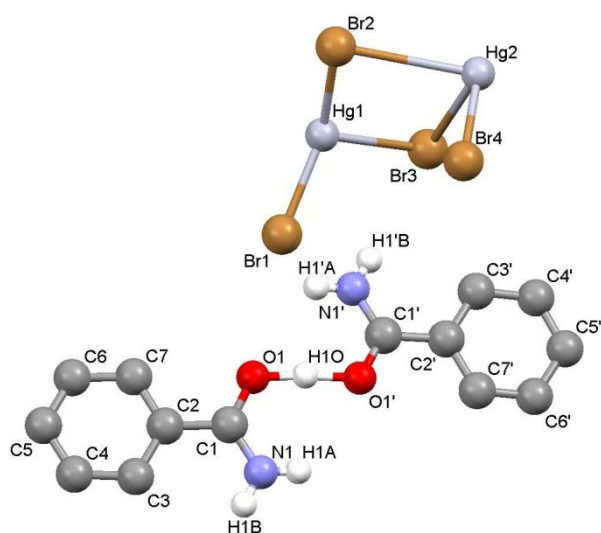
Table 23: Comparison of O...O distances for selected amides found in the CSD.

Refcode	Structure	O...O distance (Å)
ACAMCL01	Acetamide hemihydrochloride	2.426
ACAMBR	Acetamide hemihydrobromide	2.449
ACAMBR01	Acetamide hemihydrobromide	2.480
ACAMBR02	Acetamide hemihydrobromide	2.438
BZAMTI01	Benzamide hydrogen tri-iodide	2.422
SUCABT	Bis(succinamide) hexabromotellurium(iv) monohydrate	2.451
HgBr-BA	Current	2.432

In the current structure, the two crystallographically independent molecules in the asymmetric unit show the same type of orientation, with their oxygen atoms approaching each other, as observed in other protonated amide structures, as shown in Figure 62e. If it is assumed that the proton is located

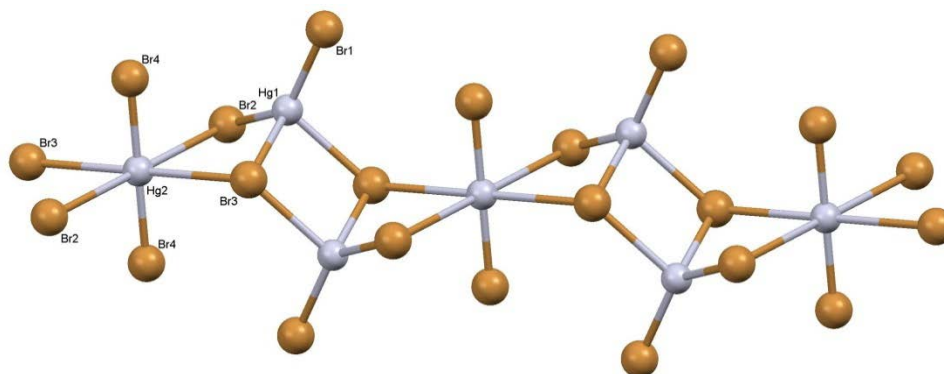
between the two oxygen atoms, as has been reported to occur in the structure ACAMCL01, it does not matter which of the organic units in the asymmetric unit are protonated, as long as it is assumed that the proton is shared symmetrically between the oxygen atoms. In the structure, the hydrogen atom was placed half-way along the vector linking the two oxygen atoms, and fixed in position.

Now that the structure has been resolved completely, the general structural discussion will continue.



**Figure 63:** Asymmetric unit of HgBr-BA showing the atomic numbering scheme. Displacement ellipsoids are drawn at the 50% probability level, and hydrogen atoms are shown as spheres of arbitrary radius. Aromatic hydrogen atoms not shown for brevity.

The asymmetric unit of HgBr-BA consists of two benzamide molecules that share a proton between the oxygen atoms of their amide groups, and one  $[\text{Hg}_{1.5}\text{Br}_4]^{-1}$  unit. Expansion of the inorganic unit results in the formation of a one-dimensional, polymeric perhalometallate anion, along the  $a$ -axis, as shown in Figure 64.



**Figure 64:** Coordination geometries of the two mercury ions in HgBr-BA. Note the compression of the axial Br4-Hg2 bonds and elongation of the Br3-Hg1 and Br2-Hg1 bonds.

Two different coordination geometries of mercury ions occur in the corrugated, anionic coordination polymer. Hg2 displays an octahedral coordination geometry, while atom Hg1 shows tetrahedral

coordination by bromido ligands. In the polymer, pairs of edge sharing tetrahedra alternate with an edge sharing octahedron, as illustrated in the polyhedron representation of the polymer in Figure 65.

In the anionic polymer, the inorganic ligands Br1 and Br4 are terminal, while ligand Br3 bridge three metal atoms, and ligand Br2 bridge two metal atoms.

The interface between each of the sharing types results in several unique ligand bridging styles. The interface between the octahedron (blue polyhedron in Figure 65) and first tetrahedron (yellow polyhedron in Figure 65), two types of  $\mu$ -bromido ligands occur. Firstly Hg1 and Hg2 are bridged by a  $\mu_3$ -bromido ligand (Br3) and secondly a  $\mu$ -bromido ligand (Br2). In the interface between the two tetrahedra (yellow and red polyhedra in Figure 65), the two tetrahedral Hg2 atoms are bridged by two  $\mu_3$ -bromido ligands (Br3).

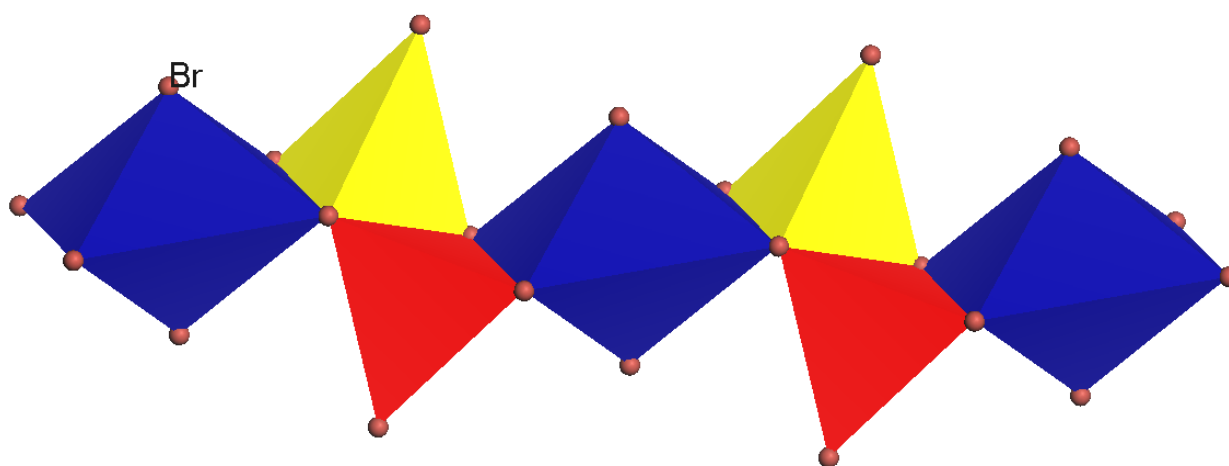


Figure 65: Polyhedral representation of the one dimensional inorganic polymer. Organic ligand not shown for clarity.

Selected Hg-Br bond lengths are listed in Table 1. It can be seen that the terminal Hg-Br bonds have similar bond lengths of 2.422(1) Å and 2.466(1) Å. The bridging Hg-Br bond lengths are longer than the terminal ones, and range from 2.504(1) Å to 3.315(1) Å.

Table 24: Selected coordination bond lengths of HgBr-BA.

Bond	Length (Å)	Type	Bond type
Hg2-Br4	2.422(1)	Axial	Terminal
Hg2-Br3	3.256(1)	Equatorial	$\mu$
Hg2-Br2	3.315(1)	Equatorial	$\mu$
Hg1-Br3 <sup>i</sup>	2.835(1)	Tetrahedral	$\mu_3$
Hg1-Br3	2.807(1)	Tetrahedral	$\mu_3$
Hg1-Br2	2.504(1)	Tetrahedral	$\mu$
Hg1-Br1	2.466(1)	Tetrahedral	Terminal

<sup>i</sup>: 1-x,-y,-z

Table 25: Selected coordination angles of HgBr-BA.

Angles (°)	
Octahedral	
Br3-Hg2-Br3	180.00(2)
Br2-Hg2-Br2	180.00(3)
Br4-Hg2-Br4	180.00(4)
Tetrahedral	
Br3-Hg1-Br3 <sup>i</sup>	89.53(3)
Br3 <sup>i</sup> -Hg1-Br1	106.30(4)
Br3 <sup>i</sup> -Hg1-Br2	106.46(4)
Br2-Hg1-Br3	100.37(4)
Br1-Hg1-Br3	110.44(4)
Br1-Hg1-Br2	134.61(5)

<sup>i</sup>: 1-x,-y,-z

There is no distortion of the coordination bond angles of the octahedrally coordinated Hg2 whilst the most distortion of the tetrahedrally coordinated Hg1 occurred in the Br3-Hg1-Br3 bond angle with a bond angle of  $89.53(3)^\circ$ . This type of perhalometallate anion has, to our knowledge, never been reported before.

In the first of the crystallographically independent organic components, containing atom N1, which will be called BA1, the amide group is rotated by a torsion angle (C7-C2-C1-O1) of  $-5(2)^\circ$  relative to the aromatic ring plane, and in the second organic molecule, BA2, (containing atom N1') the same torsion angle (C7'-C2'-C1'-O1') is  $4(2)^\circ$ .

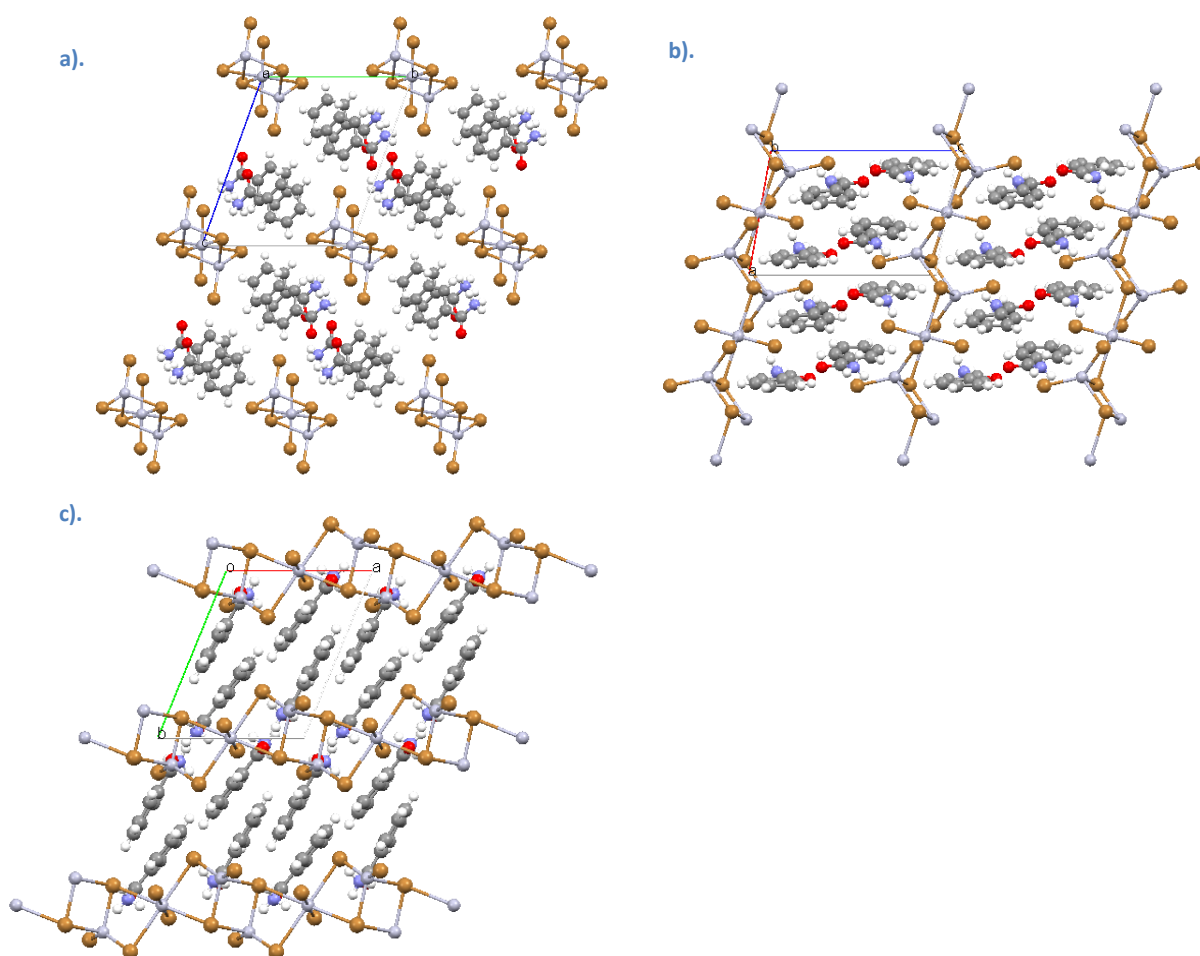


Figure 66: Packing of polymeric units in HgBr-BA viewed along the a) View down *a*-axis b). View down *b*-axis and c). View down *c*-axis

Packing diagrams for the structure are shown in Figure 66 which shows the organic and inorganic constituents of the structure pack in alternating organic and inorganic layers, parallel to the *ab*-plane. In the organic layer, which contains the benzamide moieties, the molecules pack to form two layers of aromatic rings. In this layer the aromatic ring planes are tilted by  $81.6^\circ$  relative to the inorganic layer plane. In this layer, neighbouring aromatic groups of benzamide molecules are separated from one another with a centroid-to-centroid distance of  $5.029 \text{ \AA}$ , centroid-to-plane distance of  $3.099 \text{ \AA}$  and slippage distance of  $3.961 \text{ \AA}$ . The benzamide aromatic rings are not parallel

to one another with a plane-to-plane angle of  $8.06^\circ$ . These values indicate that  $\pi$ - $\pi$  interactions are not likely to be present in this structure.

Hydrogen bonding interactions are present between the organic and the inorganic constituents of the structure, with the  $\text{NH}_2$  group on BA1 forming two bifurcated hydrogen bonding interactions, with one of these interactions involving two bromido ligands on the neighbouring polymer as hydrogen bonding acceptor, while the other has an oxygen atom on the adjacent benzamide molecule, as well as a bromido ligand on the neighbouring polymer as acceptor, as shown in Figure 67. Hydrogen bonding parameters are listed in Table 26.

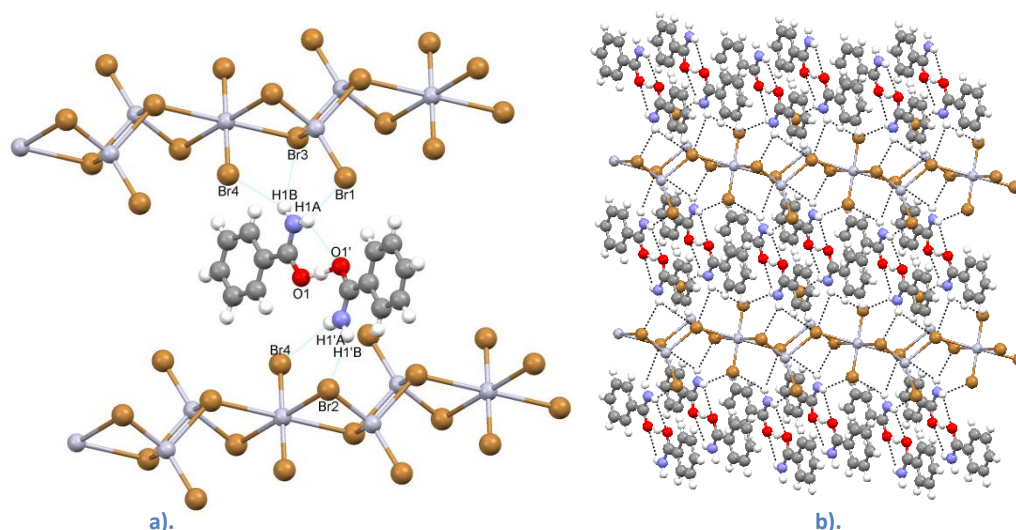


Figure 67: a). Hydrogen bonding interactions b). resulting hydrogen bonded sheet.

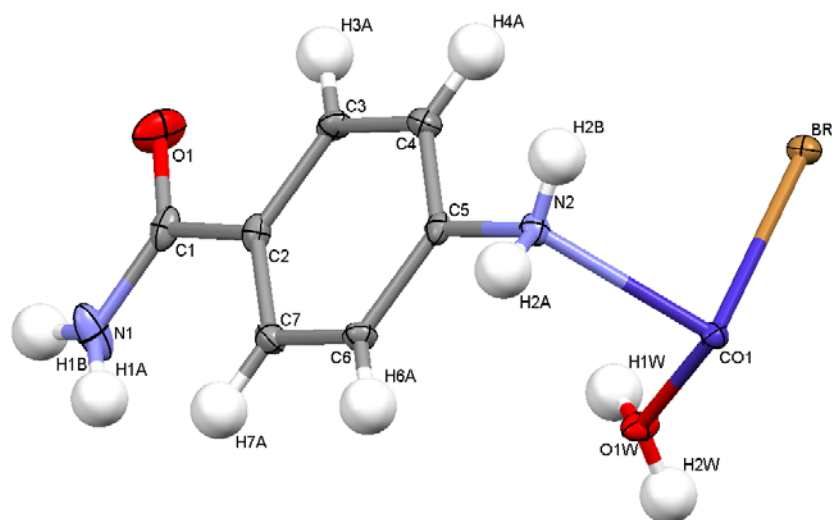
Table 26: Hydrogen bonding parameters for HgBr-BA.

Hydrogen Bond	H...A (Å)	D...A (Å)	D - H...A (°)	Symmetry operator
N1-H1A...O1 <sup>i</sup>	2.603(8)	3.18(1)	125.8(7)	<sup>i</sup> -x+1, -y, -z+1
N1-H1A...Br1 <sup>ii</sup>	2.728(1)	3.48(1)	147.1(7)	<sup>ii</sup> -x+1, -y, -z+1
N1-H1B...Br4 <sup>iii</sup>	2.981(1)	3.51(1)	121.8(7)	<sup>iii</sup> -x, -y, -z+1
N1-H1B...Br3 <sup>iv</sup>	3.071(1)	3.78(1)	141.4(7)	<sup>iv</sup> -x+1, -y, -z+1
N1-H1B...Br4 <sup>v</sup>	2.981(1)	3.51(1)	141.4(7)	<sup>v</sup> -x+1, -y, -z+1
N1'-H1'B...Br2 <sup>vi</sup>	2.677(1)	3.427(9)	146.3(7)	<sup>vi</sup> x, y, z+1

As a result of the hydrogen bonding interactions, benzamide molecules are anchored to the one-dimensional inorganic polymers, and to each other via the symmetrical O-H...O hydrogen bond. The overall result is the formation of a hydrogen bonded sheet of molecules, parallel to the  $ac$ -plane, as shown in Figure 67.

## *Trans*-di(4-amino- $\kappa$ N-benzamide)diaquadibromidocobalt(II), CoBr-4ABA

Chemical Formula:  $[(C_7H_7N_2O)_2(H_2O)_2CoBr_2]$



**Figure 68:** Asymmetric unit of CoBr-4ABA showing the atomic numbering scheme. Displacement ellipsoids are drawn at the 50% probability level and hydrogen atoms are drawn as spheres of arbitrary radii.

The asymmetric unit of CoBr-4ABA consists of a cobalt ion coordinated by one bromido ligand at a distance of 2.6392(3) Å, one water molecule coordinated at a distance of 2.038(2) Å and one 4-aminobenzamide ligand coordinated through the amine nitrogen atom with a Co-N bond distance of 2.206(2) Å, as shown in Figure 68. The cobalt ion is on a special position in the unit cell, and the full molecule is generated from the asymmetric unit through inversion.

One molecule is comprised of two asymmetric units, and the unit cell contains one molecule. The cobalt ion has perfect octahedral coordination geometry, with the Br1-Co1-Br1 angle equal to 180.00(1)°, N2-Co1-N2 angle of 180.00(7)° and O1W-Co1-O1W angle of 180.00(6)°, as shown in Figure 69. The 4-aminobenzamide ligands are coordinated *trans* to one another. The complete molecule is generated from the asymmetric unit. One molecule is comprised of two asymmetric units, and the unit cell contains one molecule.

In the molecule the 4-aminobenzamide ligands are coordinated to the cobalt ion with a C5-N2-Co1-Br1 torsion angle of 78.1(1)°. The 4-aminobenzamide molecule is coordinated to the cobalt ion with a Co1-N2-C5 angle of 118.6(1)°, which is larger than the ideal tetrahedral angle. The result is that the aromatic rings form an angle of 31.68° with respect to the bisecting plane through the cobalt, oxygen and bromine atoms.



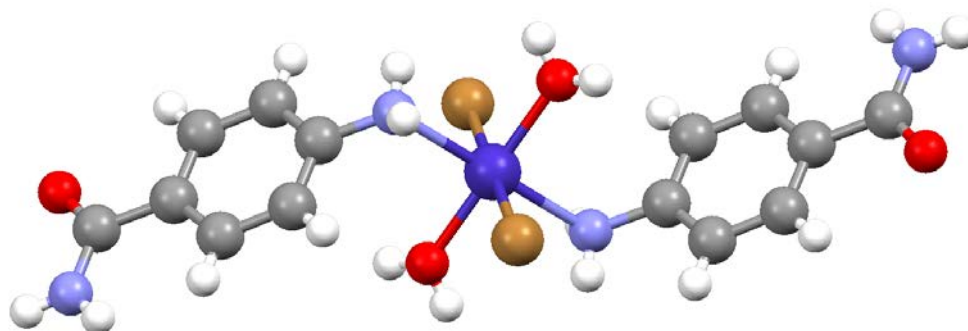


Figure 69: Coordination geometry of CoBr-4ABA.

The CoBr-4ABA structure does not form any polymeric motifs, thus consists of only isolated coordination molecules. The packing diagrams are illustrated in Figure 70. In this structure, the organic ligands pack to form an organic bilayer, while the metal ions, halogeno ligands and water molecules form an inorganic layer parallel to the *bc*-plane.

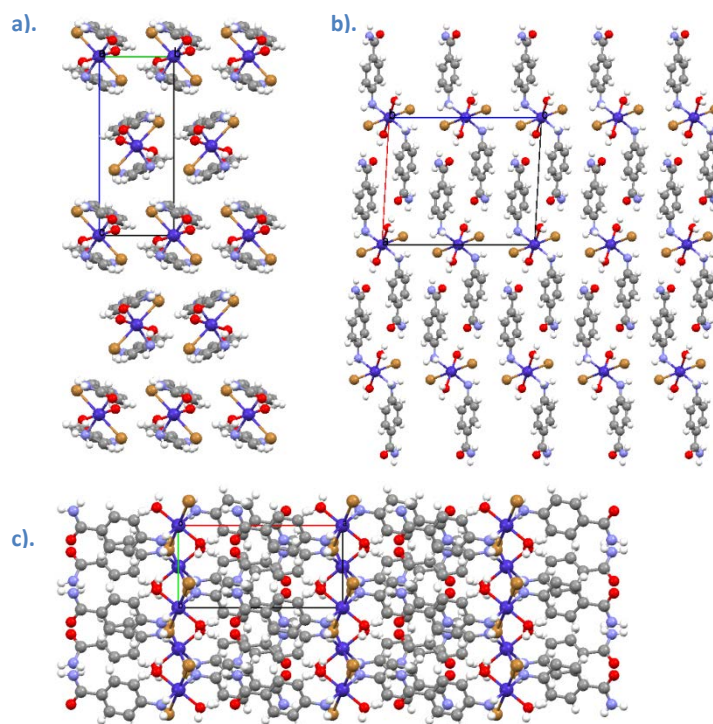


Figure 70: Packing diagram of CoBr-4ABA viewed along the a) *a*-axis  
b) *b*-axis and c) *c*-axis.

The molecules along the *a*-direction are linked by  $\pi$ - $\pi$  interactions. The aromatic rings of 4-aminobenzamide are separated by a plane-to-plane distance of 3.384 Å, a centroid-to-centroid distance of 5.205 Å and a slippage distance of 1.880 Å. In Figure 70b it seems that there are  $\pi$ - $\pi$  interactions between each of the aromatic rings molecules along the *b*-direction. But close inspection of Figure 70a reveals that the aromatic rings of the adjacent molecules in the *a*-direction are parallel, but the aromatic rings of the molecules adjacent along the *c*-direction are orientated at an angle of 53.44° with respect to each other as shown in Figure 71.

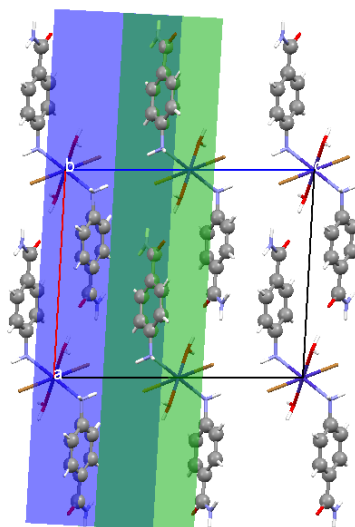


Figure 71: View along the *b*-direction of the parallel and angles arrangement of aromatic rings in CdBr-4ABA

Considering the plane-to-plane distance and the slippage distance, it is evident that  $\pi$ - $\pi$  interactions are involved in the cohesion of the structure, as observed from the packing orientation.

Hydrogen bonding interactions are present between the molecules. Adjacent CoBr-4ABA molecules are linked in the *a*-direction by two N1-H1B...Br1 hydrogen bonds at a D-A distance of 3.520(2) Å and two O1W-H1W...O1 hydrogen bonds at a distance of 2.630(2) Å. CoBr-4ABA molecules are hydrogen bonded along the *b*-direction by two N2-H2B...Br1 interactions at a distance of 3.585(2) Å and two O1W-H2W...Br1 hydrogen bonds at a distance of 3.220(2) Å. The molecules are connected in the *c*-direction by two N2-H2A...Br1 hydrogen bonds at a distance of 3.535(2) Å. The result is that CoBr-4ABA packs to form a three-dimensional network of hydrogen bonds linking molecules along the *a*-, *b*- and *c*-directions as illustrated in Figure 72. Hydrogen bonding parameters are listed in Table 27.

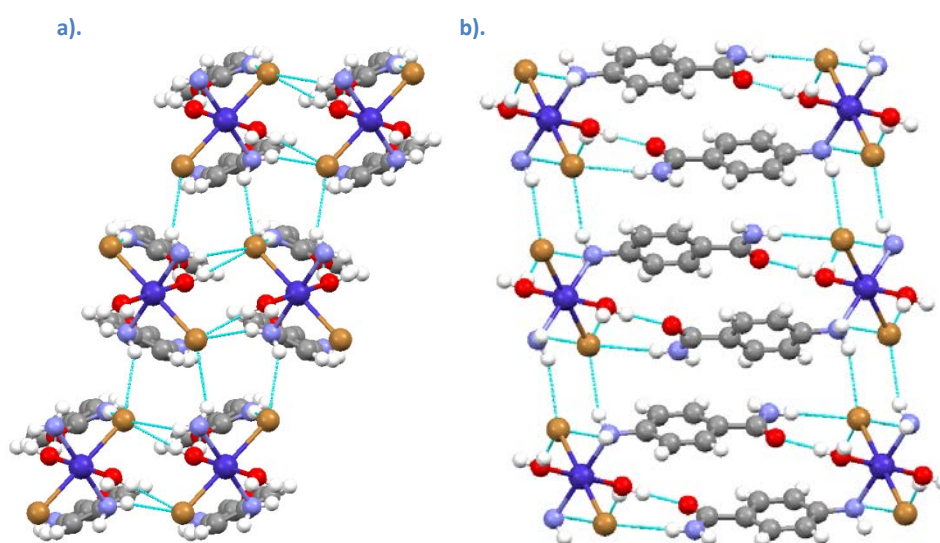


Figure 72: Three-dimensional hydrogen bonding network viewed along the a) *a*-axis and b) *b*-axis.



Table 27: Hydrogen bonding parameters for CdBr-4ABA

Hydrogen Bond	H...A (Å)	D...A (Å)	D - H...A (°)	Symmetry operator
N1-H1B...Br1 <sup>i</sup>	2.6639(3)	3.520(2)	173.9(1)	<sup>i</sup> 1-x,2-y,-z
O1W-H1W...O1 <sup>ii</sup>	1.79(3)	2.630(2)	166(3)	<sup>ii</sup> 1-x,2-y,-z
N2-H2A...Br1 <sup>iii</sup>	2.77(3)	3.535(2)	144(2)	<sup>iii</sup> x,3/2-y,1/2+z
N2-H2B...Br1 <sup>iv</sup>	2.88(3)	3.585(2)	147(3)	<sup>iv</sup> -x,1-y,-z
O1W-H2W...Br1 <sup>v</sup>	2.41(3)	3.220(2)	174(3)	<sup>v</sup> x,1+y,z

### Trans-di(4amino-κN-benzamide)aquadibromidocopper(II), CuBr-4ABA

Chemical Formula: [(C<sub>7</sub>H<sub>7</sub>N<sub>2</sub>O)<sub>2</sub>(H<sub>2</sub>O)CuBr<sub>2</sub>]

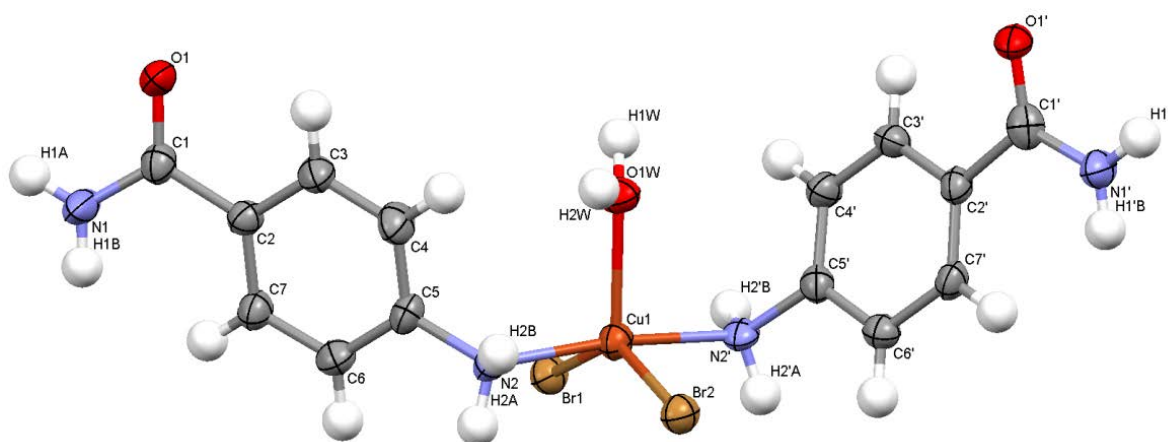


Figure 73: Asymmetric unit of CuBr-4ABA showing the atomic numbering scheme. Displacement ellipsoids are drawn at the 50% probability level and hydrogen atoms are drawn as spheres of arbitrary radii.

The asymmetric unit of CuBr-4ABA, shown in Figure 73 consists of a copper ion coordinated by one water molecule at a Cu1-O1W distance of 2.168(5) Å, two bromide ligands coordinated at Cu1-Br1 and Cu1-Br2 distances of 2.4782(8) Å and 2.469(1) Å respectively and two 4-aminobenzamide molecules coordinated through the amine nitrogen atom at Cu1-N2 and Cu1-N2' distances of 2.037(5) Å and 2.036(5) Å respectively. The copper ion has a trigonal bipyramidal coordination geometry with the water molecule and the bromide ligands in the trigonal plane with O1W-Cu1-Br1, O1W-Cu1-Br2 and Br1-Cu1-Br2 coordination angles of 114.7(1)°, 101.9(1)° and 143.37(4)° respectively. The axial N2-Cu1-N2' angle is 173.2(2)° and two the 4-aminobenzamide ligands are coordinated to the copper ion with Cu1-N2-C5 and Cu-N2'-C5' angles of 123.4(4)° and 121.0(4)° respectively and O1W-Cu1-N2-C5 and O1W-Cu1-N2'-C5' torsion angles of 58.3(5)° and -42.6(5)°. These values indicate a slightly distorted trigonal bipyramidal arrangement, with values of 180°, 90° and 120° expected for an ideal trigonal bipyramidal geometry. Selected bond lengths and angles are listed in Table 28 and Table 29.

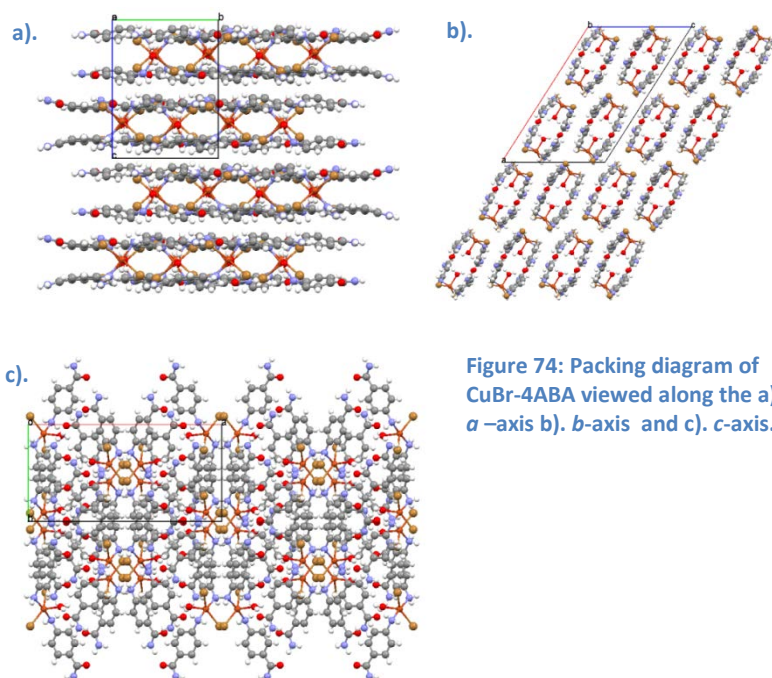
**Table 28: Selected bond distances of CoBr-4ABA**

Bond	Bond distance (Å)
Cu1-O1W	2.168(5)
Cu1-Br1	2.4782(8)
Cu1-Br2	2.469(1)
Cu1-N2	2.037(5)
Cu1 N2'	2.036(5)

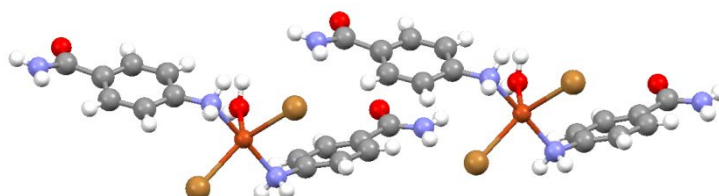
**Table 29: Selected angles of CoBr-4ABA**

Angle (°)	
O1W-Cu1-Br1	114.7(1)°
O1W-Cu1-Br2	101.9(1)°
N2-Cu1-N2'	173.2(2)°

The CuBr-4ABA structure is a zero-dimensional structure and no polymerization of the inorganic component through the sharing of bromide ligands is observed. The molecules pack to form a layered structure parallel to the crystallographic *ab*-plane as illustrated in Figure 74a. It is interesting to note that the packing of CuBr-4ABA viewed along the *b*-axis seems to indicate the formation of molecular dimers however these discrete dimers are not visible in the other directions.


**Figure 74: Packing diagram of CuBr-4ABA viewed along the a). *a*-axis b). *b*-axis and c). *c*-axis.**

The aromatic rings of adjacent molecules along the *b*-axis are illustrated in Figure 75 and are separated by a centroid-to-centroid distance of 3.953 Å. These aromatic systems are not however parallel but have a plane-to-plane angle of 27.14°. The aromatic ring orientation is also not end to end (amine group aligned with the centre of the ring) as in the case of CoBr-4ABA discussed earlier.


**Figure 75: Orientation of aromatic groups in CuBr-4ABA.**

The distance between the centroid defined by (C1, C2, C3, C4, C5, C5, C7, N1, O1) and the plane defined by the aromatic ring of the second molecule (C2', C3', C4', C5', C5', C7') is 3.317 Å. This value is comparable to the structures discussed previously. Hunter and Sanders demonstrated that the orientation of  $\pi$ -systems to one another may vary greatly (Hunter and Sanders, 1990). Janaik performed a survey of heterocyclic (specifically nitrogen containing arenes)  $\pi$ - $\pi$  interactions and found that whilst non planar rings are rare, they do exist. Based on this it is possible that neighboring rings interact in a rare form of  $\pi$ - $\pi$  interaction. Expansion of the  $\pi$ - $\pi$  "stacked" linkages along the *b*-direction reveals a novel one-dimensional triple helix interwoven structure as shown in Figure 76.

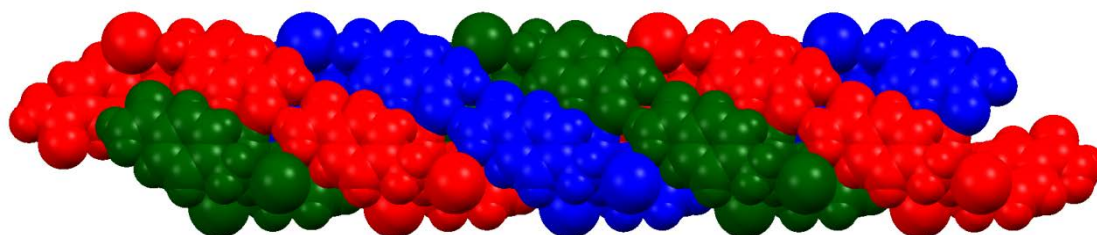


Figure 76: Novel one dimensional "triple helix" formed by CuBr-4ABA molecules.

Each one of the "strands" for example the red "strand" is comprised of a hydrogen bonded string of CuBr-4ABA molecules along the *b*-direction as shown in Figure 77. In the strand, the molecules are linked through the formation of amide synthons, and the resulting string forms a spiral.

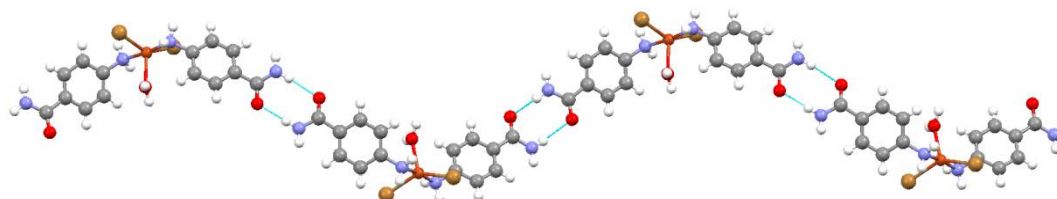


Figure 77: One dimensional hydrogen bonded network of CuBr-4ABA

Each of the molecules of the same colour strand as illustrated in Figure 76 is linked by two hydrogen bonds namely N1'-H1'A...O1 and N1-H1A...O1 at D...A distances of 2.867(7) Å and 2.991(8) Å respectively, as illustrated in Figure 77. The different coloured strands in Figure 76 are also linked via an inter-strand N1-H1B...Br2, N1'-H1'B...Br1, O1W-H2W...O1 and O1W-H1W...O1 hydrogen bonds at a distance of 3.434(7) Å, 3.434(7) Å, 2.860(5) Å and 2.728(9) Å respectively. This results in the formation of a triple helix one-dimensional hydrogen bond linked structure. Both the right and left handed helices occur in the unit cell. The triple helices are linked along the *a*-direction by a N2-H2A...Br1 and a N2'-H2'A...Br2 hydrogen bonds at a distance of 3.515(6) Å and 3.474(6) Å respectively. The helices are linked in the *c*-direction via a N2'-H2'B...Br1 hydrogen bond at a distance of 3.618(6) Å. All hydrogen bonding parameters are listed in Table 30. An intricate network of hydrogen bonds link molecules into a strand, link strands together and link helices together and results in the formation of a three-dimensional hydrogen bonded network as shown in Figure 78.

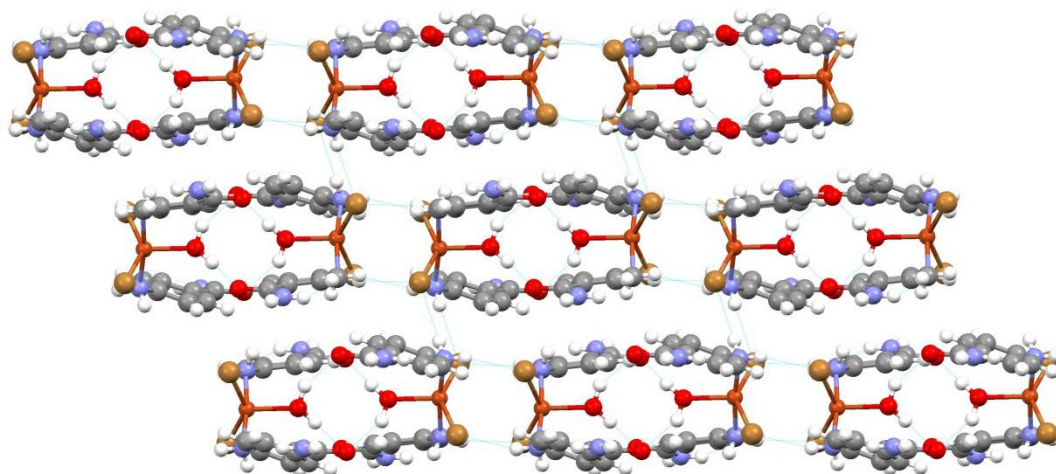


Figure 78: Three-dimensional hydrogen bonded network of CuBr-4ABA

Table 30: Hydrogen bonding parameters of CuBr-4ABA.

Hydrogen Bond	H...A (Å)	D...A (Å)	D - H...A (°)	Symmetry operator	Description
N1'-H1'A...O1 <sup>i</sup>	1.989(5)	2.867(7)	175.9(4)	<i>i</i> : 1/2-x,-3/2+y,1/2-z	Intra-strand
N1-H1A...O1 <sup>ii</sup>	2.156(5)	2.991(8)	158.3(5)	<i>ii</i> : 1/2-x,3/2+y,1/2-z	Intra-strand
N1-H1B...Br2 <sup>iii</sup>	2.6899(7)	3.434(7)	143.2(4)	<i>iii</i> : x,1+y,z	Inter-strand
O1W-H1W...O1 <sup>iv</sup>	1.78(6)	2.728(9)	166(5)	<i>iv</i> : 1/2-x,-1/2+y,1/2-z	Inter-strand
N1'-H1'B...Br1 <sup>v</sup>	2.6714(8)	3.485(6)	154.2(3)	<i>v</i> : x,-1+y,z	Inter-strand
N2-H2A...Br1 <sup>vi</sup>	2.6021(9)	3.515(6)	171.5(3)	<i>vi</i> : 1-x,y,1/2-z	Inter-helix (a)
O1W-H2W...O1 <sup>vii</sup>	1.99(4)	2.860(5)	148(4)	<i>vii</i> : 1/2-x,1/2+y,1/2-z	Intra-helix
N2'-H2'A...Br2 <sup>viii</sup>	2.5895(9)	3.474(6)	161.7(3)	<i>viii</i> : 1-x,y,1/2-z	Inter-helix (a)
N2'-H2'B...Br1 <sup>xi</sup>	2.7305(9)	3.618(6)	162.0(3)	<i>ix</i> : 1-x,1-y,1-z	Inter-helix (c)

## Experimental determination of band gap energies

The band gap energies of CuCl-BA, CuBr-BA, CdCl-BA and CdBr-BA were determined by diffuse reflectance spectroscopy.

The DRS spectrum of CdCl-BA is shown in Figure 79. This spectrum exhibits typical features expected for a DRS spectrum and has a clearly defined absorption edge between 280 nm and 320 nm with no/little absorption of photons evident above 320 nm. High absorption of photons is observed below 298nm. Estimation of the band gap through the Tauc (Tauc and Menth, 1972) method yields a band gap energy of 4.25 eV, as illustrated in Figure 79.

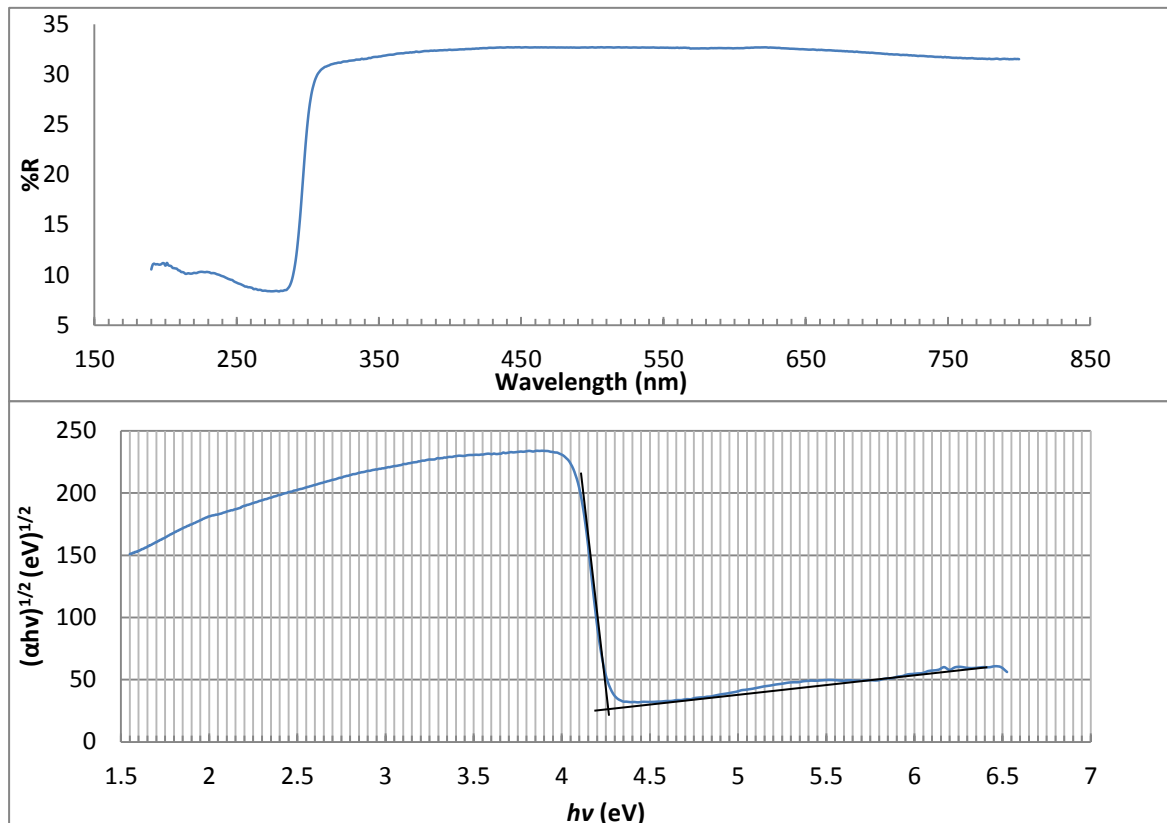


Figure 79: DRS spectrum of CdCl-BA (top). Tauc plot of CdCl-BA (bottom). The intersection of the linear absorption edge and the maximum reflectance line is the estimated band gap energy.

The DRS spectrum of CdBr-BA is shown Figure 80. Similar to the CdCl-BA spectrum, a strong absorption edge is observed between 290- 350 nm. Low absorption of photons above 350 nm is observed and high absorption of photons is observed below 290 nm. Estimation of the band gap through the Tauc method gives a band gap energy of 4.19 eV, as illustrated in Figure 80.

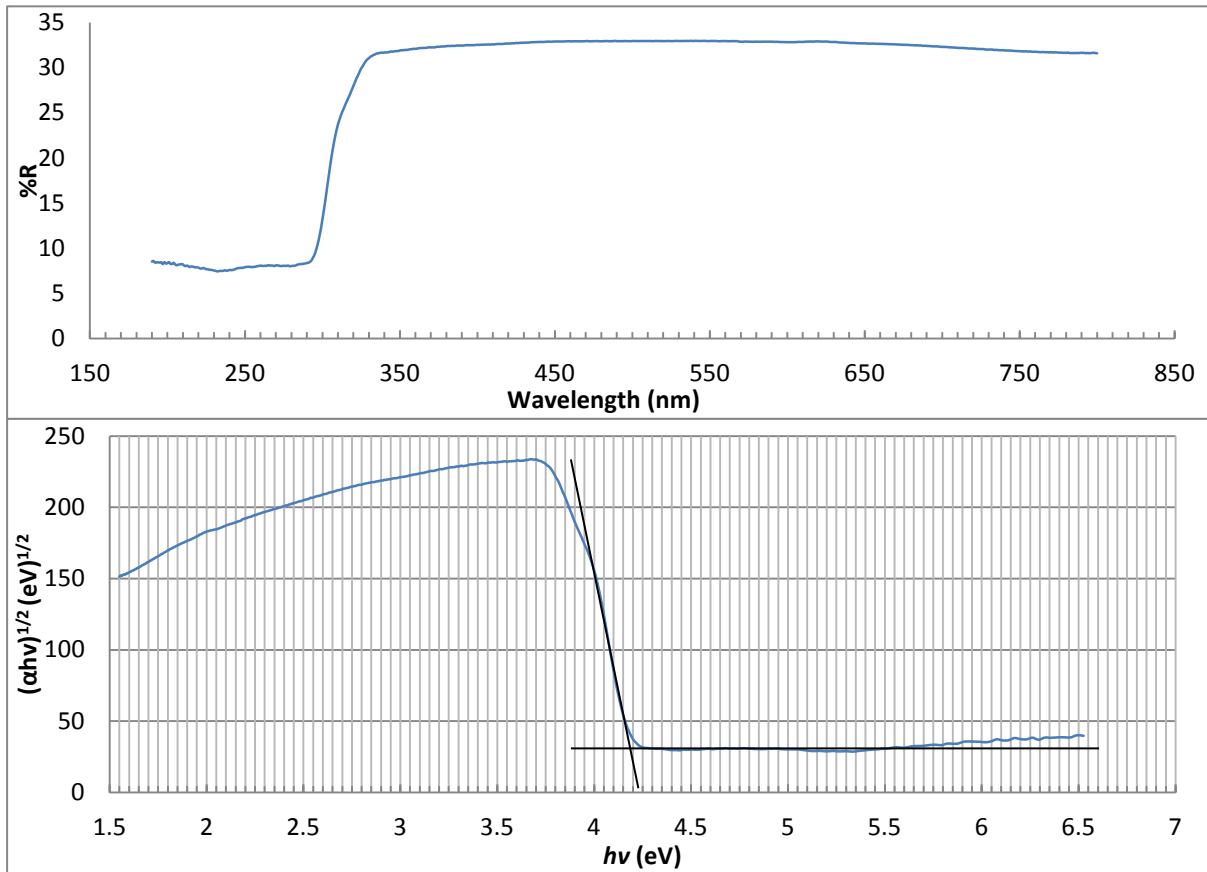


Figure 80: DRS spectrum of CdBr-BA (top). Tauc plot of CdBr-BA (bottom). The intersection of the linear absorption edge and the maximum reflectance line is the estimated band gap energy.

The DRS spectrum of CuCl-BA is illustrated in Figure 81. This spectrum is unusual if compared to the typical spectra of CdCl-BA shown in Figure 79. The spectrum has the usual high wavelength (low energy) high reflectance (Region A in Figure 81) seen in typical DR spectra and the low reflectivity in the low wavelength (high energy) region (Region D in Figure 81). There is however a second peak in reflectance at approximately 600 nm (Region C in Figure 81). The slight increase in absorption near 200 nm is due to the absorption of light by atmospheric oxygen.

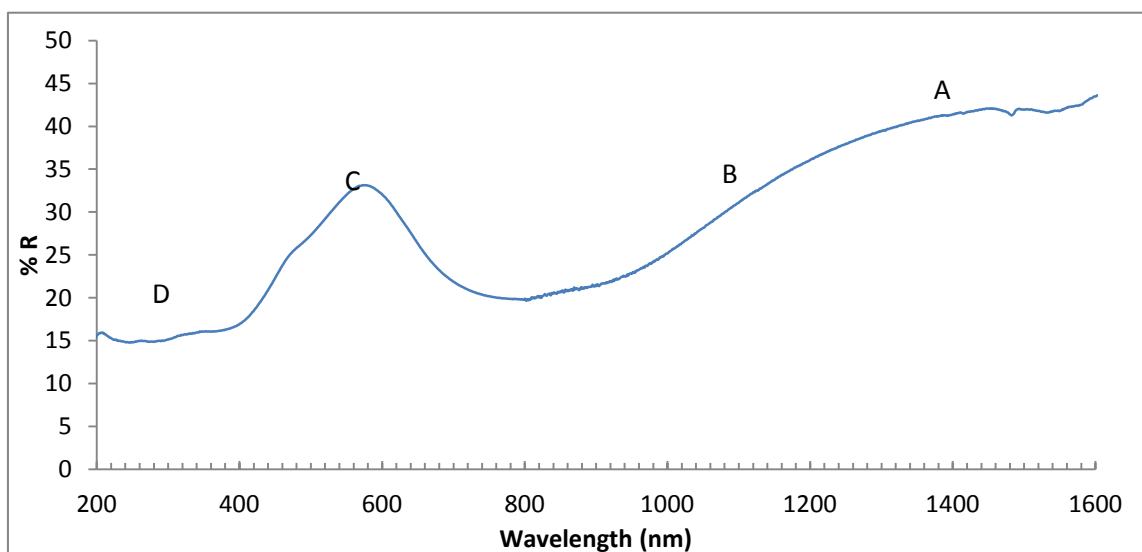


Figure 81: DRS spectrum of CuCl-BA.



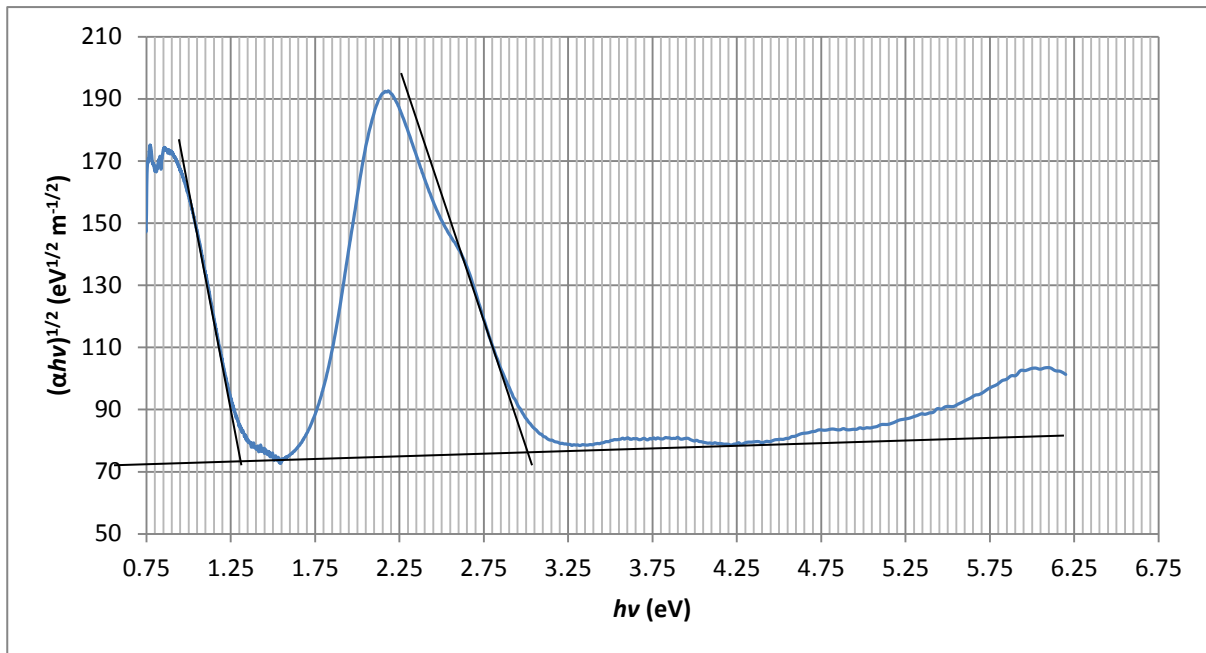


Figure 82: Tauc plot of CuCl-BA. The intersection of the linear absorption edge and the maximum reflectance line is the estimated band gap energy.

There is a wide absorption edge between 1000 - 1400 nm. There is a large reflectance peak between 450 - 700 nm indicating that the absorbance of photons does not occur in the 450 – 700 nm region, instead they are reflected. Either side of the reflectance peak C significant absorbance of photons occurs.

A similar two absorption edge spectrum was observed by Murphy where it was found that a  $\text{TiO}_2$  thin film semiconductor had two band gaps (Murphy, 2007). The author constructed a Tauc (Tauc and Menth, 1972) plot with  $(\alpha hv)^{1/2}$  vs.  $hv$  and extrapolated the band gap energies from it.

A similar plot of  $(\alpha hv)^{1/2}$  vs.  $hv$  was constructed for CuCl-BA and is shown in Figure 82.

Two absorption peaks are observed in the Tauc plot of CuCl-BA. Extrapolation of the linear part of the absorption edges to the line of the maximum reflectance is shown in Figure 82 and extrapolation by this method yields an  $E_{g1}$  value of 1.33 eV and an  $E_{g2}$  value of 3.00 eV.

The DRS spectrum of CuBr-BA is shown in Figure 83. The spectrum resembles that of the CuCl-BA spectrum shown in Figure 81. There is a wide absorption edge between 1000- 1400 nm. There is a smaller reflectance peak between 450-700 nm compared to CuCl-BA. Either side of the reflectance peak C there is high absorbance of photons.



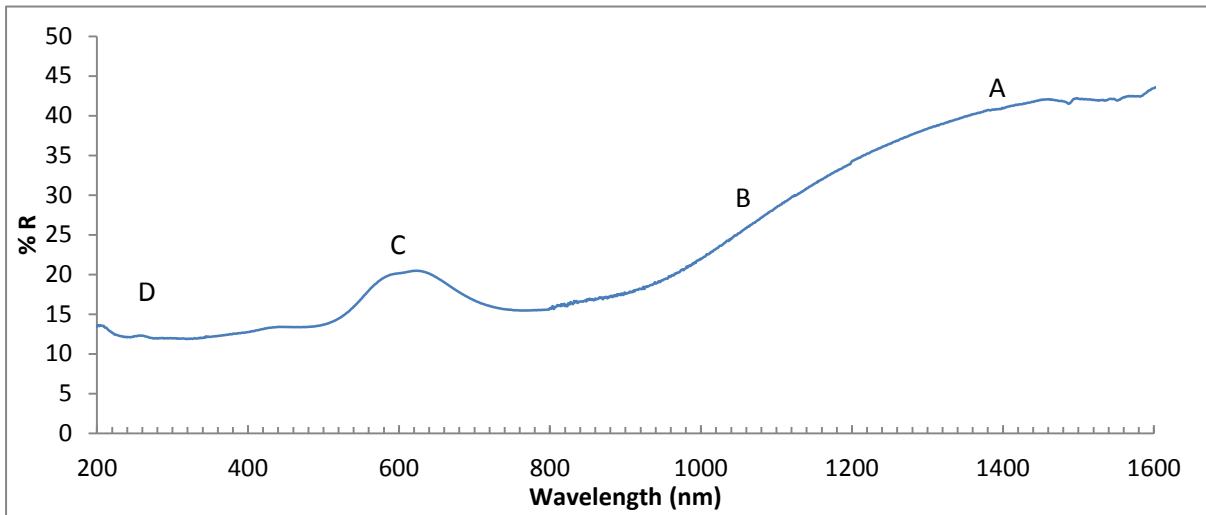


Figure 83: DRS spectrum of CuBr-BA.

A similar Tauc plot of  $(\alpha h\nu)^{1/2}$  vs.  $h\nu$  was constructed for CuBr-BA and is shown in Figure 84.

Two absorption peaks are observed in the Tauc plot of CuBr-BA. Extrapolation of the linear part of the absorption edges to the line of the maximum reflectance is shown in Figure 84 and extrapolation by this method yields an  $E_{g1}$  value of 1.33 eV and an  $E_{g2}$  value of 2.37 eV.

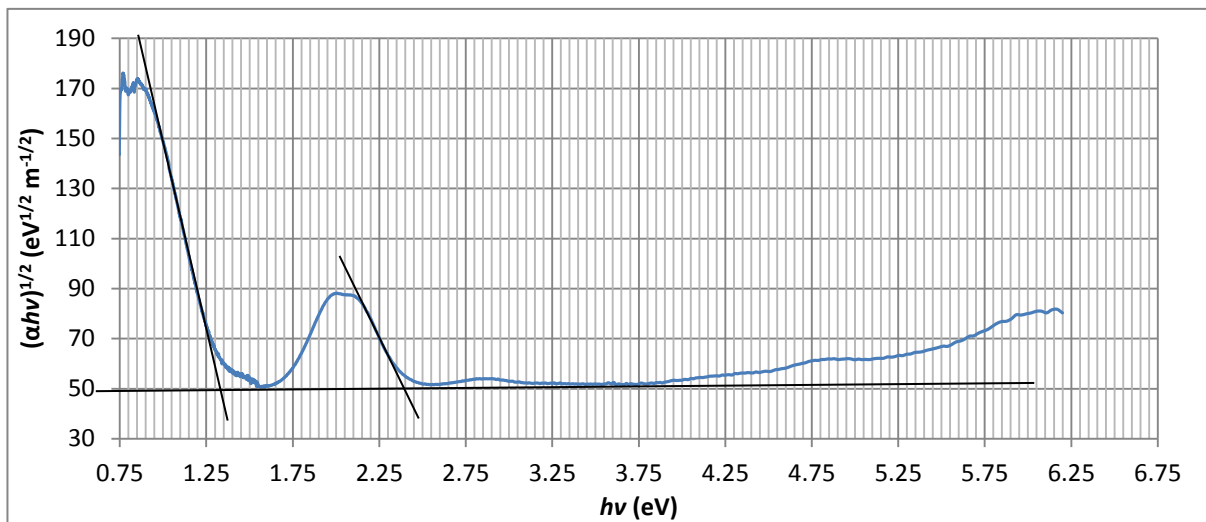


Figure 84: Tauc plot of CuBr-BA. The intersection of the linear absorption edge and the maximum reflectance line is the estimated band gap energy.

The results of the band gap measurements are summarized in Table 31.

An important attribute to note of is the relatively low intensity of the first peak in the DR spectrum compared to the higher energy peak and plateau. In terms of optical spectroscopy this may be due to two factors namely the Laporte Selection rule which states that transitions where there is no change in parity are forbidden and the Spin Selection rule which states that transitions that involve an inversion of the spin of an electron is forbidden. Either one or both of these factors can play a role in significantly lowering the intensity of an absorption/reflectance peak in a spectrum (Cotton 1990).

Table 31: Summary of band gap energies as measured by DRS.

Structure	Band gap energy (eV)
CuCl-BA	
$E_{g1}$	1.33
$E_{g2}$	3.00
CuBr-BA	
$E_{g1}$	1.33
$E_{g2}$	2.37
CdCl-BA	4.25
CdBr-BA	4.19

## Bibliography

- Carvalho, L.C.d., Schleife, A., Fuchs, F. and Bechstedt, F. (2010) 'Valence-band splittings in cubic and hexagonal AlN, GaN, and InN', *Appl. Phys. Lett.*, vol. 97, p. 232101.
- Cotton, F.A. (1990) *Chemical Applications of Group Theory*, 3<sup>rd</sup> edition, Wiley.
- Dahan, F. and Lefebvre-Soubeyran, O. (1976) 'X-ray crystal structures of hexabromotellurates of organic ions. II. Crystal structure of the monohydrate of the hexabromotellurate of protonated disuccinamide', *Acta Crystallogr., Sect. B: Struct. Sci*, vol. 32, p. 2863.
- Herbstein, F.H., Kaftory, M., Kapon, M. and Saenger, W. (1981) 'Structures of three crystals containing approximately—linear chains of triiodide ions', *Z. Kristallogr. Kristallgeom. Kristallphys. Kristallchem.*, p. 154:11.
- Hunter, C.A. and Sanders, J.K.M. (1990) 'The Nature of  $\pi$ - $\pi$  Interactions', *J. Am. Chem. Soc.*, vol. 112, pp. 5525-5534.
- Muir, K.W. and Speakman, J.C. (1979) 'Acetamide hemihydrochloride by X-ray diffraction', *J.Chem.Res.*, vol. 277, p. 3401.
- Murphy, A.B. (2007) 'Band-gap determination from diffuserelectance measurements of semiconductor films, and application to photoelectrochemical water-splitting', *Sol. Energy Mater. Sol. Cells*, vol. 91, no. 14, p. 1326–1337.
- Speakman, J.C., Lehmann, M.S., Allibon, J.R. and Semmingsen, D. (1981) 'Acetamide hemihydrochloride, by neutron diffraction at 120 K', *Acta Crystallogr., Sect. B: Struct. Sci*, vol. 37, p. 2098.
- Spek, A.L. (2003) 'PLATON', *J. Appl. Crystallogr.*, vol. 36, pp. 7-13.
- Steiner, T. (2002) 'Hydrogen bond in the solid state', *Angew. Chem. Int. Ed.*, vol. 41, pp. 48-76.
- Takeuchi, H., Sato, M., Tsuji, T., Takashima, H., Egawa, T. and Konaka, S. (1999) 'Molecular structure of benzamide as studied by gas-phase electron diffraction', *J. Mol. Struct.*, vol. 485-486, pp. 175-181.
- Tauc, J. and Menth, A. (1972) 'States in the gap', *J. Non-Cryst. Solids*, vol. 8-10, p. 569–585.

# Chapter Four – Results: Computational Chemistry

---

The aim of the computational study was to explore the ability of currently available DFT methods to determine the electronic structure of the hybrid materials studied in this project. The focus was specifically to assess if these techniques can provide information on the electronic properties of the isostructural, one-dimensional coordination polymer structures CdCl-BA, CdBr-BA, CuCl-BA and CuBr-BA. The electronic properties of these materials are important, due to their potential application as nano-wires in molecular electronics, hence the focus on the calculation of their electronic structure and band gaps.

The approach followed in the computational section is outlined in Chapter Two, and the results obtained in the different steps are given in this chapter.

## Plane-wave convergence

Bloch's theorem states that the electronic wave functions at each k-point can be expanded in terms of a discrete plane-wave basis set. In principle, an infinite number of plane waves are required for such an expansion. However, the coefficients,  $C_{\mathbf{k}+\mathbf{G}}$ , for the plane waves with small kinetic energies,  $|\mathbf{k}+\mathbf{G}|^2$ , are more important than those with large kinetic energies. The plane-wave cut-off energies are simply the truncation of the infinite sums of all the plane waves to a finite value, lowering the cost of computational effort drastically.

As multiple structures were considered in this study, the plane-wave cut-off energies for each of the band gap calculations have to be the same value to enable meaningful interpretation and comparison. Each structure's electronic behavior will be fully described at some finite plane wave cut-off energy to within a reasonable error. Therefore each structure's plane wave cut-off energy needs to be increased systematically until the free energy has converged to within a defined margin of error. The largest of all the converged plane wave cut-off energies obtained for the different structures is used as the systems' plane wave cut-off energy.

A k-point set of  $6 \times 2 \times 2$ , corresponding to a Monkhorst-Pack spacing of  $0.5 \text{ \AA}$ , was chosen to test for the convergence of the plane waves for all of the structures. The plane wave cut-off energy was systematically increased by steps of 50 eV, from 600 eV (the default "Coarse" setting in CASTEP) to 1200 eV.

The convergence criterion used in a study is typically to ensure that the comparison of any energies obtained is valid. An example of this would be to compare the energies of two magnetic states of a structure, say a ferromagnetic and anti-ferromagnetic. If the difference in energy of the FM and AFM states is smaller than the convergence criterion, comparison of the energies is not valid as the result is below the chosen margin of error, in this case the convergence criterion would have to be decreased further. If the difference in energy of the FM and AFM states is however well above the convergence criterion, the difference in energy is valid. The choice of convergence criteria is left to

the judgement of the scientist based on how accurate and quickly the calculations are to be performed.

The convergence criterion chosen for this study was:  $1 \times 10^{-5}$  eV. The normal convergence criterion for calculations of this type is 0.001 eV (Scholl and Steckel, 2009). The definition of this value is the change in free energy of successive convergence steps. In the case of plane wave cut-off energies, this step is not defined i.e. one can change the plane wave cut-off energies by 10 eV or 50 eV. As mentioned earlier, the plane wave cut-off energy step chosen in this study was 50 eV. The convergence criterion was divided by the step size of 50 eV to obtain a criterion of  $2 \times 10^{-5}$  eV. This value was then further reduced by a factor of two to as an additional measure.

The relative free energies shown in Figure 85 are obtained as follows:

$$E_{relative} = \frac{dE}{no\ of\ electrons \times dE_{cut-off}}$$

For example:

$$E_{relative} = \frac{E_{650} - E_{600}}{144 \times (650 - 600)}$$

$$E_{relative} = -5.17394E - 05$$

This means that the relative free energy is the change in free energy per electron per plane wave cut-off energy unit of 1 eV. If the value is below the  $1 \times 10^{-5}$  eV threshold, it has converged.

The results for the convergence of the plane waves for the CdCl-BA structure are shown in Figure 85.

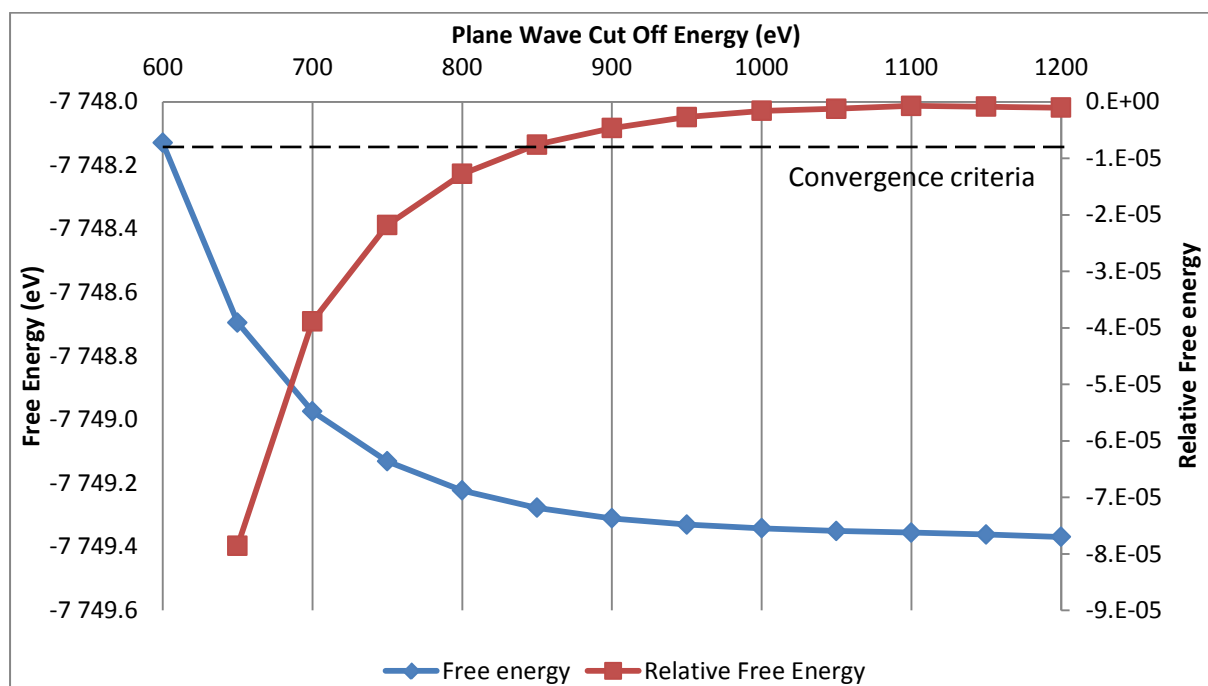


Figure 85: Plane wave cut-off energy convergence of CdCl-BA. The blue graph shows the free energy, with reference to the left axis, and the red graph illustrates the relative free energy, associated with the right axis.

The plane wave cut-off energy of CdCl-BA was converged to within  $1 \times 10^{-5}$  eV at a value of 800 eV as shown in Figure 85. Similarly the free energies of CuCl-BA, CuBr-BA, CdBr-BA converged at or below a plane wave cut-off energy 850 eV as shown in Figure 86. Therefore, a plane wave cut-off energy of 850 eV will be used for all calculations on these structures, unless stated otherwise.

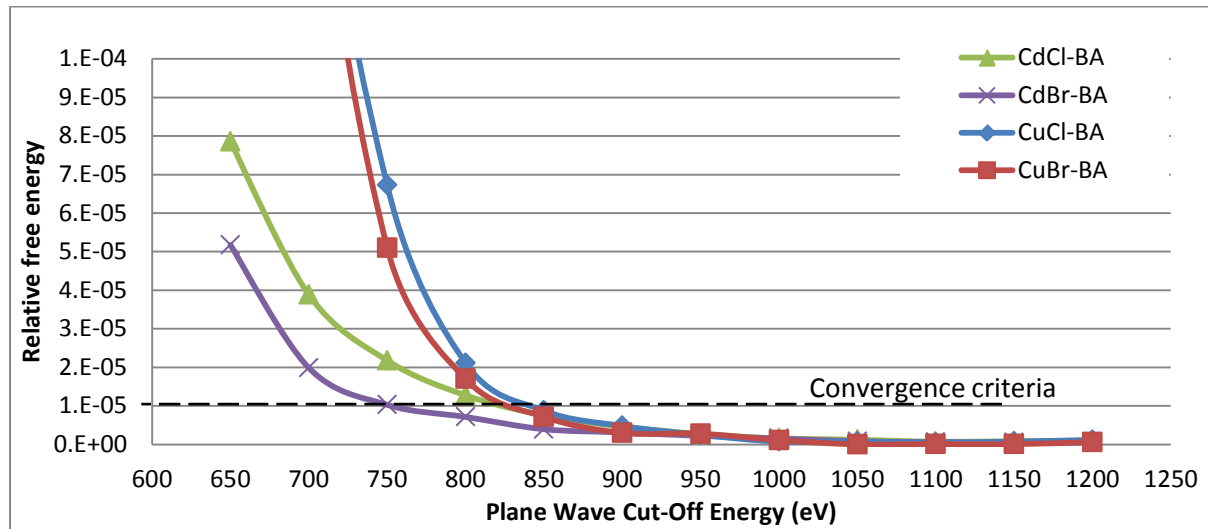


Figure 86: Plane wave cut-off energy convergence of CdCl-BA, CdBr-BA, CuCl-BA and CuBr-BA. The CuBr-BA and CuCl-BA convergence values for 650 eV and 750 eV are in the order of  $5 \times 10^{-4}$  and  $2 \times 10^{-4}$  respectively and are not shown.

## K-point convergence

The k-points in DFT are defined by:

$$\varphi_{\mathbf{k}}(\mathbf{r}) = \exp(i\mathbf{k} \cdot \mathbf{r})u_{\mathbf{k}}(\mathbf{r})$$

Where  $\exp(i\mathbf{k} \cdot \mathbf{r})$  is the plane wave basis set and  $u_{\mathbf{k}}(\mathbf{r})$  is periodic in space. This simplification of the Schrödinger solutions by Bloch's theorem leads to a solution of the Schrödinger equation for each independent k-point.

Convergence of the k-point grid is normally a trivial procedure similar to the plane wave cut-off energy discussed above. This is however only the case for cubic or orthorhombic systems where the unit cell dimensions are the same for the  $a$ ,  $b$  and  $c$  axes, or where  $a = b \neq c$ . This means that the k-point grid can be increased symmetrically for all axes simultaneously for example 1x1x1 then 2x2x2.

In the case of this study, the materials under investigation are of  $P_{-1}$  symmetry and the cell is triclinic. This means that  $a \neq b \neq c$  and  $\alpha \neq \beta \neq \gamma \neq 90^\circ$ . In order to converge the k-point grid, the number of k-points along each cell dimension has to be varied and converged independently. For a triclinic system for example, the following k-point grids need to be considered: 1x1x1, 2x1x1, 1x2x1, 1x1x2, 1x2x2, 2x2x1, 2x1x2, 2x2x2 etc. The permutations possible become very complicated and time consuming.

A plane wave cut-off energy of 850 eV, as determined previously, was used for all the k-point grid convergence tests.

In the case of the materials investigated in this study, the  $a$ -axis is normally approximately 4 Å and the  $b$  and  $c$  axes both around 10 Å. Due to the similarity of the  $b$  and  $c$  axes, they can for the purposes of this study considered as equal. This reduces the number of permutations that need to be considered.

A more elegant way by which the  $k$  points to be sampled can be defined, is obtained by using the Monkhorst-Pack (Monkhorst and Pack, 1976) method of choosing the  $k$ -point grid, so that the  $k$ -point spacing along each reciprocal axis is similar in all directions. For the structures considered here, this means that fewer  $k$ -points will be needed along the  $b$ - and  $c$ -direction (long in real space but short in reciprocal space) than for the  $a$ -direction (shorter in real space but long in reciprocal space).

The  $k$ -point grid of the CdCl-BA structure converged as shown in Figure 87.

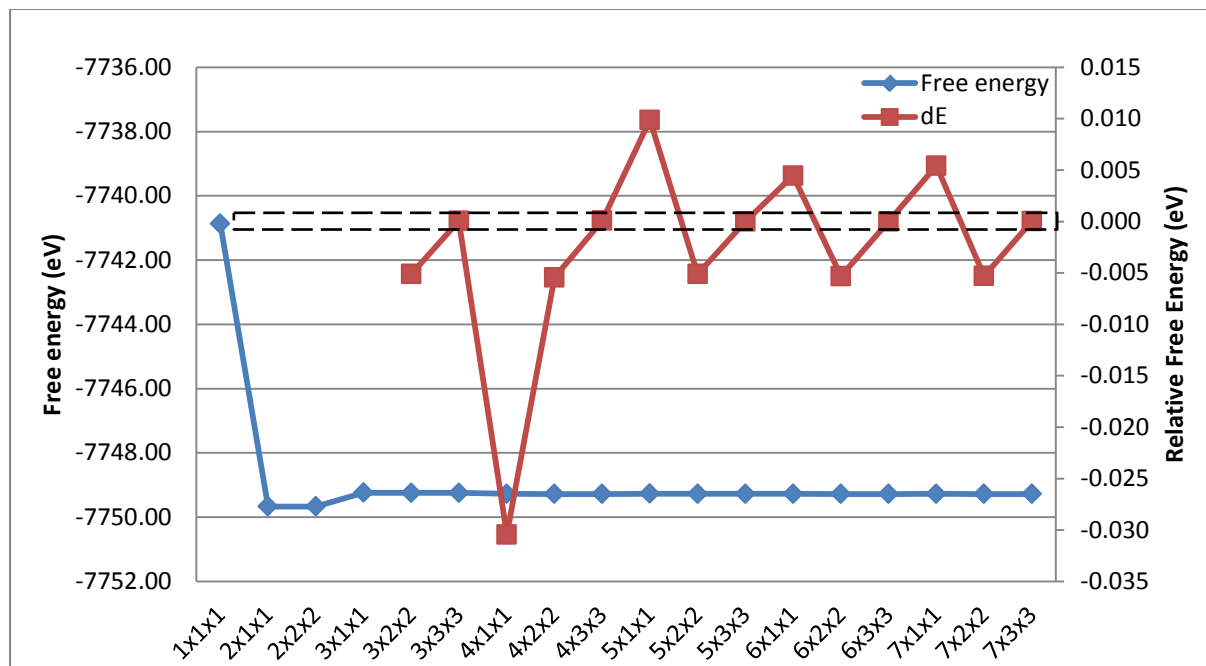


Figure 87: K-point convergence scheme of CdCl-BA. The change in free energy of 1x1x1, 2x1x1 and 2x2x2 were omitted as they were orders of magnitude larger. The blue graph shows the free energy (left axis), and the red graph the relative free energy (right axis).

It is evident from Figure 87 that the change in free energy varies much more than 0.001 eV, and do not therefore converge. It is however evident from Figure 87 that in the series of 3x2x2, 4x2x2, 5x2x2, 6x2x2 and 7x2x2 the change in energies are very small and may fall within the convergence criteria of 0.001 eV. A similar trend is observed for 3x3x3, 4x3x3, 5x3x3, 6x3x3 and 7x3x3. It is then evident that the  $k$ -points in the  $a$ -direction need to be varied independently of the  $k$ -points along the  $b$ - and  $c$ -direction and vice versa. The results of these independent convergence tests are given in Table 3 and Table 4.

**Table 32: Convergence of the k-point grid in the  $a$ -direction.**

<b>k-point grid</b>	<b>Change in energy (eV)</b>
1x1x1	
2x1x1	-8.7965
3x1x1	0.4282
4x1x1	-0.0355
5x1x1	0.0045
6x1x1	<b>-0.0006</b>
7x1x1	0.0001

As listed in Table 32, increasing the number of k-points along the  $a$ -direction leads to a convergence of free energies at 6 k-points along the  $a$ -direction. Varying the number of k-points along the  $b$ - and  $c$ -directions for a  $6 \times X \times X$  grid leads to a convergence in energies at  $6 \times 3 \times 3$  as listed in Table 33. The difference in energies between the  $6 \times 2 \times 2$  and  $6 \times 3 \times 3$  is so small, even compared to the convergence criteria of 0.001 eV, that a  $6 \times 2 \times 2$  k-point grid is more acceptable as its computational cost is approximately half that of a  $6 \times 3 \times 3$  grid. For a  $6 \times 2 \times 2$  k-point grid, the Monkhorst-Pack actual k-point spacing is approximately 0.5 Å along each axis.

**Table 33: Convergence of the k-point grid in the  $b$ - and  $c$ -direction.**

<b>k-point grid</b>	<b>Change in energy (eV)</b>
6x1x1	N/A
6x2x2	-0.005309
6x3x3	<b>0.000008</b>

## Choice of functional

Several different DFT functionals are available to computational chemists including LDA and GGA. The functionals have variable performance on different materials, therefore each functional needs to be tested in order to judge the validity of that functional as applied to the material studied. Validity in this case refers to the functional. The structures of CdBr-BA and CdCl-BA were assessed in order to validate the functional used. The crystal structures of CdBr-BA and CdCl-BA were used as input structures. The calculations were performed using the CASTEP code (Segall et al., 2005) as implemented by Materials Studio 5.5 (Accelrys Software Inc, 2010) using a plane wave cut-off energy of 850 eV and a k-point grid of  $6 \times 2 \times 2$ , which results in 12 irreducible k-points within the Brillouin zone. Norm-conserving pseudo potentials were used in all calculations throughout this study unless stated otherwise. The atomic coordinates were relaxed, and a full optimization of the structure and lattice parameters was performed with a different functional each time. Table 34 and Table 35 list the results obtained for the CdBr-BA and CdCl-BA structures.



Table 34: Functional validation for CdBr-BA

	$a$ (Å)	$b$ (Å)	$c$ (Å)	$\alpha$ (°)	$\beta$ (°)	$\gamma$ (°)	Total % error
<b>Experimental</b>	<b>3.9564</b>	<b>11.5384</b>	<b>11.6946</b>	<b>112.555</b>	<b>93.834</b>	<b>98.452</b>	
LDA	3.8887	11.2442	11.4896	114.705	93.835	97.644	
% difference	1.71	2.55	1.75	1.91	0.00	0.82	1.46
LDA+OBS	3.7447	11.0791	11.1411	115.838	90.262	97.902	
% difference	5.35	3.98	4.73	2.92	3.81	0.56	3.56
PBE	4.1422	11.9340	12.4616	108.980	98.839	99.403	
% difference	4.70	3.43	6.56	3.18	5.33	0.97	4.03
RPBE	4.2730	12.4772	12.9413	104.886	101.475	100.767	
% difference	8.00	8.14	10.66	6.81	8.14	2.35	7.35
PBESOL	4.0068	11.6585	11.8934	111.933	94.793	97.757	
% difference	1.27	1.04	1.70	0.55	1.02	0.71	<b>1.05</b>

Table 35: Functional validation for CdCl-BA

	$a$ (Å)	$b$ (Å)	$c$ (Å)	$\alpha$ (°)	$\beta$ (°)	$\gamma$ (°)	Total % error
<b>Experimental</b>	<b>3.8512</b>	<b>11.334</b>	<b>11.6292</b>	<b>112.617</b>	<b>95.091</b>	<b>98.308</b>	
LDA	3.6063	10.6816	11.2226	115.697	91.013	97.644	
% difference	6.36	5.76	3.5	2.73	4.29	0.67	3.88
LDA+OBS	3.7541	10.9531	11.4290	115.029	94.551	97.518	
% difference	2.52	3.36	1.72	2.14	0.57	0.8	1.85
PBE	4.0293	11.6517	12.0464	110.188	97.997	98.750	
% difference	4.62	2.8	3.59	2.16	3.06	0.45	2.78
RPBE	3.9152	11.3828	12.1995	110.658	98.944	99.034	
% difference	1.66	0.43	4.9	1.74	4.05	0.74	2.25
PBESOL	3.8958	11.2953	11.8271	112.012	96.286	97.914	
% difference	1.16	0.34	1.7	0.54	1.26	0.4	<b>0.9</b>

It is evident that for both the CdCl-BA and CdBr-BA structures, the PBEsol (Perdew et al., 2008) functional performs the best in terms of describing the lattice parameters. Therefore, this functional will be used primarily in this study unless stated otherwise.

## Calculated band gaps

The band gap energies were calculated using the GGA-PBESol (Perdew et al., 2008) functional employing a plane wave cut-off energy of 850 eV and a k-point grid of 6x2x2. A 0.1 eV thermal smearing of the bands was used for all calculations.

For CuCl-BA and CuBr-BA a spin polarized calculation was performed due to Cu<sup>2+</sup> ion being in a d<sup>9</sup> state. The total spin of two per unit cell was chosen as starting point. The CASTEP code optimized this spin to a ferromagnetic state with spins on the copper ions aligned in the same direction. This is the simplest model possible when considering the electronic state of the material, as an anti-ferromagnetic setup has many permutations to consider. Strictly speaking, in order to fully consider the magnetic state of a material in terms of DFT calculations each FM (ferromagnetic) and many

AFM (anti-ferromagnetic) states needs to be defined. Lattice parameters for each state needs to be optimized and the energy minima of each state needs to be determined as shown in Figure 88. This procedure of optimizing the energy of a material requires the optimization of all the lattice parameters, in the case of our materials independent optimization of the  $a$ ,  $b$ ,  $c$ ,  $\alpha$ ,  $\beta$ , and  $\gamma$  is required. In order to study the many AFM permutations possible and the significantly higher computational costs associated with these calculations, only a simple assumed FM model will be treated in this study. Future work will include a full magnetic and computational study of these molecules and others in order to elucidate the magnetic behavior of these materials.

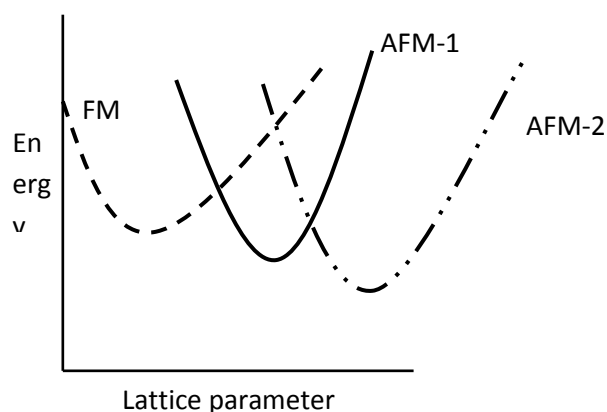


Figure 88: Determination of the true magnetic state of a material

The reader is cautioned here as different magnetic states can drastically alter the band structure and band gap energies of DFT calculations, but thorough investigation of the magnetic permutations of these structures was beyond the scope of this. This assumption of the ferromagnetic state of CuCl-BA and CuBr-BA should be kept in mind.

The calculated band gaps are listed in Table 36. Underestimation of band gap energies have been known to be a fundamental issue in solid state DFT calculations (Sham and Schluter, 1985) (Lany and Zunger, 2008) (Perdew and Levy, 1983). As a result, the band gap energies listed in Table 36 may be underestimated by anything from 10-50%. Whilst the estimation may be offset by a certain percentage, the error is expected to be relatively constant for all the materials studied therefore comparison of values is possible.

Table 36: Calculated band gap energies (GGA-PBESol, 850 eV, 6x2x2)

Species	Band gap energy (eV)
<b>CuCl-BA</b>	
$E_{g1}$	1.107
$E_{g2}$	2.96
<b>CuBr-BA</b>	
$E_{g1}$	0.904
$E_{g2}$	2.68
<b>CdCl-BA</b>	3.492
<b>CdBr-BA</b>	3.401

The calculations of the band gap energies indicate that CdBr-BA and CdCl-BA have similar calculated band gap energies of 3.401 eV and 3.492 eV respectively, and are considered to be semi-conductors

The band gap values reported in Table 36 are calculated by the Materials Studio package. The criterion for a band gap in Materials Studio is defined as the energy difference between the highest filled band (valence band) and the lowest unoccupied band (conduction band). It therefore is unable to calculate the secondary band gaps  $E_{g2}$  in Table 36. These values were calculated from the highest point in the Valence band to the lowest point in the second conduction band.

The CuCl-BA and CuBr-BA band gap energies are much lower with band gap energies of 1.107 eV and 0.904 eV respectively, indicating semi-conductive properties. The CuCl-BA and CuBr-BA structures have secondary band gap energy values of 2.96 eV and 2.68 eV respectively. Possible origins of these band gaps may be due to one of the following reasons:

Firstly, it may simply be that the higher calculated band gap energies of the copper containing compounds reflect the true band gap energy value (keeping the above mentioned underestimation in mind). Secondly it may be due to the utter failure of the DFT theory in calculating the band gap energy. Zunger & Lany (2008) suggests due to strong interactions between copper atoms and other atoms the band gap is sometimes underestimated to the point where the theory predicts a conductor whilst experimental values suggest insulators. They suggest *“introducing Hubbard-type interactions into LDA via an adjustable Coulomb parameter U.”* a formalism known as LDA+U to improve the estimation of the band gap energies. They state that: *“By applying LDA+U on the Cu d shell, the self interaction within the d shell is approximately corrected, thereby lowering the d-band energy and opening the band gap”*. The copper structures studied here seem to behave in a similar manner to what they found. The LDA+U method however is empirical. Addition of U potentials is often optimized to reproduce the experimental band gap. With this method the predictive capacity of DFT band gap energies are nullified, however, the electronic structure of the material studied may still be valid. Application of a Hubbard potential may assess whether the origin of the dual-band gap semi-conductive behavior of the copper containing structures are due to theoretical flaws.

The results of the calculations of the band gap of CuBr-BA using the LDA+U functional are listed in Table 37.

**Table 37: Effect of the addition of the Hubbard potential (U) on calculated band gap energies of CuBr-BA.**

Hubbard potential-U (eV)	Band gap energy (eV)	
	$E_{g1}$	$E_{g2}$
0	0.904	2.68
3	0.918	2.76
5	0.874	2.79
7	0.798	2.80
11	0.615	2.81

The addition of a Hubbard potential to the band gap energy calculation decreases the estimated band gap from 0.904 eV to 0.615 eV. The secondary band gap is increased from 2.67 eV to 2.81 eV. Typically the addition of the Hubbard potential is used to improve the underestimation of the band gaps. In this case it lowers the primary band gap even further, increasing the underestimation the

band gap energy, and increases the overestimation of the band gap energies from the experimentally obtained value of 2.37 eV.

The primary band migrating downward and lowering the band gap is actually the  $\beta$ -orbital of the HOMO  $\alpha$ -orbital which is a hybridized copper-2d and Cl/Br2p/3p orbital. An  $\alpha$ -orbital and  $\beta$ -orbital merely refer to a spin dependent orbital. The assignment of spin (up or down) to  $\alpha$  or  $\beta$  is arbitrary. If for example an  $\alpha$ -orbital is chosen to represent spin up, then by definition  $\beta$ -orbital would represent spin down.

As there was no improvement in the underestimation or overestimation of the band gap energies with the addition of the Hubbard potential, this calculation was limited to CuBr-BA. The increased underestimation of the primary and overestimation of the secondary band gap energies with the addition of the Hubbard potential indicates that the theoretical model used in the calculation of the band gap energies listed in Table 36 is more applicable to this system than the Hubbard potential corrected model.

B3LYP is a hybrid density functional that has been employed to accurately determine band gap energies (Perger, 2003) for molecular crystals. This hybrid functional however comes at a great computational cost and is not viable for use as the main functional in this study. However as a test of its performance, calculation of the band gap energy of CdCl-BA and CdBr-BA with the B3LYP (Becke, 1993) functional yielded a band gap energy of 4.764 eV and 4.866 eV respectively which overestimates the band gap by more than 0.5 eV (experimental: 4.25 eV, 4.19 eV respectively). Due to the computational cost of B3LYP a k-point grid of only 3x1x1 and plane wave cut-off energy of only 600 eV could be used. Increasing the k-point grid and planewave basis set may improve the estimation of the band gap, but this overestimation is more likely due to strong correlations (metal to metal interactions etc.) in the studied materials as opposed to the relatively weak interactions of the molecular crystals for which Perger proved its efficiency.

The only improvement remaining to the estimation of band gap energies is the use of the *sx*-LDA approximation (Seidl et al., 1996). This is a non-local exchange approximation and is an extremely costly computational tool. Due to the low symmetry in the studied systems, and the large unit cells, use of this approximation is not within the scope of this study.

The calculated band gaps listed in Table 36 are therefore accepted as the best description of the electronic structure of the isostructural compounds with the resources available.

The calculated band gap values will be compared with the experimental band gap values in Chapter Five.

To determine the effect of the specific functional chosen on the value obtained for the calculated band gap energy, CdBr-BA was selected as a test compound, and the band gap of this material was calculated employing a range of different functionals, with the results listed in Table 38.

**Table 38: Comparison of different functionals for CdBr-BA**

<b>Functional/corrections</b>	<b>Band Gap Energies (eV)</b>
Experimental	4.19
LDA <sup>1</sup>	3.426
PBE <sup>2</sup>	3.505
PW91 <sup>3</sup>	3.486
LDA+OBS <sup>4</sup>	3.426
PBE+TS	3.505
PW91+OBS	3.500
PBESol <sup>5</sup>	3.500
B3LYP <sup>6</sup>	4.866

<sup>1</sup> (Perdew et al., 1992)

<sup>2</sup> (Perdew, Burke and Ernzerhof, 1996)

<sup>3</sup> (Perdew and Zunger, 1981)

<sup>4</sup> *OBS* (Ortmann, Bechstedt and Schmidt, 2006) and *TS* (Tkatchenko and Scheffler, 2009) refer to dispersion corrections to the appropriate functional.

<sup>5</sup> (Perdew et al., 2008)

<sup>6</sup> (Becke, 1993)

The LDA functional underestimates the band gap energies by the most while the PBE +TS correction underestimates the band gap by the least amount. The calculated LDA band gap energies result in a band gap estimation of approximately 3.4 eV while the calculated GGA band gap estimation irrespective of the different dispersion corrections or functional implementations result in a band gap energy of approximately 3.5 eV for CdBr-BA. The B3LYP functional estimates the band gap energy significantly higher, and as mentioned earlier B3LYP overestimates the band gap energy. The dispersion corrections to the PBESol only improves the underestimation of the band gap energy by 0.005 eV which is insignificant as the experimental band gaps can only be accurately measured to one decimal as they are estimated from the Tauc plots in Chapter Three.

Despite known problems associated with the estimation of the band gap using the LDA and GGA functionals, the band structures and density of states may still provide useful insight into the electronic structures of the systems studied here.

## Calculated band structures

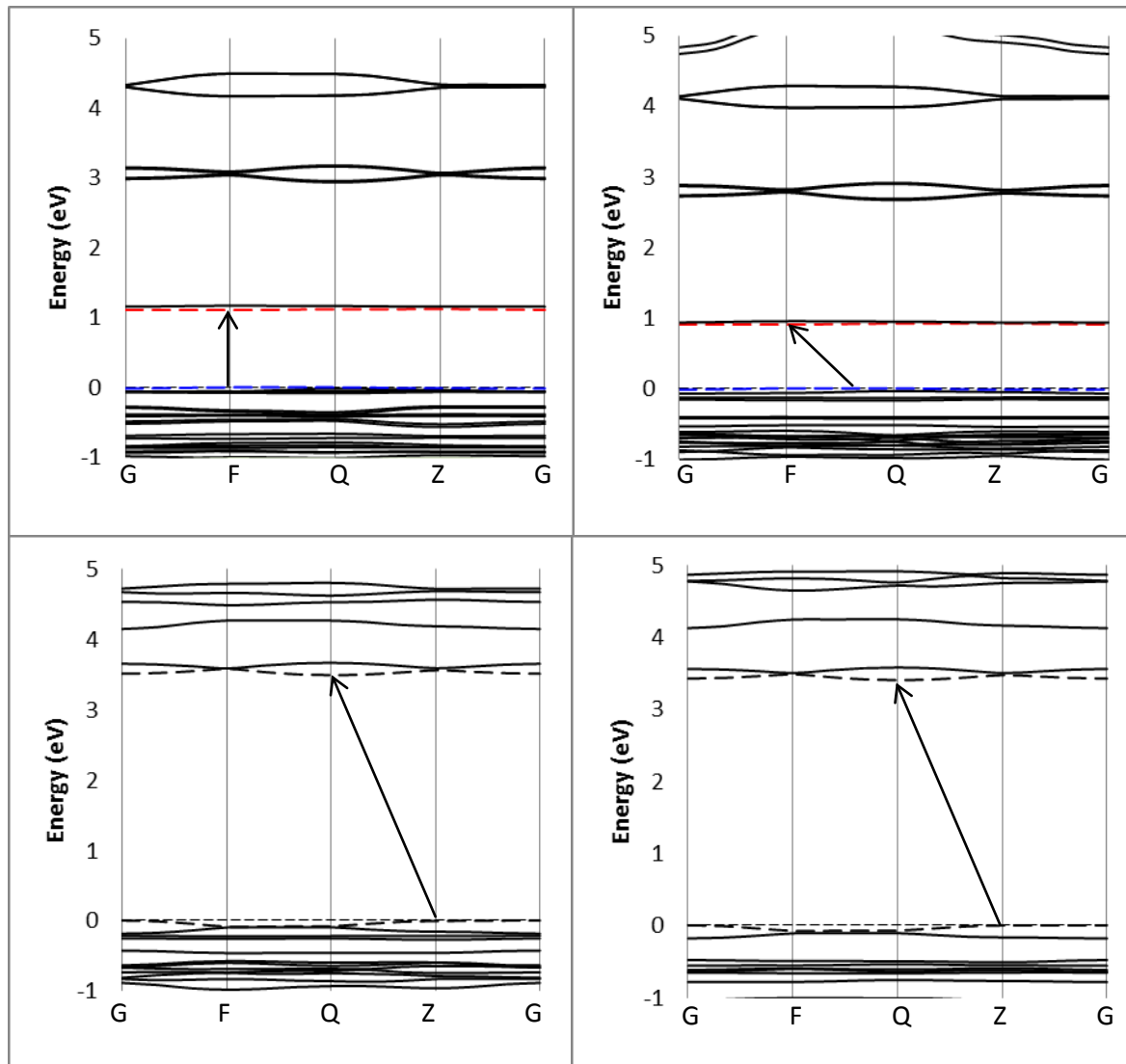


Figure 89: Calculated band structures of CuCl-BA (top left) CuBr-BA (top right) CdCl-BA (bottom left) and CdBr-BA (bottom right). Arrows indicates the transitions from valence band to conduction band. The red band indicates a  $\beta$ -orbital whilst a blue band indicated an  $\alpha$ -orbital

The calculated band structures of CuBr-BA, CdCl-BA and CdBr-BA suggest that these structures have indirect band gaps as an electron cannot be excited from the valence band to the conduction band along the same vector, while the CuCl-BA has a direct band gap as excitation can occur within the same special k-point.  $\alpha$ - and  $\beta$ -orbitals are commonly referred to as the spin up or down orbitals of a spin polarized calculation. The assignment of spin up or down to  $\alpha$  and  $\beta$ -orbitals is arbitrary.

CuCl-BA and CuBr-BA have interesting band structures. Firstly a band gap of approximately 1 eV is observed for both structures. These conduction bands only consist of two discrete bands. Secondly, 2 eV above these conduction bands, there is a second set of conduction bands. This may indicate that there are two band gaps for the copper containing compounds. One band gap of approximately 1 eV, where an electronic transition between the valence band and the lower conduction band occurs; and a second band gap of approximately 3 eV, where the transition occurs from the valence band to the second conduction band. Inspection of the DOS of the copper containing structures will be discussed again later.

## Density of States

### Cadmium containing compounds

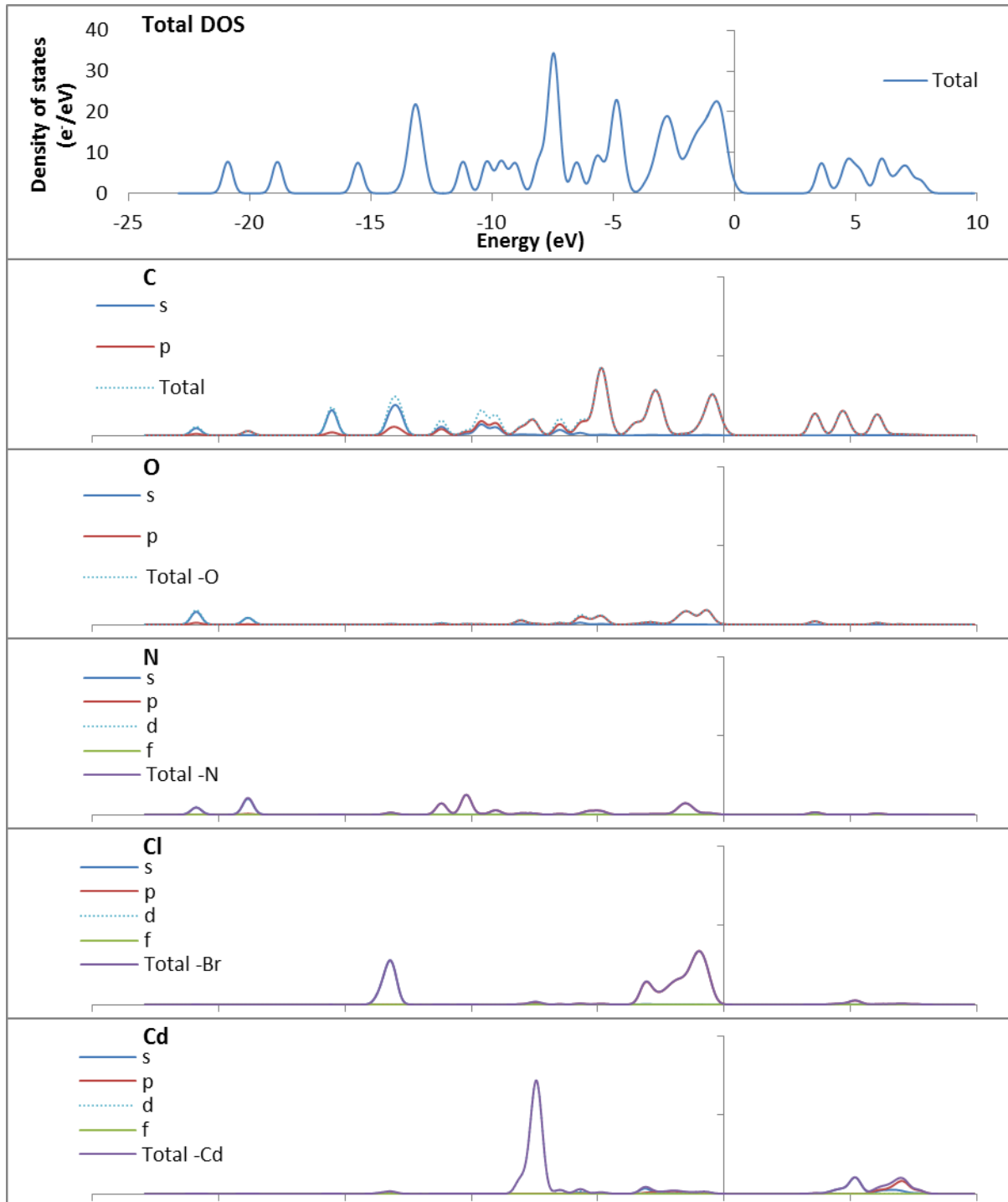


Figure 90: Total and Partial DOS of CdCl-BA. Note all of the DOS are shown to the same scale.

The Fermi levels of all DOS have been set to 0 eV. The calculated total and partial density of states of CdCl-BA are shown in Figure 90. The results suggest that the cadmium atoms' orbitals are limited to the filled 3d orbitals at -8 eV and empty 4s and 4p orbitals 4 eV above the Fermi level. The upper edge of the valence band (HOMO) is mostly comprised of the aromatic C-2p orbitals, O-2p orbitals



and Cl-2p orbitals. The lower edge of the conduction band (LUMO) is mainly comprised of a mixture of O-p, N-p and C(carbonyl)-p and C(aromatic)-p orbitals. The combination of these unfilled orbitals hybridize to form the  $\pi^*$  orbitals as shown in Figure 92. A (\*) denotation here represents an anti-bonding orbital. The “orbitals” referred to in this work are strictly speaking bands comprised of orbitals, but orbitals are a more familiar notation for chemists and will be used broadly to refer to bands.

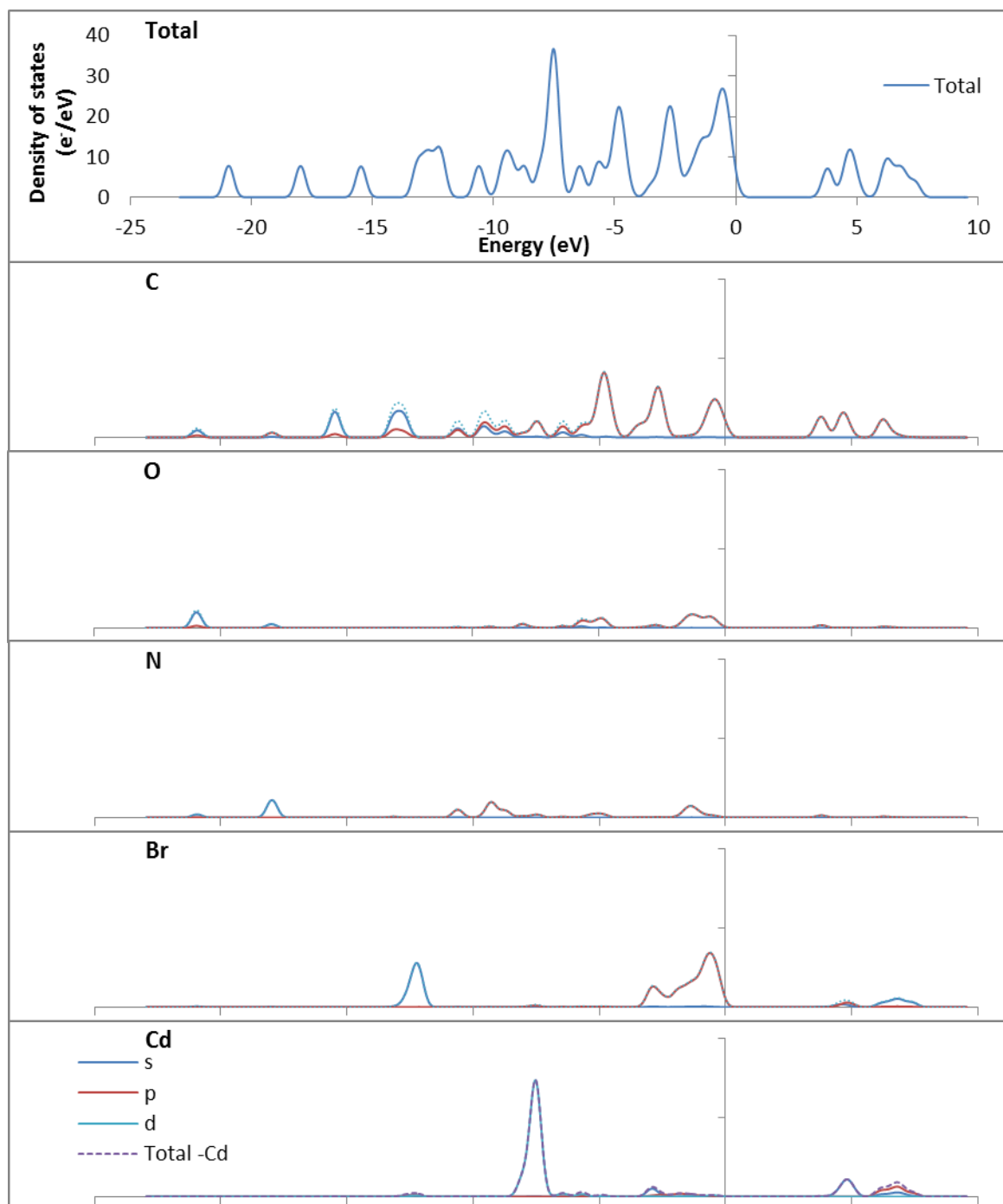


Figure 91: Total and partial DOS of CdBr-BA. Note all of the DOS are shown to the same scale.

The calculated total and partial density of states of CdBr-BA are shown in Figure 91. Similarly to CdCl-BA, the cadmium 3d orbitals are located at at -8 eV and empty 4s and 4p orbitals 4 eV above the Fermi level. The upper edge of the valence band (HOMO) is mostly comprised of the aromatic C-2p orbitals, O-2p orbitals and Cl-2p orbitals. The lower edge of the conduction band (LUMO) is mainly formed by mixture of O-p, N-p and C(carbonyl)-p and C(aromatic)-p orbitals. The combination of these unfilled orbitals hybridize to form the aromatic delocalized  $\pi^*$  orbital system as shown in Figure 92.

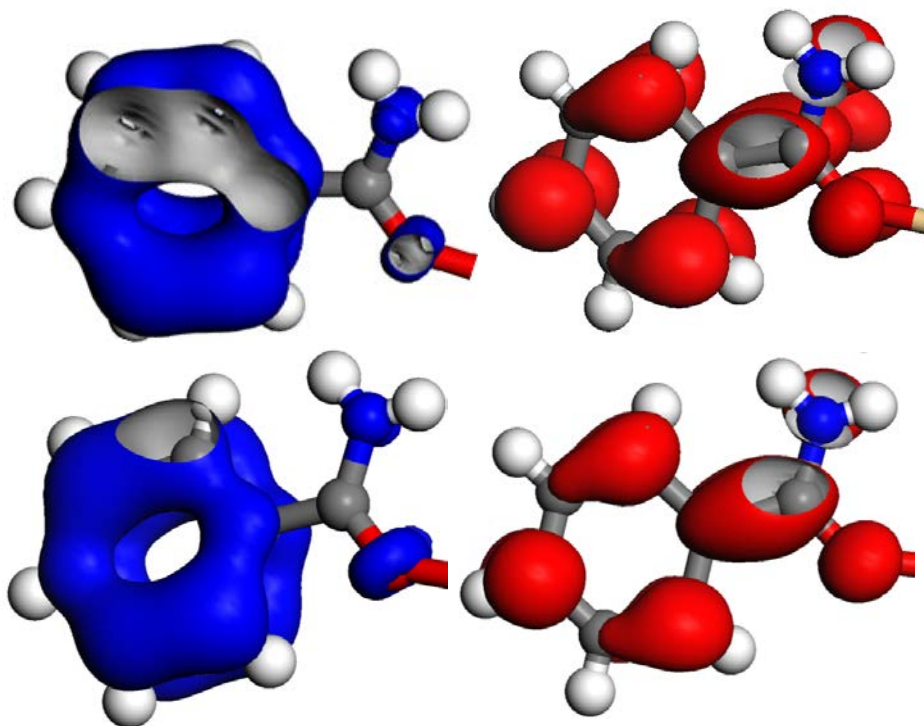


Figure 92: Aromatic- $\pi$  HOMO (left) and Aromatic- $\pi^*$  LUMO orbitals (right) of CdCl-BA (top) and CdBr-BA (bottom). All orbitals are drawn at an iso-value of 0.01.

In the orbital diagrams for both CdCl-BA and CdBr-BA, the top of the valence band is occupied by the filled delocalized  $\pi$ -orbitals of the aromatic ring and the amide group and the bottom of the conduction band by the  $\pi$ -antibonding orbital of the aromatic system.

Therefore an electronic transition from the valence to the conduction band would then involve the excitation of an electron in the aromatic  $\pi$ -system, into the aromatic  $\pi^*$ -system of the same ring. This may be the reason the band-gap is so wide, and more akin to organic semiconductors.

The calculated band gap values of 3.492 eV and 3.401 eV for CdCl-BA and CdBr-BA respectively, suggest that both of the materials are semi-conductors. In the band gap structure of these materials, the states that have a large contribution from the metal ion lie at energy levels much lower than the Fermi level. This means that the metal halide portion of the structure does not exhibit electronically conducting or semi-conducting behavior.

## Copper containing compounds

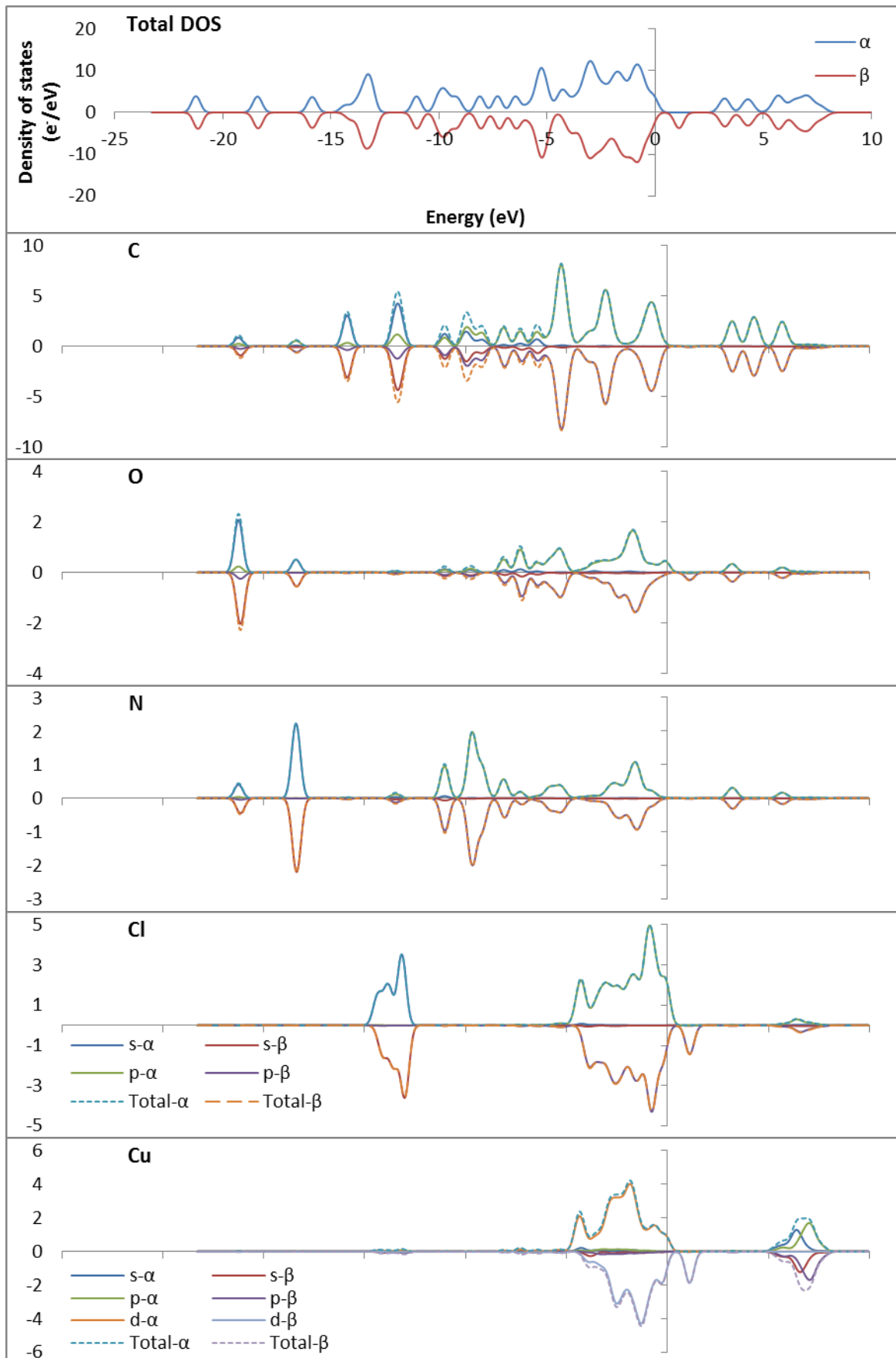


Figure 93: Total and partial DOS of CuCl-BA. Note that the DOS are not all to the same scale for clarity.

The total and partial density of states of CuCl-BA is shown in Figure 93. The DOS shown in Figure 93 is spin polarized, with  $\alpha$ -spin shown as positive (positive sign on DOS) and  $\beta$ -spin shown as negative. Orbitals with high spin will then therefore be identified by a large unsymmetrical peak, for example the copper d orbital shown in Figure 93. The partially filled copper-3d orbitals are located close to the Fermi level. The valence band upper edge (HOMO) is a mixture of a partially filled copper-3d orbital, O-2p and Cl-2p\* orbital. The HOMO (blue) orbital is an  $\alpha$ -spin and the LUMO is a  $\beta$ -spin orbital (red) as shown in. The valence band lower edge (LUMO) is a mixture of essentially the same orbitals with the only difference the orientation the chlorido-2p\* orbital.

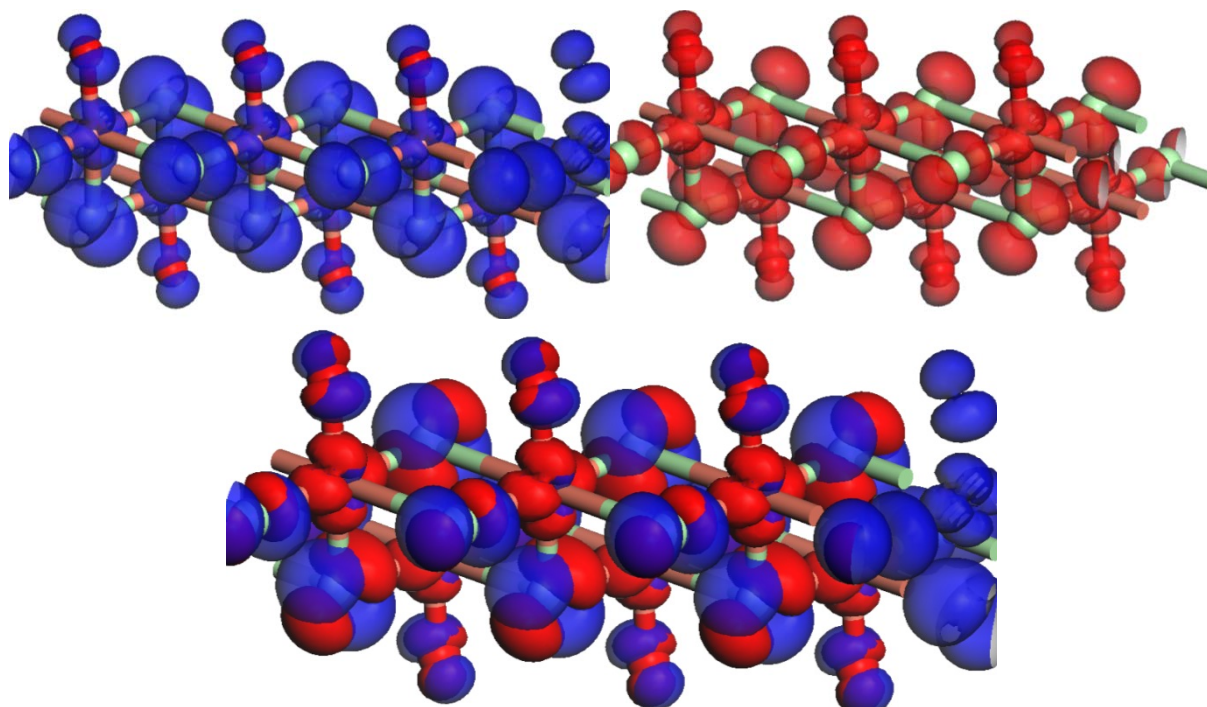


Figure 94: The HOMO; alpha spin (top left), LUMO; beta spin (top right) and combined HOMO/LUMO orbitals of CuBr-BA. The HOMO and LUMO orbitals shown differ by the band gap quoted in Table 36. All orbitals were drawn at an iso-value of 0.01

The total and partial density of states of CuBr-BA are illustrated Figure 95. Similar to what was observed for CuCl-BA compound, the partially filled copper-3d orbitals are located close to the Fermi level, and the valence band upper edge (HOMO) is a mixture of a partially filled copper-3d orbital, O-2p and Cl-2p\* orbital. The HOMO (blue) orbital is an  $\alpha$ -spin and the LUMO is a  $\beta$ -spin orbital (red) as shown in Figure 96. The valence band lower edge (LUMO) is a mixture of essentially the same orbitals, but in this case the orientation of the chlorido-2p\* orbital differs.

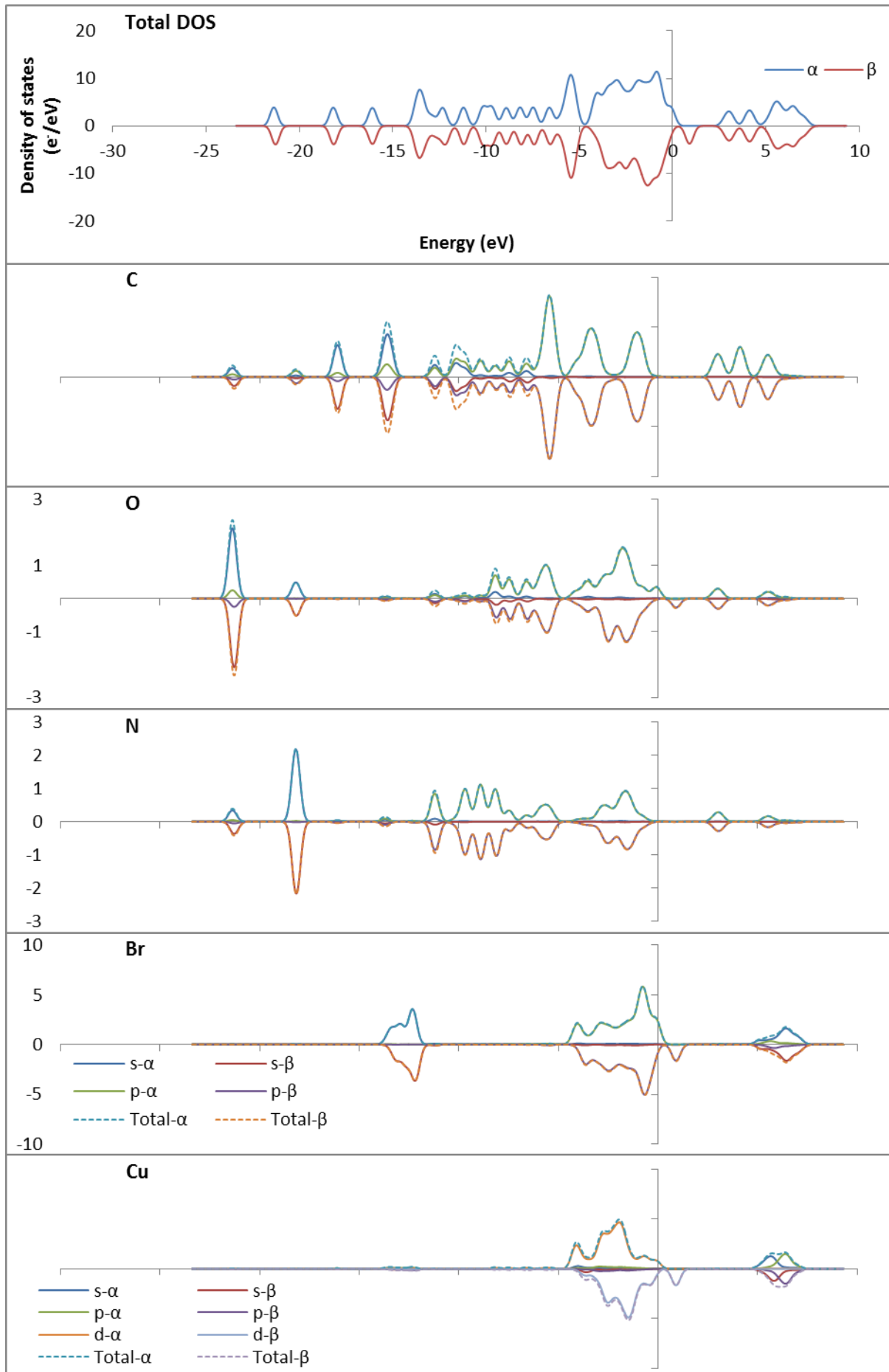


Figure 95: Total and partial DOS of CuBr-BA. Note that the DOS are not all to the same scale for clarity.



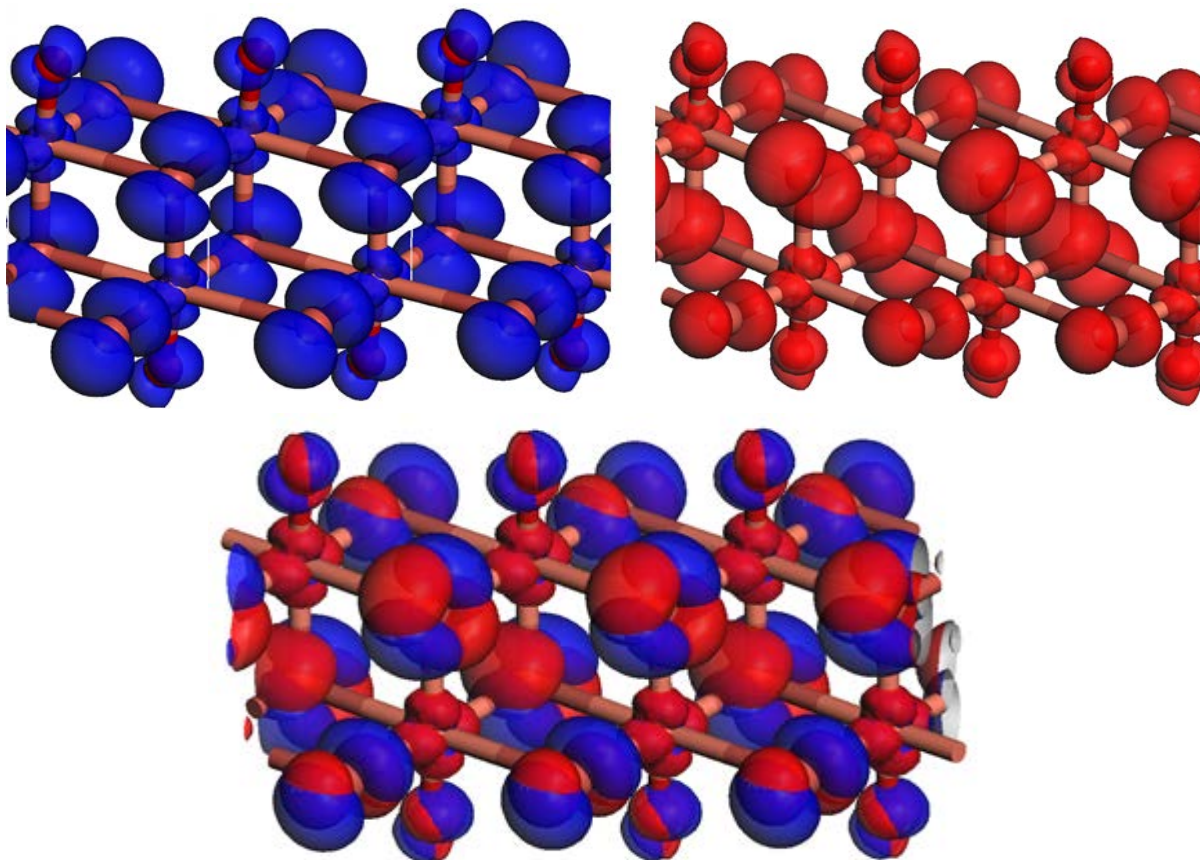


Figure 96: The HOMO alpha spin (top left), LUMO beta spin (top right) and combined HOMO/LUMO orbitals of CuBr-BA. The HOMO and LUMO orbitals shown differ by the band gap quoted in Table 36. All orbitals were drawn at an iso-value of 0.01

In both the CuCl-BA and the CuBr-BA compounds, the states with a large weight in the metal ions and the chlorido or bromido ligands are close to the Fermi level. This is important in terms of the electronic properties of the material, since this would result in an electronic conduction pathway that extends along the metal halide portion of the structure, and supports the calculated band gap values that suggests that these compounds are electronic conductors.

In both the CuCl-BA and CuBr-BA structures the excitation of an electron will therefore occur from the partially filled  $\alpha$ -orbital (HOMO) into the similar  $\beta$ -orbital. Excitation of the electron is therefore limited to the inorganic polymer. This excitation is spin forbidden, i.e. if this transition occurs, then the electron must change its spin to the opposite sign. Therefore, it is unlikely that this transition will occur. Another possibility may be that the transition occurs from a  $\beta$ -orbital slightly below the HOMO level to the LUMO mentioned earlier. Confirmation of this theory however is beyond the scope of this study.

Inspection of the DOS for both CuCl-BA and CuBr-BA indicate that there is one band gap of approximately 1 eV as shown above, but there are several carbon 2p, oxygen 2p and nitrogen 2p bands at approximately 3 eV. This is a second possible band gap, as an electronic transition from the metal halide  $\alpha$ -orbital to the organic ligand's hybridized orbitals is possible. Inspection of the lowest unoccupied band at approximately 3 eV reveals that the hybridized organic orbitals are the anti-bonding orbitals of the organic ligand as shown in Figure 97 and 98. This matter is further discussed in Chapter Five.

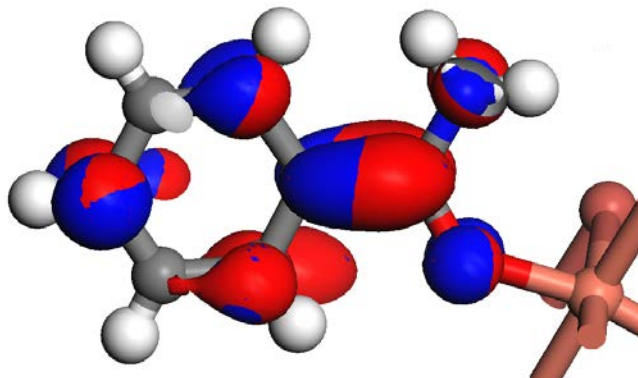


Figure 97: Upper conduction band orbitals of CuBr-BA. The  $\alpha$ -orbitals are shown in blue and the  $\beta$ -orbitals are shown in red.

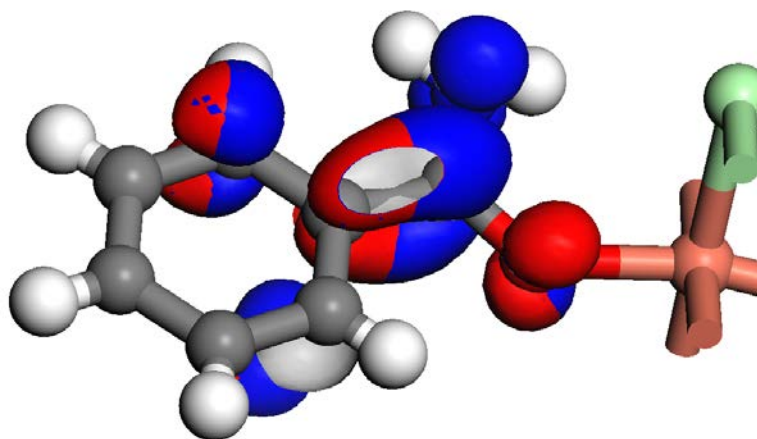


Figure 98: Upper conduction band orbitals of CuCl-BA. The  $\alpha$ -orbitals are shown in blue and the  $\beta$ -orbitals are shown in red.

The summary of results for the band gap estimation of the isostructural compounds are listed in Table 39.

Table 39: Summary of calculated band gap energies (GGA-PBESol, 850 eV, 6x2x2)

Species	Band gap energy (eV)
<b>CuCl-BA</b>	
$E_{g1}$	1.107
$E_{g2}$	2.96
<b>CuBr-BA</b>	
$E_{g1}$	0.904
$E_{g2}$	2.68
<b>CdCl-BA</b>	3.492
<b>CdBr-BA</b>	3.401



## Bibliography

- Accelrys Software Inc (2010) 'Materials Studio Release Notes, Release 5.5', San Diego: Accelrys Software Inc.
- Becke, A.D. (1993) 'Density-functional thermochemistry. III. The role of exact exchange', *J. Chem. Phys.*, vol. 98, pp. 5648-5652.
- Lany, S. and Zunger, A. (2008) 'Assessment of correction methods for the band-gap problem and for finite-size effects in', *Phys. Rev. B*, vol. 235104, pp. 1-25.
- Monkhorst, H.J. and Pack, J.D. (1976) 'Special points for Brillouin-zone integrations', *Phys. Rev. B*, p. 5188-5192.
- Ortmann, F., Bechstedt, F. and Schmidt, W.G. (2006) 'Semiempirical van der Waals correction to the density functional description of solids and molecular structures', *Phys. Rev. B*, vol. 73, p. 205101.
- Perdew, J.P., Burke, K. and Ernzerhof, M. (1996) 'Generalized Gradient Approximation made simple', *Phys. Rev. Lett.*, vol. 77, pp. 3865-3868.
- Perdew, J.P., Chevary, J.A., Vosko, S.H., Jackson, K.A., Pederson, M.R., Singh, D.J. and Fiolhais, C. (1992) 'Atoms, molecules, solids, and surfaces: Applications of the generalized gradient approximation for exchange and correlation', *Phys. Rev. B*, vol. 46, pp. 6671-6687.
- Perdew, J.P. and Levy, M. (1983) 'Physical content of the exact Kohn-Sham orbital energies: band gaps and derivative discontinuities', *Phys. Rev. Lett.*, pp. 51, 20: 1884-1887.
- Perdew, J.P., Ruzsinszky, A., Csonka, G.I., Vydrov, O.A., Scuseria, G.E., Constantin, L.A., Zhou, X. and Burke, K. (2008) 'Restoring the density-gradient expansion for exchange in solids and surfaces', *Phys. Rev. Lett.*, vol. 100, p. 136406.
- Perdew, J.P. and Zunger, A. (1981) 'Self-interaction correction to density-functional approximations for many-electron systems', *Phys. Rev. B*, vol. 23, pp. 5048-5079.
- Perger, W.F. (2003) 'Calculation of band gaps in molecular crystals using hybrid functional theory', *Chem. Phys. Lett.*, pp. 319-323.
- Scholl, D.S. and Steckel, J.A. (2009) 'Density functional theory: A practical introduction', 1<sup>st</sup> edition, New Jersey: John Wiley & Sons.
- Segall, M., Probert, M., Pickard, C., Hasnip, P., Clark, S., Refson, K. and Payne, M. (2005) 'First principles methods using CASTEP', *Z. Kristallogr.*, vol. 220, no. 5-6, pp. 567-570.
- Seidl, A., Gorling, A., Vogl, P., Majewski, J.A. and Levy, M. (1996) 'Generalized Kohn-Sham schemes and the band-gap problem', *Phys. Rev. B*, vol. 53, pp. 3764-3774.
- Sham, L.J. and Schluter, M. (1985) 'Density-functional theory of the band gap', *Phys. Rev. B*, pp. 3883-3889.
- Tkatchenko, A. and Scheffler, M. (2009) 'Accurate molecular van der Waals interactions from ground-state electron density and free-atom reference data', *Phys. Rev. Lett.*, vol. 102, p. 073005.

# Chapter Five - Discussion

This chapter aims to combine the results reported in the previous Chapters, in order to gain insight into the structural aspects of the materials under investigation. Some of the comparisons are carried out over all the structures, but others are limited to the comparison of the isostructural family of compounds.

In addition the properties of the isostructural series of compounds are compared, specifically in terms of their experimentally measured band gap. These results are further compared to the calculated band gap values obtained via DFT calculations.

## Structural Comparison

### Comparison of all Crystal Structures:

#### Stoichiometry

It was found that the organic and inorganic building blocks did not always combine in the ratio used during the synthetic procedure as indicated in Table 40.

Table 40: Comparison of synthetic molar ratios and experimental molar ratios.

Compound	Chemical Formula	Synthetic Ratio Employed		Ratio observed in crystal structure	
		Organic	Inorganic (MX <sub>2</sub> )	Organic	Inorganic (MX <sub>2</sub> )
CuCl-BA	[C <sub>7</sub> H <sub>7</sub> NOCuCl <sub>2</sub> ] <sub>n</sub>	1	1	1	1
CuBr-BA	[C <sub>7</sub> H <sub>7</sub> NOCuBr <sub>2</sub> ] <sub>n</sub>	1	1	1	1
CdCl-BA	[C <sub>7</sub> H <sub>7</sub> NOCdCl <sub>2</sub> ] <sub>n</sub>	1	1	1	1
CdBr-BA	[C <sub>7</sub> H <sub>7</sub> NOCdBr <sub>2</sub> ] <sub>n</sub>	1	1	1	1
ZnCl-BA	(C <sub>7</sub> H <sub>7</sub> NO) <sub>2</sub> ZnCl <sub>2</sub>	3	1	2	1
CuBr-4ABA	(C <sub>7</sub> H <sub>8</sub> N <sub>2</sub> O) <sub>2</sub> CuBr <sub>2</sub> ·H <sub>2</sub> O	2	1	2	1
CoCl-4ABA	(C <sub>7</sub> H <sub>7</sub> NO) <sub>4</sub> CoBr <sub>2</sub>	1	1	4	1
HgBr-BA (ionic)	(C <sub>7</sub> H <sub>8</sub> NO <sup>+</sup> ) <sub>2</sub> (C <sub>7</sub> H <sub>7</sub> NO) <sub>2</sub> [Hg <sub>3</sub> Br <sub>8</sub> <sup>2-</sup> ] <sub>n</sub>	5	1	2	1.5

The molar ratio used in the synthetic procedure did not always yield the same molar ratio observed in the crystal structure. It may be due to kinetic effects that more than one ligand is coordinated, or it may be that it is thermodynamically more stable to include a certain number of molecules into a crystal structure, in a specific fashion.

#### Structural Dimensionality

The neutral coordination compounds CuCl-BA, CuBr-BA, CdCl-BA and CdBr-BA as well as the ionic compound HgBr-BA display one-dimensional coordination structures, with the coordination polymer forming as a result of the bridging of metal atoms via halogeno ligand atoms. The rest of the

structures, ZnCl-BA, CuBr-4ABA and CoCl-4ABA form isolated, zero-dimensional coordination compounds. This is expected for ZnCl-BA, since the bridging of zinc ions via halogeno ligands does not readily occur.

## Geometry of organic component

### Benzamide

It was found that in all the structures the amide group are tilted relative to the aromatic group. Table 41 lists the angle formed between the plane through the amide and aromatic groups:

**Table 41: Comparison of amide group rotation relative to aromatic ring for benzamide containing structures**

Structure	Angle between aromatic ring plane and amide plane (°)
MnBr-BA	22.01(9)
CuCl-BA	4.3(5)
CuBr-BA	6.3(7)
CdCl-BA	1.9(2)
CdBr-BA	1.9(5)
ZnCl-BA	
Molecule 1	
BA1	2.7(8)
BA2	21.9(3)
Molecule 2	
BA1	5(2)
BA2	14.5(5)
HgBr-BA (ionic)	
BA1	6.8(8)
BA2	7.0 (5)

The largest angles between the amide group and aromatic group is observed for the benzamide ligand in the MnBr-BA structure, and for two of the benzamide ligands coordinated to each of the molecules in the asymmetric unit of the ZnCl-BA structure, with both of the ligands displaying angles of approximately 22° and one showing an angle of close to 14°. Both of these molecules are isolated, and their NH<sub>2</sub> groups form intra- and intermolecular hydrogen bonding interactions. A possible reason for the large observed angles between the two planes is fact that the aromatic group “bends away” from the amide group, to allow the amide group to participate in these hydrogen bonding interactions. For the rest of the amide ligands, this angle ranges from approximately 2° to 7°, and these values are slightly smaller compared to the angle range of 16-21° reported by crystallographic studies (Penfold and White, 1959) (Blake and Small, 1972) (Blagden et al., 2005), neutron diffraction data (Gao et al., 1991) and gas phase electron diffraction with supportive molecular modelling (Takeuchi et al., 1999).

#### 4-Aminobenzamide

The M-N-C angles for the 4-aminobenzamide structures are listed in Table 42. There is a slight deviation of the nitrogen atoms' tetrahedral angle compared to the ideal 109.5°. This is most likely due to the influence of non-covalent interactions causing a change in geometry of the molecule.

**Table 42: Comparison of M-N-C angles of the coordinated amine group in the 4-aminobenzamide containing structures**

Structure	Angle definition	Angle (°)
CoBr-4ABA	Co1-N1-C5	118.6(1)
CuBr-4ABA	Cu1-N1-C5	123.4(4)
	Cu1-N1'-C5'	121.0(4)

The amide groups' rotation relative to the aromatic 4-aminobenzamide rings of the 4-aminobenzamide structures are listed in Table 43.

**Table 43: Comparison of amide group rotation relative to aromatic ring for the 4-aminobenzamide containing structures**

Structure	Angle between aromatic ring plane and amide plane (°)
CoBr-4ABA	2.18 (0.13)
CuBr-4ABA	
4ABA1	14.34 (0.35)
4ABA2	18.63 (0.36)

In the case of the CoBr-4ABA structure, the 4-aminobenzamide ligands adopt an approximately planar geometry. However, in the CuBr-4ABA structure, the plane of the amide group is tilted relative to that of the aromatic group. This difference is most probably due to the different type of hydrogen bonding interactions present in these two structures.

#### Comparison of benzamide C-O bond distances

An increase in bond length of the C-O bond occurs in carbonyl ligands on coordination, due to the redistribution of charge. This is firstly due to the extraction of electron density from the C-O bond to form the  $\sigma$ -bond to the metal. Additionally, weak backbonding on the metal occurs, further strengthening the M-O bond, and weakening the C-O bond. This back donation of the metal is termed "pi-backbonding" and is a transfer from the metal d-orbitals to the ligand's  $\pi$ -anti-bonding orbitals. This phenomena is common to metal carbonyls. (Cotton, Wilkinson and Gaus, 1976)

Due to the fact that the benzamide molecule also coordinates through a C=O bond, the C-O bond lengths of the coordinated benzamide molecules were compared with the corresponding bond length in a free benzamide molecule to determine if a similar change in C-O bond length occurs on coordination of the benzamide molecule.

The C-O bond distances of the coordinated amide groups are listed in Table 44 and remain relatively constant and unchanged when compared to same bond in the free benzamide molecule. This may

indicate that the metal does not significantly weaken the C-O and C-N bonds but speculation on the electron withdrawing effect of the metal from the ligand is beyond the scope of this investigation.

**Table 44: Comparison of the C-O bond lengths for the amide group of the benzamide containing structures.**

Structure	Bond distance C-O (amide) (Å)
BA*	1.246(1)
MnBr-BA	1.259(2)
CuCl-BA	1.260(3)
CuBr-BA	1.254(9)
CdCl-BA	1.249(5)
CdBr-BA	1.22(1)
ZnCl-BA	
Molecule 1	
BA1	1.23(2)
BA2	1.25(1)
Molecule 2	
BA1	1.24(1)
BA2	1.25(1)
HgBr-BA (ionic)	
BA1	1.24(1)
BA2	1.24(2)

\* (Penfold and White, 1959)

### Coordination geometry

The metal ions in MnBr-BA, CdCl-BA, CdBr-BA and CoBr-4ABA have octahedral coordination geometries while CuCl-BA and CuBr-BA present Jahn-Teller effects forming tetragonal coordination geometries. ZnCl-BA is tetrahedrally coordinated and HgBr-BA has both tetrahedral and octahedral coordination geometries. CuBr-4ABA presented a trigonal bipyramidal coordination geometry. The coordination geometries of all structures are listed in Table 45.

**Table 45: Comparison of coordination geometries**

Structure	Coordination geometry
MnBr-BA	Octahedral
CuCl-BA	Tetragonal
CuBr-BA	Tetragonal
CdCl-BA	Octahedral
CdBr-BA	Octahedral
ZnCl-BA	Tetrahedral
HgBr-BA (ionic)	Tetrahedral/Octahedral
CoBr-4ABA	Octahedral
CuBr-4ABA	Trigonal bipyramidal

### Ligand Coordination Site

For the neutral coordination structures, benzamide ligand only coordinates through the oxygen atom of the amide group, and in the ionic HgBr-BA structure it was demonstrated that the protonation occurs on the oxygen atom, in agreement with the theoretical prediction of coordination and protonation site by resonance theory. For the 4ABA structures, 4-aminobenzamide coordinates through the amine group rather than the amide group. This is also in agreement with the theoretical prediction based on the 4-aminobenzamide proton affinities.

### Hydrogen bonding interactions

An analysis of the hydrogen bonding interactions present in the structures investigated indicate that hydrogen bonding interactions are important in these structures. In the neutral coordination type structures it was found that, in general, the NH<sub>2</sub> group acts as hydrogen bonding donor, while the halogeno ligands are the hydrogen bonding acceptors. In the neutral coordination compounds of benzamide studied one of the hydrogen atoms of the NH<sub>2</sub> group forms an intramolecular hydrogen bond to a halogeno ligand or an oxygen atom on the same molecule or coordination polymer, while the second hydrogen atom on the NH<sub>2</sub> group typically forms a hydrogen bond to a neighbouring molecule or polymer.

In the isostructural series CdCl-BA, CdBr-BA, CuCl-BA and CuBr-BA, a two-dimensional hydrogen bonded sheet is formed, and in the zero-dimensional structures MnBr-BA and ZnCl-BA, three-dimensional hydrogen bonding networks result from the hydrogen bonding interactions. A three-dimensional hydrogen bonded sheet is present in the structure of the zero-dimensional, coordination molecule CoBr-4ABA, while the structure of CuBr-4ABA contains an interesting, hydrogen bonded helix, with neighbouring helices further hydrogen bonded into a triple helix, and neighbouring triple helices connected via hydrogen bonding interactions to form a three-dimensional hydrogen bonding network. In the CuBr-4ABA structure, the amide groups form amide synthons with neighbouring molecules and coordinated water molecules also participate in the hydrogen bonding interactions.

### Aromatic Interactions

Janiak's definition of an aromatic interaction will be employed in this study, and a centroid-to-centroid distance of 3.5 Å to 4.6 Å will be considered to be indicative of  $\pi$ - $\pi$  interacting rings (Janiak, 2000).

### Aromatic interaction parameters

The parameters defining the aromatic interactions in the structures are listed in Table 46. Comparisons of these results indicate that the plane-to-plane distance; the distance separating the aromatic rings from one another; are very similar for all structures.

All of the structures except the HgBr-BA and MnBr-BA structures have centroid-to-centroid distances within the range specified above. The MnBr-BA structure does not display any  $\pi$ - $\pi$  interactions, as the centroid-to-centroid distance in this structure exceeds the cut-off distance of 4.6 Å. The HgBr-BA structure may have interactions based on the plane-to-plane distances, but the centroid-to-centroid distance is well outside the normal boundaries of  $\pi$ - $\pi$  interactions.

It is clear that aromatic interactions play an important role in the cohesion of most of the structures. Thus, the incorporation of an aromatic group in the organic component provides a route to the establishment of these types of interactions in the structure.

Table 46: Comparison of  $\pi$ - $\pi$  interaction parameters for all structures.

Structure	Centroid-to-centroid (Å)	Plane-to-plane (Å)	Slippage (Å)
MnBr-BA	4.858	-	-
CuCl-BA	3.831	3.381	1.925
CuBr-BA	4.074	3.399	2.246
CdCl-BA	3.851	3.452	1.707
CdBr-BA	3.956	3.498	1.848
ZnCl-BA			
Interaction 1 <sup>i</sup>	3.901	3.497	1.729
Interaction 2 <sup>ii</sup>	3.945	3.633	1.538
HgBr-BA (ionic)	5.029	3.099 <sup>iv</sup>	3.961
CoBr-4ABA	3.851 <sup>iii</sup>	3.384	1.880
CuBr-4ABA	3.953	3.317 <sup>iv</sup>	-
Average	4.125	3.407	2.104
$\sigma$	0.4	0.1	0.8

<sup>i</sup> Ring (C2 C3 C4 C5 C7 C6) – Ring (C2' C3' C4' C5' C7' C6')

<sup>ii</sup> Ring (C9 C10 C11 C12 C13 C14)– Ring (C9' C10' C11' C12' C13' C14')

<sup>iii</sup> Centroids defined through aromatic system

<sup>iv</sup> Centroid-to-plane distance (aromatic rings non-parallel)

## Comparison of Isostructural compounds with each other and with literature structures

CuCl-BA, CuBr-BA, CdCl-BA and CdBr-BA are isostructural to one another. However similar they are, there are small differences between these structures that may provide additional fundamental information about the chemistry relevant to these materials and allow for a possible explanation of the differences observed in their electronic properties. Comparing structural materials of isostructural data is therefore imperative in understanding these materials. There are many parameters that can be considered and will be discussed in this section.

### Unit cell parameters

The lattice parameters of the isostructural compounds are compared in Table 47. It is interesting to note that the metal to metal distances of each structure correspond to the unit cell length along the  $a$ -axis. This is sensible as the polymer is propagated along the  $a$ -direction. It is also interesting to note that replacing a chlorido ligand with a bromide ligand, the  $\beta$  angle also changes slightly for both the copper and cadmium structures' case.



Table 47: Unit cell parameters for the isostructural compounds.

Parameter	CuCl-BA	CuBr-BA	CdCl-BA	CdBr-BA
$a$ (Å)	3.8311(8)	4.0472(8)	3.8512(4)	3.9564(3)
$b$ (Å)	10.702(20)	10.908(2)	11.334(12)	11.5384(9)
$c$ (Å)	11.122(20)	11.288(2)	11.6292(12)	11.6946(9)
$\alpha$ (°)	110.501(4)	110.915(3)	112.617(10)	112.555(10)
$\beta$ (°)	95.756(4)	94.395(3)	95.091(2)	93.834(10)
$\gamma$ (°)	95.147(4)	94.617(4)	98.308(2)	98.452(10)
Cell Vol. (Å <sup>3</sup> )	421.16(16)	460.99(17)	457.83(8)	483.22(6)

Size considerations create the expectation that the unit cell parameters of the family of isostructural compounds should increase as the metal is changed from copper to cadmium, and as the halogeno ligand is changed from chlorido to bromido. One would then expect the unit cells of the isostructural compounds to increase in the sequence CuCl-BA, CuBr-BA, CdCl-BA, CdBr-BA. Figure 99 illustrates the unit cell parameters graphically.

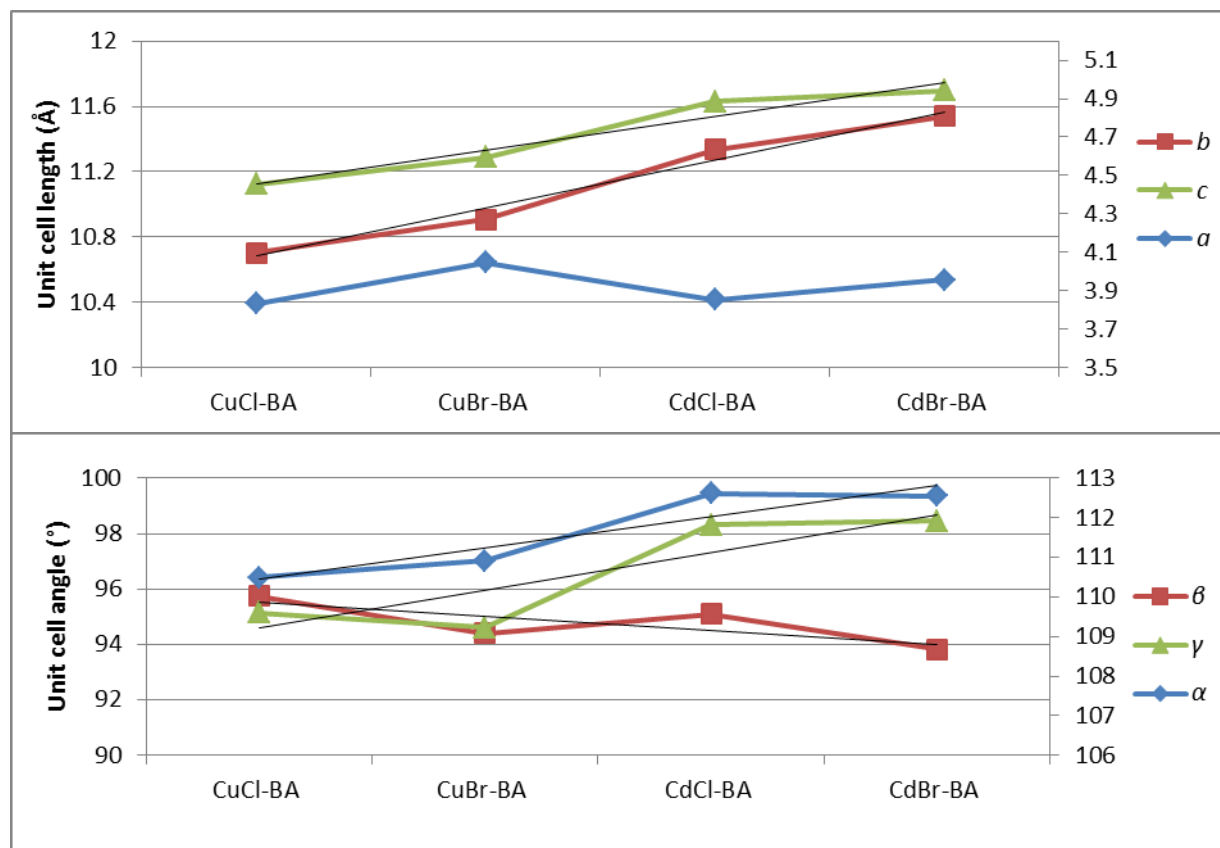


Figure 99: Comparison of isostructural compounds' unit cell parameters.

Both the  $b$ - and the  $c$ - unit cell parameters show the expected trend, i.e. an increase with metal ion size and halogeno ligand size, thus, it is larger for both of the two cadmium containing structures compared to the two copper containing structures. However, in the case of the  $a$ -unit cell parameter, such a clear trend is not observed. This unit cell parameter adopts a larger value for the CuBr-BA structure than for the CdCl-BA and CdBr-BA structure, a trend that deviates from that

observed in the other two unit cell parameters. A possible explanation of this deviation from the expected trend is the fact that Jahn-Teller distortion occurs in the CuBr-BA structure, along the direction of the  $a$ -axis, thus resulting in an elongation in this axis, but not in the other two. It should be kept in mind that the CuCl-BA structure was determined at 100 K, while data for the rest of the structures were collected at room temperature, and this, together with the effect of the smaller chloro ligand, are possible reasons why the effect of the Jahn-Teller distortion on the  $a$ -axis parameter is not clearly evident in the CuCl-BA structure.

The unit cell volumes of the isostructural compounds are illustrated graphically in Figure 100. The unit cell volume shows the same trend in increase in volume size as observed for the  $a$ -unit cell parameter, with the CuBr-BA compound deviating from the trend expected when considering the metal atom and inorganic ligand size.

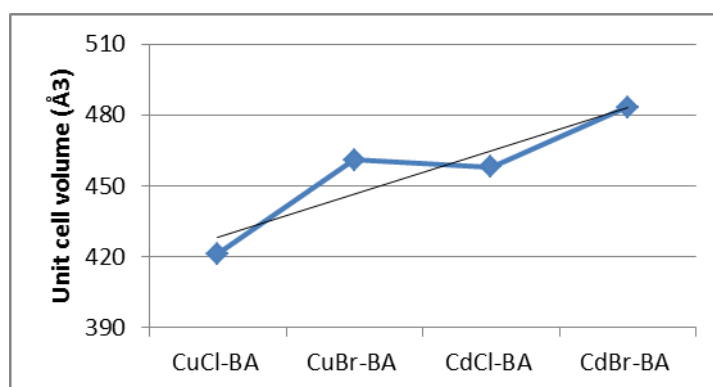


Figure 100: Unit cell volume comparison for the isostructural compounds.

### Intralayer/ Interlayer spacing

Two types of metal spacing are discussed here. The first spacing considered is the spacing between the two rows of metal atoms within the same one-dimensional polymer, thus the distance between the planes through the equatorial ligands of a top and bottom octahedron in the coordination polymer, and will be referred to as the intralayer spacing. The second is the spacing between neighbouring inorganic polymers, and will be referred to as interlayer spacing.

The layered nature of the four isostructural compounds allows for the comparison of the spacing of metal atoms within the layers, i.e. the intralayer spacing, with values listed in Table 48:

Table 48: Intralayer distances of the isostructural compounds

Compound	Interlayer Spacing (Å)
CuCl-BA	2.283
CuBr-BA	2.411
CdCl-BA	2.632
CdBr-BA	2.742

Technically this measurement should be a plane-to-plane distance but as the intralayer planes for the cadmium structures are angled at approximately  $1^\circ$ , a plane-to-plane distance measurement is not possible. An approximation is made here that the M-X2 bond, separating the two layers of the same inorganic polymeric chain is approximately equal to the intralayer spacing. A test measurement was performed with the CuBr-BA and CuCl-BA structures and it was found that the plane-to-plane distance of CuBr-BA is  $2.403 \text{ \AA}$  and the Cu-Br2 bond distance is  $2.411 \text{ \AA}$  while the CuCl-BA distance is  $2.268 \text{ \AA}$  with a Cu-Cl bond distance of  $2.2829 \text{ \AA}$ . The differences of  $0.008 \text{ \AA}$  and  $0.015 \text{ \AA}$  are small enough to assume that using the bond length as the intralayer distance is a reasonable approximation in this case, as the differences in the intralayer spacings are orders of magnitude larger.

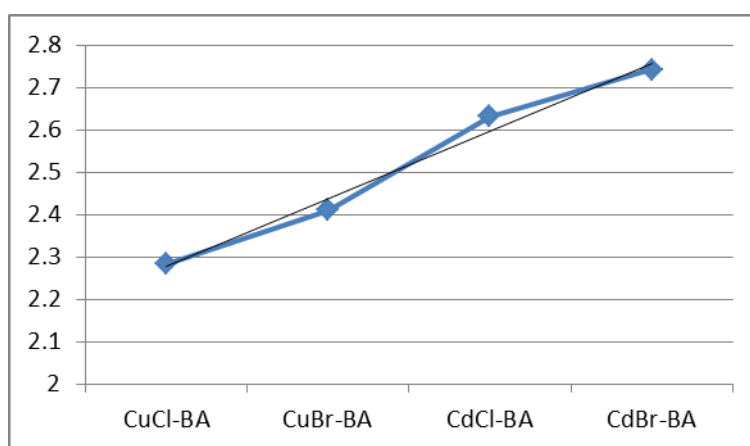


Figure 101: Comparison of the intralayer spacing for the isostructural compounds.

The intralayer spacing increases for the sequence: CuCl-BA, CuBr-BA, CdCl-BA, CdBr-BA. This is expected due to the larger ionic radius of cadmium(II) ( $109 \text{ pm}$ ) compared to that of copper(II) ( $87 \text{ pm}$ ), and similarly for the halides a larger bromide ( $182 \text{ pm}$ ) ionic radius compared to a chloride ( $167 \text{ pm}$ ) ligand.

The interlayer spacing of the isostructural compounds are listed in Table 49.

Table 49 : Interlayer spacing of the isostructural compounds

Structure	Interlayer distance (Å)
CuCl	10.515
CuBr	10.671
CdCl	10.811
CdBr	10.912

The interlayer spacing of the CuCl-BA, CdCl-BA, CuBr-BA and CdBr-BA structures increase in the trend of CuCl-BA, CdCl-BA, CuBr-BA and CdBr-BA, showing the trend expected due to an increase in atom size.

### Benzamide ligand tilt angle relative to inorganic plane

The angle between the aromatic ring plane and the inorganic layer plane, as shown in Figure 102, is listed, for each of the isostructural compounds, in Table 50.

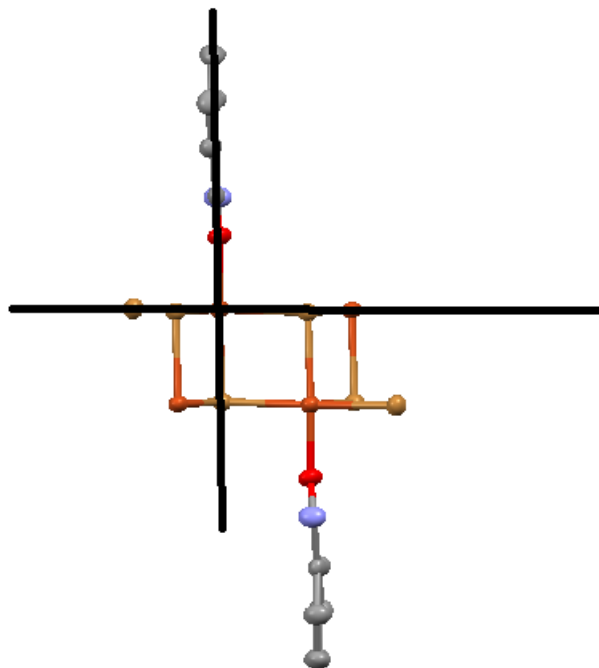


Figure 102: The angle formed between the aromatic ring plane and the inorganic layer plane.

Table 50: Comparison of the angles formed between the aromatic ring plane and the inorganic layer plane.

Structure	Angle (°)
CuCl-BA	71.36 (7)
CuBr-BA	89.8(1)
CdCl-BA	76.43(9)
CdBr-BA	76.5(2)

The angles between the aromatic ring and inorganic polymer of CdCl-BA and CdBr-BA show similar tilt angles of 76°. The CuBr-BA angle is almost perpendicular with respect to the inorganic component. This angle may also be affected by the aromatic interactions between rings and will be discussed later.

### Metal-to-metal distances in the coordination polymer

In the inorganic polymer of the isostructural structures the metal atoms are arranged in two layers as shown in Figure 103. There are three distinct metal-to-metal distances that need to be considered in this case. The first, MM1 is the distance between metal atoms of the same layer. The second MM2 and third MM3 are the distances between neighbouring metals of adjacent layers as shown in Figure

103. MM3 and MM2 may be the same in some cases, but may not in others, especially the copper containing structures.

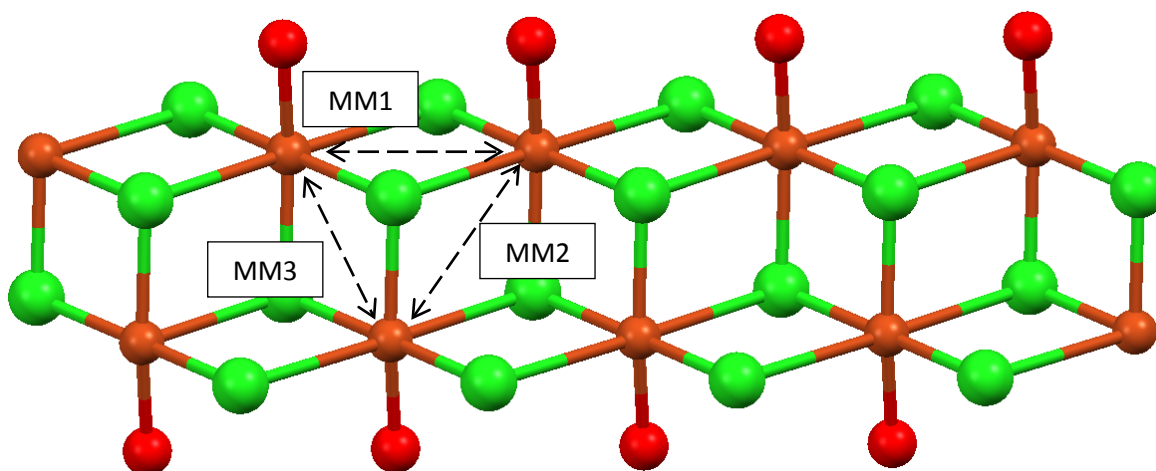


Figure 103: Definition of the Metal-toMetal distances used in this section.

The different metal-to-metal distances for the isostructural compounds are listed in Table 51. Obvious trends are observed here for example, as a chlorido ligand is replaced by a bromido ligand, all of the metal-to-metal distances increase, as expected due to the increase in size of the inorganic ligand. The metal-to-metal distances for the cadmium structures are also slightly larger than their copper analogues, and this is most likely due to the larger ionic radius of cadmium(II) compared to that of copper(II)

Table 51: Comparison of the metal-to-metal distances for the isostructural compounds

Measurement	CuCl-BA	CuBr-BA	CdCl-BA	CdBr-BA
MM1 (Å)	3.8311(7)	4.047(1)	3.8512(5)	3.9564(7)
MM2 (Å)	3.8638(7)	4.023(1)	3.9562(4)	4.0426(7)
MM3 (Å)	3.3809(9)	3.561(1)	3.9276(5)	4.0061(7)

### Ring-to-Ring distances

The  $\pi$ -rings of the benzamide ligand engage in  $\pi$ - $\pi$  stacking as discussed in Chapter Three. The distances these rings are separated differ between structures and may allude some phenomena affecting the structural aspects. The centroid-to-centroid distances, plane-to-plane distances and slippage distances as defined in Chapter Three are listed in Table 52.

Table S2: Comparison of the ring-to-ring distances of the isostructural compounds.

Parameter	CuCl-BA	CuBr-BA	Difference	
<b>Centroid-to-Centroid Distance (Å)</b>	3.831	4.074	0.2430	6.34%
<b>Plane to plane distance (Å)</b>	3.381	3.399	0.0180	0.53%
<b>Slippage distance (Å)</b>	1.925	2.246	0.3210	16.68%
	CdCl-BA	CdBr-BA	Difference	
<b>Centroid-to-Centroid Distance (Å)</b>	3.851	3.956	0.1050	2.73%
<b>Plane to plane distance (Å)</b>	3.452	3.498	0.0460	1.33%
<b>Slippage distance (Å)</b>	1.707	1.848	0.1410	8.26%

Two interesting features emerge from this data. Firstly, the plane-to-plane distances between the rings differ very slightly with the difference between the CuCl-BA and CuBr-BA structures only 0.5% and between the CdCl-BA and CdBr-BA only 1.3%. Secondly, the slippages of the rings with respect to one another show the largest difference with the difference between the CuCl-BA and CuBr-BA structures 17% and between the CdCl-BA and CdBr-BA 8%.

Therefore, we can deduce that if a chlorido ligand is replaced by a bromido ligand two things are likely to occur. Firstly, the plane-to-plane distance; i.e. the distance the ring faces are separated by; remains for all intended purposes, constant. Even comparing the copper and cadmium structures yields a difference of only approximately 0.1 Å. Secondly the slippage of the rings with respect to one another increases significantly. This may indicate that the rings interact strongly at an optimum plane-to-plane distance of approximately 3.4 Å - 3.5 Å and compensate for the increased metal-to-metal distances by simply rotating with respect to one another. This will explain the differences in tilt angle between the aromatic ring and the inorganic plane, observed for the Cd and Cu structures. Thus, in order to keep the plane-to-plane distance approximately constant, the rings compensate by a change in tilt angle relative to the inorganic plane, which also results in a different slippage distance, in going from a cadmium to a copper structure.

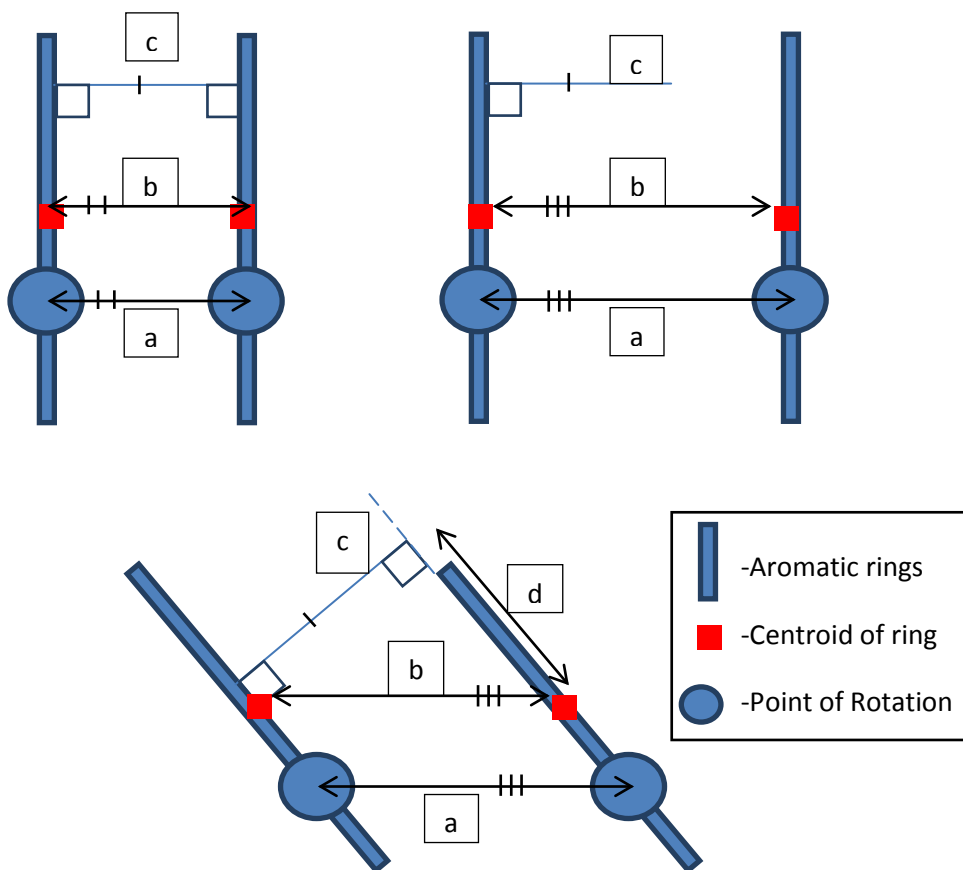


Figure 104: Schematic representing how the plane to plane distance can remain constant with rotational compensation from the aromatic rings. a: metal to metal distance, b: centroid to centroid distance, c: plane to plane distance and d: slippage

As shown in Figure 104, if the metal-to-metal distances increase, one way for the plane to plane distances to remain constant, is if the rings rotate with respect to the axis formed between the metal atoms. With elementary mathematics it is possible to estimate how much the rings have to rotate in order to give the resultant slippage, centroid-to-centroid and plane-to-plane distances observed, as illustrated in Figure 105 and Figure 106.

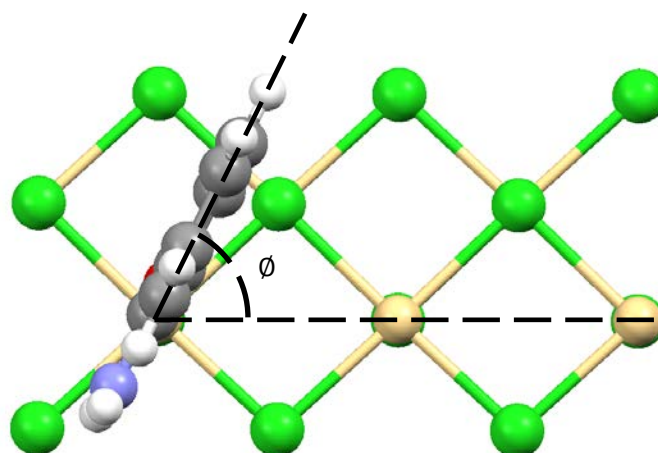


Figure 105: Definition of the angle between adjacent metals and the plane of the aromatic ring.



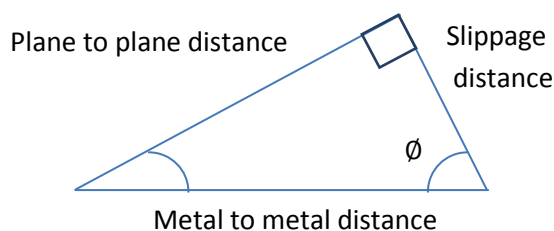


Figure 106: Simplified scheme depicting how to determine the angle that rings rotate to accommodate larger metal to metal distances.

$$\sin \emptyset = \frac{\text{opp}}{\text{hyp}} = \frac{\text{plane to plane distance}}{\text{metal to metal distance}}$$

Calculation of these parameters is trivial as listed in Table 53, but measurement is more complex. Defining the correct planes through the metal atoms and the aromatic rings is difficult due to the slight variation of other angles. The measured angles listed in Table 53 are defined by the following planes:

Plane1: This plane is defined by the six carbon atoms of the aromatic ring.

Plane2: This plane is defined by two adjacent metal atoms exactly as MM1 defined earlier, and the oxygen atom of the coordinated benzamide ligand.

Table 53: Calculated angles of the rings with respect to the metal-metal-oxygen plane

Species	Calculated angle (°)	Measured angle (°)	Difference (°)	% difference
<b>CuCl-BA</b>	61.95	59.97	1.98	3.20
<b>CuBr-BA</b>	57.13	57.54	-0.41	-0.72
<b>CdCl-BA</b>	63.68	64.18	-0.50	-0.79
<b>CdBr-BA</b>	62.15	63.10	-0.95	-1.53

The resultant measured angles compare well to the calculated angles. The change in the angle of the aromatic ring with respect to the metal to metal distances are listed Table 54 for the Cu structures, and the Cd structures, respectively. It is evident from the calculations shown in Table 54 that the angles of rotation of the aromatic rings with respect to the inter-metal distance become smaller with an increase in metal-to-metal distance. Further it shows that the angular increase per distance unit ( $\Delta(\text{Measured angle})/\Delta(\text{Metal-to-metal distance})$ ) is similar for both the copper species:  $-11.26^\circ/\text{\AA}$  and the cadmium species:  $-10.27^\circ/\text{\AA}$ . The calculated change in angle per distance unit ( $\Delta(\text{Calculated angle})/\Delta(\text{Metal-to-metal distance})$ ) of the copper species, however, differs from that of the cadmium species.

Table 54: Calculation of change in angle of aromatic rings with respect to an increase of metal to metal distances.

	CuCl-BA	CuBr-BA	CdCl-BA	CdBr-BA
<b>Metal-to-metal distance (MM1) (Å)</b>	3.8311	4.047	3.8512	3.9564
<b>Calculated angles (°)</b>	61.95	57.13	63.68	62.15
<b>Measured angles (°)</b>	59.97	57.54	64.18	63.10
<b>Calculated</b>				
$\Delta$ (Calculated Angle (MCl-BA to MBr-BA)) (°)		-4.82		-1.54
$\Delta$ (Metal-to-Metal distance (MCl-BA to MBr-BA)) (Å)		0.2159		0.1052
$\Delta$ (Calculated Angle)/ $\Delta$ (Metal-to-Metal distance) (°)/(Å)		-22.32		-14.60
<b>% difference</b>				-34.59 %
<b>Measured</b>				
$\Delta$ (Measured Angle (MCl-BA to MBr-BA)) (°)		-2.43		-1.08
$\Delta$ (Metal-to-Metal distance (MCl-BA to MBr-BA)) (Å)		0.2159		0.1052
$\Delta$ (Measured Angle)/ $\Delta$ (Metal-to-Metal distance) (°)/(Å)		-11.26		-10.27
<b>% difference</b>				-8.79 %

In the calculation of the angles listed in Table 54 it is assumed that the only angle changing upon increasing the metal-to-metal distances is the one calculated. The large discrepancy between the calculated and measured angles relationship to the metal-to-metal distances may arise from the incorrect assumption that the rings' angle with respect to the inorganic layer as defined in Figure 102 remains constant. In Table 50 it is shown that the angle does change drastically between the different compounds. It is possible that the change in angle as defined in Figure 102 along with the change in angle defined in Figure 105 is the compensation mechanism whereby the plane-to-plane distances remain constant for increased metal-to-metal distance. We can therefore conclude that the interactions between the aromatic rings play a large role in establishing observed structures of these materials.

### Comparison of isostructural compounds with literature structures

Several structures related to the CdCl-BA and CdBr-BA structures were found in a search of the CSD, and are listed in Table 55. These compounds contain the same one-dimensional coordination polymer as observed in the structures of CdCl-BA.

Table 55: Analogous structures to isostructural compounds found in the CSD.

CSD Refcode:	Organic composition	Inorganic component	Ionic/Neutral	Dimensionality
MURCDC <sup>i</sup>	Monomethyl-urea	CdCl <sub>2</sub>	Neutral	1D flanked ribbon
ZZZECM01 <sup>ii</sup>	Urea	CdCl <sub>2</sub>	Neutral	1D flanked ribbon
TOPZON <sup>iii</sup>	Dimethylformamide	PbI <sub>2</sub>	Neutral	1D flanked ribbon
DEFHUR <sup>iv</sup>	1,3-thiazolidine-2-thione	CdCl <sub>2</sub>	Neutral	1D flanked ribbon

<sup>i</sup> (Nardelli, Coghi and Azzoni, 1958)

<sup>ii</sup> (Furmanova et al., 1996)

<sup>iii</sup> (Krautscheid, Lekieffre and Besinger, 1996)

<sup>iv</sup> (Kubiak and Glowiak, 1985)

Of these structures found, three contain CdCl<sub>2</sub>. In two of these structures the organic component is coordinated through an amide group and the other coordinated through a sulphur atom. Examples of these are shown in Figure 107. The same flanked one-dimensional inorganic polymer is observed here. It appears that this is a common type of structure formed for neutral coordination compounds of simple amide containing organic molecules and CdCl<sub>2</sub>.

No CdBr<sub>2</sub>, CuBr<sub>2</sub> or CuCl<sub>2</sub> containing compounds with analogous structures could be found in the CSD.

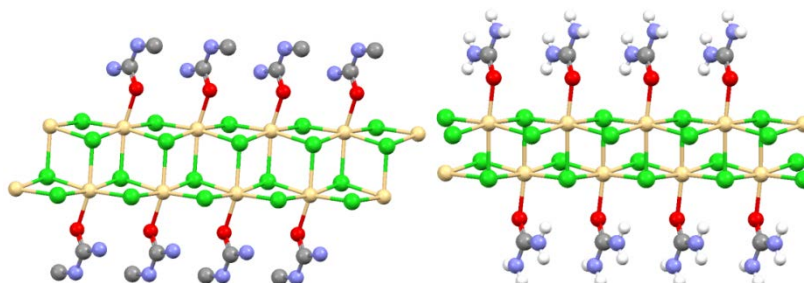


Figure 107: Examples of CdCl<sub>2</sub> containing analogous structures. Structures MURCDC (left) and ZZZECM01 (right) shown (Nardelli, Coghi and Azzoni, 1958) (Furmanova et al., 1996).

Cd-Cl bond distances of the analogous CdCl<sub>2</sub> and amide containing compounds are compared with those of CdCl-BA in Table 56. The DEFHUR structure is not included in Table 56 as the organic ligand is coordinated through a sulphur atom.

Table 56: Analogous CdCl<sub>2</sub> and amide containing compounds' bond distance comparison with CdCl-BA.

	MURCDC	CdCl-BA	Difference	2σ
Cd-Cl (μ <sub>3</sub> )	2.672	2.6816	0.0096	0.021
Cd-Cl (μ <sub>3</sub> )	2.626	2.6276	0.0016	0.024
Intralayer (Cd-Cl (μ <sub>3</sub> ))	2.604	2.632	0.028	0.018
	ZZZEMC01	CdCl-BA	Difference	2σ
Cd-Cl (μ <sub>3</sub> )	2.681	2.6816	0.0006	0.015
Cd-Cl (μ <sub>3</sub> )	2.568	2.6276	0.0596	0.019
Intralayer (Cd-Cl (μ <sub>3</sub> ))	2.775	2.632	-0.1430	0.003

The different Cd-Cl bonds are very similar in length with the only significant difference in the intralayer Cd-Cl(μ<sub>3</sub>) bond distances. This is expected as coordination bonds are typically rigid with respect to a change in bond distance.

The CuCl-BA and CuBr-BA structures are, to our knowledge, the first observed occurrence of a one-dimensional flanked ribbon motif for copper halide neutral coordination compounds.

### Comparison of ZnCl-BA with literature structure

A search of the CSD revealed a structure similar to that of ZnCl-BA, namely [Dibenzamide(κ-O)ZnI<sub>2</sub>] (abbreviated ZnI-BA) (Savinkina et al., 2009). The ZnI-BA structure found in the literature has only one molecule per asymmetric unit in contrast with the ZnCl-BA structure which has two molecules per asymmetric unit, and the two structures are not isostructural. In both the structures, the zinc ion displays a tetrahedral coordination geometry. Overlay of the asymmetric units of the ZnCl-BA and ZnI-BA structures reveals the subtle differences in their geometries, as shown in Figure 108.

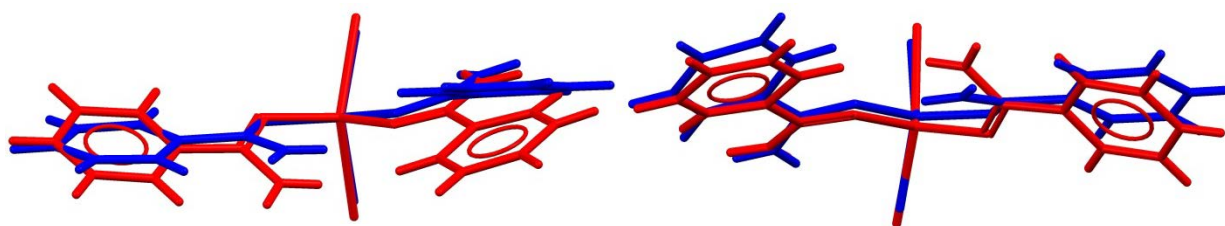


Figure 108: Overlay comparison of the ZnCl-BA (blue) (molecule 1 left and molecule 2 right) and ZnI-BA (red) structures.

Comparison of Zn-O bond lengths, however, indicates that there is a small difference of ( $\pm 0.01\text{\AA}$ ) in bond lengths between the iodido and chlorido species. This difference in bond length is smaller than  $3\sigma$  and is therefore considered negligible. This indicates that the bonding in terms of the organic ligand does not change much with a change in the inorganic ligand. Comparison of other bond lengths shows only significant differences in the halogen-metal bond length. This is expected due to the difference in ionic radii of the different halogens.

The ZnI-BA structure has a larger I1-Zn1-I2 angle of 119.84(4) ° compared to the Cl1-Zn1-Cl2 and Cl3-Zn2-Cl4 angles of 114.7(1) ° and 114.4(1) ° in the ZnCl-BA structure, respectively. This widening of the X-M-X bond angle is most likely due to the iodide ligands' size. This larger X-M-X bond angle also leads to a slightly smaller O1-Zn1-O2 angle of 97.7(2) ° in ZnI-BA compared to the O1-Zn1-O2 angle of 101.6(3) ° and the O3-Zn2-O4 angle of 100.3(3) ° in ZnCl-BA.

**Table 57: Comparison of bond distances (Å) and bond angles (°) of ZnI-BA and ZnCl-BA (This study). Values for both moieties in the asymmetric unit of ZnCl-BA are given. (Standard deviation given in brackets)**

Measurement	ZnI-BA (X=I)	ZnCl-BA (X=Cl)		Average difference
		Moiety 1 (Zn1)	Moiety 2 (Zn2)	
Zn-X(1)	2.531(1)	2.183(4)	2.202(4)	-0.3391(11)
Zn-X(2)	2.527(1)	2.236(3)	2.211(4)	-0.3038(12)
Zn-O(1)	1.954(5)	1.969(6)	1.962(6)	0.012(8)
Zn-O(2)	2.026(5)	2.016(6)	2.012(6)	-0.012(8)
O(1)-Zn-O(2)	97.7(2)	101.6(3)	100.3(3)	3.3(4)
X(1)-Zn-X(2)	119.84(4)	114.7(1)	114.4(1)	-5.3(1)

The molecules of ZnCl-BA and ZnI-BA pack to form similar structures as shown in Figure 110.

Both ZnCl-BA and ZnI-BA crystallize in a  $P2_1/c$  space group and packing of both structures is shown in Figure 110.

The molecular packing is similar when viewed down two directions, but a clear difference in packing can be observed down the third direction.

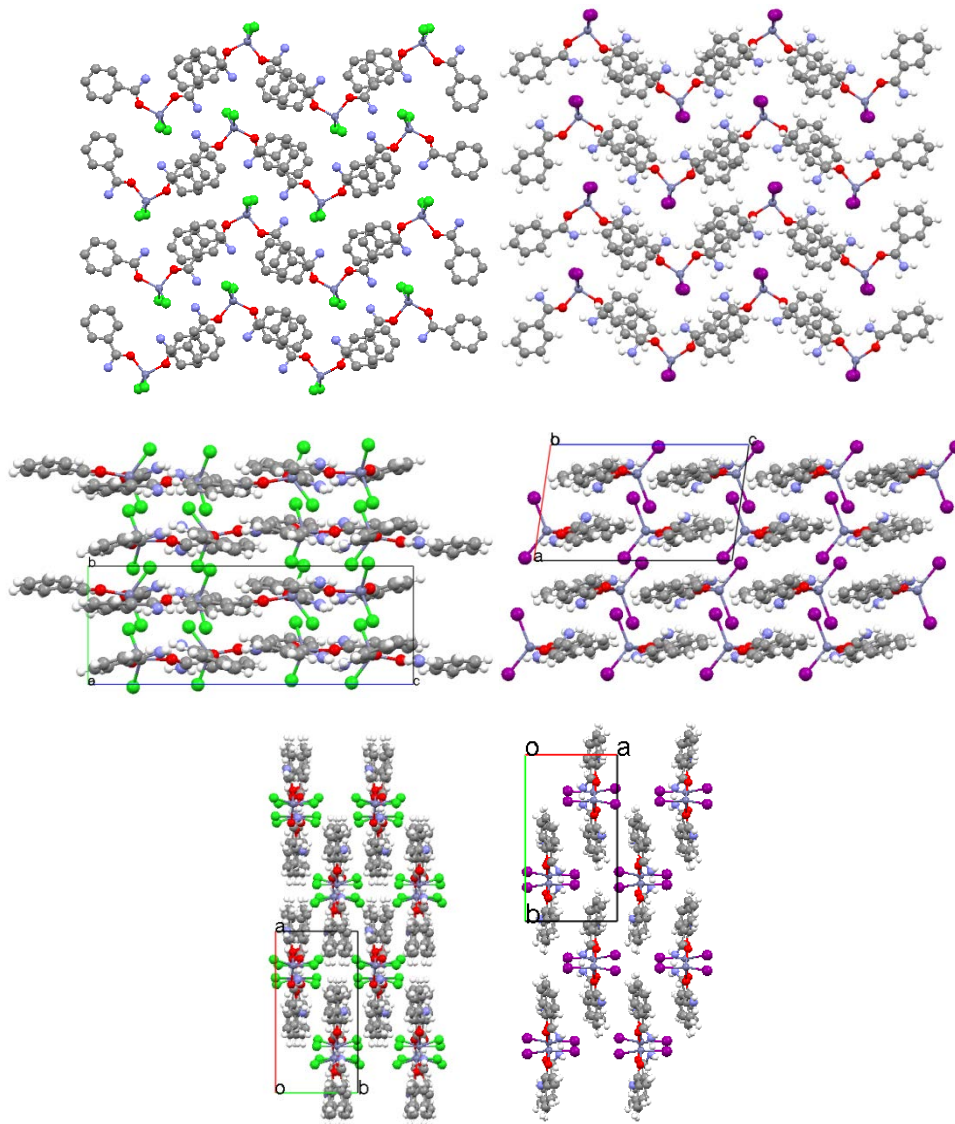


Figure 110: Comparison of packing diagrams of ZnCl-BA (left) with ZnI-BA structure (right). Top: View down *b* for ZnCl-BA and view down *a* for ZnI-BA. Middle: View down *a* for ZnCl-BA and view down *b* for ZnI-BA. Bottom: View down *c* for ZnCl-BA and ZnI-BA

Despite the fact that the compounds are not isostructural, the hydrogen bonding network of both structures is also quite similar as shown in Figure 109.

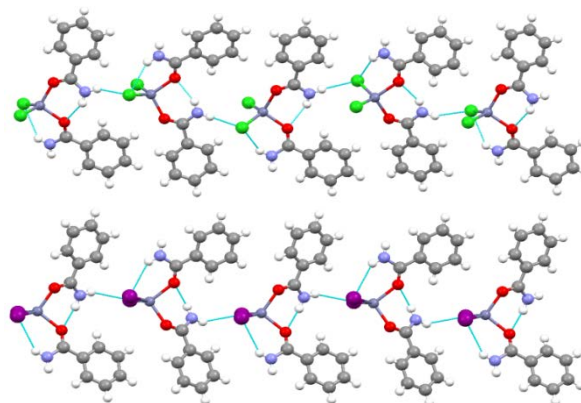


Figure 109: Comparison of ZnCl-BA (top) with similar ZnI-BA structure (bottom)

## Comparison of the CuBr-4ABA structure with literature structures

Several triple helices have been reported in the literature. Han and Hong 2005 reviewed the latest developments in helical coordination polymers. These types of polymers are common to cadmium and mercury containing structures, and less common for other metals. Copper containing helices are very rare, and typically contain tetrahedral or square planar copper (II) ions. Triple helices, similar to the structure of CuBr-4ABA, for any metal are rare. The helices are commonly synthesized by the use of chiral ligands, or non-rigid ligands (Han and Hong, 2005). The CuBr-4ABA structure is not a coordination polymer as the helix is propagated in one direction via hydrogen bonds.

The CuBr-4ABA structure has several unique features. Typical helices have large, freely rotating ligands that can easily adapt to geometrical requirements but in the CuBr-4ABA structure, however, the coordinated organic ligand is small. Therefore mechanism for this molecule adapt to its environment is significantly less than for non-rigid molecules. The copper ion has a trigonal bipyramidal coordination geometry that has not been, to our knowledge, observed in the literature before. The CuBr-4ABA structure is therefore considered a unique structure.

A one-dimensional triple helical hydrogen bonded structure containing small rigid organic molecules hydrogen bonded to one another has never been reported to our knowledge. A one-dimensional triple helical hydrogen bonded structure containing a transition metal that has a trigonal bipyramidal coordination geometry has never been reported in the literature to our knowledge.

## Comparison of Experimental Band Gaps of Isostructural Compounds

The measured band gaps of CdCl-BA, CdBr-BA, CuCl-BA and CuBr-BA are given in Table 58.

A rough guide to band gap ranges suggests that a band gap between 0-3 eV is classified as a semi-conductor and a band gap larger than 4 eV is classified as an insulator.

**Table 58: Comparison of band gap energies as measured by DRS for the isostructural compounds.**

Structure	Band gap energy (eV)	Category
<b>CuCl-BA</b>		
$E_{g1}$	1.33	Semi-conductor
$E_{g2}$	3.00	Semi-conductor
<b>CuBr-BA</b>		
$E_{g1}$	1.33	Semi-conductor
$E_{g2}$	2.37	Semi-conductor
<b>CdCl-BA</b>	4.25	Insulator
<b>CdBr-BA</b>	4.19	Insulator

The band gaps of both the CdCl-BA and the CdBr-BA compounds are large, and fall within the insulator band gap range. The difference in band gap energies between the CdCl-BA and the CdBr-BA structures is 0.06 eV. This implies that the bands associated with the transition from the valence band to the conduction band are very similar in energy, and are most likely similar in composition as well. The metal halide bonding of CdCl-BA should be slightly different from that of CdBr-BA as chlorido and bromido ligands have different chemistries. This suggests that the orbitals involved in the band transitions are not between the metal halide hybrid orbitals. The organic ligands, however, have similar chemistries, with the only difference being the nature of the coordination bonds to the



metal. This would cause a slight difference in energy of the organic components' orbitals and can be observed by comparing the DOS of the CdCl-BA and CdBr-BA structures. The M-O bond distances of CdCl-BA and CdBr-BA are 2.243(3) Å and 2.257(7) Å. The CdBr-BA bond distance is slightly longer than the CdCl-BA bond distance. The bonding between the organic ligand and the cadmium ion is, however, very similar and quantifying the effect of this bonding on the band gap is not within the scope of this study.

Both the CuCl-BA and CuBr-BA compounds were found to have two distinct band gap energies. The primary experimental band gaps of both CuBr-BA and CuCl-BA have band gap energies of 1.33 eV and fall within the semi-conductor range. The secondary band gap of the CuBr-BA compound is 2.37 eV and falls in the semi-conductor range whilst the secondary band gap of the CuCl-BA compound falls in the semi-conductor range. Possible explanations for the presence of two band gaps are included below.

The lower band gap energies of CuCl-BA and CuBr-BA ( $E_{g1}$ ) are measured to be exactly the same while the upper band gap energies of these two compounds ( $E_{g2}$ ) differ by 0.63 eV. The difference in band gap energies of CuCl-BA and CuBr-BA is a little more complicated to interpret as two band gaps are predicted for each structure compared to the cadmium containing structures.

The diffuse reflectance spectra of CuCl-BA and CuBr-BA can be interpreted as follows:

The diffuse reflectance spectra of the CuCl-BA structure will be used as an example to illustrate how the spectra were interpreted. The same arguments apply to the spectra of both structures. From 0 eV to 0.75 eV there is high reflection (low absorption of photons). The photon energy is not high enough to cause excitation of electrons into higher electronic states. In the region of 0.9 eV to 1.4 eV a strong absorption edge is observed. This indicates that the absorption of photons occurs. This region indicates an onset of excitation of electrons from one electronic state to another. This onset occurs at 1.33 eV and this value is accepted to be the band gap of the material.

In typical DR spectra, the region above the band gap is relatively flat and at a high absorbance value. This usually indicates that the photonic energy is adequate to excite the electrons from the valence band to the conduction band, and even higher bands. This usually leaves a continuous, high absorbance tail on DR spectra. In the case of the copper containing compounds, this does not occur.

For the CuBr-BA structure, there is a second reflectance peak at approximately 2 eV. This indicates that there is an energy forbidden region where electronic transitions may not occur. Above this peak again, there is again high absorbance of light, as expected as the photonic energy is high enough to excite electrons from the valence band into many high energy conduction bands.

There are two possible origins of this second forbidden energy region.

The first, illustrated in Figure 111, is that in the primary transition at 1.33 eV, a phonon assisted indirect transition occurs, and this is very likely to be the case. For photonic energies below the band gap, phonon absorption occurs, as shown in red in Figure 111. For photonic energies greater than the band gap, the emission of a phonon occurs as shown in yellow and green and in Figure 111. These different primary transitions correspond to the  $E_g$  (Indirect) band gap. The second transition may then be the direct transition of an electron from the valence to the conduction band as illustrated in purple in Figure 111 corresponding to the  $E_g$  (Direct) band gap. It unclear from the

current DR spectra if this is the case. This second transition is the direct transition of an electron from the valence band to the conduction band without a change in the momentum of the electron, i.e. along the same k-vector. This electron then slowly emits a phonon and returns to the minimum of the conduction band. It is unclear from the DRS spectra if this is occurring. This scenario, however, requires the difference in  $E_g$  (Direct) and  $E_g$  (Indirect) to be more than 1.5 eV indicating that the valence band or conduction band is highly parabolic. Secondly it is expected that the region between the direct and indirect transitions to have continued high absorbance. The spectra however show a significant increase in reflectance between  $E_{g1}$  and  $E_{g2}$ .

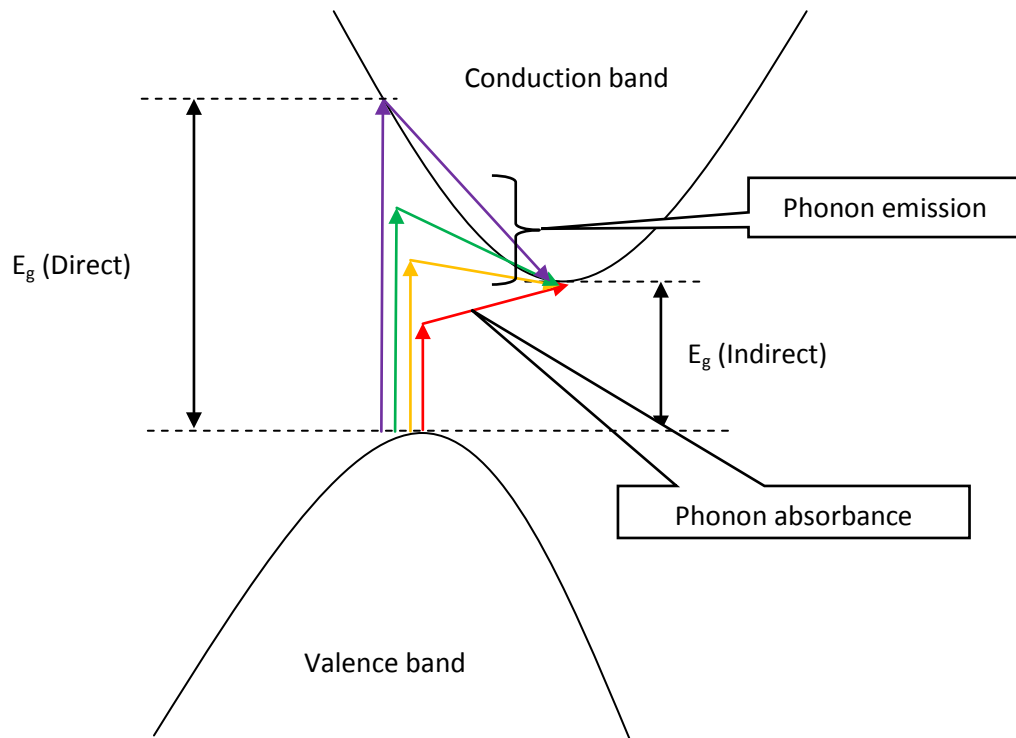


Figure 111: Indirect/direct interband transition.

The second possible origin is if the primary transition from the valence band is to one conduction band, and the secondary transition is from the valence band to another conduction band some finite energy above the first as illustrated in Figure 112. An indirect band gap material is assumed here. The primary transition occurs from the valence band into conduction band 1 through similar phonon assisted transitions as suggested in the first possible origin above shown in red in Figure 112. The phonon assisted transitions result in an overall broadening of the absorption peak as band transitions are possible quite some energy below and above the band gap. The secondary transition involves the excitation of an electron from the valence band into conduction band 2, a discrete second band as shown in purple in Figure 112. As with the primary transition, the phonon assisted transitions result in an overall broadening of the absorption peak. Above this secondary transition the phonic energy is high enough to cause multiple transitions and would result in continuous absorption. This possible origin of the DRS reproduces the trends observed in the absorption and reflectance spectra as shown on the left side of Figure 112. Below the band gap energy, high reflection of light occurs. As the photonic energy approaches the band gap energy, absorbance of the light occurs, indicating the onset electron transitions across the band gap  $E_{g1}$ . At photonic

energies between  $E_{g1}$  and  $E_{g2}$  high reflectance of light occurs and suggests a secondary band gap  $E_{g2}$ . Photonic energies above the  $E_{g2}$  band gap, the high absorbance of photons occur, indicating the continuous transitions from the valence band to many possible conduction bands above the primary and secondary band gaps.

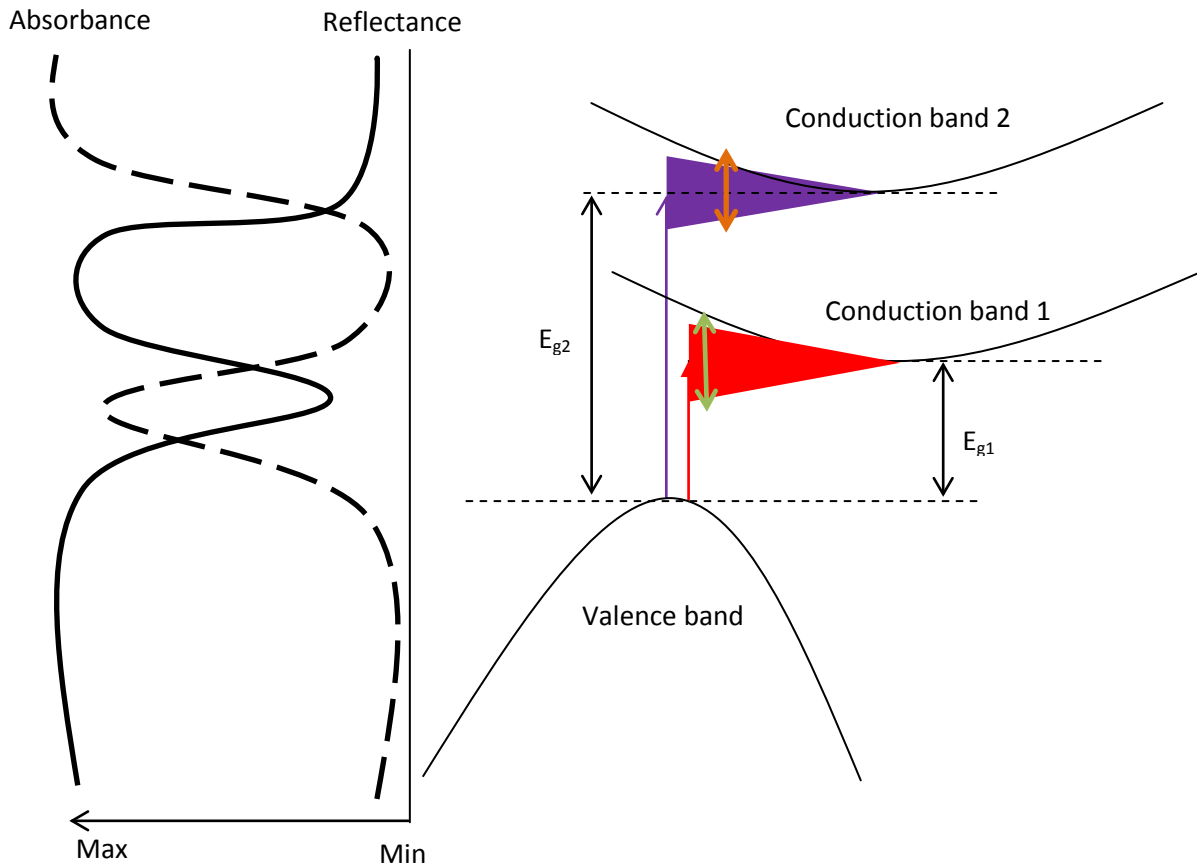


Figure 112: Possible explanation of the diffuse reflectance spectra.

The DRS data does not however give a decisive answer here. The second possible explanation that the copper containing compounds have two band gaps seems to reproduce the experimental spectra the best. However, the first possible explanation of the spectra cannot be excluded simply because the dual-band gap theory seems to fit the experimental data better.

A possible solution to this problem is to record the DRS data at low temperature. This would limit the phonon assisted transitions to a large degree. This would result in much better resolved DR spectra with sharper peaks. This investigation will be carried out in future studies of these materials.

## Comparison of Computational Results for Isostructural Compounds

The initial calculated band gaps of the isostructural compounds are listed in Table 59.

**Table 59: Comparison of calculated band gap energies for the isostructural compounds.**

Species	Band gap energy (eV)
CuCl-BA	1.107
CuBr-BA	0.904
CdCl-BA	3.492
CdBr-BA	3.401

The band gap values reported in Table 59 are calculated by the Materials Studio package. The criterion for a band gap is defined as the energy difference between the highest filled band (valence band) and the lowest unoccupied band (conduction band).

The CdCl-BA and CdBr-BA structures have similar calculated band gaps with the difference between them only 0.091 eV. The CuCl-BA and CuBr-BA structures also have similar calculated band gaps, with a difference of 0.203 eV. The band gaps of the cadmium structures differ significantly from those of the copper structures.

### Comparison of Cadmium Containing Compounds

The calculated band gaps of both the CdCl-BA and CdBr-BA compounds put them in the insulator category and the experimentally obtained band gaps are also classified as insulators.

The band structures of CdCl-BA and CdBr-BA are shown in Figure 89. The band structures of CdCl-BA and CdBr-BA are both flattened and appear very similar. Both CdCl-BA and CdBr-BA have calculated indirect band gaps as an electronic transition cannot occur between the maximum of the valence band to the minimum of the conduction band along the same k-vector. The DOS for both CdCl-BA and CdBr-BA are shown in Figure 90 & 91. Both the CdCl-BA and CdBr-BA structures' valence bands are comprised of O-2p character, C-2p character, a small amount of N-2p character and some Cl-2p. The valence orbitals for CdCl-BA and CdBr-BA are shown in Figure 92. The valence bands of both CdCl-BA and CdBr-BA consist of the benzamide ligand's aromatic  $\pi$ -bonding orbitals. The conduction bands of both structures are the anti-bonding aromatic  $\pi$ -anti-bonding orbitals as illustrated in Figure 92.

The electronic transition from the valence band to the conduction band is therefore from the organic component's bonding orbitals to the organic component's anti-bonding orbitals.

In the band gap structure of these materials, the states that have a large contribution from the metal ion lie at energy levels much lower than the Fermi level. This means that the metal halide portion of the structure does not exhibit electronically conducting or semi-conducting behaviour.

### Comparison of Copper Containing Compounds

The band structures of CuCl-BA and CuBr-BA are shown in Figure 113. The band structures of CuCl-BA and CuBr-BA are very similar, with the only visible difference the slight compression of bands of the CuBr-BA structure compared to the CuCl-BA structure. The CuCl-BA structure has a calculated primary direct band gap, whereas the CuBr-BA has a calculated primary indirect band gap.

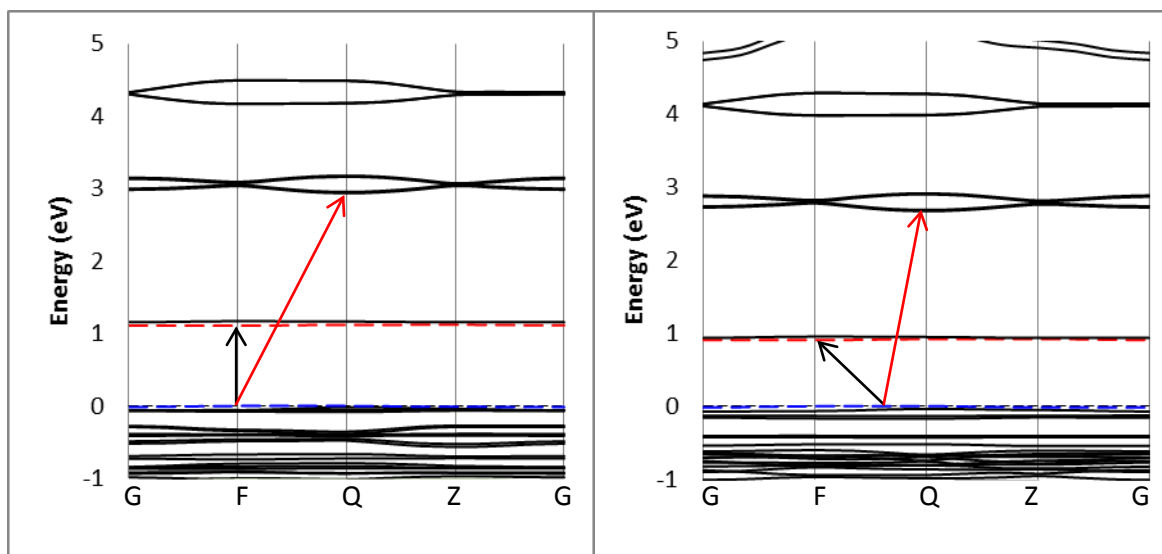


Figure 113: Calculated band structures of CuCl-BA (left) and CuBr-BA (right). The black arrows indicate the electronic transitions from valence band to conduction band 1 ( $E_{g1}$ ) and red arrows indicates the electronic transitions from the valence band to the second conduction band ( $E_{g2}$ ). The red band indicates a  $\beta$ -orbital whilst a blue band indicated an  $\alpha$ -orbital.

Further inspection of the CuCl-BA and CuBr-BA band structures revealed that there are two additional calculated conduction bands at a band gap of approximately 1 eV for both structures (conduction band 1), and additional conduction bands 2 eV above the first conduction bands (conduction band 2). The second band gaps predicted by the band structures of the copper containing compounds are not reported by the Materials Studio software package as band gaps, as the second band gap does not adhere to the criterion of a band gap defined in Materials Studio; the difference between the highest occupied band and lowest unoccupied band. These values were manually calculated by subtracting the energy at the lowest point of the third band (conduction band 2) from the highest energy point of the valence band. These secondary band gaps are listed as  $E_{g2}$  in Table 60.

In the case of both CuCl-BA and CuBr-BA the valence band is a metal halide hybrid  $\alpha$ -orbital whereas the conduction bands at 1.33 eV are both metal-halide  $\beta$ -orbitals. This implies that for the 1 eV band gap in both structures, the primary electronic transition occurs from the metal halide hybrid  $\alpha$ -orbital or a  $\beta$ -orbital slightly below the HOMO to the metal-halide hybrid  $\beta$ -orbitals.

The secondary electronic transition from the valence band into the second set of conduction bands (conduction band 2) with band gap energy  $E_{g2}$  occurs though the electronic transition from the metal-halide hybrid bonding orbitals into the benzamide's aromatic anti-bonding  $\pi$ -orbitals as shown in Figure 114 and Figure 115. In the CuBr-BA compound the aromatic bonding orbitals are spread throughout the aromatic system whereas in the CuCl-BA compound, the orbitals are more localized about the amide group.

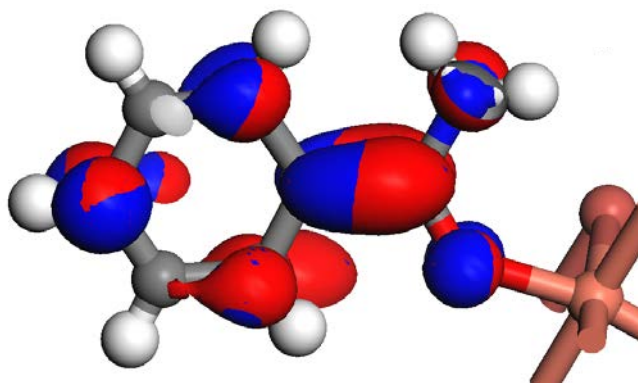


Figure 114: Upper conduction band orbitals of CuBr-BA. The  $\alpha$ -orbitals are shown in blue and the  $\beta$ -orbitals are shown in red.

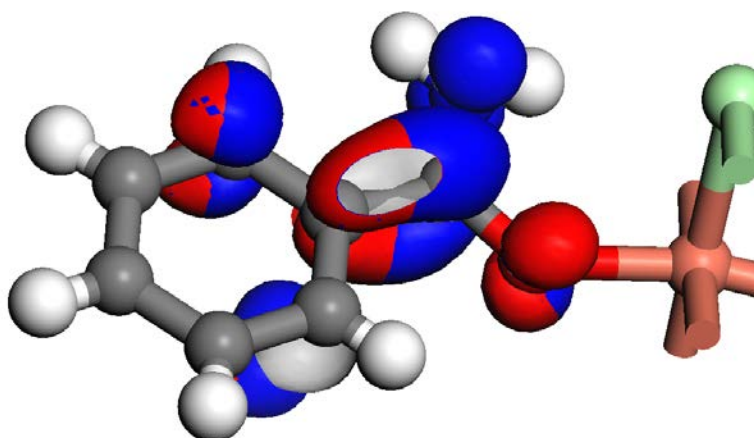


Figure 115: Upper conduction band orbitals of CuCl-BA. The  $\alpha$ -orbitals are shown in blue and the  $\beta$ -orbitals are shown in red.

The significance in the difference of the arrangement of the anti-bonding orbitals is unclear, and therefore the difference in energy of the secondary band gap energies is also unclear.

The band gap between valence band and the secondary conduction band is 2.96 eV for CuCl-BA and 2.68 eV for CuBr-BA. This suggests that the copper containing compounds are possibly dual-band gap semiconductors, which agrees with the experimental observation of two band gaps for the compounds.

The summary of all calculated band gaps are given in Table 60.

**Table 60: Summary of calculated band gap energies for the isostructural compounds.**

<b>Species</b>	<b>Band gap energy (eV)</b>
<b>CuCl-BA</b>	
$E_{g1}$	1.107
$E_{g2}$	2.96
<b>CuBr-BA</b>	
$E_{g1}$	0.904
$E_{g2}$	2.68
<b>CdCl-BA</b>	3.492
<b>CdBr-BA</b>	3.401

The DFT results indicate that the cadmium band gaps are associated with a transition from the organic ligand's bonding orbitals into the organic ligand's anti-bonding orbitals and as a result is predicted to be an insulator. For the copper containing compounds, the DFT theory predicts a dual band gap where the first transition occurs from the metal halide hybrid  $\alpha$ -orbital into the metal halide hybrid  $\beta$ -orbital. The second transition is predicted to occur from the metal halide hybrid  $\alpha$ -orbital into the anti-bonding orbitals of the organic component. As a result of this, the first transitions (from the metal hybrid  $\alpha$ -orbital into the metal hybrid  $\beta$ -orbital) of the CuCl-BA and CuBr-BA structures are classified as a semi-conductor and conductor respectively with band gaps similar to silicon. The second transitions of the CuBr-BA and CuCl-BA structures (from the metal hybrid  $\alpha$ -orbital to the anti-bonding aromatic orbitals of the organic ligand) are classified as semi-conductors.

## Comparison of calculated and measured band gap results for isostructural compounds

The calculated and experimental band gap energies of the isostructural compounds are compared in Table 61.

The difference between the calculated and experimental band gaps is relatively large, but this is to be expected due to the underestimation of the band gap by DFT methods, which has been reported widely. The calculated band gaps predict semi-conductive material properties and the experimental results indicate insulator like material properties. The experimental and calculated band gaps are on the boundary between the classification of a material as a semi-conductor and insulator. The definition of the boundary between semi-conductors and insulators is however not clearly defined. Therefore this difference in predicted electronic properties is not considered to be significant.

It is interesting to note that there are similar trends between the experimental and calculated band gaps.



Table 61: Comparison of experimental and calculated band gaps.

Species	Band gap energy (eV)				
	Calculated		Experimental		Difference
<b>CuCl-BA</b>					
$E_{g1}$	1.107	Semi-Conductor	1.33	Semi-Conductor	-0.223
$E_{g2}$	2.96	Semi-conductor	3.00	Semi-Conductor	-0.04
<b>CuBr-BA</b>					
$E_{g1}$	0.904	Conductor	1.33	Semi-Conductor	-0.426
$E_{g2}$	2.68	Semi-Conductor	2.37	Semi-Conductor	0.31
<b>CdCl-BA</b>	3.492	Semi-Conductor	4.25	Insulator	-0.758
<b>CdBr-BA</b>	3.401	Semi-Conductor	4.19	Insulator	-0.789

For the CdCl-BA and CdBr-BA structures the calculated band gaps predict a 0.091 eV difference, whilst the difference in the experimental band gaps is only 0.06 eV. The calculated band gaps predict that the CdCl-BA compound has the largest band gap, and CdBr-BA compound a slightly lower band gap. This is confirmed by the experimental band gaps where the CdCl-BA compound has a larger band gap, and the CdBr-BA compound has a slightly smaller band gap. The difference between the experimental and calculated band gaps for the cadmium containing compounds is very similar, with both being underestimated by approximately 17%. Underestimation of the band gap by as much as 40% may be expected according to the literature (Perdew and Levy, 1983).

The trends observed for the CuCl-BA and CuBr-BA band gap values are very interesting. The calculated band gaps underestimate the band gaps by about 17 % for CuCl-BA and 32% for CuBr-BA. The second band gaps are underestimated, by 1.33% for CuCl-BA and 13% for CuBr-BA. For both the CuCl-BA and CuBr-BA compounds two band gaps are predicted, and two band gaps are observed. Moreover, the values of these band gaps are estimated relatively well. The second band gap of CuBr-BA, for example, is smaller than the second band gap for the CuCl-BA structure in both the experimental and calculated band gaps.

The large difference in the calculated and experimental band gap energies of the copper species may be attributed to the simple assumption made that the copper containing structures are treated as ferromagnetic materials in the DFT models. To improve the band gap estimation several other magnetic structures need to be considered and will be treated in future work.

The band gaps for all of the isostructural compounds replicate the experimental band gaps quite well, and it is assumed that the theoretical electronic structure is quite reasonably approximated for the isostructural compounds.

We can therefore conclude, based on the calculated and experimental evidence, that the calculated electronic band structures, orbital approximations and band gaps represent a reasonable approximation of the true electronic states of the isostructural compounds.

## Composition effect on properties

The differences between the experimental and theoretical band gaps of the two different cadmium containing structures are 1.4% and 2.6% respectively. Based on this it can be concluded that the halide composition difference of the CdCl-BA and CdBr-BA does not alter the electronic properties of the material significantly.

The differences in experimental and theoretical band gaps of the first possible band gap of the copper containing structures are 18% and 0%. The difference in experimental and theoretical band gaps of the second possible band gap is 9% and 21%. Therefore we can conclude that for the copper containing structure, the halide composition of the material significantly affects the electronic properties.

The theoretical and experimental band gap values for the cadmium and copper containing compounds differ drastically. It can therefore be concluded that the metal composition in the material has a drastic effect on the electronic properties of these types of materials. The copper and cadmium metal have similar coordination chemistry, as similar structures are observed. Their electronic behaviour are however very different. It may be useful in future to compare the electronic properties of compounds containing metal atoms from the same row with one another. The valence shell would then at least be constant for each class of metal compared.

Despite the problems associated with the results obtained from the DFT calculations, these calculations proved to be useful in predicting the band gap energies to a moderate degree. Due to the shortfalls in DFT, the exact estimation of band gaps will likely not be obtained in the near future. The DFT method does however give very comparable results.

The DFT theory also provided insight into the electronic phenomena contributing to the observed band gap energies by the analysis of the density of states and the orbitals involved in the electronic transitions.

## Bibliography

Blagden, N., Davey, R., Dent, G., Song, M., David, W., Paulham, C. and Shankland, K. (2005) 'Woehler and Liebigs Revisited: A small molecule reveals its secrets- the crystal structure of the unstable polymorph of benzamide solved after 173 years', *Cryst. Growth Des.*, vol. 5, no. 6, pp. 2218-2224.

Blake, C.C.F. and Small, R.W.H. (1972) 'The Crystal Structure of Benzamide', *Acta Crystallogr., Sect. B: Struct. Sci.*, vol. 28, pp. 2201-2206.

Cotton, F.A., Wilkinson, G. and Gaus, P.L. (1976) *Basic Inorganic Chemistry*, 3<sup>rd</sup> edition, John Wiley & Sons.

Furmanova, N.G., Sulaimankulova, D.K., Resnyunskii, V.F., Sulaimankulov, K.S. (1996) 'Crystal structure of a cadmium chloride carbamide complex  $CdCl_2 \cdot CO(NH_2)_2$ ', *Kristallografiya(Russ.)(Crystallogr.Rep.)*, vol. 41, p. 669.

Gao, Q., Jeffrey, G.A., Ruble, J.R. and McMullan, R.K. (1991) 'A single-crystal neutron diffraction refinement of benzamide at 15 and 123 K', *Acta Crystallogr., Sect. B: Struct. Sci.*, vol. 47, pp. 742-745.

- Han, L. and Hong, M. (2005) 'Recent advances in the design and construction of helical coordination polymers', *Inorg. Chem. Comm.*, vol. 8, pp. 406-419.
- Janiak, C. (2000) 'A critical account on  $\pi$ - $\pi$  stacking in metal complexes with aromatic nitrogen-containing ligands', *J. Chem. Soc., Dalton Trans.*, pp. 3885-3896.
- Krautscheid, H., Lekieffre, J.F. and Besinger, J. (1996) *Z. Anorg. Allg. Chem.*, vol. 622, p. 1781.
- Kubiak, M. and Glowiak, T. (1985) 'Structure of catena-poly[(1,3-thiazolidine-2-thionecadmium)--chloro-3-chloro]', *Acta Crystallogr. C.*, vol. 41, p. 1580.
- Nardelli, M., Coghi, L. and Azzoni, G. (1958) 'The crystal and molecular structure of bistiourea-cadmium formate' *Gazz. Chim. Ital.*, vol. 88, p. 235.
- Penfold, B.R. and White, J.C.B. (1959) 'The crystal and molecular structure of Benzamide', *Acta Crystallogr.*, vol. 12, pp. 130-135.
- Perdew, J.P. and Levy, M. (1983) 'Physical content of the exact kohn-sham orbital energies: Band gaps and derivative discontinuities', *Phys. Rev. Lett.*, pp. 51, 20: 1884-1887.
- Savinkina, E.V., Buravlev, E.A., Zamilatskov, I.A., Albov, D.V., Kravchenko, V.V., Zaitseva, M.G. and Mavrin, B.N. (2009) 'Zinc iodide complexes of propaneamide, benzamide, dimethylurea, and thioacetamide: syntheses and structures' *Z. Anorg. Allg. Chem.*, vol. 635, p. 1548.
- Takeuchi, H., Sato, M., Tsuji, T., Takashima, H., Egawa, T. and Konaka, S. (1999) 'Molecular structure of benzamide as studied by gas-phase electron diffraction', *J. Mol. Struct.*, vol. 485-486, pp. 175-181.

# Chapter Six – Conclusions and Future Work

---

## Conclusions

The conclusions drawn from the study of the hybrid materials formed from the combination of divalent transition metal halides and benzamide or 4-aminobenzamide are summarised in this section.

It was found that the synthetic molar ratio employed and the molar ratio observed in the crystal structures are not always the same. This could be due to the formation of a stable product with a specific ratio of organic to inorganic component. In addition, kinetic effects may also play a role.

The benzamide ligand was found to always coordinate and protonate through the amide group's oxygen atom, whereas the 4-aminobenzamide ligand coordinates exclusively through the amine nitrogen atom. The two 4-aminobenzamide containing compounds both contain aquo ligands coordinated to the central metal atom, but this phenomenon is not observed in the benzamide ligand containing compounds.

The metal ions were found to have several types of coordination geometries including tetrahedral, trigonal bipyramidal and octahedral, and an anionic coordination polymer with mixed octahedral and tetrahedral metal ion geometries was observed in the ionic compound of benzamide and  $\text{HgCl}_2$ . The most prominent geometry observed is the octahedral geometry.

Hydrogen bonding interactions are important in all the structures. In the case of the neutral benzamide containing compounds the  $\text{NH}_2$  group participates in intramolecular and intermolecular hydrogen bonding, and for the 4-aminobenzamide containing structures, the amide group of the 4-aminobenzamide ligand engages in hydrogen bonding. In addition to hydrogen bonding interactions, aromatic  $\pi$ - $\pi$  interactions between the organic aromatic rings of the organic component were observed in a large number of the structures. In the isostructural compounds the plane-to-plane distances of the aromatic rings were on average between 3.4 Å to 3.5 Å, and it was found that the aromatic rings tilt and rotate with respect to the inorganic polymer to find an optimal positioning as to keep the plane-to-plane distance within this range.

The one-dimensional flanked ribbon inorganic polymer observed for the isostructural compounds has been observed for other cadmium containing compounds reported previously in the literature, but to our knowledge is novel for copper halide containing compounds.

The  $\text{CuBr-4ABA}$  structure exhibits a unique, one-dimensional hydrogen bonded helix, with three of these helices hydrogen bonded together to form a triple helix structure. This type of hydrogen bonded one dimensional triple helix has never been reported before for these types of materials, to our knowledge.

Experimental measurements of the band gaps of the isostructural compounds indicate that CdCl-BA and CdBr-BA have band gap energies of 4.25 eV and 4.19 eV respectively and are classified as semi-conductors. In the case of the CuCl-BA and CuBr-BA compounds, two band gaps were measured for each of the structures experimentally. For the CuCl-BA band gap energies of 1.33 eV and 3.00 eV were measured and for the CuBr-BA structure, band gap energies of 1.33 eV and 2.37 eV were measured.

Theoretical DFT calculations indicate that the CdCl-BA and CdBr-BA compounds fall within the semi-conductor range with calculated band gap energies of 3.492 eV and 3.500 eV respectively. The DFT calculations predicted two band gaps for the CuCl-BA and CuBr-BA compounds. The values of the bands gaps for these compounds fall within the 0.904 eV to 1.107 eV and 2.68 eV and 3.00 eV range.

Experimental and theoretical band gaps of CdBr-BA and CdCl-BA are relatively similar. Transitions from the valence band to the conduction band occurs selectively in the organic ligand and therefore CdCl-BA and CdBr-BA are classified as semi-conductors.

The experimental and theoretical band gaps for CuCl-BA and CuBr-BA indicate two distinct band gaps. It is unlikely that the experimentally observed band gaps are indicative of transitions that occur to and from the same bands based on the high difference in energy of the two transitions. Exclusion of this possibility is however beyond the scope of this work and will be included in future work. A possible hypothesis is that the transitions for the first band gap occur in the metal halide hybrid orbitals whereas the second transition occurs from the metal halide hybrid orbitals to the organic ligand anti-bonding orbitals. CuCl-BA and CuBr-BA are both classified as possible dual-band gap semiconductors.

The halide composition difference does not significantly influence the electronic properties of the cadmium containing compounds, but significantly affects the electronic properties of the copper containing structures. The metal ion composition has a drastic effect on the electronic properties of a material, as evidenced by the difference in the electronic properties of the isostructural Cd and Cu containing materials.

## Future work

The powder products obtained in the synthetic procedures which yielded no good quality single crystals will be studied by powder X-ray diffraction, and this will be made possible by purchasing new, plastic sample holders that will not react with the unreacted metal halide reagents. The obtained powder diffraction pattern will be compared with the diffraction patterns of the reagents, and also with the powder diffraction patterns calculated from the single crystal structure data of compounds in this family. This will allow for the identification of unreacted reagents, and also allow for the identification of powder products that are isostructural to the materials that have already been characterised by single crystal X-ray diffraction.

The magnetic copper containing compounds will be characterized via SQUID (Superconducting Quantum Interference Device) magnetometry, in an attempt to assess the validity of the ferromagnetic assumption made as part of the DFT calculations in this work.

The electronic properties of the isostructural compounds will be investigated further, specifically for the copper containing compounds, by “current-voltage” measurements performed on a single crystal, to provide additional insight into the electronic behaviour of these materials, and to understand the two band gap behaviour of the copper containing compounds more clearly.

The conductivity of individual “fibres” of the copper containing polymers will be measured through Atomic Force Microscopy (AFM) in order to assess the copper containing compounds’ capacity as molecular wires.

The range of metals ions investigated will be broadened to the second and third transition metal rows in order to reduce the variable that different  $d^n$  metals introduce. It may be more systematic to compare the structures of compounds containing metals that fall in the same group.